



**HAL**  
open science

# Design of molecular systems for artificial pattern formation and gene regulation

Anis Senoussi

► **To cite this version:**

Anis Senoussi. Design of molecular systems for artificial pattern formation and gene regulation. Biological Physics [physics.bio-ph]. Sorbonne Université, 2020. English. NNT: . tel-02963319v1

**HAL Id: tel-02963319**

**<https://theses.hal.science/tel-02963319v1>**

Submitted on 10 Oct 2020 (v1), last revised 28 May 2021 (v2)

**HAL** is a multi-disciplinary open access archive for the deposit and dissemination of scientific research documents, whether they are published or not. The documents may come from teaching and research institutions in France or abroad, or from public or private research centers.

L'archive ouverte pluridisciplinaire **HAL**, est destinée au dépôt et à la diffusion de documents scientifiques de niveau recherche, publiés ou non, émanant des établissements d'enseignement et de recherche français ou étrangers, des laboratoires publics ou privés.



École doctorale 564 : Physique en Île de France

## THÈSE DE DOCTORAT

présentée par

**Anis SENOUSI**

pour obtenir le grade de

**DOCTEUR DE SORBONNE UNIVERSITÉ**

### **Design of molecular systems for artificial pattern formation and gene regulation**

Thèse soutenue le 11/09/2020 devant le jury composé de :

Hélène DELANOË-AYARI	Rapportrice
Francesc SAGUÉS	Rapporteur
Hélène BERTHOUMIEUX	Examinatrice
Zoher GUEROUI	Examinateur
Yannick RONDELEZ	Examinateur
André ESTÉVEZ-TORRES	Directeur de thèse
Jean-Christophe GALAS	Co-encadrant

Laboratoire Jean Perrin  
UMR 8237 (SU/CNRS)  
Institut de Biologie Paris-Seine  
Sorbonne Université





## Abstract

Can we engineer matter that shapes itself? To elucidate this question we have built molecular systems that mimic two essential features of life: pattern formation and gene regulation. We have designed an active reconstituted system composed of kinesin clusters and microtubules. Depending on their concentrations, we have rationally reported dynamic patterns such as local and global contractions, active flows and a new 3D regular pattern consisting of a corrugated active nematic sheet with tunable wavelength and dynamics. We have combined this active fluid with a programmable chemical reaction network composed of short DNA strands and enzymes. In particular we have observed the propagation of a DNA reaction-diffusion front in an active environment; they form then a complex system in which two patterning mechanisms — active matter and reaction-diffusion — are coupled to shape a material, which is reminiscent of morphogenetic processes happening during embryo development. Finally, we have used de novo engineered RNA translational regulators and have showed that a cell-free transcription-translation system composed of recombinant proteins can provide valuable information about the performances of in silico designed riboregulators. We hope that these approaches will help in the design of out-of-equilibrium materials with new properties.

## Résumé

Comment concevoir des matériaux qui se façonnent eux-même ? Nous proposons dans cette thèse de répondre en partie à cette question en construisant des systèmes moléculaires imitant deux caractéristiques essentielles de la vie : la formation de formes et motifs et la régulation génétique. Nous avons reconstitué un système actif composé de multimères de kinésines et de microtubules. Ainsi, nous avons décrit le comportement d'un tel système en fonction d'un nombre restreint de paramètres : contractions locales et globales du réseau de microtubules, écoulement actif des faisceaux de microtubules ou encore formation d'une nouvelle structure 3D constituée d'une feuille nématique ondulée. Ce fluide actif a ensuite été combiné avec des réactions chimiques programmables composées de courts brins d'ADN et d'enzymes. Ce système donne naissance à un front réaction-diffusif d'ADN capable de se propager dans un environnement actif, montrant ainsi la possibilité de créer un système complexe où deux mécanismes d'auto-organisation — matière active et réaction-diffusion — sont mis en œuvre en même temps. Enfin, nous avons utilisé des régulateurs ARN de la traduction conçus de novo. Nous avons montré qu'un système de transcription-traduction composé de protéines recombinantes fournit des informations précieuses sur les performances de tels riborégulateurs conçus in silico. Nous espérons que ces approches contribueront à la conception de matériaux hors-équilibre dotés de propriétés uniques.

## List of Figures

1.1	D'Arcy's theory of deformation and conserved <i>Hox</i> genes . . . . .	6
1.2	DNA and the genetic code . . . . .	7
1.3	Chapter 2: Active matter and reaction-diffusion, two self-organization mechanisms in molecular systems . . . . .	12
1.4	Chapter 3: Self-organization of active matter composed of microtubules and kinesins	13
1.5	Chapter 4: Coupling DNA reaction-diffusion front and a cytoskeletal active gel . .	13
1.6	Chapter 5: RNA control of genetic expression in a cell-free system . . . . .	14
2.1	Diversity of living active matter systems . . . . .	20
2.2	Artificial active matter systems . . . . .	21
2.3	Structure and localization of the main components of the cytoskeleton . . . . .	24
2.4	Force generation by (de)polymerization . . . . .	26
2.5	Kinesin hydrolyzes ATP and walks on microtubules . . . . .	27
2.6	Molecular motors . . . . .	28
2.7	Reconstituted active matter systems . . . . .	31
2.8	The Lotka-Volterra oscillator . . . . .	37
2.9	Synthetic reaction-diffusion patterns . . . . .	39
2.10	In vitro reconstituted reaction-diffusion systems - The Min system . . . . .	41
2.11	In vitro reconstituted reaction-diffusion systems - Cell-free TXTL fronts . . . . .	42
2.12	DNA strand displacement. . . . .	43
2.13	Basic reactions with the PEN-DNA toolbox . . . . .	45
2.14	Analogy between a gene regulatory network and the PEN-DNA toolbox . . . . .	46
2.15	Examples of reaction networks designed with the PEN-DNA toolbox . . . . .	47
2.16	Reaction-diffusion patterns designed with the PEN-DNA toolbox . . . . .	48
2.17	Turing-like patterns in <i>Pomacanthus imperator</i> . . . . .	49
2.18	Establishment of cell polarity in <i>C. elegans</i> . . . . .	50
2.19	Positional information during <i>Drosophila</i> blastoderm development. . . . .	52
2.20	Formation of the ventral and cephalic furrows in <i>Drosophila</i> . . . . .	52
2.21	Self-oscillating gels . . . . .	55
2.22	DNA-responsive hydrogel and active gel . . . . .	56
3.1	Strategies to build kinesin clusters for the preparation of a reconstituted active gel	62
3.2	Sketches of the kinesins used in this thesis . . . . .	64
3.3	Purification of kinesins: SDS-PAGE gel and gel filtration profile . . . . .	66
3.4	Distributions of microtubules length . . . . .	67
3.5	ATP regeneration and anti-oxidant systems . . . . .	68
3.6	Sketch and picture of channels . . . . .	69
3.7	Initial orientation of microtubules in the xy plane for different heights in a flow cell	70
3.8	Bundles bend and break under the forces of kinesin clusters . . . . .	73
3.9	Formation of an aster made of microtubule bundles . . . . .	74

3.10	A connected active network exhibits several morphologies depending on the motor concentration . . . . .	75
3.11	Experimental state diagram of contractile active networks . . . . .	76
3.12	A 3D active nematic fluid creates a corrugated sheet of well-defined wavelength . . . . .	78
3.13	Dynamics and mechanism of the formation of the corrugated patterns. . . . .	79
3.14	Passive formation of the gel sheet in the absence of motors. . . . .	80
3.15	Sketch of the mechanism for the active buckling of a thin membrane . . . . .	81
3.16	Dynamics, shape, and stability of the patterns as function of K430-HSNAP motor concentration . . . . .	82
3.17	Wavenumber and growth rate of the patterns as a function of K430-HSNAP motor concentration . . . . .	83
3.18	Effect of the geometrical confinement on corrugated patterns . . . . .	84
3.19	Effect of the channel ratio width/height on corrugated patterns . . . . .	85
3.20	Effect of the microtubule concentration on corrugated patterns . . . . .	85
3.21	Bending instabilities and wavelength selection in a 3D active gel . . . . .	87
3.22	Successive orthogonal bending instabilities lead to chaotic flows . . . . .	88
3.23	Final patterns obtained for different K430-HSNAP concentrations . . . . .	89
3.24	Evolution of the local orientation of bundles . . . . .	89
3.25	Evolution of the local order parameter . . . . .	90
3.26	Distribution of local bundle orientations and evolution of the global order parameter . . . . .	91
3.27	Recent experiments on the compartmentalization of cytoskeletal active gels . . . . .	93
3.28	Methods of production of water-in-oil droplets . . . . .	94
3.29	Formation of 2D active nematics on the inner surface of a droplet. . . . .	95
3.30	Caged-ATP as a tool to impose boundary conditions . . . . .	98
4.1	Monitoring of DNA . . . . .	105
4.2	Dynamics of the T1_20 autocatalyst system at 25°C. . . . .	108
4.3	Effect of the temperature on the autocatalyst dynamics . . . . .	108
4.4	Effect of the buffer composition on the autocatalyst dynamics . . . . .	109
4.5	$\tau_{1/2}$ as a function of BstLF, NBI, dGTP and microtubules concentrations . . . . .	111
4.6	Pictures and sketch of PMMA channels . . . . .	113
4.7	Data processing . . . . .	114
4.8	Reaction-diffusion front in the presence of the active gel . . . . .	115
4.9	Quantification of the front and the active gel . . . . .	116
4.10	Corrugated patterns in the presence of a reaction-diffusion front . . . . .	116
4.11	The velocity of the front does not depend on kinesin concentration . . . . .	117
4.12	Influence of dNTP on internally driven chaotic flows . . . . .	118
4.13	Different dGTP concentrations lead to inhomogeneous patterns . . . . .	119
4.14	Evolution of the inhomogeneous patterning of the active gel in the presence of 25 $\mu$ M of dGTP. . . . .	120
4.15	Qualitative comparison between experimental and simulated kymographs as a function of dGTP concentration . . . . .	121

4.16 Bulk dynamics of the LT2LT system as a function of NT.CviPII and K401-BCCP concentrations . . . . .	124
4.17 Propagation of a front (LT_10) in the presence of K401-BCCP . . . . .	125
4.18 Strategy to attach DNA on SNAP-tag kinesin motors . . . . .	127
4.19 Chemical reaction between the amino-DNA and BG-GLA-NHS . . . . .	127
4.20 Analysis and purification of the reaction between an amino-DNA and BG-GLA-NHS	128
4.21 Chemical reaction between the BG-DNA and kinesin K430-FLAG-SNAP . . . . .	129
4.22 SDS-PAGE analysis of the reaction between K430-FLAG-SNAP and BG substrates	130
4.23 Gliding motility assay . . . . .	131
4.24 Propagation of a front in a population of DNA-functionalized beads . . . . .	133
4.25 DNA-functionalized beads immersed in an active bath . . . . .	134
5.1 Sketch of the Central dogma of molecular biology . . . . .	138
5.2 Example of a natural riboregulator found in <i>E. coli</i> . . . . .	141
5.3 The PURE TXTL system: composition and main reactions . . . . .	144
5.4 Sketches of conventional riboregulators and toehold switches . . . . .	145
5.5 Secondary structures of the two types of riboregulator used . . . . .	146
5.6 Production of GFP with the TXTL cell-free system from a DNA or a RNA template	150
5.7 Simulation of the dynamic range . . . . .	153
5.8 The dynamic range of a riboregulator strongly depends on the concentration of the transactivating DNA . . . . .	154
5.9 Effect of a non-coding DNA strand on the overall gene expression . . . . .	155
5.10 Titration of a riboregulator at the RNA level measures the dissociation constant of the riboregulator complex . . . . .	158
5.11 Titration of translational riboregulator G03 by mobility shift capillary electrophoresis	159
B.1 DNA attached to sepharose beads . . . . .	170
B.2 Integrity of RNA regulators . . . . .	171
G.1 Matière active - Gels actifs . . . . .	188
G.2 Réaction-diffusion - La boîte à outils PEN-ADN . . . . .	189
G.3 Formation de faisceaux de microtubules en étoiles et contraction d'un réseau actif .	191
G.4 Formation d'une feuille nématique active 3D . . . . .	191
G.5 Dynamique, structure et stabilité de la feuille nématique en fonction de la concentration en kinésines . . . . .	192
G.6 Instabilités de flexion et perte de l'ordre orientationnel . . . . .	192
G.7 Formation de nématiques actifs 2D à la surface d'une gouttelette . . . . .	193
G.8 Réaction autocatalytique de production d'ADN et propagation du front associé au sein du gel actif . . . . .	194
G.9 En présence d'une faible concentration de dGTP le gel actif se structure de façon non-homogène . . . . .	195
G.10 Attacher de l'ADN sur une kinésine. . . . .	196
G.11 Riborégulateurs ARN et système de transcription-traduction in vitro . . . . .	198
G.12 Expression de la protéine GFP à partir d'un ARN ou d'un ADN codant . . . . .	198

G.13 Mesures de la gamme dynamique et de la constante de dissociation d'un régulateur  
ARN . . . . . 199



## List of Tables

2.1	Types and localisation of intermediate filament proteins . . . . .	23
3.1	List of the kinesins used in this thesis . . . . .	64
3.2	Composition of the active mix in standard conditions . . . . .	67
3.3	Tunable parameters of the active mix . . . . .	68
3.4	Relation between K430-HSNAP concentration and the initial wavelength in the active gel composed of GMPCPP-microtubules . . . . .	88
3.5	Volumes of oil and water phases for droplets production . . . . .	93
4.1	Composition of the PEN buffer . . . . .	106
4.2	Composition of the active-PEN buffer . . . . .	106
4.3	The lifetime of the active system strongly depends on temperature . . . . .	107
4.4	Sequences of the low temperature autocatalyst . . . . .	107
4.5	Parameters used to tune the dynamics of the autocatalyst and the active gel. . . . .	110
4.6	Sequences of the autocatalyst without dGTP (LT2LT_20) . . . . .	123
4.7	Sequences of amino-modified DNA . . . . .	127
5.1	RNA sequences of the regulators . . . . .	146
5.2	Comparison of the performance of five riboregulators in vivo and in vitro . . . . .	156
5.3	Dissociation constants $K_d$ at 37°C for the studied riboregulator devices . . . . .	159
B.1	List of PCR primers used to produce linear DNA templates . . . . .	170
B.2	Typical PCR protocol to produce linear DNA templates . . . . .	171
B.3	Composition of the PURE TXTL system . . . . .	172

## List of Boxes

1.1	Ethical perspectives . . . . .	10
2.1	Biomimetic self-sustained systems: where does the energy come from? . . . . .	25
2.2	DNA nanotechnology . . . . .	44

## List of Abbreviations

<b>ADP</b>	Adenosine diphosphate
<b>ARS</b>	Aminoacyl-tRNA synthetases
<b>ATP</b>	Adenosine triphosphate
<b>BCCP</b>	Biotin carboxyl carrier protein
<b>BG</b>	Benzylguanine
<b>bp</b>	Base pair
<b>BZ</b>	Belousov-Zhabotinsky
<b>CK</b>	Creatine kinase
<b>CP</b>	Creatine phosphate
<b>DMSO</b>	Dimethyl sulfoxide
<b>dsDNA</b>	double-stranded DNA
<b>DTT</b>	Dithiothreitol
<b>EGTA</b>	Ethylene glycol-bis( $\beta$ -aminoethyl ether)-N,N,N',N'-tetraacetic acid
<b>GFP</b>	Green fluorescent protein
<b>GMPCPP</b>	Guanosine-5'-[( $\alpha,\beta$ )-methylene]triphosphate
<b>HEPES</b>	4-(2-hydroxyethyl)-1-piperazineethanesulfonic acid
<b>IF</b>	Intermediate filaments
<b>MTF</b>	Methionyl-tRNA transformylase
<b>MWCO</b>	Molecular weight cut-off
<b>NHS</b>	N-hydroxysuccinimide
<b>PBS</b>	Phosphate-buffered saline
<b>PCR</b>	Polymerase chain reaction
<b>PEM</b>	PIPES-EGTA-Magnesium buffer
<b>PEP</b>	Phosphoenolpyruvate
<b>PIPES</b>	Piperazine-N,N'-bis(2-ethanesulfonic acid)
<b>PK</b>	Pyruvate kinase
<b>PMMA</b>	Poly(methyl methacrylate)
<b>PURE</b>	Protein synthesis using recombinant elements
<b>qPCR</b>	Quantitative polymerase chain reaction
<b>SDS-PAGE</b>	Sodium dodecyl sulfate–polyacrylamide gel electrophoresis
<b>ssDNA</b>	single-stranded DNA
<b>T7 RNAP</b>	T7 RNA polymerase
<b>Trolox</b>	6-hydroxy-2,5,7,8-tetramethylchroman-2-carboxylic acid
<b>TXTL</b>	Transcription-translation

# Contents

Abstract . . . . .	i
List of Figures . . . . .	ii
List of Tables . . . . .	vi
List of Boxes . . . . .	vii
List of Abbreviations . . . . .	viii
<b>1 Introduction</b>	<b>3</b>
1.1 Diversity and conservation in living systems . . . . .	5
1.2 Learning from life to build new materials . . . . .	8
1.3 Architecture of the thesis . . . . .	11
<b>2 Active matter and reaction-diffusion, two self-organization mechanisms in molecular systems</b>	<b>15</b>
2.1 Active matter . . . . .	19
2.2 Pattern formation by reaction-diffusion . . . . .	36
2.3 Interplay of chemical and mechanical forces: two examples from embryo development	50
2.4 Experimental efforts to couple active matter and reaction-diffusion systems in vitro	54
2.5 Conclusion . . . . .	57
<b>3 Self-organization of an active gel composed of microtubules and kinesins</b>	<b>59</b>
3.1 Preparation of the active gel . . . . .	62
3.2 Formation of asters and contraction of the active network . . . . .	72
3.3 Tunable corrugated patterns in an active nematic sheet ★ . . . . .	77
3.4 From aligned nematics to active flows . . . . .	86
3.5 Compartmentalization of active nematics . . . . .	92
3.6 Conclusion . . . . .	97
<b>4 Coupling a DNA reaction-diffusion front and a cytoskeletal active gel</b>	<b>101</b>
4.1 Finding common conditions for the reaction-diffusion front and the active gel . . .	104
4.2 Propagation of a reaction-diffusion front in an active gel . . . . .	112
4.3 Hydrodynamical coupling: design of a three-letter autocatalyst . . . . .	123
4.4 Chemical coupling: towards active matter controlled by DNA . . . . .	126
4.5 Conclusion . . . . .	132

<b>5 RNA control of genetic expression in a cell-free system</b>	<b>135</b>
5.1 RNA and genetic regulation . . . . .	138
5.2 A cell-free TXTL system for the study of RNA riboregulators . . . . .	142
5.3 Experimental protocol and assembly of the system . . . . .	147
5.4 In vitro TXTL provides valuable information on RNA riboregulators ★ . . . . .	149
5.5 Conclusion . . . . .	160
<b>6 Conclusion</b>	<b>161</b>
<b>Appendices</b>	<b>165</b>
A Movies . . . . .	165
B Protocols . . . . .	167
C Hydrodynamic theory of an undulating active film . . . . .	173
D Kinetic model of the PURE TXTL system . . . . .	177
E Article: Tunable corrugated patterns in an active nematic sheet . . . . .	181
F Article: Quantitative characterization of translational riboregulators using an <i>in vitro</i> transcription-translation system . . . . .	183
G Résumé détaillé en français . . . . .	185
<b>Bibliography</b>	<b>201</b>

# Chapter 1

## Introduction

<b>1.1 Diversity and conservation in living systems . . . . .</b>	<b>5</b>
1.1.1 Biodiversity . . . . .	5
1.1.2 Developmental biology and conservation of mechanisms . . . . .	5
1.1.3 Molecular building blocks of life . . . . .	6
<b>1.2 Learning from life to build new materials . . . . .</b>	<b>8</b>
1.2.1 Synthetic biology . . . . .	8
1.2.2 Engineering living materials . . . . .	8
1.2.3 Cell-free materials . . . . .	9
<b>1.3 Architecture of the thesis . . . . .</b>	<b>11</b>

Defining life is laborious. At the same time ‘chacun de nous sait ce qu’est la vie’<sup>1</sup>, but fails to give a precise answer. We dare not give a definition of life, and prefer to adopt the relational and functional point of view on vital phenomena stated by Claude Bernard [22]: ‘On peut caractériser la vie, mais non la définir’<sup>2</sup>. Thus, life is often associated with attributes such as growth, adaptation to environment, reproduction, maintenance of homeostasis and metabolism, subject to evolution. The combination of some of these properties provides information to distinguish between living and non-living materials.

We aim to illustrate in this short introduction that in spite of the diversity and complexity of life forms, these attributes arise from general conserved characteristics, in particular concerning the mechanisms and the molecules involved in self-organization and gene regulation of organisms. They are in particular the result of interactions between molecules that are universally shared, in the sense that all living organisms are composed of the same molecular building blocks. From the precise understanding of how these mechanisms operate, it is possible to use and repurpose the implicated molecules for the creation of living and cell-free materials with unique properties. The present thesis falls into this context. It aims to build from scratch artificial molecular systems in order to understand pattern formation and gene regulation, with the long-term goal of conceiving novel materials that own some of the properties of living systems.

---

<sup>1</sup>‘each of us knows what life is’, Inaugural lecture of the *Université de tous les savoirs* by Francois Jacob, January 1<sup>st</sup> 2000 [[link](#)]

<sup>2</sup>‘We can characterize life, but not define it’

## 1.1 Diversity and conservation in living systems

### 1.1.1 Biodiversity

Life on earth dates at least from 3.5 billion years ago [247]. Living organisms are everywhere: from deserts to poles, from mountain peaks to deep sea floors with a colossal diversity in size, covering about ten orders of magnitude, from nanometers to tens of meters. Estimations suggest that there would be around 8.7 million eukaryotic species, of which around 1.2 million are identified and described [188]. Microorganisms are largely under-represented in databases, especially in oceans [273]. Organisms are organized into highly inter-dependent multi-species communities ranging from few individuals to entire ecosystems such as forests or lakes. Even at the scale of a human body, bacteria are as numerous as the human cells ( $10^{13}$ ) [252]. Behind this multiplicity of forms and behaviors, living organisms share a number of common mechanisms, in particular the genes and mechanisms that shape them and their molecular building blocks.

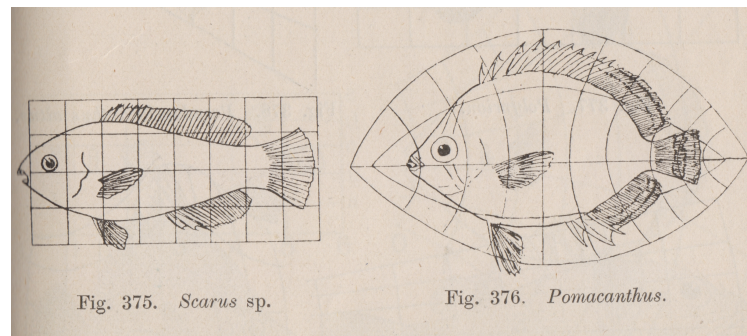
### 1.1.2 Developmental biology and conservation of mechanisms

Despite their huge diversity, living systems can be classified using diverse morphological criteria and degrees of similarities, such as bone structure for animals or shape of flowers for plants. However, by looking at individuals at a fixed time only — adult form for mammals for instance — it is hard to understand the mechanisms involved in the shaping of a living being.

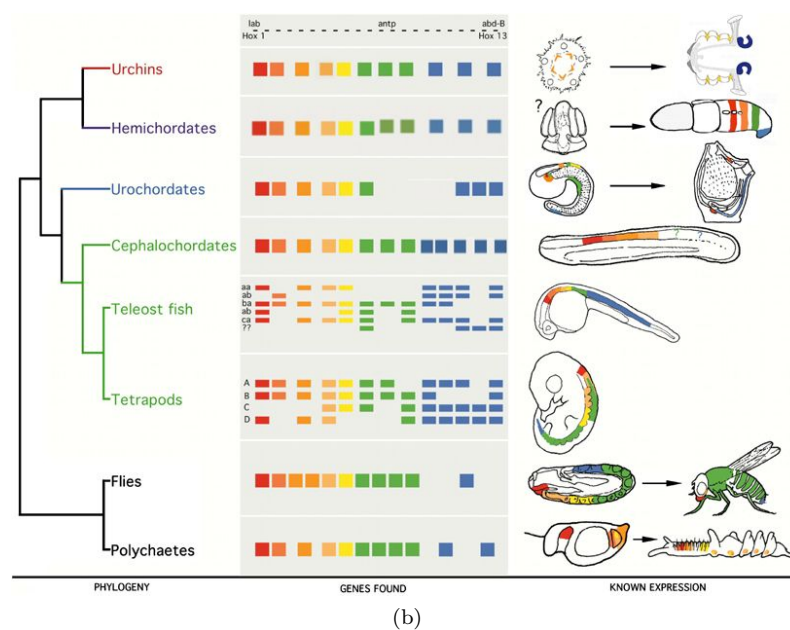
In his book, *On Growth and Form* published in 1917 [283], D’Arcy Thompson proposes general mathematical and physical explanations to the diversity of forms. For example he argues that geometrical transformations can be applied to the shape of a species to give the shape of other species within the same group (Figure 1.1 (a)). The general structure is thus conserved. By comparison with soap films, he points out the importance of physical forces and suggests that cells are shaped according to physical laws like surface tension.

A modern way to understand how organisms are shaped and what the mechanisms involved are is the comparative study of genes that regulate the morphological changes during their development. Through their observation, it is possible to compare developmental processes across species and to observe the phylogenetic links between them. In multicellular eukaryotic species, embryo development is a conserved process that transforms a relatively homogeneous egg into a highly differentiated final organism. Indeed, the embryo is structured by the interplay of chemical and physical forces. Succinctly, development can be divided into four processes: pattern formation, morphogenesis, cell differentiation and growth. This series of events is conserved among relatively close species and is precisely coordinated by genetic information encoded in so-called *Hox* genes. The corresponding *Hox* proteins encode positions along the body during embryogenesis, ensuring that the correct structures are formed at the right places (Figure 1.1 (b)). Thus, the development is orchestrated by the same processes. Spatio-temporal structures arise from the interactions between molecules — that are largely shared among all living organisms — and can lead to macroscopic forces and patterns of proteins.





(a)



(b)

Figure 1.1 | **D’Arcy’s theory of deformation and conserved *Hox* genes.** (a) Closely related forms may be transformed into one another via deformation of the coordinate system. A system of forces is responsible for deformations [283]. (b) Shared expression of *Hox* genes in deuterostomes. Adapted from [275].

### 1.1.3 Molecular building blocks of life

At a molecular level, similarities between species are even more important and are supported by some universal features. Living organisms are mostly composed of molecules containing a few different chemical elements: carbon, oxygen, nitrogen, hydrogen, sulphur and phosphorus. Of course, other elements are needed, such as monovalent or divalent cations (potassium and magnesium for example), but they are generally incorporated in a non-covalent manner. These essential chemical elements assemble into small molecules — ranging from water to glucose — and large macromolecules that can be classified into four classes : proteins, lipids, nucleic acids and carbohydrates. Proteins catalyze specific chemical reactions and form structural elements in cells. Lipids separate the cell from the outside and compartmentalize internal structures. Nucleic acids act as the memory and operating instructions that enable cells to generate all the other

classes of macromolecules and to replicate themselves. Carbohydrates — or saccharides — are used for energy storage and production of structures outside the cell membrane. One of the most striking example of the universality of processes across living organisms is the use of biopolymers as biological information. Deoxyribonucleic acid (DNA) (Figure 1.2 (b)), ribonucleic acid (RNA) and proteins are built from an alphabet of ‘chemical letters’: five nucleotides for nucleic acids (based on the nucleobases adenine (A), guanine (G), thymine (T) and cytosine (C) or uracil (U)) (Figure 1.2 (a)) and twenty distinct amino acids for proteins. We can notice that among the 500 naturally-occurring amino acids known, only 20 are used for building proteins. The information is encoded in the sequence of letters. There is information transfer from one biopolymer to another: the two alphabets are linked through the genetic code where three consecutive nucleotides code for one amino acid (Figure 1.2 (c)).

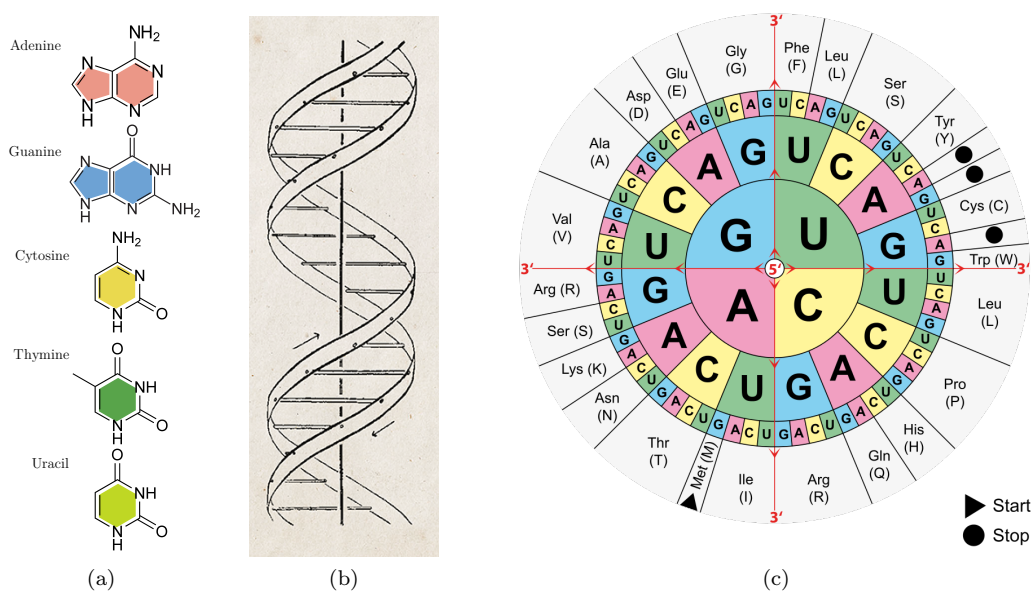


Figure 1.2 | **DNA and the genetic code.** (a) Chemical structure of the five nucleobases composing the five nucleotides. (b) Drawing of the double-helix structure of DNA (drawing by Odile Crick) [307]. (c) The genetic code: translation of information encoded from nucleic acids to proteins. Credit: Wikimedia Commons.

Thus, in virtually any organism DNA can be transcribed into RNA. Then RNA can be translated into a protein. The diversity arises then from the details — which matter a lot in biology — of the regulation of the information transfers between biopolymers. For example, despite its universality, big differences exist between the regulation of gene expression in eukaryotic or prokaryotic cells. The study of these mechanisms is essential to learn about the emergence of life-like properties. Furthermore, this knowledge can be used to modify and eventually repurpose mechanisms and molecules from living organisms, in order to create materials with interesting functions.

## 1.2 Learning from life to build new materials

From the study of the general aspects and particularities of life, it is possible to understand how living organisms shape themselves in space and time, at all scales. From an engineering point of view, one can consider that nature has explored and solved many optimization problems over the billion years of evolution: self-assembly, energy efficiency, self-healing abilities and adaptation to environment. These solutions — such as the conserved molecules and mechanisms involved in gene expression and embryo development — can be mimicked to build new materials — in a broad sense — with novel properties, through for example, the rational design of genetic elements. We will briefly discuss two approaches to make life-inspired, biomimetic, materials that have arisen from the field of synthetic biology in the following.

### 1.2.1 Synthetic biology

Since the beginning of the 21<sup>st</sup> century, a new interdisciplinary research topic has emerged using engineering principles as guidelines to understand living systems: synthetic biology. It aims to design and construct new biological entities: basic regulatory elements are assembled into large genetic circuits in cells. These entities can be modeled, understood and tuned to meet specific performance criteria and to solve specific problems. Since the first designs, for instance an artificial oscillator [61], a synthetic switch [79] or a multicellular pattern-formation system [15], the field has improved and diversified. Organisms are now redesigned to produce drugs and fuels, and have gained new sensing abilities [59]. Concurrently, at the frontier with genomics, huge efforts have been made to build genomes from scratch [105]. Examples include the incorporation of non-natural nucleobases [335, 117] or the use of other amino-acids [130]. Recently, a minimal bacterial genome has been totally synthesized [123], and even recoded [69].

Using synthetic biology principles and tools, two different approaches are possible to create new materials. The first one takes cells, especially unicellular organisms such as bacteria and yeast, modifies and repurposes them in order to enhance existing functions or to create new ones. At a higher spatial level cells are designed to self-assemble into complex multicellular structures and communities. Such materials are often refer as ‘living materials’. The second approach uses reconstituted elements from cells. Molecules are mixed together in a open or closed reactor. Molecules from different organisms or even new chemical compounds can be incorporated in more or less complex ‘cell-free materials’.

### 1.2.2 Engineering living materials

Cell tissues and bacterial communities are now starting to be engineered as living materials capable of performing defined functions and at the same time are robust and adaptable. The designed materials can combine genetic modifications developed by synthetic biology at a multicellular level. Progress in three dimensions (3D) bioprinting has made possible the production of tissue-like materials composed of different cells [302, 151] and of multi-material structures allowing numerous surface interactions [265]. Such materials are multifunctional and embedded with living cells that perform specific functions such as sensing, chemical synthesis, energy production or motion. For example, custom-shaped printed hydrogels containing bacteria that can sense and kill *Staphylococcus*

*aureus* — a causative agent of infections — have been assembled [94]. Living functional materials based on the specific machinery of the bacterium *Bacillus subtilis* can degrade an organophosphate pesticide through a two-step biocatalytic cascade reaction using two co-cultured strains [120]. It is also possible to harness microbes to make biomaterials for use directly in vivo. Modified *E. coli* create fibrous matrices that promote gut epithelial integrity [221]. Material science scientists and biologists have built self-reproducing bricks composed of a nutrient-based gel, sand and the modified photosynthetic cyanobacteria *Synechococcus* allowing the hardening of the hydrogel matrix via calcium carbonate biomineralization [112]. The original brick can be split in half and when extra sand, hydrogel, and nutrients are brought in, bacteria grow again into two full-size bricks in 6 hours. These new tunable living materials offer potential applications in biomaterials, biotechnology and biomedicine.

### 1.2.3 Cell-free materials

A second powerful method to understand and mimic the properties of living organisms consists in a bottom-up reconstitution of interacting elements to recreate the complexity of cellular life. Many cellular mechanisms arise from the interactions of small molecules and larger building blocks. Using single molecules or more complex reconstitutions, bottom-up approaches have successfully rebuilt important cellular mechanisms: gene expression, metabolic pathways and force generation. A long-standing goal of bottom-up engineering is the assembly of an artificial cell. Both mechanical parts — with the reconstitution of the cell-division machinery — and chemical parts — with the reconstitution of gene expression, signaling pathways and the synthesis of biomolecules — have been achieved. Compartmentalization is a key feature and is largely studied, for instance from the point of view of cell-cell communication [1, 56].

Ideas have emerged to create materials that process information, respond to their environment and even build themselves following chemo-mechanical instructions, similar to the role of a genome in organisms. Because the organization and the complexity of living organisms is based on nucleic acids, these appear to be a building material of choice. Therefore a DNA and RNA nanotechnology field has emerged. It is possible to compute, emulate functions and solve problems with nucleic acids [2]. This ability to process information is exploited to create DNA or RNA-responsive nanostructures and materials [133]. For example nanostructures with arbitrary shapes have been built [238]. Hydrogels have been designed to react specifically in the presence of a nucleic acid stimulus [224, 31, 257]. Hybrid systems composed of nucleic acids and enzymes have been conceived [220, 70, 106] and interfaced with electric circuits [62]. Such stimuli-responsive materials activated by biological signals play an increasing role in biotechnology applications.

This is the approach chosen in this thesis.

### Ethical perspectives

Biological engineering and synthetic biology have the potential to develop new products, materials and services that could have substantial impacts on global society, in sectors such as health, energy, agriculture and the environment [313]. The new techniques can contribute to the *2030 United Nations Sustainable Development Goals* related to poverty, inequality, climate change, environmental degradation, peace and justice [link]. For example, bacteria can be engineered to valorize waste as a source of energy instead of glucose and reactive nitrogen, or to produce high-value compounds and drugs [71].

In parallel to the potential benefits, it is essential to evaluate the possible damages of using modified plants and other organisms in a given area. They include biological risks such as the gene drive technology, which can be used to eradicate disease-carrying insect populations but, at the same time, raises concerns of unintended ecological impacts [59]. But there are also socio-economic risks regarding the production and use of bio-based products, to ensure fair-use policies and a minimal harm to the availability and quality of natural resources and ecosystem services. International agreements provide legal frameworks for the effective consideration of these issues. *The Cartagena Protocol on Biosafety to the Convention on Biological Diversity* [link] aims to ensure the safe handling, transport and use of living modified organisms resulting from biotechnology that may have adverse effects on biological diversity, and takes also into account risks to human health. *The Nagoya Protocol on Access to Genetic Resources and the Fair and Equitable Sharing of Benefits Arising from their Utilization to the Convention on Biological Diversity* [link] aims at sharing the benefits arising from the utilization of genetic resources in a fair and equitable way.

### 1.3 Architecture of the thesis

In this thesis, I have used different strategies to build molecular cell-free systems that reproduce two conserved features of life: pattern formation and gene regulation, thus contributing to the two following general questions:

- how does spatio-temporal order emerge in molecular systems, particularly in the molecules of life? It is, in a sense, the question asked by Erwin Schrödinger in *What is Life?: ‘How can the events *in space and time* which take place within the spatial boundary of a living organism be accounted for by physics and chemistry?’* [248]. A subsequent question is, what are the molecular requirements needed to mimic the patterns and their regulation?
- From a material science angle, how to engineer materials that emulate properties of living systems? How to implement adaptability and autonomy in materials?

Inspired by the aforementioned achievements, these questions have been investigated in the continuity of the work of the group where the *in vitro* approach is taken to study biologically-inspired mechanisms of pattern formation and gene expression in a well-controlled manner. In collaboration with Y. Rondelez and coworkers, the group has previously engineered synthetic biochemical systems based on nucleic acid hybridization reactions where the reactivity can be easily predicted by the Watson-Crick pairing rule (the system will be presented in Section 2.2.4) coupled to enzymes. These chemical systems generate spatio-temporal patterns.

Leveraging this knowledge, I have extended the question of self-organization to molecular systems that are able to exert physical forces: what are these molecular systems? What is their composition? What are the emerging structures when chemical and physical self-organizing systems are combined?

Answering these questions may pave the way for the construction of new materials that share properties with living systems: self-sustainability — can the system be maintained for a long time in a closed reactor? —, programmability — can the system behave as rationally designed? — and biocompatibility in order to work with other living structures like cells and enzymes.

Therefore, the work presented in this thesis is focused on pattern formation and gene regulation, at the frontier between material science and synthetic biology. More particularly, my contributions involve the production, the development and the characterization of an *in vitro* reconstituted active matter system that has allowed the discovery of a previously unknown patterning instability in cytoskeletal active gels [253]. In addition, I have found experimental conditions where DNA/enzymes reactions form reaction-diffusion patterns and cytoskeletal gels form activity patterns and I have demonstrated a chemical coupling between these two fundamental processes. Besides cytoskeletal active gels and DNA/enzyme networks, I have investigated a third biochemical system that reconstitutes transcription and translation *in vitro*. With this system I have studied gene regulation by RNA. For both approaches, I have used cell-free controlled systems, in closed reactors, comprised of molecules found in living systems. They consume chemical energy in the form of nucleotide hydrolysis. They are taken either without modifications, with some changes in the sequence or in a chemical group (in the case of proteins and nucleic acids), or completely created *de novo* (for

instance with new sequences of DNA and RNA).

The thesis is composed of five chapters including the present one. Chapter 2 reviews two important mechanisms and systems involved in the self-organization of molecular systems: active matter and reaction-diffusion. Some parts of this chapter reuse material from the book chapter *Learning from embryo development to engineer self-organizing materials* that we have written and which will be published in Fall 2020 [89]. Chapter 3 describes the active system that I have developed together with Shunnichi Kashida. Several results presented in this chapter have been published in ref. [253] (Appendix E). Chapter 4 presents results concerning the coupling between the two self-organizing mechanisms presented in Chapter 2 (active gel and reaction-diffusion). A part of the work exposed here has been done in collaboration with Yuliia Vyborna. Chapter 5 presents the works initiated by Jonathan Lee Tin Wah and continued by myself on the study of the temporal control of gene expression in a cell-free transcription-translation system using RNA regulators. Results from this chapter have been published in ref. [254] (Appendix F). More precisely, the manuscript is divided as follows:

### **Chapter 2: Active matter and reaction-diffusion, two self-organization mechanisms in molecular systems**

In this chapter, two self-organization mechanisms are introduced: active matter and reaction-diffusion. For each mechanism we give a definition and examples. We focus particularly on two systems that we will use in the following chapters (Chapters 3 and 4): an in vitro reconstituted cytoskeletal active gel and a programmable reaction-diffusion system made of DNA and a few enzymes (the ‘PEN-DNA toolbox’). We discuss the relevance and the interactions of these mechanisms in vivo by taking two examples from embryo development. Finally, we review the in vitro materials that have been engineered using the combination of active matter and reaction-diffusion and that have inspired the present thesis.

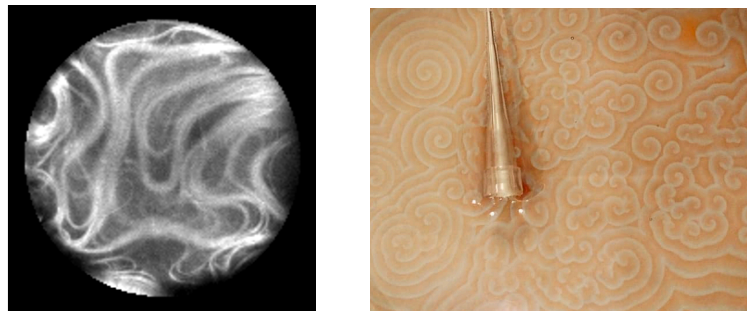


Figure 1.3 | **Active matter and reaction-diffusion, two self-organization mechanisms in molecular systems.**

### **Chapter 3: Self-organization of an active gel composed of microtubules and kinesins**

In Chapter 3, we rationally design an active matter system composed of protein filaments and clusters of molecular motors that can convert chemical energy into large-scale motion. By changing relevant parameters such as activity, depletion forces, length or concentration of protein filaments,

we report previously described patterns (asters, contractions and active chaotic flows) and we also describe a novel type of pattern: a 3D corrugated active nematic sheet of microtubules, where the wavelength and the dynamics can be precisely tuned.

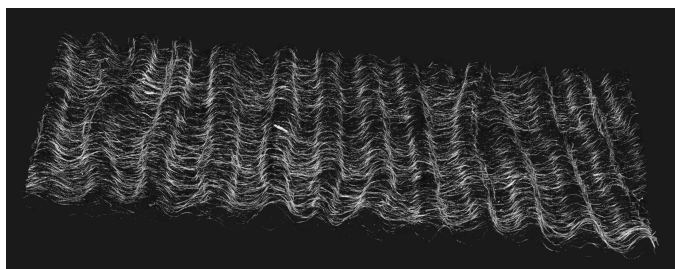


Figure 1.4 | Self-organization of an active gel composed of microtubules and kinesins.

#### Chapter 4: Coupling a DNA reaction-diffusion front and a cytoskeletal active gel

In Chapter 4, we create an autocatalytic reaction (made with the PEN-DNA toolbox) and we combine it with the active gel used in the previous chapter. We show that a reaction-diffusion front can propagate in an active solution. In a regime of low concentration of nucleotide resources, the two systems are competing, leading to the patterning of one system by the other. The end of the chapter is dedicated to ongoing projects and preliminary experiments regarding the coupling of DNA chemical reaction networks and the active gel using either a hydrodynamical or a chemical strategy.

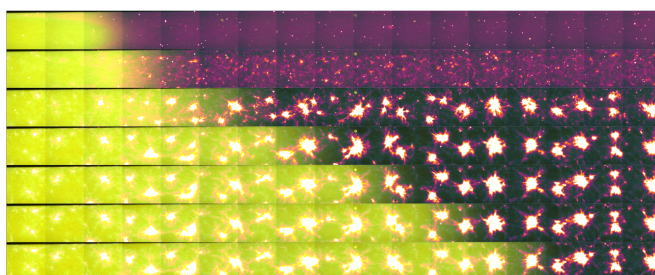


Figure 1.5 | Coupling DNA reaction-diffusion front and active gel.

#### Chapter 5: RNA control of genetic expression in a cell-free system

In the last chapter, we study de novo engineered gene regulators made of RNA using a cell-free transcription-translation system. Upon binding to a second RNA, they change their secondary structure and influence the expression rate of a downstream gene. I show that a reconstituted cell-free transcription-translation system composed of recombinant proteins can be successfully used to provide valuable information about the performances of in silico designed riboregulators.



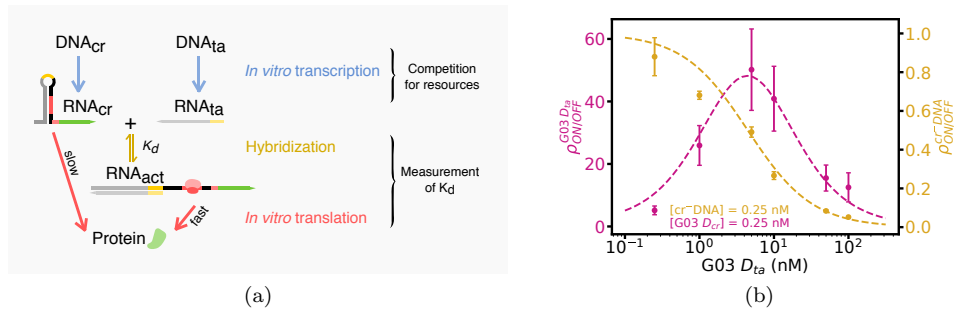


Figure 1.6 | **RNA control of genetic expression in a cell-free system.**

Sections that directly use materials from the aforementioned articles are indicated by the ‘star’ sign ★. Movies of the time-lapse experiments are individually available for download 📄 or online watching 🎥 (password: *pattern*). They are also available combined into one file (📁 .zip, 110 Mo). A list of the movies is presented in Appendix A.

## Chapter 2

# Active matter and reaction-diffusion, two self-organization mechanisms in molecular systems

<b>2.1 Active matter</b> . . . . .	<b>19</b>
2.1.1 Definition . . . . .	19
2.1.2 Examples of living and artificial active systems . . . . .	19
Living active matter systems . . . . .	19
Artificial active matter systems . . . . .	19
2.1.3 Reconstituted active gels . . . . .	21
Cytoskeletal polymers . . . . .	22
Hydrolysis of nucleotides as the source of energy . . . . .	23
Polymerization forces . . . . .	24
Walking on cytoskeletal polymers: molecular motors . . . . .	25
Examples of active gel experiments . . . . .	28
2.1.4 Hydrodynamics of 1D active gels . . . . .	32
Equations of conservation . . . . .	32
Free energy density of a 1D active fluid . . . . .	33
<b>2.2 Pattern formation by reaction-diffusion</b> . . . . .	<b>36</b>
2.2.1 Reaction-diffusion formalism . . . . .	36
Kinetics . . . . .	36
Reaction, diffusion and propagation of fronts . . . . .	37
2.2.2 Patterns in redox reactions . . . . .	38
2.2.3 In vitro reconstituted biochemical reactions . . . . .	40
The Min bacterial system . . . . .	40
Cell-free transcription-translation fronts . . . . .	40

2.2.4	Reaction-diffusion patterns made of DNA . . . . .	42
	Using DNA to build chemical reaction networks . . . . .	43
	The PEN-DNA toolbox . . . . .	44
	Reaction-diffusion patterns constructed with the PEN-DNA toolbox . . . . .	46
2.2.5	Turing-like patterns in vivo . . . . .	47
<b>2.3</b>	<b>Interplay of chemical and mechanical forces: two examples from embryo development . . . . .</b>	<b>50</b>
2.3.1	Cell polarity establishment in <i>C. elegans</i> . . . . .	50
2.3.2	Early stages of <i>Drosophila</i> blastoderm development . . . . .	51
	The French flag problem . . . . .	51
	Patterning genes . . . . .	51
	Formation of the cephalic and the ventral furrows . . . . .	51
<b>2.4</b>	<b>Experimental efforts to couple active matter and reaction-diffusion systems in vitro . . . . .</b>	<b>54</b>
2.4.1	Self-oscillating gels . . . . .	54
2.4.2	DNA-responsive systems . . . . .	54
	Coupling with hydrogels . . . . .	54
	Coupling with reconstituted active matter systems . . . . .	55
<b>2.5</b>	<b>Conclusion . . . . .</b>	<b>57</b>

The assembly of artificial out-of-equilibrium materials that emulate the properties of living systems requires the identification of self-organization mechanisms. Some of them are particularly manifest during the formation of an embryo. Embryo development can be seen as a process that consumes chemical energy and converts chemical information into controlled changes in the composition and the shape of a living organism. Basically, development is described as four sequential processes that are commonly interlaced:

- **Pattern formation:** a process during which out-of-equilibrium chemical reaction networks generate highly-ordered concentration patterns of micrometers to millimeters size, that chemically structure the embryo.
- **Morphogenesis:** where the embryo changes its shape due to internal and external cell movement promoted by molecular motors and filaments, as it happens during gastrulation.
- **Cell differentiation:** in which cells become structurally and functionally different.
- **Growth:** resulting in an increase in the mass of the embryo.

Therefore, the embryo is structured by the interplay of chemical and physical forces. Pattern formation creates a blueprint of chemical species. Morphogenesis responds to chemical signatures generated by pattern formation but also to the mechanical constraints of the cell and tissue. Chemo-mechanical and mechano-chemical couplings link the two processes that together, control cell differentiation and growth.

In this chapter we review two mechanisms allowing pattern formation and morphogenesis in molecular systems: active matter and reaction-diffusion. Pattern formation refers to the self-organization of well-defined concentration patterns. It is linked to the dynamics of chemical reactions and controlled by reaction rates and diffusion. Morphogenesis concerns the implementation of controlled shape changes in a macroscopic material. It implies chemo-mechanical transduction pathways that generate mechanical forces at particular points in space.

This chapter is composed of four sections and a conclusion. The first one is dedicated to active matter. We define the term and shortly give important examples of natural and artificial systems. We focus particularly on reconstituted systems based on biopolymers and molecular motors that form a class of matter called active gels. In Chapter 3 and Chapter 4 we will design and use an active gel system that exhibits self-organization properties. We detail their composition, provide examples from the field and explicit a simple one dimensional (1D) hydrodynamics theory that models such out-of-equilibrium gels. The second section is committed to the description of reaction-diffusion systems. Here we present the concept by successively introducing kinetics of chemical reactions in the absence and in the presence of diffusion. We give several examples. We first look at patterns that emanate from redox reactions. We then describe recent experiments of reaction-diffusion patterns that emerge from in vitro reconstitution of molecules found in living systems: protein waves in the Min bacterial system and fronts in a cell-free transcription-translation system. We focus our attention on a third — de novo built — system composed of DNA strands and three enzymes: the PEN-DNA toolbox. Using these elements, one can easily design chemical reaction networks and subsequently, patterns. We will use this system to design chemical fronts in Chapter 4

in the presence of an active gel. In the third section we go back to embryogenesis and give two precise examples using notions introduced in the previous sections. We show how the two order-generating mechanisms are deeply intertwined during the early embryo development of *Drosophila melanogaster* and *Caenorhabditis elegans*. Finally, in the last section, we briefly introduce artificial systems that have been successfully engineered from the coupling of active matter and reaction-diffusion but lack either biocompatibility, self-sustainability or programmability: hydrogels coupled to redox reactions and gels (passive and active) controlled by DNA molecules. Note that the first three sections borrow material from the book chapter we have written *Learning from embryo development to engineer self-organizing materials* [89] which will be released in Fall 2020.

## 2.1 Active matter

### 2.1.1 Definition

Active matter refers to systems and materials composed of many active components that are able to consume energy at the individual scale and dissipate it in the form of mechanical work or motion. Influenced by the study of flocks, two other properties are sometimes added to this definition: self-propelled motion is force-free (the sum of the forces that a particle exerts on a fluid plus the forces that the fluid exerts on a particle is null) and its direction is set by the orientation of the particle itself [226]. These systems are intrinsically out-of-thermal equilibrium. When the active components interact with each other, collective behaviors can emerge and form dynamical structures. For example, they exhibit flocking and herding, autonomous motility or internally generated flows. Active matter is an eminently multidisciplinary subject; it spans disciplines such as physics, biology, chemical and mechanical engineering.

The definition of active matter covers many different systems spatially ranging from a few micrometers to tens of kilometers. We have decided to divide systems into three categories: living, artificial and reconstituted systems. Other classifications are possible, such as those based on symmetry classes (polar, nematic or isotropic) or on momentum conservation (‘wet’ or ‘dry’ active matter) [173]. In the following sections we give examples of active systems. Living and artificial systems are reviewed succinctly; while reconstituted systems are described in detail because one system from this category will be used in Chapters 3 and 4.

### 2.1.2 Examples of living and artificial active systems

#### Living active matter systems

Animals can get organized into groups of individuals both for natural and social reasons, forming systems that exhibit complex spatio-temporal dynamics. Among others, the dynamics and interactions of populations have been investigated in flocks of birds [13], herds of sheep [77], schools of fishes [215] and swarms of insects [95, 11] (Figures 2.1 (a) and (b)). In these examples, groups of individuals are collectively migrating without leaders. At the scale of an individual many out-of-equilibrium processes are occurring. One of the most impressive example happens during embryo development: the biochemical hydrolysis of nucleotides, mainly adenosine triphosphate (ATP), induces large flows of cells [230]. Thus, a relatively homogeneous living material fueled by chemical energy is shaped into a whole organism (Figure 2.1 (c)). Cellular tissues [55] and communities of unicellular organisms are also active matter. For instance, bacteria organized in biofilms interact, compete and cooperate for resources [333, 47] (Figure 2.1 (d)).

#### Artificial active matter systems

In addition to natural systems, efforts have been made to design artificial active systems. They have been built to simplify and understand collective effects that can arise spontaneously. We choose to present some of these systems by decreasing size of the individual components.

Inspired by the study of insect swarms, robots are one of the first totally synthetic active matter

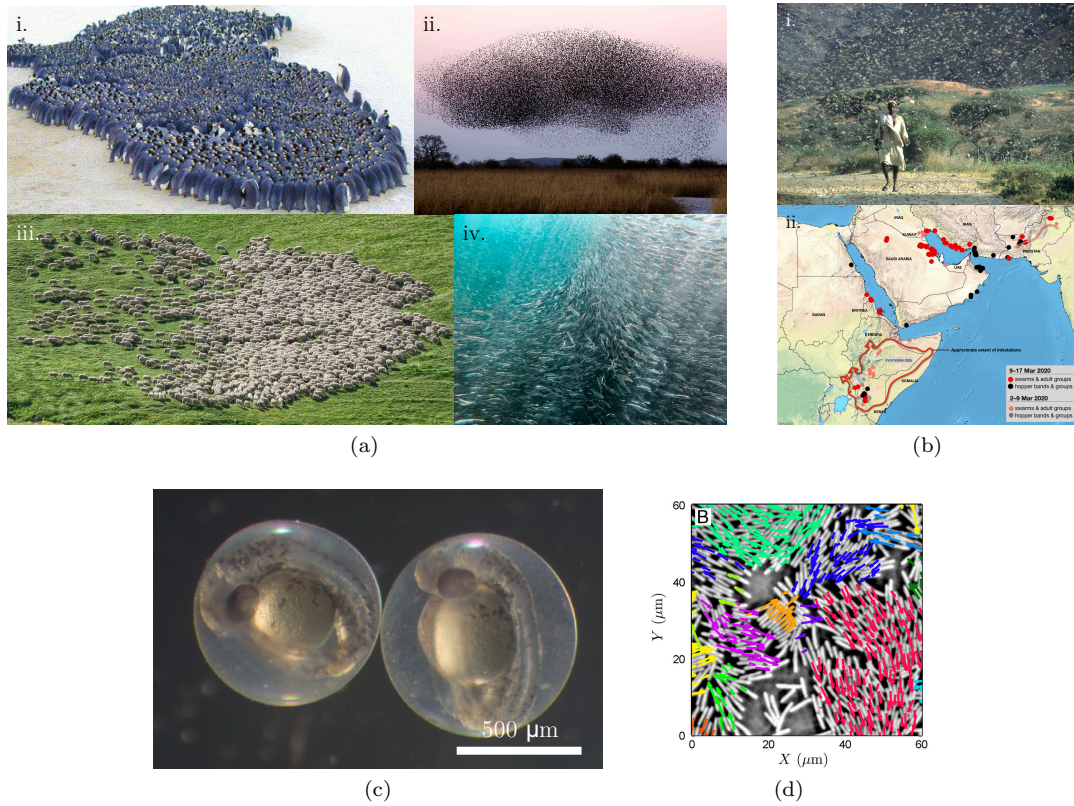


Figure 2.1 | **Diversity of living active matter systems.** (a) Collective behavior of animals in 2D and 3D: i. huddling behavior in emperor penguins (adapted from [85]), ii. flock of birds, iii. herd of sheep and iv. school of fishes. (b) Swarm of desert locusts. Up to 150 million locusts can be found per square kilometer, with a maximum size of 1200 square kilometers. When carried by the wind, a swarm can travel up to 150 km in one day. i. A swarm of desert locusts in Ethiopia during the outbreak of 1968. ii. Extension of the 2019-2020 desert locust infestation (red line). Images from ©G. Tortoli/FAO/ESA and FAO Locust Watch [link]. (c) Two-day-old zebrafish embryos. Image from Steven J. Baskauf [link]. (d) Clusters of self-propelled bacteria. Adapted from [333].

to be designed. Here the energy input often comes from conventional batteries. Engineering large systems poses challenges in both the programming of efficient algorithms and the implementation into actual physical systems. In 2014, a swarm of a thousand centimeter-sized robots was built [239]. The robots operate in large groups, cooperate through local interactions and can collectively take part in shape formation. The implementation of interaction rules can lead to complex structures [264]. These concepts and technologies are now implemented into drones to create autonomous swarms evolving in 3D environments [300].

Two important artificial systems used to test active matter theories are vibrated nematic rods [194] and polar disks [49, 50]. These are objects placed on a delimited surface and that are subjected to vertical vibrations. In a dilute system, components behave as persistent random walkers. As their number increases, collective motion starts occurring and a polar order emerges due to hard-core collisions (Figure 2.2 (a)).

Several strategies have been investigated to motorize colloids with the aim of creating syn-

thetic active swimmers. For example, asymmetric colloidal particles capable of generating local concentration gradients — Janus particles — have been conceived. The most famous ones are composed of gold colloids half-covered with platinum. The decomposition of hydrogen peroxide is catalyzed on the platinum side [282, 88] (Figure 2.2 (b)). Other systems can be either light-powered [212] (Figure 2.2 (c)), electrically-powered [27] (Figure 2.2 (d)) or magnetically-powered [267] (Figure 2.2 (e)). When components are sufficiently close to each other they exhibit collective effects such as clustering and the formation of density waves.

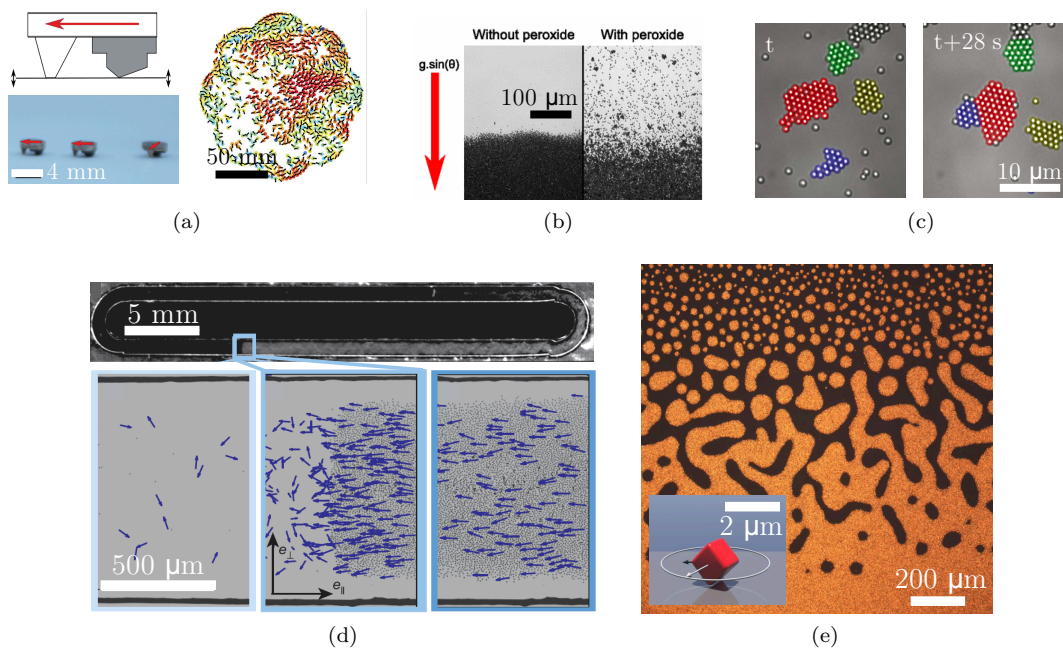


Figure 2.2 | **Artificial active matter systems.** (a) (Left) Self-propelled polar disks with built-in polarity (white: copper-beryllium, grey: nitrile). (Right) Emergence of a collective motion (from red to blue: from perfectly aligned to anti-aligned neighbors). Adapted from [50]. (b) 2D sedimented Janus particles with and without  $\text{H}_2\text{O}_2$ . The direction of the effective gravity is indicated by the red arrow. Adapted from [282]. (c) Clustering of a suspension of synthetic photo-activated colloidal particles. Adapted from [212]. (d) Directed collective motion of a roller population fueled by an electric field. It spontaneously forms a macroscopic band propagating along the racetrack. Adapted from [27]. (e) Chiral fluid of spinning colloidal magnets. (Insert) Schematic diagram of one  $1.6 \mu\text{m}$  haematite colloidal cube. Each magnet has a permanent magnetic moment and is spun by a rotating magnetic field. Adapted from [267].

### 2.1.3 Reconstituted active gels

Because of their intrinsic ability to harvest chemical energy, molecules from living cells have been purified and used *in vitro* to make reconstituted active systems. Indeed, cells are highly dynamic systems: they move, divide, change their shape and adapt to their environment. Alone or as a part of a tissue, they perform many essential functions. Among these functions some require forces such as cell migration, cell growth, endocytosis and exocytosis, directional transport of molecules, cell division and all the subsequent mechanisms such as the segregation of chromosomes or the formation of a contractile ring during cytokinesis. These mechanisms are intimately related to



the cytoskeleton, a dynamic supramolecular assembly of bio-monomers. They are associated with numerous proteins, the most important being crosslinker proteins and molecular motors. The cytoskeleton provides the mechanical stability necessary to interact with the environment but it is also highly dynamic and adaptable. For these reasons, elements of the cytoskeleton and related molecules have been purified and reconstituted in the presence of a chemical source of energy (ATP or GTP) to build active matter systems. When combined these molecules generate a wide diversity of non-equilibrium behaviors.

As we will use a reconstituted active matter system composed of microtubules and kinesin motors in Chapters 3 and 4, we carefully introduce below the following elements: the cytoskeleton, the origin of the chemical energy in these systems and the molecular motors. Moreover, we describe some experimental realizations of so-called active gels.

### Cytoskeletal polymers

In eukaryotes, the cytoskeleton is composed of three distinct protein polymers: microtubules, actin filaments, and intermediate filaments. In contrast with other biological polymers — like DNA and RNA — cytoskeletal polymers are held together by weak non-covalent interactions. Thus, assembly and disassembly happen quickly. Each of these three biopolymers have different mechanical properties and can interact with each other or with other cellular structures including membranes. To quantify mechanical properties of an individual filament, a useful physical quantity is the persistence length  $l_p$ . It is defined as the decay length of the angular correlation along the polymer. It is a measure of the stiffness of a filament. A common relation between  $l_p$  and the bending modulus  $\kappa$  is given by

$$l_p = \frac{\kappa}{k_B T}, \quad (2.1)$$

with  $k_B$  the Boltzmann's constant and  $T$  the temperature. A polymer is considered as flexible if  $l_p \ll L$ , with  $L$  the contour length, and as stiff if  $l_p \gg L$ . In the following we briefly describe each cytoskeletal polymer and we provide a value of its persistence length.

- **Microtubules.** Microtubule filaments are cylindrical rigid biopolymers of about 25 nm in diameter. Each microtubule is composed of approximately 13 protofilaments, a stack of alternating  $\alpha$  and  $\beta$  tubulin monomers (they, together, form a dimer). The polymerization of each 100 kDa dimer is accompanied by GTP hydrolysis. Microtubules are highly dynamic structures that undergo cycles of polymerization and depolymerization triggered by dynamical instabilities. Due to their hollow tubular structure, they have a persistence length in the order of several millimeters, which is much longer than the diameter of cells (typically about tens of  $\mu\text{m}$ ). In cells, they enable intracellular transport by serving as ‘highways’ for motor proteins transporting cargoes and are the main driver for establishing cell polarity and separating the chromosomes during cell division.
- **F-actin.** Filamentous actin, also called actin filaments or F-actin is composed of two protofilaments polymerized from monomers of globular actin (G-actin) and forming a double helix. Each monomer is a 5 nm, 42 kDa ATPase protein (Figure 2.3 (b)). The persistence length of an actin filament is about 10  $\mu\text{m}$ , much smaller than the one of a microtubule. Several isoforms of G-actin exist: for example, in humans, the  $\alpha$  isoform is present in muscle

tissues whereas the  $\beta$  and  $\gamma$  isoforms are located in non-muscle cells. F-actin is involved in many structures with the help of numerous other proteins (ABP, actin-binding protein). They accomplish functions like crosslinking (filamin), bundling ( $\alpha$ -actinin, fascin), nucleating (formin, Arp2/3) or severing (ADF/cofilin). Actin filaments are organized inside cells into large structures like for instance the actomyosin cortex, lamellipodia, lamellae, stress fibers or cytokinetic rings.

- **Intermediate filaments.** In contrast with F-actin and microtubules, intermediate filaments belong to a large family of proteins. They are categorized into six types based on similarities in sequences and structures (see Table 2.1). Their diameters typically range from 8 to 10 nm. Despite their diversity in size and sequence, intermediate filament proteins have a conserved central helical rod domain of about 310 amino acids. This domain plays a fundamental role in filament assembly, while the variable head and tail domains determine the specific function of each filament. They are soft filaments with a persistence length of about 1  $\mu\text{m}$ . They form dense networks in the cell and have slow turnover rates. Because of these two properties, intermediate filaments are known to provide mechanical stability against external forces.

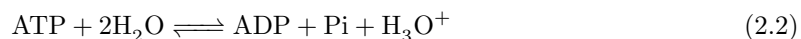
Type	Protein	Weight (kDa)	Localization
I	Acidic keratins	40 - 60	Epithelial cells
II	Neutral/basic keratins	50 - 70	Epithelial cells
III	Vimentin, desmin, glial fibrillary acidic protein, peripherin	50 - 60	Fibroblasts, white blood cells, muscle cells, glial cells, peripheral neurons
IV	Neurofilament proteins	60 - 200	Neurons
V	Nuclear lamins	60 - 75	Nuclear lamina of all cell types
VI	Nestin	200	Stem cells of central nervous system

Table 2.1 | **Types and localisation of intermediate filament proteins.** Adapted from [40].

- **Septins** are often considered as the fourth component of the cytoskeleton [189]. They are 30-65 kDa GTP-binding proteins that can form structures such as filaments and rings. Molecular functions of septins include scaffolds for protein recruitment. They are also involved in cell division.

### Hydrolysis of nucleotides as the source of energy

The generation of forces in cells comes mainly through two different mechanisms: polymerization of cytoskeleton filaments and molecular motors (described in the next paragraph). These active processes use the energy from the hydrolysis of ATP or GTP. For example, in order to apply forces on cytoskeletal filaments, molecular motors undergo conformational changes that require the hydrolysis of a phosphate group from ATP, according to the following reaction:



where Pi is a phosphate. Hydrolysis of the phosphate group in ATP is especially exergonic. In standard conditions  $\Delta_r G$  varies between -28 and -34 kJ/mol (about 12  $k_B T$ ) depending on the

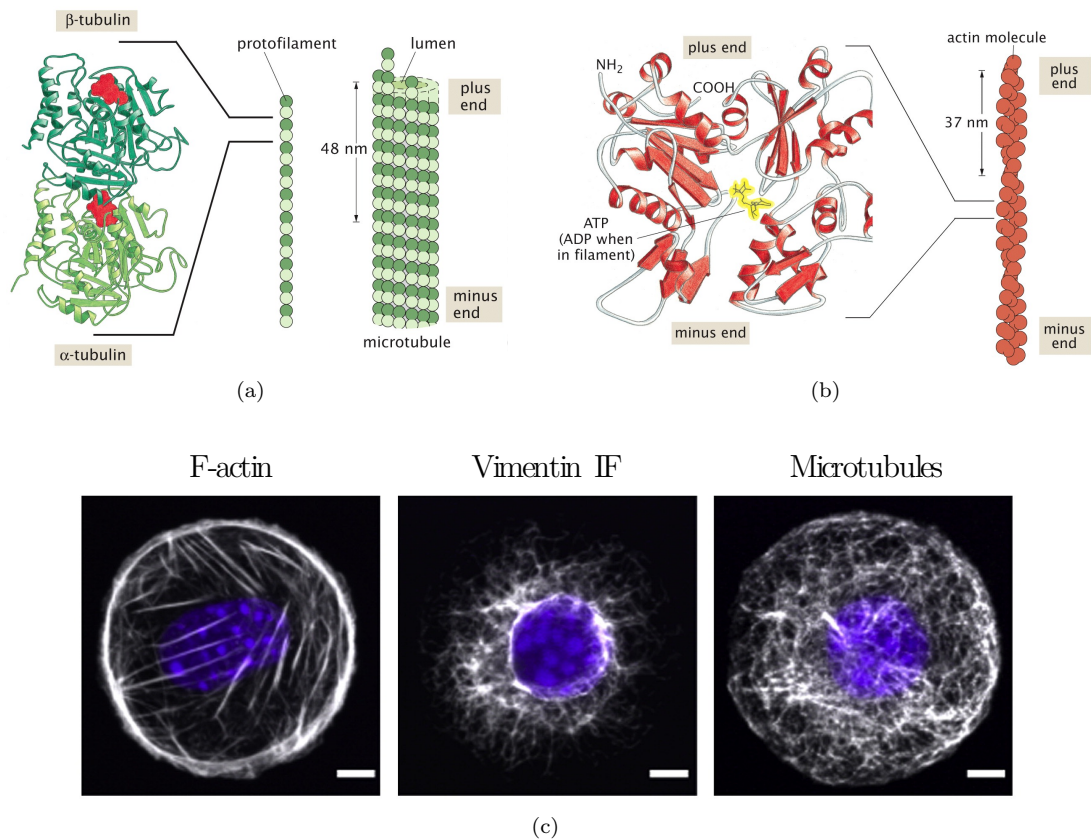


Figure 2.3 | **Structure and localization of the main components of the cytoskeleton.** (a) Structure of a microtubule. Ribbon diagram of a dimer composed of two subunits ( $\alpha$  and  $\beta$  subunits). Bound GTP molecules are shown in red. (b) Structure of G-actin and F-actin. (c) Immunofluorescence/phase images of a NIH/3T3 cell on a circular micropattern where F-actin, vimentin intermediate filaments (IF), microtubules and nuclei (blue) have been stained. Scale bars are 5  $\mu$ m. Figures (a) and (b) are adapted from [216], (c) is adapted from [255].

concentration of the constituents and  $Mg^{2+}$ . ATP is biologically active only when bound to a magnesium cation.

### Polymerization forces

The polymerization of F-actin and microtubules is implicated in cellular force generation processes. Both types of filaments are polar — with a minus and a plus end — and both polymerization and depolymerization rates are significantly biased by polarity. Polymerization consumes energy from ATP in the case of F-actin and from GTP for microtubules, while depolymerization may happen spontaneously. Two striking examples of polymerization forces are the propulsion of the *Listeria* bacteria against their host cell and the chromosome segregation by microtubules during cell division. *Listeria* bacteria can move from cell to cell [285] thanks to a comet-like tail that is driven by actin polymerization pushing the bacterium forward and deforming the plasma membrane until it invades the neighboring cell. An *in vitro* reconstitution of the necessary propulsion machinery has been grafted on colloidal beads, which were able to move ballistically [23] (Figure 2.4 (a)). Chromosome

### Biomimetic self-sustained systems: where does the energy come from?

Living biological materials are far from equilibrium and thus require a constant input of energy to be sustained. In living systems, most of the energy comes from the hydrolysis of adenosine triphosphate, guanine triphosphate and nicotinamide adenine dinucleotide (NADH). Eukaryotic cells make these molecules via energy pathways such as photosynthesis, glycolysis, the citric acid cycle and oxidative phosphorylation, by drawing energy sources — in the form of sunlight or organic food molecules — from their surrounding environment. When energy is abundant eukaryotic cells make larger energy-rich molecules — polysaccharides and lipids — to store their energy excess. In artificial systems, maintaining energy resources for a sufficient amount of time is a tricky problem. In robotics, the energy usually comes from electric energy released from chemical energy in batteries. In molecular artificial systems, natural metabolism pathways based on the hydrolysis of nucleotides are used to engineer the dissipative assembly of molecules [280]. Inspired by biology, researchers have started to couple energy-dissipative chemical reaction cycles to create supramolecular materials. Examples include the hydrolysis of dimethyl sulfate or carbodiimides, the oxidation of dithionite, a change of pH or UV irradiation [232].

segregation during anaphase relies on forces generated by (de)polymerizing microtubules that are translated into chromosome movement through the interaction with kinetochores. These systems can be studied *in vitro* by mimicking the closed environment of a cell [115] (Figure 2.4 (b)).

An important conceptual model for force-generating polymerization is the polymerization brownian ratchet model (Figure 2.4 (c)). A growing filament induces a displacement of the obstacle, which pushes back with a force  $F$ . In the cell, this obstacle may represent the stiffness of a membrane or the drag on an intracellular larger object. In the absence of thermal fluctuations there is no space between the filament and the obstacle: monomers are physically prevented from attaching to the growing end of the filament. However, because of thermal fluctuations, the barrier is able to move back and forth along the main axis, occasionally opening up a space large enough for the insertion of a new monomer. After this insertion, the obstacle can no longer diffuse back to its original position and has thus been pushed forward by the assembling filament. One can also envisage that monomers detach with a certain probability, independently of the presence of the barrier. Using more accurate models — for example, a microtubule is actually composed of 13 protofilaments — the theoretically predicted stall force is about 7 pN [184].

Experimentally, the filament length may be stabilized by the addition of drugs such as taxol for microtubules and phalloidin for actin filaments. In addition, polymerization and depolymerization rates can be adjusted by using nucleotides-derivatives such as guanosine-5'-(( $\alpha,\beta$ )-methylene)triphosphate (GMPCPP), a derivative of GTP.

### Walking on cytoskeletal polymers: molecular motors

Forces in cells are also applied by molecular motors. These are proteins capable of providing mechanical work — thanks to a conformational change — in response to a chemical reaction. An important class of motors is the one associated with the cytoskeleton. Motors belonging to this class are responsible for motile processes as diverse as the transport of vesicles or the running, swimming and flying of animals based on muscle contractions. As we will see in more detail, they

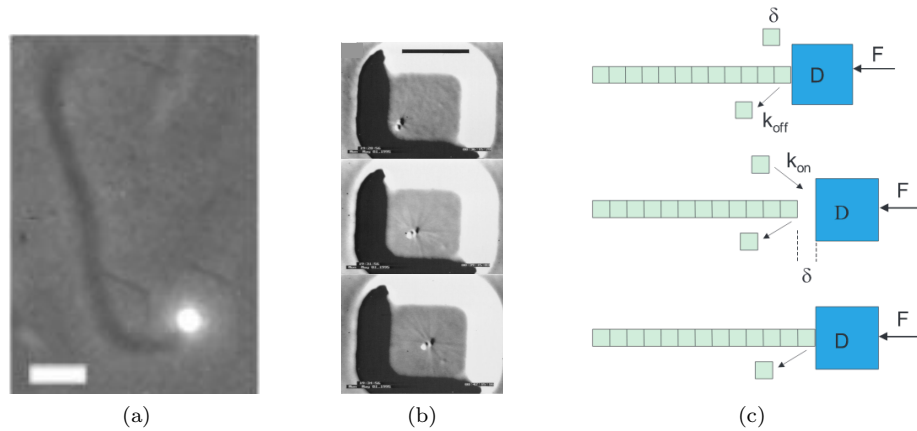


Figure 2.4 | **Force generation by (de)polymerization.** (a) A bead covered with an activating protein of an actin nucleator forms a comet and exhibits a continuous motion thanks to actin polymerization. Scale bar is  $5 \mu\text{m}$ . Adapted from [23]. (b) Assembly and positioning of microtubule asters in micro-fabricated chambers driven by microtubule polymerization. Images are 3 min apart and scale bar is  $10 \mu\text{m}$ . Adapted from [115]. (c) Schematic representation of the single-filament polymerization ratchet. Adapted from [51].

can be classified into three protein families: kinesins, dyneins and myosin (Figure 2.6). A motor moves along a track — microtubule or F-actin, depending on the motor family — by taking a series of discrete steps. Each step coincides with a single chemical cycle of ATP binding, hydrolysis and product release. Thus, the amount of force that can be exerted is upper bounded by the amount of chemical energy liberated during ATP hydrolysis. For kinesins, one can estimate the force  $F$  exerted by a motor as the ratio between the free energy of ATP hydrolysis and the step size:  $F = 12 k_B T / 8 \text{ nm} \approx 6 \text{ pN}$  (with  $k_B T \approx 4 \text{ pN} \cdot \text{nm}$ ). An important characteristic of a molecular motor is its processivity that quantifies how many steps a single motor can take along a single filament before it falls out.

- **Kinesins.** Kinesins are processive molecular motors that walk on microtubules (Figures 2.5 and 2.6 (a)). They deal with intracellular transport and are particularly important during cell division, as they participate in the segregation of chromosomes. Since their discovery in the squid giant axon [294], extensive research has been undertaken to discover their structure and the molecular mechanisms of the walk. In terms of structure, we are describing the kinesin-1 motor because it is emblematic of the members of the kinesin superfamily (Figure 2.6 (a)). It weights about 100 kDa and is composed of two motor subunits — called heavy chains — that form a protein dimer. They also bind two smaller light chains. A heavy chain has a globular head, the motor domain. This head has two separate binding sites: one for the microtubule and the other for ATP. The head is connected via a short flexible neck linker to the stalk. Thus, the two stalks of two heavy chains intertwine to form a coiled-coil that directs dimerization. The motor ends with a tail that is associated to the light chains. In most cases a transported cargo binds to the kinesin light chains. The motor domain is able to bind and hydrolyze ATP. The ADP release changes the conformation of the microtubule binding domains and the orientation of the neck linker with respect to the head resulting in

the motion of the whole kinesin. Kinesin motor is sometimes referred as the world's tiniest biped: it walks using an 'hand-over-hand' mechanism, with an alternation of 16 nm-long steps by each head (Figure 2.5 (b)) to the plus-end of a microtubule.

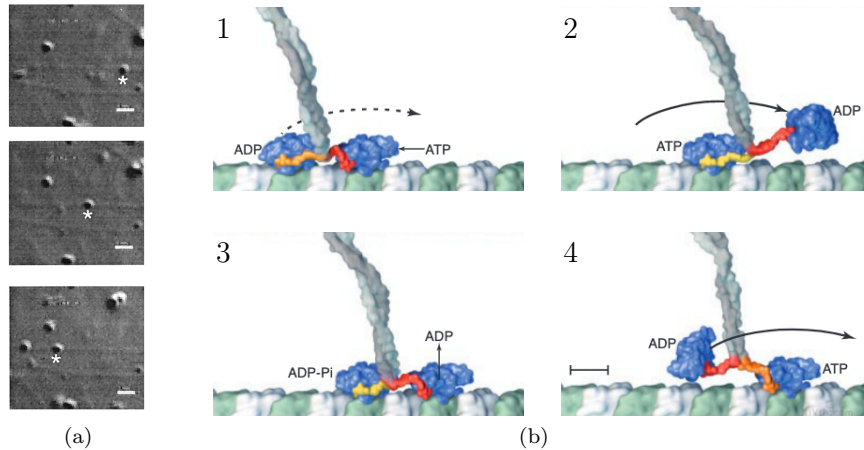


Figure 2.5 | **Kinesin hydrolyzes ATP and walks on microtubules.** (a) Movement along microtubules of 200 nm diameter silica beads coated with kinesin. The motion of one bead is marked by an asterisk. Interval between images is 2 s and the scale bar is 1  $\mu\text{m}$ . Adapted from [42]. (b) Model for the motility cycles of kinesin. 1. Each motor domain is bound to a tubulin heterodimer along a microtubule protofilament. The binding of an ATP molecule on the leading head initiates neck linker strong docking (in red). 2. Neck linker docking is completed by the leading head (yellow), which throws the trailing head forward by 16 nm (arrow) toward the next tubulin binding site. 3. After a random diffusional search, the new leading head docks onto the binding site. This triggers the ADP release. At the same time, the trailing head hydrolyzes ATP to ADP-Pi. 4. After ADP dissociation, an ATP binds to the leading head. The trailing head, which has released its Pi and detached its neck linker (red) from the core, is in the process of being thrown. Contrary to myosin, the two heads of a kinesin are coordinated in order to move processively along a microtubule. Adapted from [293].

- **Dyneins.** The second important motor family is dynein (Figure 2.6 (b)) that is composed of two subfamilies: cytoplasmic dyneins and axonemal dyneins. They are known to be very large molecules — sometimes heavier than 1.5 MDa — due to the length of their heavy chains, and contain approximately twelve polypeptide subunits. Like kinesins, they move on microtubules thanks to their motor domain. In cells, they are involved in processes such as transport, force generation during mitosis, and they allow eukaryotic cilia and flagella to beat. In most cases they move towards the minus-end of microtubules (retrograde transport).
- **Myosins.** The myosin motor family is composed of many different motors performing very diverse mechanical and chemical tasks, ranging from muscle contraction to intracellular transport. They use the hydrolysis of ATP to apply forces on actin filaments in a directed manner. Except in rare cases, myosins move specifically towards the plus-end of the polar filament. There are dozens of different types of myosin motors. Two well studied kinesins are the myosin II and the myosin V. Myosin II (Figure 2.6 (c)) is present in muscle cells within contractile structures called sarcomeres, but other isoforms also exist and allow contractility

in non-muscle cells, forming stress fibers. In such cells, they are involved in force generation at the cellular cortex, adhesion and motility. Myosins II are large dimeric proteins (about 500 kDa) consisting of 6 subunits. The long coiled-coil tails of the individual myosin molecules join together and form the thick filaments of the sarcomere in muscle cells. Myosin V (Figure 2.6 (d)) transports a variety of intracellular cargo along actin filaments. It is a dimeric myosin with two motor domains. Contrary to myosin II, the motion of the mammalian myosin V is processive [177].

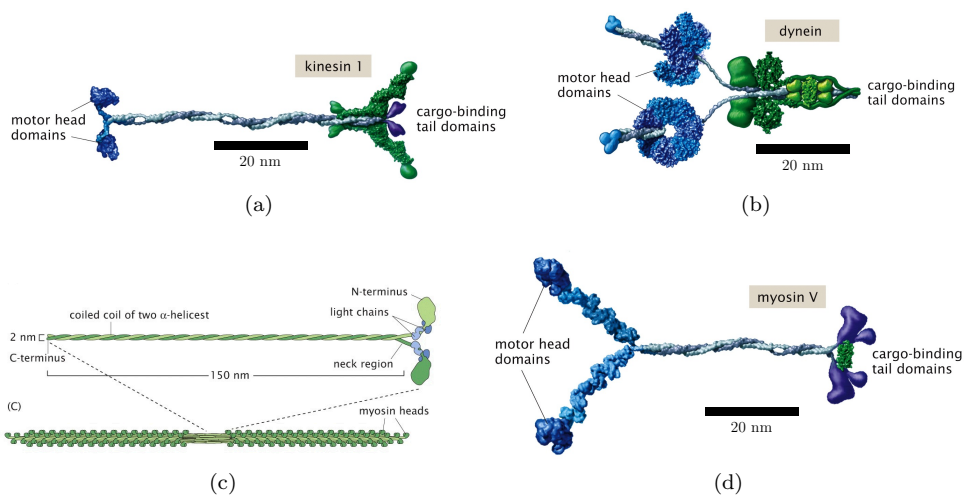


Figure 2.6 | **Molecular motors.** (a) Kinesin I and (b) dynein motors apply forces on microtubules. (c) Myosin II and (d) myosin V motors apply forces on actin filaments. Adapted from [216, 292].

Other molecular motors exist *in vivo*. Motors from the  $F_0F_1$ -ATP synthetase family are rotary motors that convert the chemical energy from ATP to the electrochemical potential energy of a proton gradient across a membrane, and the other way around. They participate in ATP synthesis in the mitochondria, chloroplasts or in bacterial flagella. Other examples include dynamin GTPases involved in the endocytosis in eukaryotic cells, helicase ATPases that separate double strands of nucleic acids prior to transcription or replication, topoisomerases of type II that reduce supercoiling of DNA in the cell. Interestingly, molecular motors share several structural elements: for example, kinesins are related to GTPase proteins.

### Examples of active gel experiments

The combination of cytoskeletal molecular motors, polar filaments and filament crosslinkers constitutes an out-of-equilibrium system where the energy coming from the ATP hydrolysis is injected through molecular motors, which then apply forces on the cytoskeleton biopolymers.

The study of the activity of molecular motors was historically done by looking at their abilities to translate cytoskeletal filaments. In these gliding experiments, motors are adsorbed on a surface and filaments move parallelly to this surface entrained by the motors in the presence of

ATP [295, 152]. Inspired by the study of macroscopic flocks, researchers have investigated what is happening when the concentration of the filaments increases. In such conditions, collective motions are observed: for example density waves of actin filaments [246, 122] (Figure 2.7 (a)) or vortices of microtubules on dynein [271] and kinesin [126] layers.

When components are mixed in bulk, they form active gels. These are materials with unique rheological properties due to their ability to convert chemical energy into macroscopic stress. At a high enough concentration of their components, a displacement of the filaments is induced and set the gel in motion. The mechanical properties of cytoskeleton-based networks have been extensively analyzed using passive techniques — passive micro-rheology, dynamic light scattering, fluorescence correlation spectroscopy — or active techniques — rheometer shearing, atomic force microscopy, micropipette aspiration, optical or magnetic traps, microplates [183, 223]. For example, crosslinked actin reconstituted networks exhibit exceptional elastic behaviors [78] and the presence of molecular motors [145] stiffens the network by more than two orders of magnitude. Moreover, many physico-chemical interactions exist between the different components of the cytoskeleton. For a comprehensive review on the physical interactions between the cytoskeletal components via direct bonding, crosslinkers or molecular motors, and their contributions to the mechanical properties of cells, the reader may refer to ref. [121].

Because such gels are far from equilibrium they can self-organize into complex dynamical structures that are described in the following.

- **Asters.** When clusters of motors — that are thus able to walk on several filaments at the same time — are mixed with filaments at low motor/filament ratios in a solution containing ATP, star-shaped structures of radially-oriented filaments appear spontaneously. These structures called asters, were first observed by Nédélec, Surrey and co-workers using kinesin-1 clusters mixed with static microtubules stabilized with taxol [195] (Figure 2.7 (b)). Kinesin clusters were obtained with biotinylated kinesin coupled to streptavidin as an artificial mimic of natural microtubule-crosslinking motors such as kinesin Eg5. Note that in Chapter 3 we will describe and use this kind of kinesin clusters. Asters are polar structures with filament plus-ends at the center and minus-ends at the periphery when plus-end kinesin aggregates were used [274]. Computer simulations suggest that aster formation is due to the accumulation of motors at the microtubule plus-ends [274]. Asters have also been recently observed in myosin II/actin filament systems [315].
- **Contractions.** When motor clusters are mixed with filaments at higher motor/filament ratios than for asters, a global contraction of the 3D meshwork made of filaments and motors is observed. Global contraction was first reported by Szent-György in 1942 in actomyosin gels from cell extracts [196]. Actomyosin contractions have been quantified in purified solutions containing actin filaments, myosin II motor aggregates, and sometimes crosslinkers such as  $\alpha$ -actinin [20, 145, 229, 4]. Typically, 10  $\mu$ L of this active gel contracted to 5% of its volume within 30 min, exerting forces of  $\sim 1 \mu$ N. Contractions were observed at sufficiently high myosin/actin ratios and at intermediate crosslinker/actin ratios [20] (Figure 2.7 (c)). So far, it has not been possible in vitro to restart a collapsed actin network. In contrast, in vivo, actomyosin induces highly dynamic behaviors due to the rapid renewal of actin filaments



[179]. Global contractions of microtubule networks have been observed in egg extracts [67], where they were suggested to arise from dynein aggregates, and in purified microtubule gels [288] in the presence of kinesin Eg5, a motor with two heads that pulls on two filaments at once.

- **Active flows.** Aster formation needs the accumulation of motor aggregates at one end of the filament. Suppressing motor accumulation should make filaments continuously slide along each other, creating filament flows that may induce macroscopic flows in the solution. This is of particular interest to physicists because it is a novel way of inducing liquid flow without applying an external pressure [305, 173]. This fascinating behavior was first observed by Sanchez, Dogic and collaborators [241] by simply adding a depletion agent (a hydrophilic polymer) to a solution of kinesin aggregates and short microtubules (Figure 2.7 (d)). Depletion forces induce a net attraction between microtubules that aggregate into bundles [113, 26]. These bundles contain filaments oriented in both plus and minus directions and are thus weakly polar. As a result, motor aggregates will no more accumulate preferentially at one end of the bundle and these will incessantly slide along each other carried away by motors. Passive brownian particles immersed in such a solution were entrained by the active flow of bundles with velocities up to  $2 \mu\text{m/s}$ , demonstrating the generation of macroscopic fluid flows. These flows were chaotic with vortices of typically  $100 \mu\text{m}$ , but could be rectified in a toroidal geometry, generating coherent flows that allowed the macroscopic transport of liquid along circuits up to one meter long [319], confirming previous theoretical predictions [305].
- **2D Active nematics.** Interestingly the 3D active gels self-organize into unique structures when the active solution is put in the presence of a water/oil interface. In particular, they form a 2D phase at the interface, creating a new type of soft material: an active nematic liquid crystal. The defects that inevitably appear in the nematic phase display rich dynamics [241, 46, 101, 155, 174]. 2D active nematics can be confined on a plane [241, 207, 108] or on the inner surface of droplets [241, 140, 103]. Very recently, 3D active nematics have been reported [53].

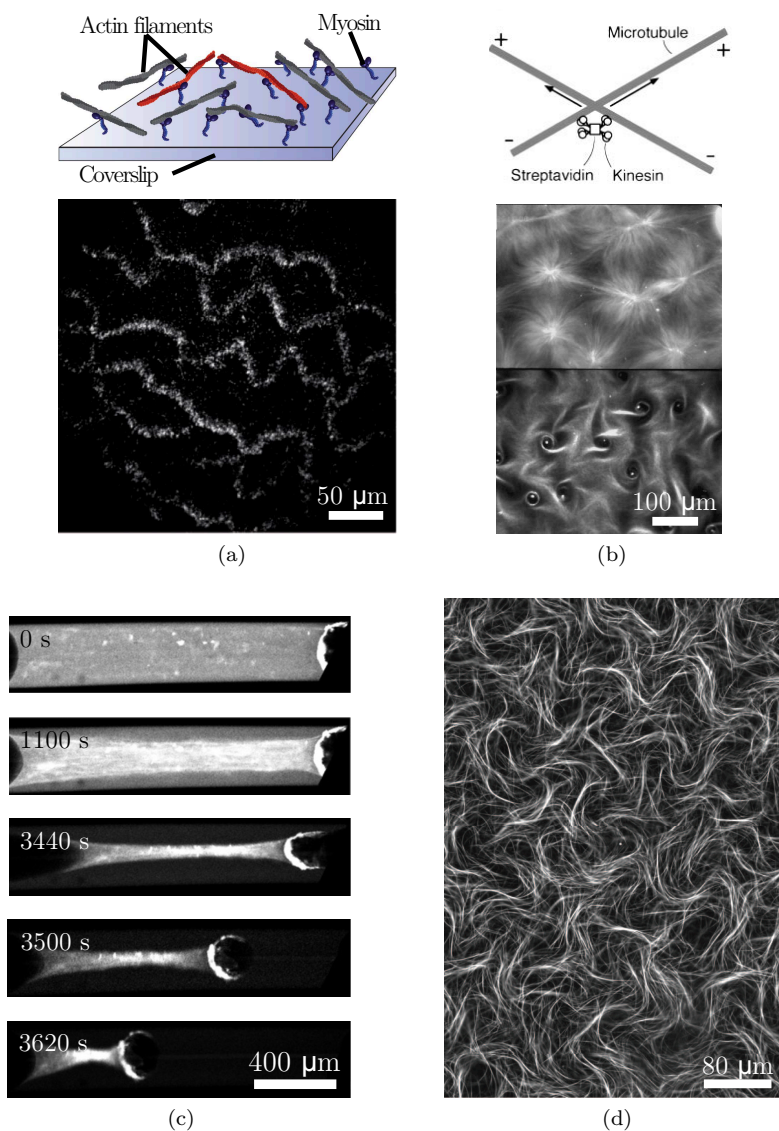


Figure 2.7 | **Reconstituted active matter systems.** (a) At high enough density, actin gliding filaments motorized by myosin motors show collective motion, such as moving structures and density waves. Adapted from [246]. (b) Large-scale patterns — asters and vortices — formed through the self-organization of microtubules and multimeric kinesins motors. Adapted from [195]. (c) Time-lapse of a contractile actin-myosin- $\alpha$ -actinin gel. Adapted from [20]. (d) When microtubules are short enough and in the presence of strong depletion interactions, the microtubule-kinesin system forms an active gel that exhibits internally generated flows. Adapted from [241].

### 2.1.4 Hydrodynamics of 1D active gels

Active matter is inherently out-of-equilibrium, thus equilibrium thermodynamics is no longer valid to describe these systems. As a result, new theories have been developed to describe active matter systems. Notably, flocks have been the object of important theoretical works [301, 286].

Here, we try to give a simple understanding of how to model active systems using a hydrodynamic theory of active gels. The reasoning is quite general and can be applied to different systems regardless of their microscopic details (theories can also be built using microscopic descriptions of mechanisms like in ref. [18]). This section is inspired by two lectures given by S. Grill in 2018 (Cargese, France) and in 2019 (Munich, Germany) [link] and borrows some material from the book chapter that we have written *Learning from embryo development to engineer self-organizing materials* [89].

Active gels are materials with unique rheological properties. As we have seen, they are composed, among others, of molecular motors that induce macroscopic displacements. One way to characterize these systems in which chemical reactions lead to motion, is to add chemical terms to the hydrodynamic equations that describe the deformation of a gel. To obtain the expression of these *chemical forces* we follow the approach developed by Onsager in 1931 and applied to active gels by Kruse, Sekimoto and co-workers [153]. We determine the *fluxes* and the corresponding conjugate *forces* that govern the out-of-equilibrium evolution of the gel [206]. In Onsager's vocabulary, a thermodynamic *force* is a quantity whose difference induces a *flux* between two points. For instance, the temperature is a force that induces a heat flux. For a system not too far from an equilibrium state, the fluxes can be expressed as linear combinations of the different forces by introducing phenomenological coefficients. This is for example what happens in the Soret effect where a diffusive particle flux is induced by a temperature gradient identified as a thermodynamic force.

As an example, we derive the dynamical equations that describe the deformation of a 1D active gel. The unidimensional hypothesis can be experimentally justified when looking at the behavior of the thin actomyosin cortex of a cell. First we write equations of conservation and then exploit the relations provided by thermodynamics near equilibrium. Finally we deduce the free energy density of the 1D active fluid and the constitutive equations of the active material.

#### Equations of conservation

The mechanical state of the gel is described by the mass density  $\rho(x, t)$  and the local velocity field  $v(x, t)$ . The spatial coordinate is noted  $x$ . We also define the mass density flux (momentum density)  $j(x, t) = \rho(x, t)v(x, t)$ . The conservation of mass density in a piece of gel delimited by  $X_1$  and  $X_2$  is given by

$$\frac{\partial}{\partial t} \int_{X_1}^{X_2} \rho(x, t) dx = - (\rho(X_2, t)v(X_2, t) - \rho(X_1, t)v(X_1, t)) \quad (2.3)$$

$$= - [\rho(x, t)v(x, t)]_{X_1}^{X_2} \quad (2.4)$$

$$= - \int_{X_1}^{X_2} \partial_x(\rho v) dx, \quad (2.5)$$

which must hold for all fragments in the gel, giving

$$\frac{\partial \rho}{\partial t} + \partial_x(\rho v) = 0. \quad (2.6)$$

Momentum is also conserved:

$$\frac{\partial j}{\partial t} - \partial_x(\tau^{tot}) = 0, \quad (2.7)$$

with  $\tau^{tot}$  the momentum flux, which is also the stress (in 1D, the tension). Its spatial derivative  $\partial_x(\tau^{tot})$  is the local force. The stress can be decomposed into the sum of an advective stress  $jv$  and a material stress  $\tau$  that describes the material mechanical property,  $\tau^{tot} = -jv + \tau = -\rho v^2 + \tau$ ,

$$\frac{\partial \rho v}{\partial t} + \partial_x(\rho v^2) = \partial_x \tau. \quad (2.8)$$

For example, if the material stress is proportional to the strain rate, like in the term  $\eta \partial_x v$ , eq. (2.8) leads to the compressive Navier-Stokes equation. In the next paragraph we are going to find a constitutive expression for the stress when the consumption of energy is taken into account.

### Free energy density of a 1D active fluid

As an out-of-equilibrium process, the consumption of energy is described using thermodynamics near equilibrium. To begin with, the system is in contact with a heat bath at temperature  $T$  and has state variables  $\Phi_i$  (density, orientation, ...). Its free energy can be written as  $F = U - TS$ , with  $U$  the internal energy,  $T$  the temperature and  $S$  the entropy. During the non-equilibrium process that we are trying to describe, the rate of change  $dF/dt$  can be written as the sum of a reversible part  $dF_{rev}/dt = dU/dt$ , that we assume to vanish here as no work or external forces are considered, and an irreversible part

$$\frac{dF_{irr}}{dt} = -T \frac{dS}{dt}. \quad (2.9)$$

We note  $f_i = -dF/d\Phi_i$  the conjugate *force* of  $\Phi_i$ . Near equilibrium  $\frac{dF_{irr}}{dt} = -\sum f_i d\Phi_i/dt$ , with  $d\Phi_i/dt$  the thermodynamic *fluxes*, which are linear functions of all *forces*. The coefficients of proportionality are constrained and their contributions depend on their time-reversal symmetry [206].

We now have to write the free energy  $F$  of the active gel. It is composed of the free energy due to chemistry and the one due to mechanics  $F_{irr} = F_{chem} + F_{mec}$ . We compute successively the rate of change of free energy  $dF_{chem}/dt$  and  $dF_{mec}/dt$ .

As a first approximation, one may consider solely the reaction  $\text{ATP} \rightarrow \text{ADP} + \text{Pi}$ . The reactive state of the gel is described using the concentrations  $c_i$  and the chemical potentials  $\mu_i$  of the

chemical species  $i$ . Then,

$$\frac{dF_{\text{chem}}}{dt} = \frac{d}{dt} \int dx (\mu_{\text{ATP}} c_{\text{ATP}} + \mu_{\text{ADP}} c_{\text{ADP}} + \mu_{\text{Pi}} c_{\text{Pi}}) \quad (2.10)$$

$$= \int dx (\mu_{\text{ATP}} \frac{\partial c_{\text{ATP}}}{\partial t} + \mu_{\text{ADP}} \frac{\partial c_{\text{ADP}}}{\partial t} + \mu_{\text{Pi}} \frac{\partial c_{\text{Pi}}}{\partial t}) \quad (2.11)$$

$$= \int dx \frac{\partial c_{\text{ATP}}}{\partial t} (\mu_{\text{ATP}} - \mu_{\text{ADP}} - \mu_{\text{Pi}}) \quad (2.12)$$

$$= \int dx \frac{\partial c_{\text{ATP}}}{\partial t} \Delta\mu, \quad (2.13)$$

with  $\Delta\mu = \mu_{\text{ATP}} - \mu_{\text{ADP}} - \mu_{\text{Pi}}$  the molar free enthalpy of ATP hydrolysis. The balance equation of ATP gives  $\frac{\partial c_{\text{ATP}}}{\partial t} + \partial_x j_{\text{ATP}} = -r$ , with  $r$  the rate of ATP hydrolysis. Thus the term of entropy production is

$$\frac{dF_{\text{chem}}}{dt} = - \int dx r \Delta\mu, \quad (2.14)$$

where the surface terms have been omitted.

Now, using momentum conservation as written in eq. (2.7) and successive integrations by parts, we compute the rate of free energy change due to motion in the form of kinetic energy as

$$\frac{dF_{\text{mec}}}{dt} = \frac{d}{dt} \int dx \frac{1}{2} \rho v^2 = - \int dx \tau \partial_x v. \quad (2.15)$$

For the sake of simplicity the surface terms have been again omitted. Finally, following eq. (2.9), the irreversible part of the free energy rate can be written as

$$T \frac{dS}{dt} = - \frac{dF_{\text{irr}}}{dt} = - \frac{d(F_{\text{chem}} + F_{\text{mec}})}{dt} = - \int dx (r \Delta\mu + \tau \partial_x v). \quad (2.16)$$

The entropy production rate is the sum of two dissipative terms that can each be decomposed into a *flux* and a thermodynamic *force*: (i) a chemical contribution  $r \Delta\mu$ , where the free enthalpy of the ATP hydrolysis  $\Delta\mu$ , and the reaction rate  $r$ , are identified as the chemical thermodynamic force and the associated flux, respectively, and (ii) a mechanical contribution  $\tau \partial_x v$ , where the velocity gradient  $\partial_x v$  and the 1D stress  $\tau$  can be identified as conjugate force and flux. Assuming that the system evolves close to an equilibrium state, the fluxes ( $\tau, r$ ) can be expressed as linear functions of the forces ( $\partial_x v, \Delta\mu$ ). Introducing Onsager coefficients  $\eta, \zeta$  and  $\Lambda$ , one gets

$$\tau = \eta \partial_x v + \zeta \Delta\mu \quad (2.17)$$

$$r = -\zeta \partial_x v + \Lambda \Delta\mu, \quad (2.18)$$

where  $\eta$  can be identified as the 1D viscosity of the gel. The coefficient  $\Lambda$  is equal to the rate constant of ATP hydrolysis rescaled by  $k_b T$ . Finally, the proportionality coefficient between the chemical force  $\Delta\mu$  and the mechanical flux  $\tau$ , and between the chemical flux  $r$  and the mechanical force  $\partial_x v$ ,  $\zeta$ , is identical due to Onsager reciprocal relations. The first equation (2.17) illustrates the chemo-mechanical coupling present in these systems at the macroscopic scale. The stress  $\tau$  is the sum of a passive viscous term  $\eta \partial_x v$  and an active term  $\zeta \Delta\mu$  proportional to the free enthalpy of

ATP hydrolysis. The second equation (2.18) illustrates that these systems also present a mechanochemical coupling, the rate of hydrolysis depending on the velocity gradient of the flow within the gel. As the active gel theory has been developed by physicists with the goal of describing the shape change of active gels, the first equation has been largely studied for systems of increasing complexity. The second equation, on the contrary, is less considered.

To illustrate the contraction of an active gel, we apply eq. (2.17) to the deformation of a 1D active gel under a constant active tension  $\zeta\Delta\mu$  induced by molecular motors. The active forces are offset by external forces applied at the edges. At  $t = 0$ , the external forces and the stresses at the boundaries vanish and the gel contracts under active tension. In this regime, inertia can be neglected and thus the equilibrium of forces must be met at every point, which is written  $\partial_x\tau = 0$ . This equation combined with eq. (2.17) yields

$$0 = \eta \frac{d^2v}{dx^2} + \frac{d\zeta\Delta\mu}{dx}. \quad (2.19)$$

As the active tension is uniform, the last term vanishes and we have  $0 = \eta \frac{d^2v}{dx^2}$ . Integrating this last equation, we find that the initial velocity of the gel material is negative and equal to  $v = -\frac{\zeta\Delta\mu}{\eta}x$  which corresponds to a contraction of the gel.

More generally, the theory of active gels can also take into account the polarity of the filaments by incorporating concepts from the hydrodynamic theory of liquid crystals [153, 304, 132]. This translates into a polarization supplementary term in the free energy associated to the conjugated orientational field. This powerful theory accounts for many experimental observations especially in living systems [93, 190].

Active matter encompasses systems that are able to locally transduce energy into physical forces. In the case of reconstituted active gels, the energy is injected in the system thanks to the hydrolysis of ATP mediated by molecular motors. Thus, such systems are able to self-organize into complex shapes and patterns. Self-organization through pattern formation is also possible using other mechanisms. Indeed, well-defined concentration patterns of chemicals arise from chemical reaction and diffusion of molecules, as we will discuss in the next section.

## 2.2 Pattern formation by reaction-diffusion

Beside active matter in which self-organization happens through the coupling of reaction and mechanics, a molecular system may also self-organize when molecules are involved in chemical reactions and transported by diffusion. In this section we explore the patterning properties of such reaction-diffusion systems. Originally observed experimentally in redox reactions, reaction-diffusion patterning is increasingly studied in living systems, but can also be investigated in reconstituted *in vitro* systems and even be rationally re-engineered.

### 2.2.1 Reaction-diffusion formalism

#### Kinetics

We consider two reactive species A and B. In the absence of diffusion, for example in a well-stirred reactor, the evolution of the concentrations  $A$  and  $B$  is given by

$$\frac{dA}{dt} = f(A, B) \quad (2.20)$$

$$\frac{dB}{dt} = g(A, B), \quad (2.21)$$

where  $f$  and  $g$  are functions accounting for reaction kinetics. This case is called the 0D case, since no spatial dependence is considered. For example, the elementary reaction  $A + B \xrightarrow{k} 2A$  is represented by the functions  $f(A, B) = kAB$  and  $g(A, B) = -kAB$ .

More complex chemical reactions have been examined. As a historical example, we introduce the Lotka-Volterra system, an example of a predator-prey system. It was simultaneously introduced in 1926 by Vito Volterra, to explain the increase of predator fishes in the Adriatic Sea during World War I, and by Alfred Lotka in 1925, to describe a hypothetical chemical reaction in which the chemical concentrations are oscillating. It is the simplest model of predator-prey interactions. The model has been extensively studied and extended in order to take into account experimental data in chemistry, biology and ecology, such as the — criticized — data on rabbits and lynx in Canada (Figure 2.8 (b)). Two coupled non-linear differential equations govern the evolution: the populations of predators (L, for lynx) and preys (R, for rabbits) change through time according to

$$\frac{dR}{dt} = \alpha R - \beta RL \quad (2.22)$$

$$\frac{dL}{dt} = \delta RL - \gamma L, \quad (2.23)$$

where  $\alpha$ ,  $\beta$ ,  $\delta$  and  $\gamma$  are constants that, respectively, correspond to the growth rate of R, the predation rate of R by L, the growth rate of L due to the predation and the death rate of L. This system exhibits out-of-phase periodic oscillations of R and L (Figure 2.8 (a)).

The way chemical species interact with each other is called a chemical reaction network. How they are linked defines the topology of the network, where the nodes are the chemical species and the links are the rates of reaction.

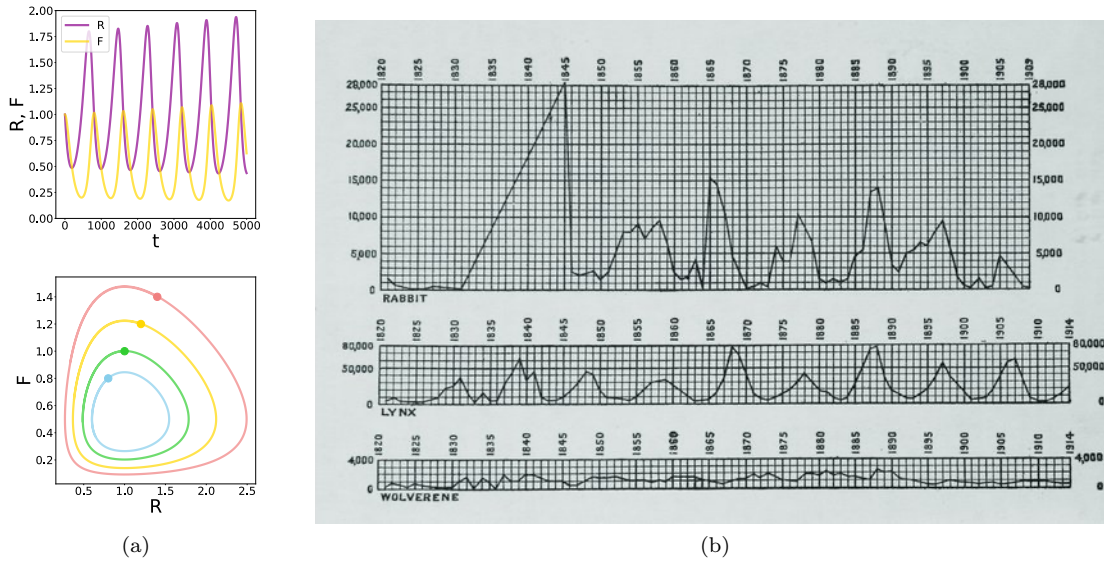


Figure 2.8 | **The Lotka-Volterra oscillator.** (a, top) Simulation of the temporal oscillations of the Lotka-Volterra predator-prey system. The parameters used are:  $\alpha = 2/3$ ,  $\beta = 4/3$ ,  $\delta = 1$  and  $\gamma = 1$ . (a, bottom) Phase portrait using the same parameters, for different initial conditions (large dots). (b) Evolution of the number of pelts captured by the Hudson's Bay Company in Canada between 1820 and 1914 (data collected by Hewitt, 1921) for rabbits, lynx and wolverines. The number of rabbits and lynx exhibits periodic oscillations that have been interpreted as a predator-prey system, but are more probably due to other factors [150]. The linear growth in rabbits after 1830 is an interpolation.

### Reaction, diffusion and propagation of fronts

In a non-stirred 1D reactor, diffusion has to be taken into account. Thus, equations (2.20) and (2.21) become

$$\frac{\partial A}{\partial t} = f(A, B) + D_A \frac{\partial^2 A}{\partial x^2} \quad (2.24)$$

$$\frac{\partial B}{\partial t} = g(A, B) + D_B \frac{\partial^2 B}{\partial x^2} \quad (2.25)$$

where the diffusion coefficients of A and B are  $D_A$  and  $D_B$ , respectively, and they are supposed to remain constant here. Nevertheless, in some conditions, diffusion coefficients can be concentration-dependent. The coupling of space and time and the non-linearities of the chemical functions give birth to a rich variety of behaviors and patterns. Some experimental examples will be presented in Section 2.2.2.

An important example is the reaction-diffusion equation associated to the autocatalytic production of a chemical species that can lead to chemical fronts traveling at constant velocity. If the reaction involves only one chemical species, the spatio-temporal dynamics is now given by

$$\frac{\partial A}{\partial t} = f(A) + D_A \frac{\partial^2 A}{\partial x^2}, \quad (2.26)$$



where  $f(A)$  is the reaction term. In the simple case where the reaction is given by  $A \xrightarrow{k} 2A$  then  $f(A) = kA$ . One can search for a wave solution  $A(x - vt) = A(u)$  of eq. (2.26). This gives  $DA'' + vA + kA = 0$ . To obtain a traveling solution, the discriminant has to be positive, leading to  $v \geq 2\sqrt{kD}$ . The faster the reaction is — or the diffusion — the greater is the velocity. More generally, for a function  $f(A)$  assuming the following reasonable conditions: (i) bounded growth, i.e. there exists  $A_{max} > 0$ , such that  $f(A_{max}) = 0$ , (ii)  $f(0) = 0$ , (iii)  $f'(0) > 0$ , (iv) on  $[0, A_{max}]$   $f(A) > 0$  and (v)  $f'(A) < f'(0)$ , we come across the Fisher-Kolmogorov-Petrovskii-Piscunov (FKPP) case [146] where a unique stable asymptotic traveling wave solution exists and where the minimum velocity is given by

$$v_m = 2\sqrt{f'(0)D}. \quad (2.27)$$

Experimentally, chemical fronts in autocatalytic systems are easy to observe if the initial condition takes the form of a step function along a linear reactor, thus breaking the symmetry of concentration. In Chapter 4, following the work of Zadorin et al. [325], we will design reaction-diffusion fronts from an autocatalytic reaction involving DNA strands.

Stable patterns in reaction-diffusion systems can also arise spontaneously as Alan Turing demonstrated in his very influential single mathematical biology paper *The Chemical Basis of Morphogenesis* [289]. Such patterns — also known as Turing patterns — happen if the functions describing the chemical reactions ( $f$  and  $g$ ) are more constrained [63]. The experimental design of Turing-compatible reaction networks is difficult to achieve because of the tightness of these constraints. It notably requires a difference of diffusion between chemical species [84].

### 2.2.2 Patterns in redox reactions

Reaction-diffusion patterns were originally observed and studied by chemists looking at redox reactions. Indeed, these reactions display strongly non-linear kinetics, are composed of inexpensive chemicals and often exhibit changes of color. We describe in this short section some pioneer works of the field.

The first studies of macroscopic chemical waves and patterns originating from the coupling of reaction kinetics and diffusion were initiated by Robert Luther, more than a century ago, using several experiments including a mix of sulfuric and oxalic acid in the presence of permanganate [169]. Propagating fronts of chemical reactivity were observed later in the iodate oxidation of arsenous acid by Epik and Shub in 1955. An extensive experimental and analytical treatment of wave propagation in the arsenous acid-iodate reaction was performed by Showalter and coworkers in 1982 [107].

Oscillating reactions have been broadly examined for pattern formation. One of the best known reactions is the one discovered by Boris Belousov in 1950, a Russian biochemist interested in the Krebs cycle (or citric acid cycle), and redesigned in 1961 by Anatol Zhabotinsky. The Belousov-Zhabotinsky (BZ) reaction is composed of coupled redox reactions where bromic acid oxidizes malonic acid into bromomalonic acid, formic acid and  $\text{CO}_2$  in the presence of a metal catalyst, for example  $\text{Ce}^{4+}/\text{Ce}^{3+}$  or  $\text{Ru}^{3+}/\text{Ru}^{2+}$ . The BZ reaction can generate up to several thousand

oscillatory cycles in a closed system. Using a thin layer of unstirred solution containing the ferroin version of the BZ reaction, Zaikin and Zhabotinsky observed periodic propagation of chemical waves generated by point pacemakers [327]. Collision of such waves leads to mutual annihilation due to the presence of non-excitable refractory zones. When the waves are broken the excitation fronts curl around their refractory tails and form spiral waves [312] (Figure 2.9 (a)).

Finally, stable Turing patterns were observed for the first time in vitro in 1990 by de Kepper and colleagues in the chlorite-iodide-malonic acid reaction (CIMA) [34] almost forty years after Turing's discovery (Figure 2.9 (b)). Experiments were carried in a thin disk of gel whose upper and lower sides were connected to open reactors in order to keep the system truly out-of-equilibrium. The role of the gel was to suppress convection and thus allow the observation of reaction-diffusion phenomena. In addition, the reaction was performed in the presence of starch, initially used as a color indicator for  $I_3^-$  ions, but also playing a crucial role in modifying the effective reaction and diffusion rates of  $I^-$  and helping to satisfy the Turing conditions mentioned in the previous section. Starting in 2001, Vanag and Epstein published a series of remarkable observations of complex reaction-diffusion patterns in closed reactors, including Turing patterns [299]. They reduced the diffusion coefficient of some reactants of the BZ oscillator by dispersing the reaction inside water-in-oil droplets stabilized by the surfactant aerosol OT (aerosol sodium bis(2-ethylhexyl) sulfosuccinate). The advantage of this reaction medium is that hydrophilic BZ species are retained inside the droplets whereas hydrophobic ones can freely diffuse from droplet to droplet across the oil phase. As a result, hydrophobic species such as  $Br_2$  or  $BrO_2^{\cdot}$  diffuse fast (with a diffusion constant of  $10^{-9} \text{ m}^2\text{s}^{-1}$ ) while the diffusion of hydrophilic species such as  $Br^-$  is limited by the diffusion of the droplets ( $10^{-11}$  to  $10^{-12} \text{ m}^2\text{s}^{-1}$ ).

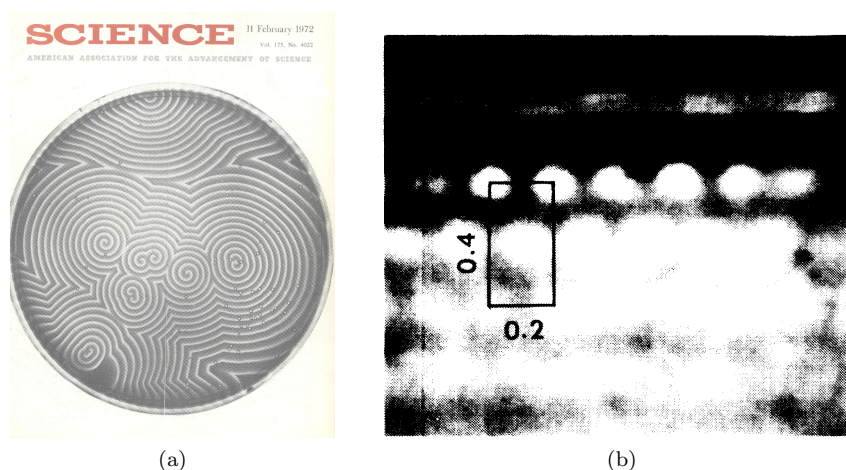


Figure 2.9 | **Synthetic reaction-diffusion patterns.** (a) Propagation of chemical spiral waves in the Belousov-Zhabotinski reaction [312]. Image from Arthur T. Winfree in *Science Front Matter* Vol. 175, Issue 4022, 11 February 1972. (b) Sustained Turing-type chemical pattern using the CIMA reaction. Dimensions are in mm. Adapted from [34].

### 2.2.3 In vitro reconstituted biochemical reactions

Above, we have given examples of reaction-diffusion patterns arising in redox reactions. However, despite many efforts, in particular in the systematic studies undertaken to create new chemical oscillators, redox reactions remain difficult to engineer de novo: the reactivity and the diffusion of molecules are most of the time fixed a priori. Moreover, these reactions often happen in extreme pH conditions (acidic in the case of the BZ reaction) which precludes any effort to combine them with biological materials such as the active gels presented in Section 2.1.3 or DNA/enzymes and transcription-translation systems adumbrated in Chapter 1. To solve this issue, researchers have looked at in vivo chemical reaction networks. We are presenting two systems found in living organisms that have been studied in vitro. Firstly, the Min bacterial system that has been purified and reconstituted and, secondly, a cell-free transcription-translation system that has been repurposed to generate reaction-diffusion fronts.

#### The Min bacterial system

In normal conditions, growing bacteria are able to divide with an extraordinary precision. The position of the division plane is located at the middle of rod-shaped bacterial cells such as *E. coli* with a 3% accuracy. Thus, cells must ‘calculate’ the position where division — triggered by the polymerization of protein FtsZ into a Z-ring structure — will take place. The midpoint is determined thanks to the Min system (and also by another mechanism based on nucleoid occlusions). Briefly, the system is composed of three proteins MinC, MinD and MinE whose intracellular dynamics inhibit cell division at the poles and promote the formation of the Z-ring at the centre. In vivo, MinC and MinD, which are located at the membrane, continuously oscillate from pole to pole, forming a standing wave of period  $\sim 1$  min [227]. Free-diffusing MinD-ADP is phosphorylated into MinD-ATP, triggering its dimerization and binding onto the membrane. MinC and MinE can both bind to the membrane-bound MinD. MinE de-phosphorylates membrane-bound MinD and regenerates free MinD-ADP (Figure 2.10 (a)). At the same time MinE forms a ring at the frontier between high and low MinC/MinD surface concentration.

In vitro, in the presence of ATP and a lipid bilayer surface, fluorescently-labeled MinE and MinD generate spiral patterns and traveling concentration waves on the surface of the lipid membrane (Figure 2.10 (b)) with typical velocities of  $30 \mu\text{m}/\text{min}$  and wavelengths of  $50 \mu\text{m}$  [166, 337]. The in vitro wave speeds are comparable to in vivo ones and are determined by the ratio between the concentrations of MinE and MinD. This system has been rationally redesigned by taking into account protein sequences and motifs [90]. It has been reported that the Min oscillatory system could induce vesicle shape deformation possibly by the transient recruitment of protein MinE on the membrane [163].

#### Cell-free transcription-translation fronts

Gene regulation is used by all living organisms to dynamically produce proteins from DNA allowing them to adapt to a changing environment and process chemical information. During gene regulation, a gene is transcribed by an RNA polymerase into an RNA which is subsequently translated by the ribosome into a protein. It may happen that the produced protein has the property of regulat-

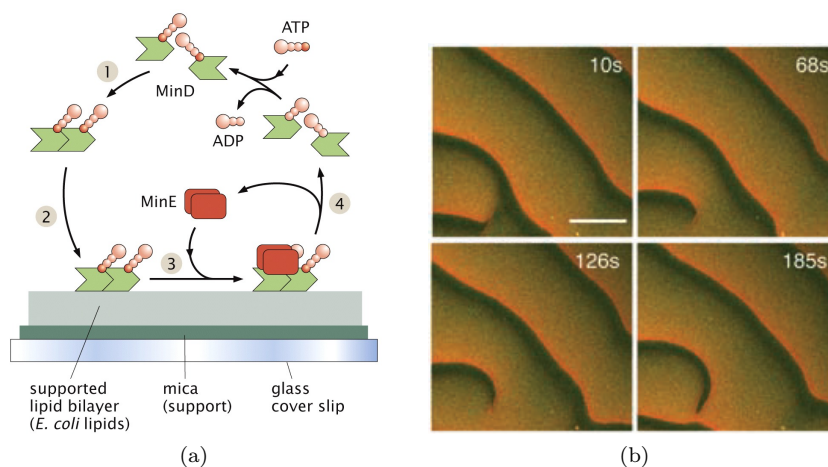


Figure 2.10 | **In vitro reconstituted reaction-diffusion systems - The Min system.** (a) Mechanism of the Min bacterial system. Adapted from [216]. (b) In vitro Min-protein surface waves on a supported lipid membrane. Adapted from [166].

ing gene production, either from a different gene or from itself for instance by blocking or promoting the transcription reaction, thus causing the repression or the activation of the downstream protein. In that case the protein is called a transcription factor. This way, regulatory networks can be constructed using the transcription and translation reactions. Regulation may also happen thanks to other molecules such as RNA. Since the 1960s it is possible to recapitulate these reactions outside of living cells using the so-called cell-free transcription-translation (TXTL) systems [203]. In the last two decades the purity and performance of cell-free TXTL systems have been greatly enhanced by improving, for example, the chemical energy regeneration pathways. Cell-free TXTL systems are nowadays used in a wide range of domains like the production of cytotoxic molecules or the rapid evaluation of gene regulatory networks [262]. The latter application is studied in Chapter 5 where we will look at the RNA control of gene expression using a TXTL reconstituted system. During the transcription-translation process, proteins are produced by a regulated network whose topology and dynamics can be precisely tuned. For this reason these systems can be repurposed to study reaction-diffusion patterns.

Isalan, Lemerle and Serrano published in 2005 a seminal paper demonstrating that stable patterns of protein concentrations could be obtained using cell-free TXTL reactions [129]. More recently Karzbrun, Tayar, Bar-Ziv and collaborators introduced an open microfluidic spatial reactor where TXTL reaction networks could be maintained out-of-equilibrium for long periods of time without perturbing reaction-diffusion dynamics [138]. It is composed of a suite of microchamber reactors connected to each other through thin channels where gene products can diffuse, forming a one-dimensional array. The DNA molecules carrying the corresponding genes are attached to the surface of the microchambers. In addition, each reactor is connected by another thin channel to a wider channel parallel to the array, where a continuous flow of all the components necessary for transcription and translation is maintained. This second set of thin channels allows exchange of enzymes and small molecules from and to the wider channel but precludes hydrodynamic flow, and acts as a physical sink, thus keeping the system out of equilibrium. Using this inventive system

the authors reported the first observation of a traveling front in a TXTL system [278]. They did so by using a bistable network composed of an autocatalytic loop and a repressor (Figure 2.11 (a)). The transcription factor  $\sigma^{28}$  activates its own promoter and a reporter construct which synthesizes GFP. The positive feedback of the autocatalytic loop is inhibited by the  $A\sigma^{28}$  protein which binds to the factor  $\sigma^{28}$  preventing its binding. A monostable autocatalytic network did not provide fronts because TXTL networks are known to have leak reactions (RNA is synthesized even in the absence of an activating transcription factor) that lead to homogeneous growth instead of a traveling front. In this system, the authors measured front velocities of about  $10 \mu\text{m}/\text{min}$  (Figure 2.11 (b)).

In an other experiment, the authors investigated the reaction-diffusion dynamics of a TXTL oscillator inside the same set-up [279]. When the chambers were not connected by diffusion, oscillations were uncoupled, while they synchronized when the coupling was sufficiently strong. Interestingly, the authors observed traveling waves in the presence of a gradient of concentration of one of the components of the network.

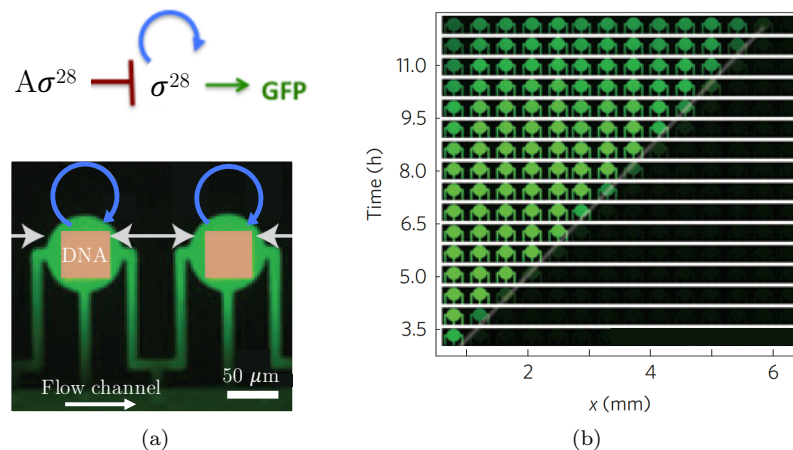


Figure 2.11 | **In vitro reconstituted reaction-diffusion systems - Cell-free TXTL fronts.** (a) A fluorescent protein front generated by a bistable cell-free TXTL network inside a unidimensional microchamber array. The bistable network based on the regulation of the  $\sigma^{28}$  transcription factor (top) and a picture of two coupled microchambers (bottom). (b) Images of the 1D channel for different times showing the propagating front. Adapted from [278].

### 2.2.4 Reaction-diffusion patterns made of DNA

In vitro reconstituted systems are natively biocompatible but rely on protein interactions which are hard to engineer. However cell-free TXTL expression systems can be partially tuned through the DNA sequences coding for proteins or by using RNA regulators (see Chapter 5) and the Min bacterial system has been redesigned by taking a modular approach [90]. In this section we show that nucleic acids, and especially DNA, can easily overcome these two main difficulties of biocompatibility and programmability when used to create chemical reaction networks.

### Using DNA to build chemical reaction networks

The design of new chemical reaction networks goes through the precise adjustment of the reaction rates and the topology of the network. These two properties are very difficult to engineer in chemical functions due to the lack of structure/function relationships, except for hybridization reactions involving nucleic acids. Indeed, nucleic acid reactivity derives from its structure composed of two single stranded DNA (ssDNA) that obey Watson-Crick base-pairing rules (A/T, G/C). The length and the sequence of the DNA strands literally code for the reaction rates and the network topology: an ssDNA can only hybridize with a strand having the complementary sequence. The number of nucleobases involved in the pairing, the temperature and the salt concentrations set the reaction rates.

The idea that DNA can be used as a substrate to engineer dynamic networks has been implemented with a reaction scheme called strand displacement (Figures 2.12 (a) and (b)). Two strands with partial or full complementarity hybridize to each other, then displacing one or more pre-hybridized strands in the process. Strand displacement is initiated at complementary single-stranded domains called ‘toeholds’. Thus, in this process, a new toehold can be generated. By varying the strength of toeholds sequences — principally the length — the rate of strand displacement reactions can be quantitatively controlled over a factor of  $10^6$  [332]. By combining multiple strand displacement reactions with controlled kinetics, one can create a chemical reaction network entirely made of DNA. Since the first design [323], DNA strand displacement reactions have been used to design molecular circuits, motors and sensors in cell-free settings [331]. These reactions can also operate in a biological environment such as mammalian cells [100]. Complex reaction networks have been engineered including oscillations [268].

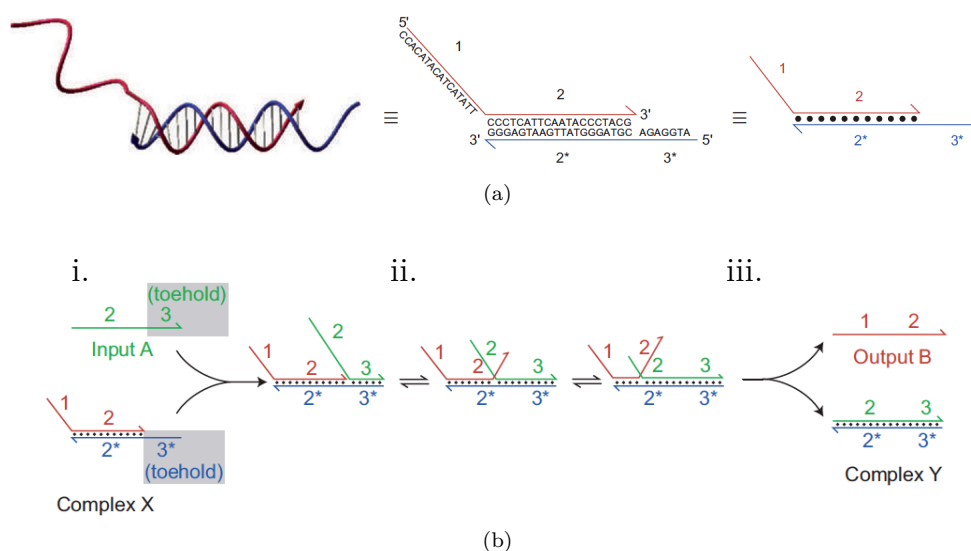


Figure 2.12 | **DNA strand displacement.** (a) DNA is represented as directional lines, with the hook denoting the 3' end. The sequences of the nucleotide bases are usually not shown. (b) Example of a DNA strand displacement reaction. i. Toehold domains initiate binding, ii. then domain 2 undergoes branch migration and iii. strand displacement is completed. Both figures are adapted from [331].

DNA reaction networks are fully programmable but have three important drawbacks. Firstly, many DNA strands are required to compute elementary functions such as autocatalysis, leading to a great increase in complexity. Secondly, the relevant timescales of such systems are in the order of a few hours. That can be problematic if coupled to other biochemical processes where timescales are measured in terms of seconds or minutes. Thirdly, fuel DNA complexes — that serve to maintain the system away from equilibrium — ‘leak’, meaning that they react through undesired pathways.

Thus, other systems combining nucleic acids with a small number of proteins have been designed to overcome these difficulties. In particular polymerases are used to increase the rate of production of nucleic acids [266]. The two most notable systems involving nucleic acids and enzymes are the ‘genelets’ system, developed by Kim, Winfree and coworkers and the ‘PEN-DNA toolbox’ developed by Rondelez and coworkers. In the genelets system, RNA strands are produced and inhibited from DNA template molecules. The production and the degradation are achieved by an RNA polymerase and an RNase. Using this system, a bistable network [143] and an oscillator have been designed [144]. The PEN-DNA toolbox [186, 12], composed of three enzymes and DNA strands, is going to be presented in more detail in the next section as we will use it to build an autocatalytic amplification in Chapter 4.

### DNA nanotechnology

Proposed in the 1980s by Seeman [249], the utilization of nucleic acids to build nanomaterials that self-assemble has led to the DNA nanotechnology field. Following Watson–Crick base-pairing rule, many static and dynamic nanostructures have been conceived: from the original design of a DNA cubic structure [38] to large DNA/RNA origamis of arbitrary shapes [238, 80] that can be responsive [6, 149]. In addition, small DNA-based nanomachines have been created such as tweezers [323] or cargo-sorting robots [284]. When coupled to other molecules and objects, DNA plays an important role in the design of responsive smart nanomaterials where the interactions can be precisely tuned [133], like those that govern droplet and colloid aggregation [134, 235, 81]. Among others, DNA nanostructures have thus found applications in diagnostics, nanoparticles and proteins assembly, drug delivery and synthetic biology [250]. DNA nanotechnology has always been related to computer sciences where DNA molecules are exploited to solve complex problems [2, 172].

### The PEN-DNA toolbox

This system combines short DNA strands and three enzymes. The term ‘PEN’ refers to the three enzymes involved in the reactions: a polymerase, an exonuclease and a nicking enzyme. They are, in addition, two types of ssDNA species: nodes that are produced and degraded by the enzymes, and templates that are not modified. Following DNA hybridization rules, the sequence of the ssDNA template species defines the topology of the reaction network. The production and degradation of node species consume deoxyribonucleoside triphosphates (dNTP) and produce deoxynucleoside monophosphates (dNMP). This is a dissipative process that stops once the dNTPs are depleted. Importantly, leak reactions are strongly reduced by the specificity of the enzymes.

By combining these different elements, one can emulate basic functions such as activation, degradation and inhibition:

- **Activation and autocatalysis** (Figure 2.13, i.). The input ssDNA A (a node) hybridizes on an activation template  $T_{AB}$  before being elongated by a polymerase, resulting in a dsDNA. The sequence has been chosen to exhibit a recognition site for the nicking enzyme. Thus the newly formed strand is nicked into two fragments: the original A and a new one B. In the case where the sequence of B is the same as the sequence of A, the activation becomes an autocatalytic amplification.
- **Inhibition** (Figure 2.13, ii.). The input ssDNA A hybridizes on an inhibition template R (also called ‘repressor’ or ‘pseudotemplate’) before being elongated by a polymerase resulting in a dsDNA. Contrary to the previous case there is no nicking site. Thus, this strand cannot interact any more with an activation template and will be degraded by the exonuclease.
- **Degradation** (Figure 2.13, iii.). In the presence of a third enzyme — an exonuclease — inputs and outputs are recognized and degraded. Moreover the exonuclease destroys any species that is not actively produced by a template. Templates are protected against degradation by phosphorothioate modifications located in the 3'-end.

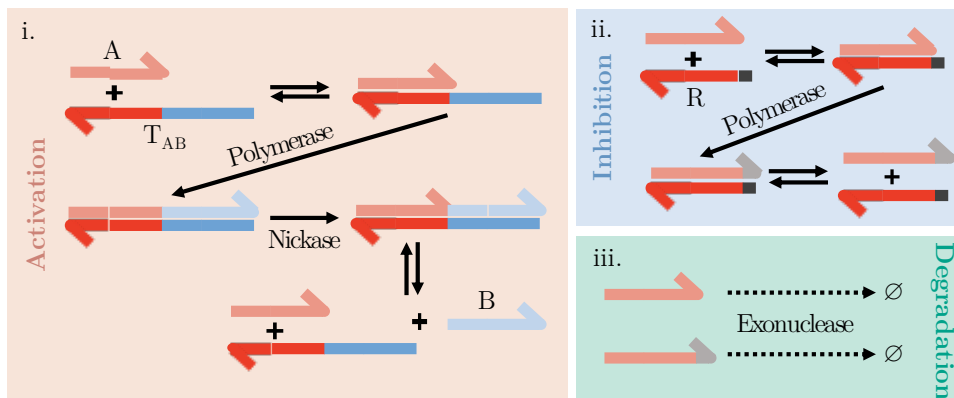


Figure 2.13 | **Basic reactions with the PEN-DNA toolbox.** i. Activation, ii. inhibition and iii. degradation. They involve one to three of the following enzymatic reactions: extension of input over a template by a DNA polymerase, cutting of an extended strand by a nicking enzyme and degradation of single strands by an exonuclease

Although the PEN-DNA toolbox was completely de novo engineered, it was inspired from gene regulatory networks. Indeed, they both rely on the three basic mechanisms of activation, inhibition and degradation (Figure 2.14). In vivo, or in cell-free TXTL systems, a gene is transcribed into an RNA which is consecutively translated into a protein. This protein can be a regulator of the transcription of a second gene. In this sense, the transcription and translation steps are activation steps, while the regulation can be either an activation or inhibition event. Furthermore, RNA and proteins can be degraded. In the PEN-DNA toolbox, genes are replaced by ssDNA templates and dynamic effectors — RNA and proteins — are replaced by ssDNA inputs and outputs (the nodes) created from replication of the templates (Figure 2.14 (b)). Nevertheless, gene regulatory networks



are much more complicated than this simple picture. We can mention for example, regulatory mechanisms, not displayed in Figure 2.14 (a), based on RNA molecules that directly regulate the translation of an other gene. These are called translational riboregulators and will be discussed in Chapter 5.

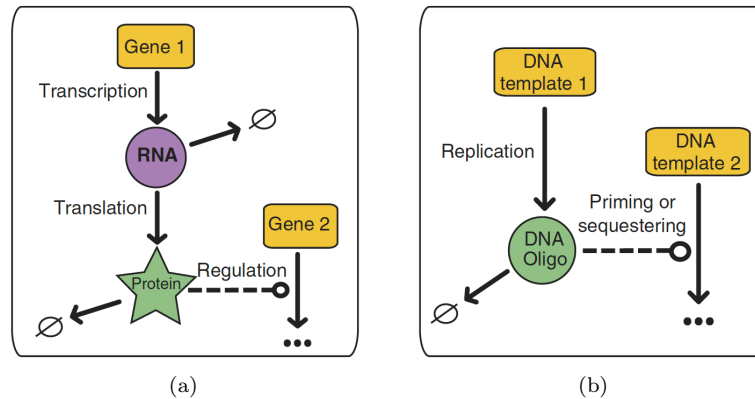


Figure 2.14 | **Analogy between a gene regulatory network and the PEN-DNA toolbox.** (a) Schematic description of a simple gene regulatory network. (b) Similar representation of the PEN-DNA toolbox. Both sketches are adapted from [186].

In PEN-DNA reactions, the network topology is changed by designing input and output sequences and connecting them through activating or inhibiting modules. Various reaction networks have been built from relatively simple modules such as autocatalysis [185] and inhibited amplification [185, 186] (Figure 2.15 (a)) to complex switchable memories (Figure 2.15 (b)) [210, 178, 326] and oscillations (Figure 2.15 (b)) [186, 72]. The space of parameters (concentrations) of these reaction networks can be mapped using high throughput microfluidic methods [82] (Figure 2.15 (d)).

### Reaction-diffusion patterns constructed with the PEN-DNA toolbox

Reaction-diffusion patterns appear when an attention is paid to the spatio-temporal dynamics of the chemical reaction networks built with the PEN-DNA toolbox in non-homogeneous reactors. One of the easiest network to probe is the autocatalytic amplification. It leads to a traveling front propagating at constant velocity (of about  $60 \mu\text{m}/\text{min}$ ) that can last a few hours and even several days [325, 290] (Figure 2.16 (a)). In such systems we have seen that the velocity is proportional to  $\sqrt{kD}$  where  $k$  and  $D$  are respectively the constant of reaction and the diffusion constant. Interestingly both of these two parameters are tunable in the PEN-DNA toolbox. The reaction constant is directly tunable via the concentration of the template or the concentration of the polymerase. Moreover, the diffusion constant of the DNA template can be decreased by attaching a micelle [325] or a polymer [290] to one of their ends. In Chapter 4 we will see that it is possible to couple a PEN-DNA traveling front with a cytoskeletal active gel.

Patterns emerge in more complex PEN-DNA chemical reaction networks. The predator-prey molecular system whose temporal behavior in bulk is depicted in Figure 2.15 (c), exhibits traveling waves or pulse of preys followed by predators [209, 328] (Figure 2.16 (c)). Propagation of DNA

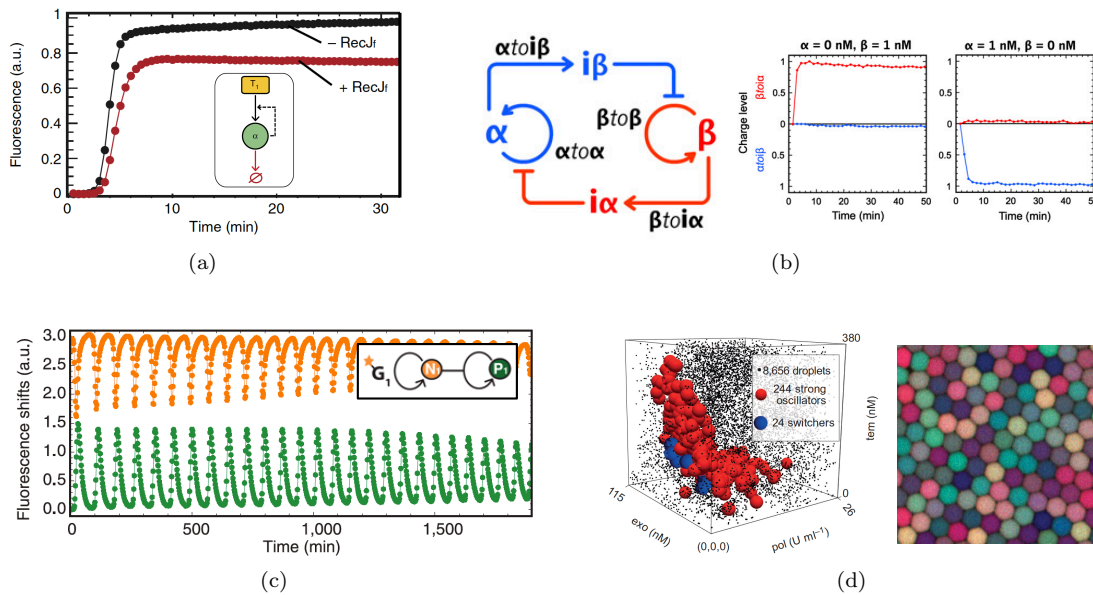


Figure 2.15 | **Examples of reaction networks designed with the PEN-DNA toolbox.** (a) Autocatalytic production of a DNA input. The fluorescence (i.e. DNA concentration) reaches a plateau when the template gets saturated. Adapted from [186]. (b) Bistable circuits in which two autocatalytic modules negatively regulate one another (left). Normalized time plots of the bistable switch: the final state depends on the initial combination of  $\alpha$  and  $\beta$  concentrations (right). Adapted from [210]. (c) Predator-prey molecular oscillator. Adapted from [72]. (d) Bifurcation diagram of the molecular predator-prey oscillator using thousands of droplets with different experimental conditions. Adapted from [82].

fronts across a population of colloids covered with DNA template has been conceived [87]. Stable patterns have been also engineered: a bistable network in response to a gradient of a DNA template concentration leads to two immobile fronts that repel each other [326] (Figure 2.16 (b)).

Reaction networks only composed of DNA molecules can also give rise to stable patterns like linear and hill shapes [330], or perform spatial detection by computing edges [39]. However, as mentioned above, these enzyme-free networks often require many DNA strands.

## 2.2.5 Turing-like patterns in vivo

Finally, we would like to conclude this section by briefly discussing the case of stable patterns found in vivo which are often interpreted as Turing patterns. Indeed, the Turing spatial instability could explain why the stripe patterns on the surface of the tropical fish *Pomacanthus imperator* move on the scale of days [147] (Figure 2.17). In addition, colored patterns on the skin of an ocellated lizard have been proven to be produced by a cellular automaton. This mechanism emerges from a continuous Turing system when particular spatial conditions are imposed. The skin thickness variation causes the reaction-diffusion dynamics to separate into microscopic and mesoscopic spatial scales, the latter generating the cellular automaton [171]. Evidence of an underlying Turing mechanism has also been reported during digit patterning in mice [256]. However, the spots and the stripes of large mammals (zebras, tigers, ...) are not due to a Turing mechanism but rather arise from the migration and the multiplication of pigmented cells.

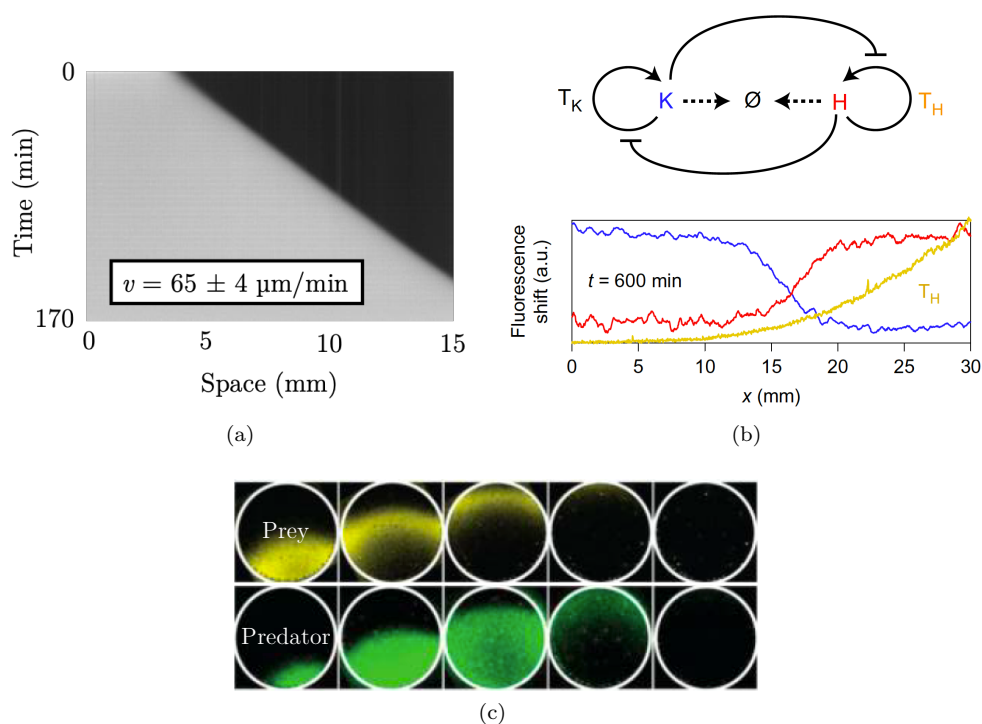


Figure 2.16 | **Reaction-diffusion patterns designed with the PEN-DNA toolbox.** (a) Kymographs (time versus position) showing the propagation of a DNA front engineered from an autocatalytic amplification from left to right. A high concentration of DNA is indicated by a white color. Adapted from [325]. (b) A DNA-based network with two self-activating nodes that repress each other generates two immobile fronts (red and blue) that repel each other in response to the gradient of DNA template (yellow). Adapted from [326]. (c) Propagation of waves in a predator-prey molecular network. Images are taken every 10 min in an 11 mm diameter, 200  $\mu\text{m}$  thick circular reactor. Adapted from [209].

Reaction-diffusion concepts can be extended to other patterning concepts. For example the ‘lateral-inhibition’ mechanism participates in the assembly of complex spatial structures. In this mechanism, a cell with a particular fate communicates with the neighboring cells to prevent them to have the same one. The ‘Notch-Delta’ system is an archetype of such mechanism: the inhibition is accomplished thanks to the Notch membrane-bound receptor and can be activated by the transmembrane ligand Delta supplied by a neighboring cell. In particular, this system is involved in the cell specification process during *Drosophila* eye development. It is possible to genetically engineer lateral-inhibition mechanisms in cells [175]. Moreover, molecules can be transported by other means and not only by diffusion. This is the case of phyllotaxis, the mechanism used by plants to organize the arrangement of branches, leaves, petals and seeds. Regulation of the signaling molecule auxin is controlled in many ways including growth and external physical stimulus (gravity, light).

In vivo, these reaction-diffusion mechanisms between molecules (and especially proteins) are

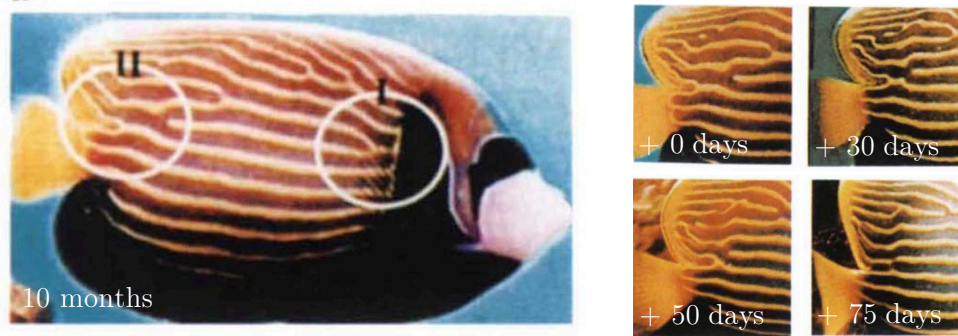


Figure 2.17 | **Turing-like patterns in *Pomacanthus imperator*.** Rearrangement of the stripe patterns of *Pomacanthus imperator*. Adapted from [147].

often combined with other self-organizing mechanism, such as those associated with active matter. These intricate links are particularly visible during embryo development when chemical and physical forces act in concert, as we will see in the following.

## 2.3 Interplay of chemical and mechanical forces: two examples from embryo development

The patterning mechanisms described in the previous sections — active matter and reaction-diffusion — are not mutually exclusive. In many cases, such as during embryo development, both happen synchronously. In this section we concisely review two *in vivo* examples of pattern formation and morphogenesis: the establishment of cell polarity in the *C. elegans* nematode and the development of the *Drosophila* blastoderm with the concept of positional information.

### 2.3.1 Cell polarity establishment in *C. elegans*

Cell polarity emerges from the interplay between chemical and mechanical systems [92]. The establishment of the antero-posterior axis in the one-cell stage of *C. elegans* embryos depends both on mechanical — actin/myosin — and on biochemical — partitioning-defective protein (PAR) — networks. These PAR proteins, conserved throughout the animal kingdom, are essential in many processes: cell migration, cell fate, establishment of body plans and epithelial tissue architecture. They are typically composed of two groups of antagonistic PAR proteins. In *C. elegans*, these include PAR-3, PAR-6 and aPKC, which localize on the anterior membrane, and PAR-1, PAR-2 and LGL, which localize to the posterior. They form a reaction-diffusion system (Figure 2.18 (a)) that self-organizes into a non-polarized or a polarized state. Pattern formation in this embryo is then induced by advection of PAR proteins by an actomyosin-dependent cytoplasmic flow. It allows membrane binding of posterior PAR proteins, resulting in an asymmetry that can be amplified by the PAR reaction-diffusion system 2.18 (b)).

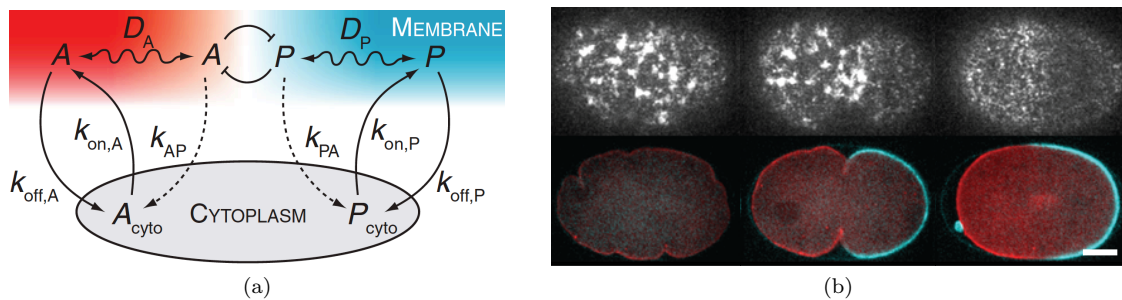


Figure 2.18 | **Establishment of cell polarity in *C. elegans*.** (a) The reaction-diffusion PAR model. The two proteins PAR-6 (A, in red) and PAR-2 (P, in blue) switch between the cytoplasm and a membrane-associated state where they can only diffuse laterally. Adapted from [93]. (b) Cell polarization involves a reaction-diffusion system and long range flows of a thin layer of contractile actomyosin cortex. (top) Fluorescence images of myosin motors driving cortical flows, (bottom) fluorescence images of the proteins PAR-6 (red) and PAR-2 (cyan). Total time is 15 min and scale bar is 10  $\mu\text{m}$ . Images adapted from Goehring's lab [link].

### 2.3.2 Early stages of *Drosophila* blastoderm development

#### The French flag problem

In developing embryos, cells ‘need to know’ where they are in order to determine their fate. Lewis Wolpert in 1969 proposed a conceptual framework [316] to explain how an embryo with a single break of symmetry (induced through a Turing process or an initial gradient) could differentiate further into several distinct regions. How will the cells on the left become the head, the cells on the right the abdomen and the cells in the middle the thorax? He proposed the term ‘French flag problem’ to illustrate the challenge of generating distinct regions of space with sharp borders from an amorphous mass and a shallow concentration gradient. Wolpert’s idea makes it easy to visualize how a morphogen gradient spread within an embryo can be used to define the fate of the embryo’s cells. As depicted in the Figure 2.19 (a), each cell may define its fate by simply measuring the morphogen concentration around itself. Two concentration thresholds,  $T_1$  and  $T_2$ , will then be sufficient to provide three cell fates. The gradient thus provides to the cells what is called a *positional information*.

#### Patterning genes

The first clear evidence of positional information was observed during the early development of the fruit fly *Drosophila melanogaster*, which is one of the best studied model organisms. In *Drosophila* the complete growth process from egg to adult takes approximately ten days and it involves four distinct stages: embryo, larva, pupa and adult. Embryogenesis lasts only 24 h, after which the egg hatches into a larva [317]. *Drosophila* embryogenesis is singular among model organisms as it initially takes place in a syncytium, a single cytoplasm where nuclei divide without cell membranes, which could facilitate morphogen transport by diffusion. During these stages the embryo is called a syncytial blastoderm, with the yolk occupying a large central part and the cortex containing a monolayer of nuclei. The blastoderm — a 500  $\mu\text{m}$ -long ovoid — has two hierarchical systems of patterning, an antero-posterior and a dorso-ventral. Since the work of Driever and Nüsslein-Volhard in 1988 [52], positional information has been experimentally proved. Positional information during antero-posterior patterning is provided by three maternally-induced protein gradients. One of them is bicoid, whose concentration decreases gradually from the anterior to the posterior of the embryo. These gradual maternal gradients regulate the expression of downstream gap genes that produce sharp concentration profiles of their protein products. For example, the bicoid gradient generates a sharp hunchback gap profile. There are more than twelve gap gene proteins. Subsequently, gap and maternal proteins control the formation of pair-rule protein patterns, such as even-skipped that forms seven 50  $\mu\text{m}$ -wide stripes that will help to define the positions of body segments that appear later in development (Figure 2.19 (c)).

#### Formation of the cephalic and the ventral furrows

The *drosophila* embryo is sequentially subdivided into an array of different types of tissues and specialized segments that express various combinations of genes. These singular compositions trigger local variations of shape that lead to global changes in morphology. Thus, two invaginations called the ventral and cephalic furrows are among the first morphological manifestations of cell fate.

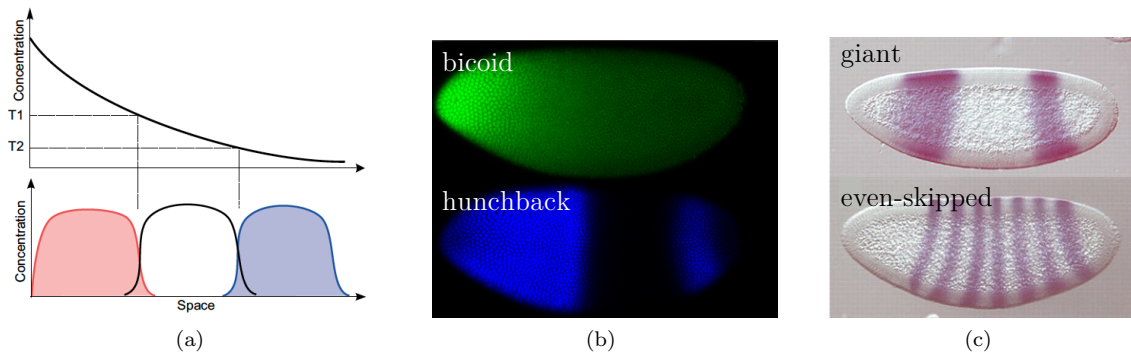


Figure 2.19 | **Positional information during *Drosophila* blastoderm development.** (a) Illustration of Wolpert’s concept as a solution of the ‘French flag problem’. Adapted from [99]. (b) The maternal protein bicoid generates the gap protein hunchback. Adapted from [167]. (c) Pair-rule protein patterns along the antero-posterior axis. Adapted from [208]. The length of the embryo is about 500  $\mu\text{m}$ .

The ventral furrow invaginates along most of the ventral midline, bringing the mesoderm into the interior of the embryo. This event begins by the constriction of a band of about four cells. Like the surrounding non-constricting cells, they express the mesoderm-determining genes *twist* and *snail* but are the only ones to express the folded gastrulation gene (*fog*) [161]. The secretion of fog protein polarizes the cells and triggers a pathway that ultimately drives myosin to the apical side of the cell (Figure 2.20 (a)) and generates contraction through the actomyosin network [44]. Cephalic furrow invagination takes place laterally on both sides of the embryo. The initial step is a change in shape and apical positioning of a single row of cells (Figure 2.20 (b)). The position of these initiator cells is defined by the overlapping expression of the segmentation genes *btd* and *eve* [303] (Figure 2.20 (c)).

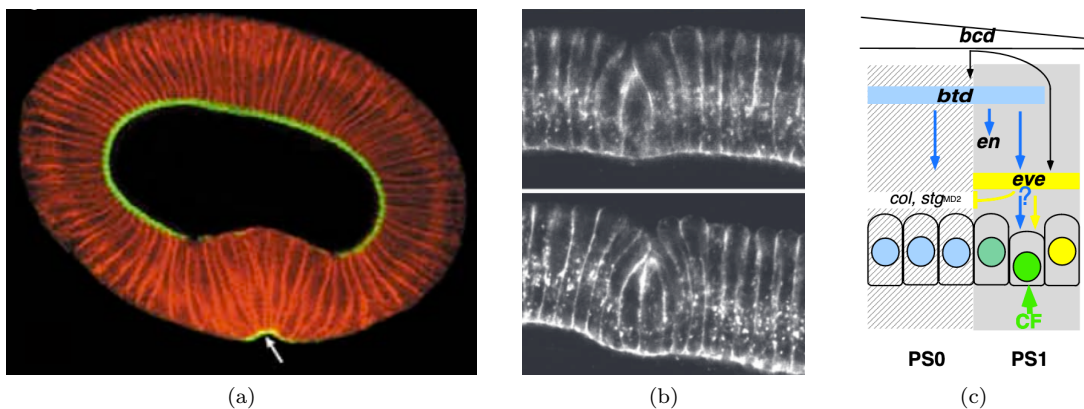


Figure 2.20 | **Formation of the ventral and cephalic furrows in *Drosophila*.** (a) Myosin (green) localizes to the apical surface of ventral cells (arrow) during gastrulation. Adapted from [44]. (b) Cell constriction initiates the cephalic furrow formation. (c) Interaction between *btd* and *eve* contributes to cell constriction (in green) at the frontier of the two parasegments PS0 and PS1. The gradient of the bicoid protein and the three genes *col*, *stg* and *en* are also indicated. The two last figures are adapted from [303].

The interplay between mechanics and chemistry during embryogenesis has been observed beyond these two examples. For instance patterning by positional information is involved in the development of vertebral neural tube [28]. A reaction–diffusion system that couples cytoskeletal elements is required for the cytokinesis of starfish oocytes [19]. This coupling has been the subject of numerous theoretical works [25, 154, 228] and has begun to be implemented in artificial systems, as we will see in the next section.



## 2.4 Experimental efforts to couple active matter and reaction-diffusion systems in vitro

The two order-generating mechanisms presented in this chapter may be used to create self-organizing materials that will be autonomous, programmable and biocompatible, which is the main objective of this thesis. Although many efforts to mimic biological systems have generated numerous synthetic responsive materials for smart tissue engineering and therapeutic applications, existing systems lack autonomy or tunability and are not always compatible with living systems. In this section we describe inspiring works that have coupled mechanisms in order to overcome some of the aforementioned flaws: self-oscillating gels and DNA-responsive systems.

### 2.4.1 Self-oscillating gels

A first and important implementation achievement was accomplished by embedding the BZ reaction, that exhibits spontaneous periodic temporal and spatial patterns, into a responsive polymer gel. The mechanical coupling during the periodic oscillations of the BZ reaction was accomplished thanks to a copolymer gel of N-isopropylacrylamide (NIPAAm) in which the ligand of the complex ruthenium (II) tris(2,2'-bipyridine) ( $\text{Ru}(\text{bpy})_3^{2+}$ ) was covalently bound to the polymer chain [321] (Figure 2.21 (a) (top)). The poly(NIPAAm-co- $\text{Ru}(\text{bpy})_3$ ) gel can swell and deswell at the oxidized and reduced states of  $\text{Ru}(\text{bpy})_3$ , respectively (Figure 2.21 (a) (bottom)). The BZ reaction in the gel generates periodic redox changes of  $\text{Ru}(\text{bpy})_3$ , and the chemical oscillation induces mechanical oscillations of the polymer network. Self-oscillating polymer gels have been transformed into functional materials that are able to perform original tasks such as self-flocculation of particles, self-propelled motion, beating of artificial cilia and autonomous transportation by peristaltic motion [322] (Figure 2.21 (b)). However, although these gels are autonomous, they are still powered by the BZ reaction which occurs in lethal pH and oxidizing conditions.

### 2.4.2 DNA-responsive systems

As already mentioned, biocompatibility can be accomplished by introducing DNA molecules. Thus, it has also been adopted for the conception of responsive hydrogels and have been coupled to reconstituted active matter systems.

#### Coupling with hydrogels

DNA can form hydrogels. It can be the only component, the backbone or a crosslinker that connects the main building blocks through chemical reactions or physical entanglement. Since their conception in 1996 [192], DNA hydrogels have been engineered to bend, twist or actuate in response to external stimuli. A recent work has demonstrated that the addition of a specific DNA molecule can induce 100-fold volumetric hydrogel expansion by the successive extension of crosslinks to reach centimeter-sized gels [31] (Figure 2.22 (a)). In addition, using a DNA-polymerase to elongate DNA chains, hydrogels made entirely of DNA weaved chains have been created [159]. The resulting gel has liquid-like properties when taken out of water and solid-like properties when in water. Moreover, the gel returns to its original shape upon the addition of water and after

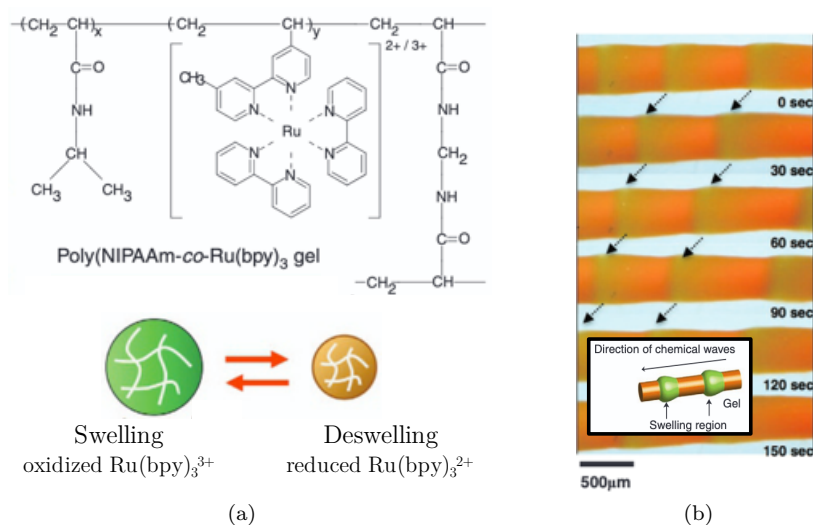


Figure 2.21 | **Self-oscillating gels.** (a) Copolymer gel of N-isopropylacrylamide (NIPAAm) with ruthenium(II) tris-(2,2'-bipyridine) ( $\text{Ru}(\text{bpy})_3^{2+}$ ) covalently bonded to the polymer chain. The poly(IPAAm-co- $\text{Ru}(\text{bpy})_3$ ) gel swells and deswells at the oxidized and reduced states of  $\text{Ru}(\text{bpy})_3$ . (b) Time-lapse of the peristaltic motion of poly(NIPAAm-co- $\text{Ru}(\text{bpy})_3$ -co-AMPS) gel in a solution of BZ substrates. The green and orange colors correspond to the oxidized and reduced states of Ru. Both figures are adapted from [322].

complete deformation. Another interesting example is a DNA gel that can contract upon the addition of an enzyme which is known to condensate DNA [24]. Because these DNA hydrogels are biocompatible, biodegradable, inexpensive to fabricate and easily molded into desired shapes and sizes, they have been the object of important development regarding biomedical applications [74].

### Coupling with reconstituted active matter systems

DNA molecules have also been directly coupled to active matter constituents such as molecular motors and microtubules. In single molecule experiments, DNA has been used to construct well-defined systems such as assembly of kinesins [73] or myosins V [104] and large DNA nanostructures composed of kinesins and dyneins [48].

In 2014, Wollman, Tuberfield and collaborators reported the first DNA-coupled active gel composed of reconstituted microtubules and DNA-kinesin chimeras [314] (Figure 2.22 (b)). They showed that a DNA strand was able to direct the assembly of microtubules and to control the loading and unloading of cargo, or to trigger the disassembly of the biopolymer network. After this pioneer work, few systems that link nucleic acids to reconstituted active matter have been designed. Among them two important experimental systems deserve attention. First, a ten micrometer-sized vesicle made from a lipid bilayer can be deformed in response to a DNA molecule [244]. DNA molecules were attached to the lipid membrane in order to transmit the force generated by a DNA-kinesin motor in response to a signal molecule composed of another sequence-designed DNA. Secondly, the swarming of DNA-functionalized microtubules propelled by kinesin motors attached to a surface was programmed to be reversibly regulated by DNA signals [142]. In this system swarm behaviors such as translational and circular motion were observed.

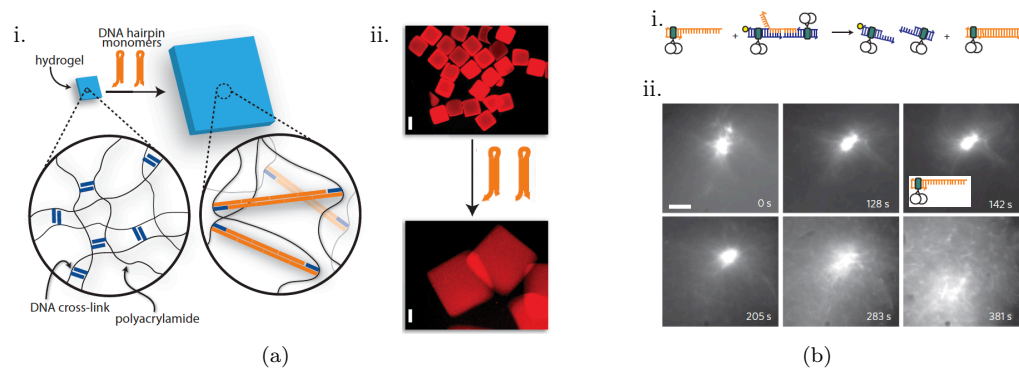


Figure 2.22 | **DNA-responsive hydrogel and active gel.** (a) i. DNA-directed expansion of DNA-crosslinked polyacrylamide gels. ii. The gel expands substantially in a  $20 \mu\text{M}$  DNA hairpin solution. Scale bars are  $1 \text{ mm}$ . Adapted from [31]. (b) DNA-control of an aster disassembly. i. The kinesin cluster has two sections, each containing a zinc finger binding site and a single-stranded overhang (blue). These sections are linked by a complementary strand (orange). This kinesin is stripped off by the signal strand (orange). ii. Time-lapse of the aster disassembly before and after addition of the disassembly signal. Scale bar is  $10 \mu\text{m}$ . Adapted from [314].

Inspired by these works, we have created in this thesis (Chapters 3 and 4) a system in which reaction-diffusion patterns and active matter are coupled thanks to the use of the PEN-DNA toolbox and an in vitro reconstituted active gel composed of microtubules and kinesin clusters. The combination of the two may lead to the creation of new materials with unique properties.

## 2.5 Conclusion

The reproducible formation of patterns is one of the key characteristics of living organisms. It is particularly visible during embryo development, which can be considered as a molecular self-sustained construction process that transforms an amorphous mass into a highly differentiated material. The whole process is a complex blend of chemical reactions, mechanical interactions, gene expression and signaling. In this chapter, we have focused our attention on active matter that uses the energy consumed by many elements and restored in the form of mechanical work, and on patterns that emerge from the reaction and diffusion of molecules.

First, we have seen that active matter covers a broad range of systems from animal flocks to artificial motorized colloids. We have focused our presentation on reconstituted gels of cytoskeletal proteins, which take advantage of powerful biological motors and display a rich variety of dynamical behaviors; from force-induced pattern formation to motion and deformation of macroscopic soft materials. Secondly, we have examined reaction-diffusion systems which can give birth to complex chemical patterns. Well-studied in non-linear redox reactions such as the famous BZ oscillator, they have been more recently investigated using biocompatible systems. For example, patterns have been obtained with the help of the *Min* bacterial system or the *in vitro* use of the transcription-translation machinery. We have pinpointed a *de novo* designed, programmable and biocompatible system made of DNA strands and a few enzymes which can be used to construct chemical reactions systems and reaction-diffusion patterns: the PEN-DNA toolbox. These two patterning mechanisms are ubiquitous *in vivo* where they are intertwined during embryo development. *In vitro*, efforts have been made to design systems that couple the two mechanisms. Besides BZ-coupled and DNA-responsive gels already discussed, important other results have been achieved: the microfabrication of homeostatic materials [109], the printing of biomaterials [302], the obtention of patterns in supramolecular systems [160] and the use of synthetic molecular motors [139] that have been coupled to shape changes of macroscopic materials [162]. However they lack programmability, self-sustainability or biocompatibility.

The combination of self-organization mechanisms is an important step in the quest to build materials inspired from embryogenesis. This combination is common in natural systems, such as the developing embryo, but is unknown in synthetic materials. This knowledge is critical for the advanced programming of self-organizing macroscale shapes at the molecular level. The systems discussed in this chapter could all be used to reach this goal in a near future. The development of such materials will undoubtedly lead to so far elusive self-fabricated, force-exerting synthetic soft matter with the potential of integration in soft robotics and biological environments.

In the next two chapters we will investigate a cytoskeletal active gel and a reaction-diffusion system made with DNA that can potentially overcome the aforementioned problems. First we will consider the patterning properties of a reconstituted active gel made of kinesin clusters and microtubules (Chapter 3) in the aim to realize then the effective coupling between this active matter system and a programmable reaction-diffusion front built from the PEN-DNA toolbox (Chapter 4).



## Chapter 3

# Self-organization of an active gel composed of microtubules and kinesins

<b>3.1</b>	<b>Preparation of the active gel</b>	<b>62</b>
3.1.1	Design and expression of kinesin clusters	62
	K401-BCCP kinesin: biotin-streptavidin interactions	62
	K430-HSNAP and K430-FLAG-SNAP kinesins: non-specific clusters	63
	Kinesin purifications	64
3.1.2	Assembly of the active gel and data processing	65
	Microtubule preparation	65
	Active mix assembly	66
	Channel passivation, assembly and imaging	68
	Data processing	69
<b>3.2</b>	<b>Formation of asters and contraction of the active network</b>	<b>72</b>
3.2.1	From bundles to asters	72
3.2.2	Contractions	73
<b>3.3</b>	<b>Tunable corrugated patterns in an active nematic sheet ★</b>	<b>77</b>
3.3.1	A 3D active nematic fluid forms a corrugated sheet that buckles	77
	From a nematic solution to a corrugated sheet	77
	Dynamics of the formation	77
3.3.2	Motor concentration tunes pattern properties	78
	A hydrodynamic theory that predicts the wavenumber of the corrugations	78
	Evolution of the nematic sheet according to motor concentration	80
	Quantitative characterization	81
3.3.3	Dependence on the geometry and on the microtubule concentration	82
3.3.4	Partial conclusion	83
<b>3.4</b>	<b>From aligned nematics to active flows</b>	<b>86</b>

3.4.1	Successive instabilities generate chaotic flows from an initial nematic ordered state . . . . .	86
3.4.2	Dynamics of the loss of nematic order . . . . .	88
<b>3.5</b>	<b>Compartmentalization of active nematics . . . . .</b>	<b>92</b>
3.5.1	Brief state of the art . . . . .	92
3.5.2	Experimental systems and preliminary results . . . . .	92
3.5.3	Open questions . . . . .	95
<b>3.6</b>	<b>Conclusion . . . . .</b>	<b>97</b>
3.6.1	Summary . . . . .	97
3.6.2	Perspective: patterning with light . . . . .	98

Active gels are matter driven out-of-equilibrium thanks to a chemical reaction. Major representatives of them are reconstituted biological active gels, where the energy comes from the hydrolysis of a nucleotide. Their basic constituents are taken from cells and reconstituted in vitro. In the presence of an energy source (mostly ATP or GTP) they exhibit complex patterning behaviors. In this chapter, inspired by the earlier works presented in Chapter 2, we experimentally build an active gel composed of polymerized microtubules and clusters of kinesins. Using this system we recapitulate the different patterns previously observed in similar — but different — systems and show that they can be understood with a relatively low number of parameters: activity (in terms of motor or ATP concentration), microtubule length and concentration, and depletion forces. Thus, depending on these parameters, the system can exhibit diverse structures such as asters, local or global contractions, corrugated patterns and active turbulent flows. When geometrically constrained, new behaviors can be observed like, for instance, confined active nematics in water-in-oil droplets.

We have organized this chapter as follows. The first section describes the composition of the active gel. It includes the step of creation of the kinesin clusters that are able to apply forces on several filaments. We use two different strategies, one based on the specific biotin-streptavidin link and the other on non-specific interactions. We then explicit the mix preparation, the assembly of the reaction and the data processing. In the second section we depict the formation of bundles from long microtubules due to depletion forces. These bundles form asters or contract if involved in a denser microtubule network. The contraction can be either local or global depending on the initial density of the active network. Our main contribution to the field of reconstituted active gels is presented in the third section. We show that starting from a nematic network that is dense enough, a sheet of microtubules forms and buckles in the transverse direction leading to a very regular corrugated pattern. The wavelength of the pattern is tuned by the motor or the microtubule concentration, or by the geometrical constraints of the channel (the height for example). Interestingly the pattern is stable at a relatively low concentration of kinesin clusters but breaks into chaotic flows at higher concentrations. These flows are described in the fourth section in which we recover previously-described chaotic flows using short microtubules. We focus our analysis on the initial wavelength selection and the path to turbulence. In the last section we present a protocol that can be used to generate water-in-oil droplets of various sizes, method that can be employed to study the physics of active droplets. We finally conclude this chapter by summarizing the diverse results and by proposing a way to control the spatio-temporal organization of active gels using light and caged-ATP molecules.



### 3.1 Preparation of the active gel

The reconstituted cytoskeletal active gel that we prepare is composed of the following essential elements: microtubules, kinesin clusters, depleting polymers and ATP. In this section we describe the preparation of such an active gel. An important part is dedicated to the preparation of the kinesin clusters, using two different strategies. The first one is built upon the important works of Nédélec and Surrey [195, 274] and of Sanchez, Dogic and collaborators [243, 241]. It is based on the biotin-streptavidin link (Figure 3.1 (a)). The second one is based on non-specific clusters of SNAP-tag motors (Figure 3.1 (b)). Notably, SNAP-tag motors may be used in the future to design reversible clusters controlled by ssDNA (Figure 3.1 (c)). We then present the preparation of the active mix — including the preparation of microtubules —, the construction of the channels where the experiments take place and the data processing.

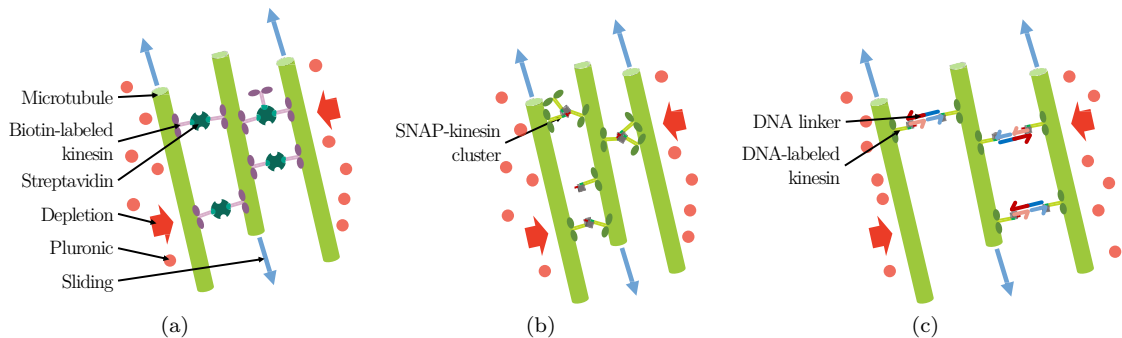


Figure 3.1 | **Strategies to build kinesin clusters for the preparation of a reconstituted active gel.** Sketches of the components of an active gel formed by microtubule bundles and clusters of kinesin motors. Clusters of motors can be made using (a) specific biotin-streptavidin links (strategy used by Dogic and collaborators [243, 241]) or (b) non-specific links. (c) A potential strategy to design reversible kinesin clusters using DNA.

#### 3.1.1 Design and expression of kinesin clusters

One of the essential elements of the active gel is the cluster of kinesin motors that is able to exert forces on several filaments at the same time. We use different strategies to create controlled clusters of kinesins that we describe in the following.

##### K401-BCCP kinesin: biotin-streptavidin interactions

The first strategy is based on the specific interaction between biotin and streptavidin. The bond formed between biotin and streptavidin is specific and stable for tens of hours. It allows the creation of a physical link between two molecules without any chemical reaction. The high affinity is the consequence of about fifty hydrogen bonds that constrain the biotin, as much in rotation as in translation, leading to one of the strongest non-covalent bond, requiring a force of more than 100 pN to break [318]. This biochemical link has been broadly used in molecular biology and has been developed for the study of kinesin motors by Gelles and collaborators [21]. This approach is the one used by Nédélec and Surrey in their seminal work of the early 2000's [195, 274] and by

Dogic and collaborators in their exciting experiments starting from 2011 [243, 241, 319]. The biotin is attached to the kinesin thanks to the Biotin Carboxyl Carrier Protein (BCCP). It is a part of a natural enzyme (the acetyl-CoA carboxylase) that serves as a carrier for biotin. During its *in vivo* production in *E. coli*, the BCCP polypeptide is recognized and efficiently post-translationally biotinylated. In terms of genetic construct, the DNA sequence coding for the BCCP protein is fused to the sequence coding for the first 401 amino acids of the N-terminal motor domain of the heavy chain of *Drosophila melanogaster* kinesin-1 (also known as ‘KHC’). In order to facilitate the purification, we use a recent version of this kinesin where a HIS-tag sequence has been added [270]. This kinesin is called ‘K401-BCCP’ in this manuscript (Figure 3.2 (a)).

However this approach has some drawbacks. First the number of kinesin motors in a single cluster is not known since streptavidin is a tetravalent protein: a cluster can be composed of one to four motors. Secondly, the link is not reversible in the standard conditions of experiments. Kinesin clusters are always applying forces on several filaments. Thus it is impossible to dynamically control the state of the cluster and vary the activity of the gel spatially and temporally.

#### **K430-HSNAP and K430-FLAG-SNAP kinesins: non-specific clusters**

In order to control the number of kinesins involved in a cluster and the reversibility of the link, an ingenious idea rests on the use of DNA molecules. Therefore, the modulation of the link can be easily tuned using techniques such as strand displacement. This idea has been implemented for the first time by Wollman, Tuberfield and coworkers who used zinc-fingers to connect kinesin and DNA [314].

A second way to specifically attach a molecule (here a DNA) to a protein can be achieved with specific tags such as the SNAP-tag. The SNAP-tag is a small protein (20 kDa) based on the mammalian protein O6-alkylguanine-DNA-alkyltransferase. During the labeling reaction, the substituted benzyl group of the substrate (that are derivatives of benzylpurines and benzylchloropyrimidines) is covalently attached to the SNAP-tag. With this strategy, a benzyl-guanine modified DNA can be covalently attached to a protein. Furuta and coworkers have created a modified kinesin with a SNAP-tag derived from the first 430 amino acids of the kinesin-1 found in *Rattus norvegicus* [73]. It is important to control the number of SNAP-tags in a single kinesin if one wants to control the number of kinesins in a single cluster. Indeed, a kinesin is composed of two arms that dimerize. To solve this problem, they have designed a kinesin with two different arms: one with a HIS-tag (the arm containing the SNAP-tag) and one with a FLAG-tag. We call this motor ‘K430-FLAG-SNAP’ (Figure 3.2 (b, left)). Now, the purification requires two steps: first a purification using the HIS-tag that leads to kinesins with two HIS-tag arms and kinesins with one HIS-tag arm and one FLAG-tag arm. The second purification uses the FLAG-tag: only kinesins composed of one HIS-tag arm and one FLAG-tag arm are selected. The maximum number of DNA molecules that can be attached to one kinesin via the SNAP-tag is one.

We also create a homodimer version of this kinesin: it is composed of the two identical arms containing the HIS-tag and the SNAP-tag (‘K430-HSNAP’) (Figure 3.2 (b, right)). Thus, the maximum number of molecules that can be attached to one kinesin is now of two.

However, we observe that after the purification of both K430 kinesins, non-specific clusters are present. Indeed, active gels built from these kinesins (the method to assemble such gels is described in the next subsection) exhibit activity: kinesin motors are able to exert forces on several microtubules at the same time, which is possible only if they form clusters. Our efforts to eliminate these nonspecific multimers by size exclusion chromatography do not change the observed patterns, suggesting that these clusters either form rapidly or do so in the working buffer. So these non-specific clusters have the same drawbacks than before: we do not know the number of kinesins present in one cluster and it is impossible to go from a clustering state to a single motor state. However, even if this approach is not successful to make DNA-controllable kinesin clusters as originally desired, K430 kinesins can be used in the form of clusters. Surely,

- these non-specific clusters work perfectly and provide an orthogonal — interactionally speaking — system to the biotin-streptavidin system, and can then be used at the same time (for example with biotin-labeled microtubules).
- As we will see in Section 4.4, it is possible to specifically attach modified DNA on these kinesins. These may be used in DNA-related reaction networks or in gliding assay experiments.

The three types of kinesins used in this thesis are recapitulated in the following table (Table 3.1):

Name	Tags	Clusters	Usage
K401-BCCP	HIS	Biotin-streptavidin	Chapter 3 (Section 3.5), Chapter 4 (Sections 4.2, 4.3)
K430-FLAG-SNAP	HIS, SNAP, FLAG	Non-specific	Chapter 3 (Section 3.2), Chapter 4 (Section 4.4)
K430-HSNAP	HIS, SNAP	Non-specific	Chapter 3 (Sections 3.3, 3.4)

Table 3.1 | **List of the kinesins used in this thesis.**

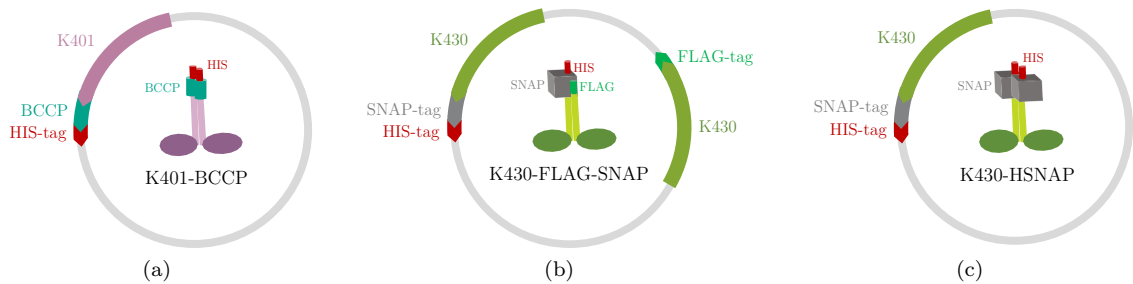


Figure 3.2 | **Sketches of the kinesins used in this thesis.** Sketches of the kinesins and their plasmid representation. (a) K401-BCCP, (b) K430-FLAG-SNAP and (c) K430-HSNAP.

### Kinesin purifications

Although the proteins are different and do not come from the same organisms, the development and the standardization of protein purification methods allow us to purify kinesins using the same

kind of protocol. Here we present the main steps. The reader will find detailed protocols for each one of the three purifications in Appendix B.1.

We start the expression steps from DNA plasmids. We do not have to construct the plasmids for kinesins K430-FLAG-SNAP and K401-BCCP as they have been kindly provided by K. Furuta and Z. Gueroui, respectively. We build the K430-HSNAP plasmid from K430-FLAG-SNAP plasmid by removing the sequence coding for the FLAG-tag arm.

*E. coli* DH5 $\alpha$  cells are used to multiply the plasmid. The expression of the protein is done in *E. coli* BL21(DE3) or Rosetta 2 cells. After growth to an optical density (OD) of about 0.5, cells are induced using isopropyl  $\beta$ -D-1-thiogalactopyranoside (IPTG) at room temperature (21°C to 23°C) for the appropriate amount of time. Importantly, K401-BCCP production also requires the induction of the biotinylation. Bacteria are then collected by centrifugation. From this point, all the steps are performed on ice or at 4°C. Bacteria are lysed using a sonicator and the cell extract is centrifuged and filtered. The filtrate containing the target protein with a tag is specifically and reversibly bound to a chromatographic resin containing a binding substance (ligand) with affinity for the tag. Three steps follow: (i) the sample is applied to the column under conditions that favor binding to the ligand, (ii) unbound material is washed out of the column and (iii) the bound tagged protein is recovered (eluted) using a competitive ligand. This step is performed for the three kinesins thanks to the HIS-tag using a Ni-IMAC resin and an elution buffer containing a high concentration of imidazole. K430-FLAG-SNAP kinesin is purified a second time using a FLAG-tag column. The buffer is changed by overnight dialysis, and the protein can be concentrated using MWCO (molecular-weight cutoff) filters. Depending on the level of purity desired, the protein can be further purified by a size-exclusion chromatography (Figure 3.3 (b)). The long-term storage is greatly dependent on the nature of the protein. Our kinesins are flash frozen in liquid nitrogen and kept at -80°C in the presence of a cryoprotectant such as sucrose or glycerol.

During the purification process, it is important to keep a small volume of solution at each step in order to analyze the contents on a denaturing electrophoresis gel (here a SDS-PAGE). For example, in Figure 3.3 (a) we present a gel recapitulating the double purification of K430-FLAG-SNAP, using the HIS-tag and then the FLAG-tag.

### 3.1.2 Assembly of the active gel and data processing

We describe here the assembly of the reaction. We explicit the microtubule preparation, the composition of the mix, assembly of the channel in which the gel is observed, the imaging and finally the data processing of microscopy images.

#### Microtubule preparation

Microtubules are polymerized from porcine brain tubulin proteins ordered from Cytoskeleton, Inc. According to the manufacturer, tubulin has been purified by cation exchange chromatography to yield a purity > 99%. Tubulin is supplied as a white lyophilized powder stable for at least 6 months at 4°C. A complete polymerization protocol is written in the Appendix B.1. Importantly microtubule polymerization has to be performed at a relatively high concentration of tubulin monomers.

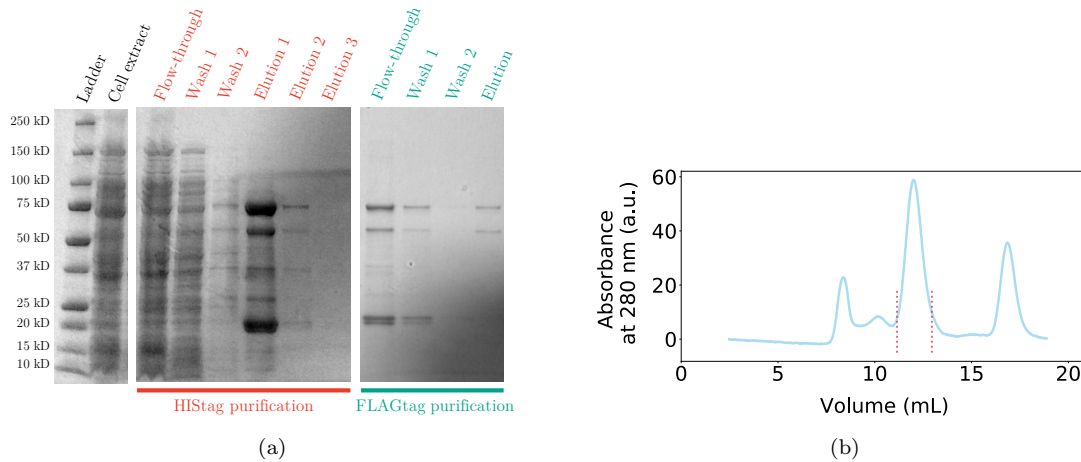


Figure 3.3 | **Purification of kinesins: SDS-PAGE gel and gel filtration profile.** (a) SDS-PAGE gel of the purification steps of K430-FLAG-SNAP. The purification process for this kinesin is double: first a HIS-tag purification (red), then a FLAG-tag purification (green). K430-FLAG-SNAP is composed of two arms which weigh 50 kDa and 70 kDa. (b) Gel filtration profile of dialyzed kinesin K430-HSNAP at 280 nm. The latter comes out at 12 mL (between red dashed lines). The peak at 17 mL corresponds to the SNAP-tag which is produced alone and peak before 12 mL is attributed to large clusters (they show activity in an active gel experiment).

Indeed, the critical concentration is above 5 mg/mL in standard conditions but can be decreased using glycerol for example. We use two different microtubules: GTP-grown taxol-stabilized microtubules or GMPCPP-microtubules. In both cases we use 2.5% of TRITC-labeled tubulin in order to obtain fluorescent microtubules. Although they also have different mechanical properties, we will essentially remember that these two types of microtubules reach different lengths. We measure them using the *Ridge detection* plugin for ImageJ. Taxol-microtubules have a mean length of  $8.1 \pm 5.8 \mu\text{m}$  and GMPCPP-microtubules of  $3.0 \pm 2.4 \mu\text{m}$  (Figure 3.4), with an exponential distribution.

### Active mix assembly

The composition of the active mix is indicated in Table 3.2. Besides the salts, the mix contains other important elements:

- An ATP regeneration system used to maintain a constant concentration of ATP. It is composed of a kinase which is able to transfer a phosphate group from a phosphate donor to ADP, thus generating ATP. We use two different systems. Creatine phosphate (CP) as a donor and creatine kinase (CK) as the transfer enzyme, or phosphoenolpyruvate (PEP) as a donor and pyruvate kinase (PK) as the transfer enzyme. The CP/CK reaction is schematized in Figure 3.5 (a).
- An anti-oxidant and anti-photobleaching system composed of DTT, Trolox and the enzymatic reaction of glucose catalyzed by glucose oxidase and catalase. This reaction is schematized in Figure 3.5 (b).

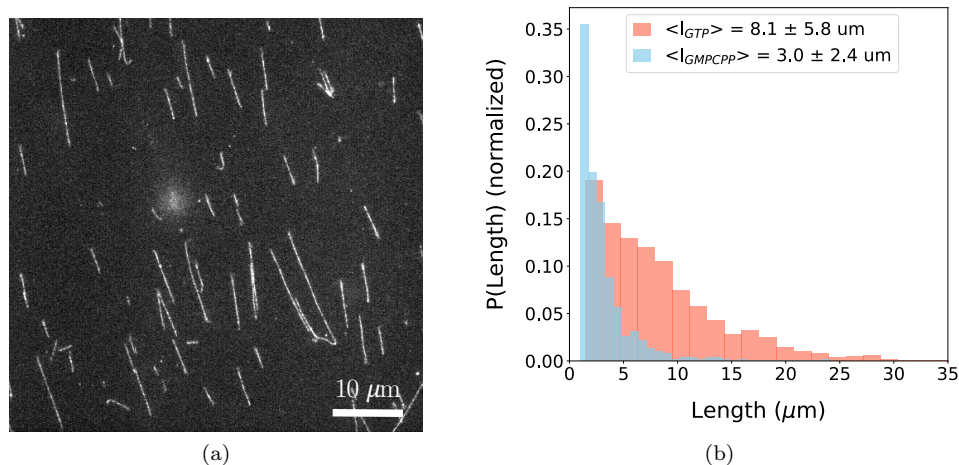


Figure 3.4 | **Distributions of microtubule lengths.** (a) Image of taxol-stabilised microtubules. (b) Normalized probability distribution of taxol-stabilized microtubules (red) and GMPCPP-microtubules (blue).

– Taxol when taxol-stabilized microtubules are used.

The mix is assembled on ice in this order: water, salts, pluronic F-127, ATP, ATP regeneration system, anti-oxidant, anti-photobleaching and kinesin clusters. Microtubules tend to depolymerize at low temperature even when they are stabilized. For this reason they are always added at the end at room temperature. They are gently mixed by pipetting for 30 s to 1 min in order to prevent them for breaking. Clusters of K430-HSNAP or K430-FLAG-SNAP kinesin naturally occur and thus can be added to the mix directly. K401-BCCP clusters have to be prepared in advance. They are formed by incubating the kinesin and streptavidin on ice at the stoichiometric ratio 2:1 for at least 10 min.

Name	Concentration
PEM-KOH <sup>1</sup>	1X
K-acetate	10 mM
KCl	10 mM
MgCl <sub>2</sub>	5 mM
DTT	3 mM
Trolox	1 mM
D-glucose	20 mM
Glucose oxidase	150 μg/mL
Catalase	25 μg/mL
BSA	1 mg/mL
Taxol* (paclitaxel)	20 μM
ATP	2 mM
CK	5 μg/mL
CP	20 mM

Table 3.2 | **Composition of the active mix in standard conditions.** <sup>1</sup>80 mM PIPES, 1 mM EGTA, 1 mM MgCl<sub>2</sub>, adjusted with 130 mM KOH to pH 6.9. \*Taxol is used only if the microtubules are taxol-stabilized and not GMPCPP-stabilized.

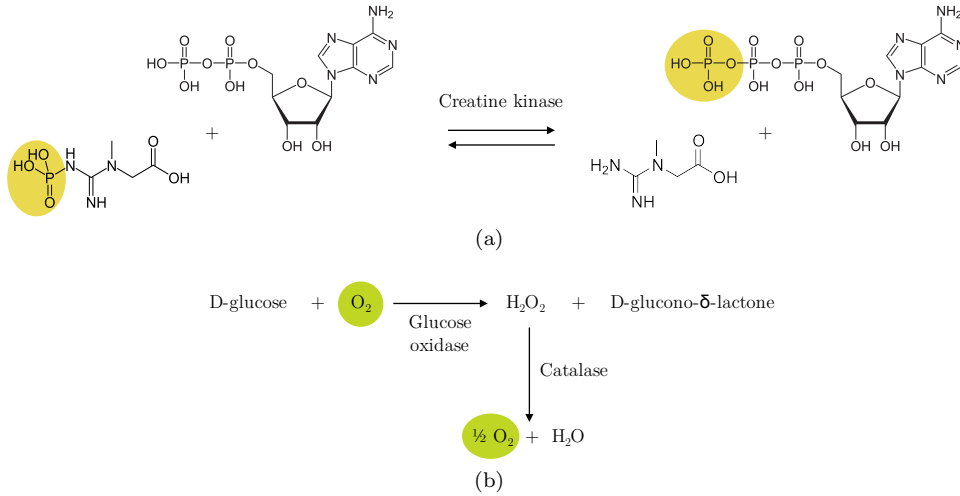


Figure 3.5 | **ATP regeneration and anti-oxidant systems** (a) The ATP regeneration system CP/CK. (b) The anti-oxidant system keeps the level of  $O_2$  at a low value and preserves integrity of molecules.

In this chapter we tune the concentration of the microtubules, the kinesin clusters and the depleting polymers (pluronic F-127) in the following ranges (Table 3.3):

Name	Concentration
Microtubules	0 - 1 mg/mL
Kinesin clusters	0 - 100 nM
Pluronic F-127	0 - 2 %(w/v)

Table 3.3 | **Tunable parameters of the active mix.**

In order to gain some time in the preparation, it is possible to prepare in advance a mix containing everything except the tunable parameters (microtubules, kinesin clusters and pluronic). The mix is then flash frozen and kept at  $-80^\circ\text{C}$ . We do not observe any degradation of this mix after 3 months.

### Channel passivation, assembly and imaging

Most of the experiments are performed in acrylamide-coated glass slides to prevent protein adsorption [157, 242] especially from microtubules and kinesins, and to ensure that the molecular motors internally drive the active gel. Acrylamide forms a repulsive brush keeping protein far from the surface of the glass. Channels are assembled using an acrylamide-coated microscope glass slide and a coverslip separated by strips of parafilm (Figure 3.6). The height between the glass slide and the glass coverslip can be adjusted by changing the number of layers of parafilm. Thus we are able to vary from  $70\ \mu\text{m}$  (one layer of a stretched parafilm) to  $500\ \mu\text{m}$  (four layers). We also use directly squared glass capillaries of  $0.5 \times 0.5\ \text{mm}$  when needed. The active mix is filled in the channel by capillarity and sealed with vacuum grease.

Images are obtained with an epifluorescence microscope. Images are recorded automatically every 1 to 3 min using an excitation at  $550\ \text{nm}$  with a LED lamp. In order to resolve 3D structures

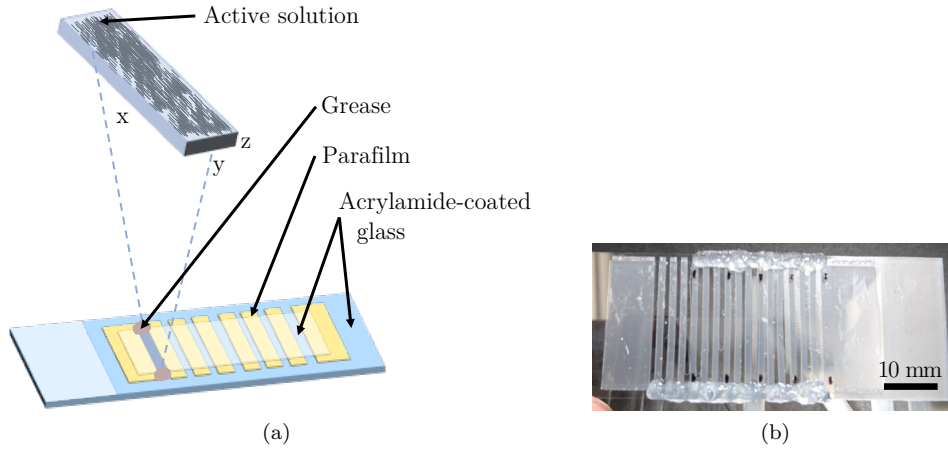


Figure 3.6 | **Sketch and picture of channels.** (a) Sketch and (b) picture of the channels where the active nematic fluid is observed

we record confocal images when needed. They are recorded automatically every 1 to 10 min with a  $z$  step of 3 to 5  $\mu\text{m}$ .

All the experiments are done at room temperature ( $22 \pm 1^\circ\text{C}$ ). Such variations in temperature do not change the dynamics of the active gel.

These protocols can be found in detail in [B.1](#).

## Data processing

Time-lapse images from microscopy experiments are treated by ImageJ/Fiji (NIH) and Python. Images of the channels are first cropped manually to remove the edges. The active gel patterns the space, meaning that the fluorescence intensity from the microtubules along a channel is non homogeneous. We quantify the temporal formation of the pattern as a change in the distribution of intensities by computing the local/global variance or the difference between the 90<sup>th</sup> and the 10<sup>th</sup> percentile of intensities.

An important feature of our system is the orientation of the microtubules, we will use it in Section 3.4. We determine the orientation map of each frame. The local orientations are computed from the structure tensor defined for each pixel as the  $2 \times 2$  symmetric positive matrix  $J(x, y)$  derived from the gradient of pixel intensities  $I(x, y)$

$$J(x, y) = \begin{pmatrix} \int_{ROI} dx dy \nabla_x I(x, y) \cdot \nabla_x I(x, y) & \int_{ROI} dx dy \nabla_x I(x, y) \cdot \nabla_y I(x, y) \\ \int_{ROI} dx dy \nabla_y I(x, y) \cdot \nabla_x I(x, y) & \int_{ROI} dx dy \nabla_y I(x, y) \cdot \nabla_y I(x, y) \end{pmatrix}, \quad (3.1)$$

where ROI denotes the ‘region of interest’. The diagonalization of  $J$  gives two eigenvectors  $\lambda_{min}$  and  $\lambda_{max}$  that point respectively in the direction of the minimum and the maximum gradient of intensity. The dominant orientation is therefore given by the direction of  $\lambda_{min}$ . Other isotropic properties such as the gradient energy  $E$  (trace of the structure tensor) and the coherence  $C$  are



given by:

$$E = \text{trace}(J) = \lambda_{max} + \lambda_{min} \quad (3.2)$$

$$C = \frac{\lambda_{max} - \lambda_{min}}{\lambda_{max} + \lambda_{min}}. \quad (3.3)$$

We implement this processing using a python routine based on the *scikit-image* (also known as *skimage*) collection for image processing and computer vision. First, we apply on  $I$  a gaussian filter (with a standard deviation of  $\sigma = 2$  px, about  $4 \mu\text{m}$ ). We then compute the structure tensor and determine the local orientation in a small ROI of a typical size 5 px (about  $10 \mu\text{m}$ ). In order to remove orientations from areas where they are difficult to compute (like uniform areas), we follow the method of ref. [231]: we use the gradient energy and the coherence values, computed above, to discriminate significantly oriented regions. Thus, orientations are considered only where pixels have at least 0.5% of normalized energy. We also define the 2D order parameter  $Q$  for an apolar nematic [45] as

$$Q = \sqrt{\langle \cos 2\theta \rangle^2 + \langle \sin 2\theta \rangle^2}, \quad (3.4)$$

where  $\theta$  is the local angle obtained from the local gradient analysis and the long axis of the channel. The average  $\langle \cdot \rangle$  is taken for a local window or on all the field of view if we want to estimate the local or the global order parameter, respectively. When all the microtubules are aligned,  $Q$  is close to 1 and it tends to 0 as the network gets disorganized.

Initially, when the concentration of microtubules is sufficiently high ( $> 250 \mu\text{g}/\text{mL}$ ) and forms a percolated network (see Section 3.2 for more details), the density of microtubules is homogeneous in 3D. Microtubules are aligned along the long axis of the channel, parallel to  $x$  (Figure 3.7). This nematic order arises spontaneously during the filling process of the channel by capillarity, the angle of the director of the nematic with the  $x$  axis being  $-2 \pm 16^\circ$ .

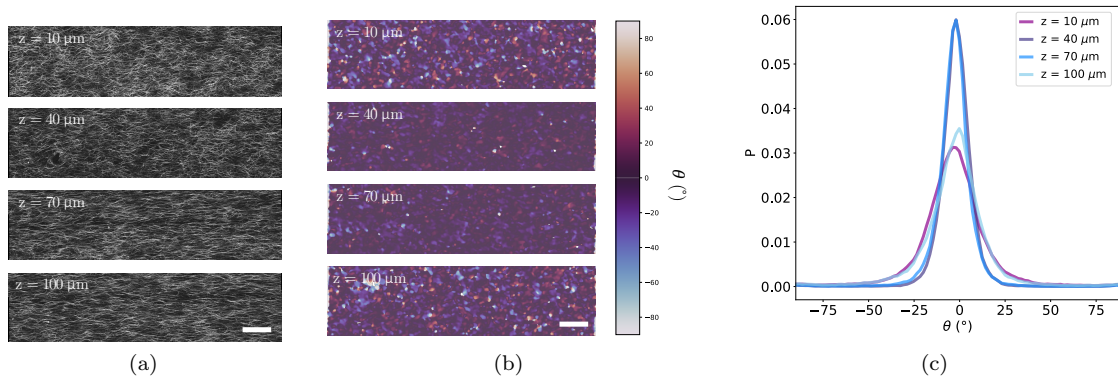


Figure 3.7 | **Initial orientation of microtubules in the xy plane for different heights in a flow cell.** (a) and (b) Initial fluorescence images and local orientation fields of taxol-stabilized microtubules placed in a  $130 \mu\text{m}$ -high channel for different heights. Scale bars are  $250 \mu\text{m}$ . (c) Angular distributions for different heights.  $\theta$  is the angle between the bundles and the  $x$  axis in the  $xy$  plane.  $\langle \theta \rangle = -2 \pm 16$ .

In the following sections we describe the behavior of the active gel when the parameters in Table 3.3 are changed.

## 3.2 Formation of asters and contraction of the active network

In this section we explore the behavior of the active gel that we have just designed. We obtain different patterns depending on two key parameters: the concentration of taxol-stabilized microtubules and the concentration of clusters of motors. Depleting polymers induce the formation of thick microtubule bundles that are, upon the action of the kinesin clusters, dynamic: they merge, bend, break and recombine with the surrounding bundles. They form higher polar structures called asters. When the initial density of microtubules is increased (with a concentration between  $50 \mu\text{g/mL}$  and  $250 \mu\text{g/mL}$  in terms of tubulin), the percolating active network organizes into a final state which can either be a prestressed, a globally contractile or a locally contractile network, starting from various cluster concentrations. We finally propose a simplified state diagram.

### 3.2.1 From bundles to asters

In the presence of non-adsorbing polymers in solution, particles and filaments experience attractive interactions induced by depletion forces. More generally these interactions take place when large colloidal particles are suspended in a solution of smaller particles. Microtubules can be assembled into bundles thanks to these interactions even if, as charged biopolymers, they display repulsive electrostatic interactions. Two microtubules put in the presence of many depleting polymers are subjected to an osmotic pressure. When the microtubules are dispersed within a solution of polymers of size  $r_0$ , there is an excluded volume surrounding each microtubules of size  $r_0/2$ . As the microtubules aggregate, this excluded volume is reduced. For this reason, the depletion forces are often regarded as entropic forces [9]: the free volume available for depleting polymers is maximized and largely compensates the enthalpy penalty due to the aggregation of charged microtubules. In vivo, depletion forces are mentioned as ‘molecular crowding’ and are essential to many processes, in particular for enzymatic reactions [216]. Optical tweezers experiments have shown that the strength and the range of the attraction forces between microtubules can be tuned by both the concentration and size of the depleting polymers [113].

Starting from a diluted solution of fluorescent microtubules ( $< 50 \mu\text{g/mL}$  in terms of tubulin concentration), bundles are forming and are becoming visible simply by using fluorescence microscopy imaging at low magnification (10 X). Besides facilitating the formation of bundles, depletion forces also increase the probability that kinesin clusters crosslink on adjacent microtubules in a bundle. Clusters of kinesins apply large forces to bundles. These forces are able to bend and ultimately break the bundles (Figure 3.8 and Movie A.1 [[↓](#), [🎞](#)]) which are then merged into other bundles.

In this diluted solution, the bundles are initially in random configurations. Under the action of kinesin clusters, they assemble into star-shaped structures called asters (Figure 3.9 and Movie A.2 [[↓](#), [🎞](#)]). The whole microtubule network then slowly contracts. The microtubules associated with the asters have a defined polarity, generating a flux of microtubules toward the center of the aster that results in local attractions between two neighboring structures. Such behavior has been

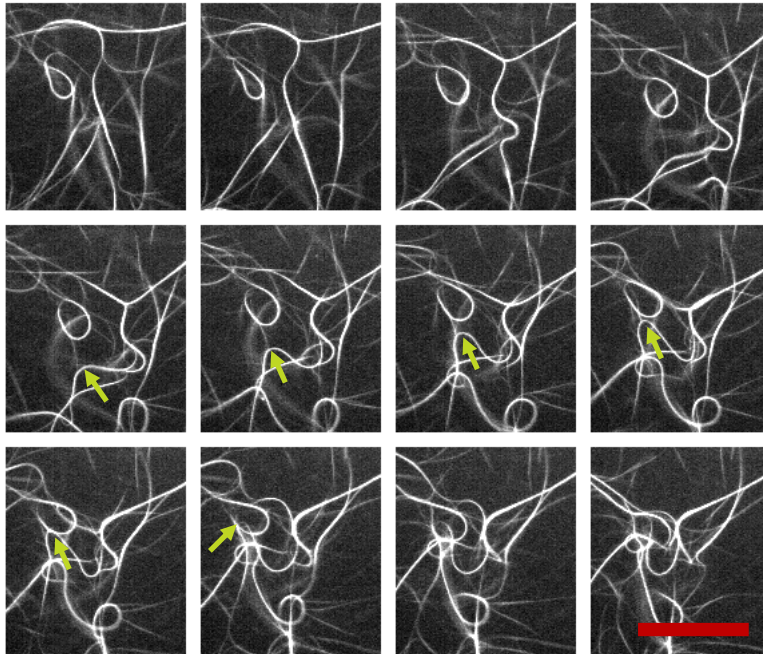


Figure 3.8 | **Bundles bend and break under the forces of kinesin clusters.** Under the forces of kinesin clusters (K430-FLAG-SNAP) bundles are bent and are broken (green arrow). They would then merge with other bundles. In this experiment K430-FLAG-SNAP = 40 nM, taxol-microtubules = 30  $\mu\text{g}/\text{mL}$  and pluronic = 1.0%(v/v). Interval between images is 100 s. Scale bar is 100  $\mu\text{m}$ . Movie A.1 [[↓](#), [🎞](#)].

reported using the naturally-occurring tetrameric motor Eg5 [111, 288, 236]. These structures are dynamic: at the same time they contract — meaning that the density of bundles is increasing at the center of the structure — and they form long radial bundles. We have not looked carefully at the dynamics of these bundles, but they are reminiscent of cilia-like beating microtubule bundles [243]. Hypothetically, such beating phenomenon can happen in our system using the right range of experimental conditions (motor concentration, depleting polymer concentration), concomitantly with the contractions.

### 3.2.2 Contractions

The same mix but with a higher microtubule concentration (between 50 and 250  $\mu\text{g}/\text{mL}$ ) forms a connected network that displays a range of spatio-temporal dynamics depending on their constituent concentrations (Figure 3.10 and Movie A.3 [[↓](#), [🎞](#)]). At a fixed microtubule concentration (here 250  $\mu\text{g}/\text{mL}$ ), a low motor concentration leads to a globally connected static microtubule network. The increase in the cluster concentration makes the links between microtubules easier to form and leads to a global contraction of the network. A further increase in motor concentration produces local clusters and segments the network into isolated contracting sub-networks. This type of system is described as contractile.

Based both on our experiments and on other recent studies on similar but different systems (XCTK2 and Eg5 tetrameric motors [111, 288], *Xenopus* egg extracts [67]), we propose the fol-

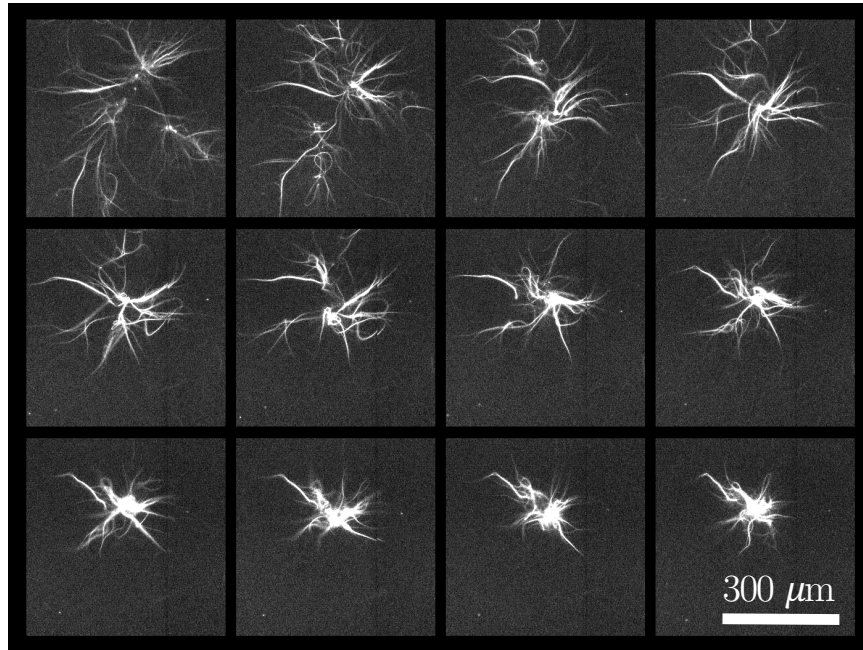


Figure 3.9 | **Formation of an aster made of microtubule bundles.** (a) Time-lapse of the formation of an aster structure that contracts. In this experiment  $K430\text{-FLAG-SNAP} = 24 \text{ nM}$ ,  $\text{taxol-microtubules} = 50 \text{ } \mu\text{g/mL}$  and  $\text{pluronic} = 2.0\%(v/v)$ . Interval between images is 6 min. Movie A.2 [[↓](#), [🔍](#)].

lowing qualitative state diagram for a microtubule-kinesin contractile system (Figure 3.11 (a)). It depends on two parameters: the concentration in motor clusters and the concentration in taxol-microtubules. At low concentration, microtubules do not form a connected network. They eventually merge into bundles and asters with a time-scale that depends on their concentration. When the network is sufficiently connected, it constitutes a ‘percolating network’ (in terms of interweaving of the bundles). In this regime, its behavior depends on the magnitude of the active forces and thus on the concentration in kinesin clusters. A low motor concentration only results in the local application of forces. The motors fail to counterbalance the mechanical passive forces of the network and to transmit the forces over large distances. However, when the force is high enough, but not too strong to untangle the network, the network is globally contracting. If the force is further increased — by the increase of motor concentration — the network is rapidly broken into several sub-networks that contract. To the best of our knowledge, the transitions between the regimes have not been described and thus we do not know how steep they are. However, their relative position can be controlled by modifying the concentration of the chemical fuel ATP or by changing the salt conditions. For example, in our system the network contractions are prevented by the addition of 100 mM of KCl.

Many experimental and theoretical works have been done with reconstituted actomyosin networks, which are well-known for contracting [20, 145, 229, 4]. These studies have pinpointed the interplay between motor activity and the connectivity of the network. In particular, the different observations can be understood in terms of percolation transitions where the motor activity and

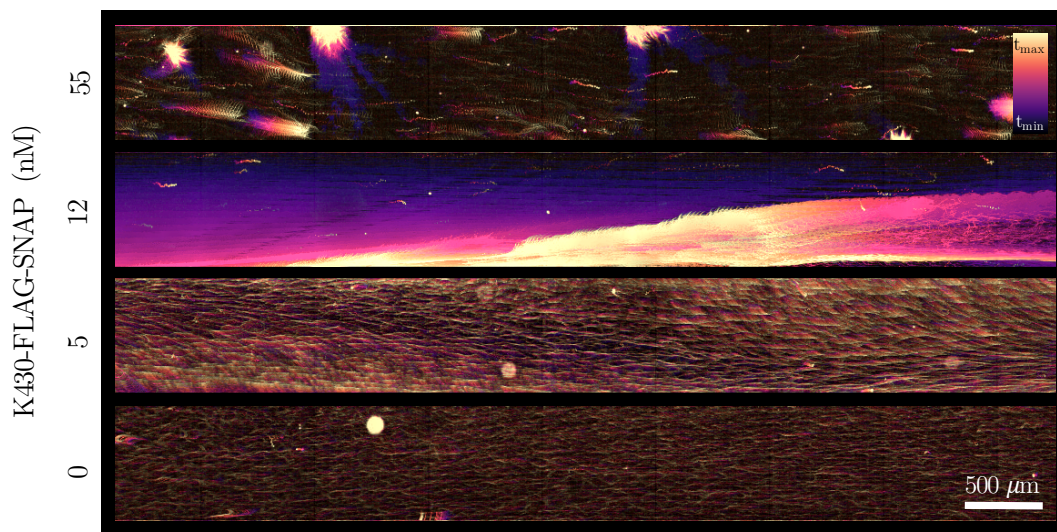


Figure 3.10 | **A connected active network exhibits several morphologies depending on the motor concentration.** Temporal, color-coded time-lapse for different K430-FLAG-SNAP concentrations. Depending on the motor concentration, three active states are observed: a prestressed, a globally contractile or a locally contractile active gel. In these experiments taxol-microtubules =  $250 \mu\text{g}/\text{mL}$  and pluronic =  $1.5\%(\text{v}/\text{v})$ . Total time is 300 min. Movie [A.3](#) [[↓](#), [▶](#)].

the connectivity of the network (which can also be modified by adding a crosslink protein such as  $\alpha$ -actinin [4]) are the main controlling parameters. Alvarado *et al.* have proposed a state diagram that combines the experimental observations using this framework [5]. Briefly, this diagram consists in four regimes that are separated by more or less abrupt transitions (Figure 3.11 (b)). These regimes are qualitatively identical to those presented in our diagram. However, the ‘active solutions’ regime of Alvarado *et al.* depicts both a free-to-move state in solution and gliding assays experiments of actin filaments (explained in Section 2.1.3 for the latter). The boundaries between each region are carefully explained: they represent either a stress percolation (where the motor stresses balance mechanical constraints and spread across the network), a failure percolation (where the motor stresses overwhelm the mechanical constraints and lead to a global contraction), a strain percolation (which refers to the boundary between local and global contraction and how to go — progressively — from one regime the other) or a coarsening regime (where motors begin to contract the network around them).

Active gels are not always contractile; conditions exist where the system can also be extensible. In an extensile active gel composed of microtubules and kinesin clusters, the bundles extend along their length. At high density they are entangled with other neighboring bundles: they then generate extensile forces. It can subsequently lead to bending and buckling of the bundles, as we will see in the following.

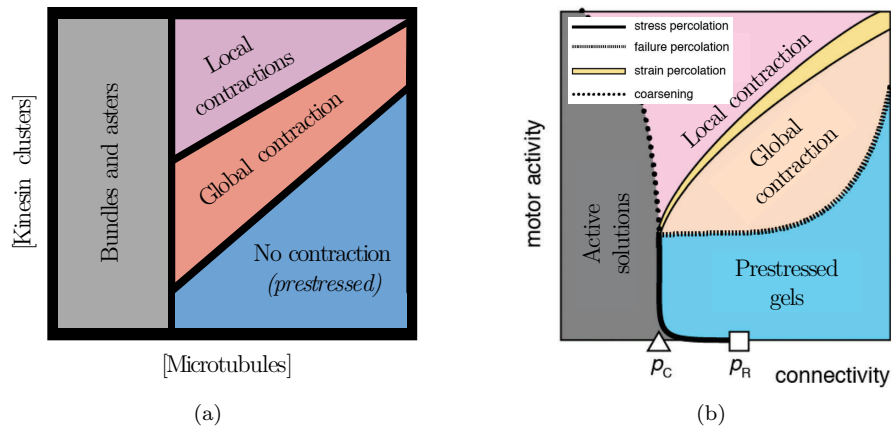


Figure 3.11 | **Experimental state diagram of contractile active networks** (a) Qualitative state diagram of the contractile microtubule-kinesin active network in the presence of depletion forces (this work). We have experimentally observed four states: the formation of microtubule bundles and asters, a prestressed, a globally contractile or a locally contractile active gel. The transitions between the regimes are not described and thus are not represented. (b) Conceptual detailed state diagram of active systems with four regimes of mechanical response to motor activity adapted from Alvarado *et al.* [5]. There are four boundaries between the regimes: a stress percolation (motor stresses balance mechanical constraints and percolate across the network), a failure percolation (motor stresses overwhelm the mechanical constraints and cause contraction), a strain percolation (boundary between local and global contraction) and a coarsening regime (motors begin to compact the network around them).  $p_C$  and  $p_R$  are respectively the conductivity threshold (characterizing the connectivity between cytoskeletal filaments) and the rigidity threshold (characterizing the rheological properties of the network).

### 3.3 Tunable corrugated patterns in an active nematic sheet



This section is adapted from our article *Tunable corrugated patterns in an active nematic sheet* that has been published in PNAS [253]. It is reproduced in Appendix E.

When long, taxol-stabilized microtubules form a dense ( $> 500 \mu\text{g/mL}$ ) aligned network in the presence of kinesin clusters and depleting polymers, new patterns arise. Here, we show that, in these conditions, a thin static corrugated sheet in three dimensions is formed, a behavior that has only recently been observed in isotropic and cross-linked actin/myosin gels [125]. Essentially, the fluid contracts anisotropically along its two shortest dimensions to form a thin sheet of gel that freely floats in the aqueous solution, mainly due to passive depletion forces. Simultaneously, the extensile active stress generated by the motors buckles the sheet along the direction perpendicular to its plane, forming a corrugated sheet of filaments with a well-controlled wavelength of the order of  $100 \mu\text{m}$  over an area of  $10 \text{ mm}^2$ . At high enough activity, the pattern is only transient and ultimately breaks into chaotic flows [241, 319] that we will describe in the next section (Section 3.4). The transition between static corrugations and chaotic flow is experimentally controlled by two parameters, the motor concentration and the attraction between microtubule filaments due to depletion forces.

#### 3.3.1 A 3D active nematic fluid forms a corrugated sheet that buckles

##### From a nematic solution to a corrugated sheet

Initially, microtubules are aligned in the direction of the channel (Figures 3.12 (a) and 3.7). In the presence of  $0.5 \text{ nM}$  of clusters of K430-HSNAP motors, confocal images recorded after 300 min show that the active fluid has contracted along  $z$  and buckled in the  $xz$  plane to form a corrugated sheet whose hills and valleys reach the top and bottom walls of the channel and whose grooves are strikingly parallel to the  $y$  axis (Figure 3.12 (c)). The thickness of the sheet is  $\ell_z = 35 \pm 5 \mu\text{m}$  and the wavelength of the corrugations is  $\lambda = 285 \pm 15 \mu\text{m}$ . This periodic pattern extends along an area of at least  $9.5 \times 1.4 \text{ mm}^2$  with dislocations corresponding to the junction of two valleys or hills. The pattern can also be visualized in epifluorescence, where it appears in the form of focused and defocused bands (Figure 3.12 (b)).

##### Dynamics of the formation

Two processes take place at the same time: a buckling along the  $z$  direction and a contraction along  $z$  and  $y$ . We observe that buckling is principally an active mechanism while contractions in  $y$  and  $z$  are mainly passive. Buckling is quantified by the angle  $\phi$  between the microtubule bundles and the  $x$  axis in the  $xz$  plane. It initially proceeds at a rate  $\omega_\phi = 0.3 \text{ min}^{-1}$  but later slows down until reaching a maximal buckling angle  $\phi^{max} = 32.2 \pm 0.5^\circ$  (Figure 3.13 and Movie A.4 [[↓](#), [🔍](#)]) and an amplitude  $h^{max} = 22 \pm 3 \mu\text{m}$  after 100 min.

Contraction is quantified by  $\Delta\ell_z$  and  $\Delta\ell_y$ , the contracted lengths of the fluid along the  $z$  and  $y$  axes respectively. Contraction along  $z$  and  $y$  is significantly slower with onset rates  $\omega_z =$



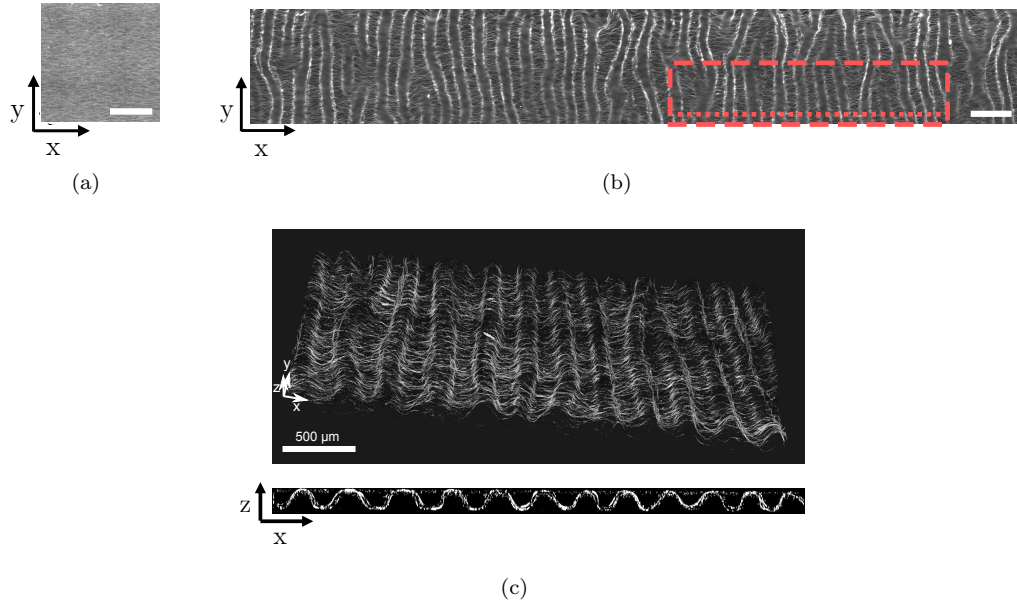


Figure 3.12 | **A 3D active nematic fluid creates a corrugated sheet of well-defined wavelength** (a) Epifluorescence image of the fluid at initial time. (b) Epifluorescence image of the same sample after one day and over a  $9.5 \times 1.4 \text{ mm}^2$  area, the red dashed rectangle and the red dotted line respectively indicate the region where the top and bottom images in panel c are recorded. (c) Confocal images in 3D (top) and cross-section in the  $xz$  plane (bottom) of the fluid after 300 min. Scale bars are  $500 \mu\text{m}$  and K430-HSNAP motor concentration is  $0.5 \text{ nM}$ .

$6.4 \times 10^{-2} \text{ min}^{-1}$  and  $\omega_y = 1.5 \times 10^{-2} \text{ min}^{-1}$ , respectively, to reach maximum amplitudes  $\Delta\ell_z^{max} = 40 \mu\text{m}$  and  $\Delta\ell_y^{max} = 210 \mu\text{m}$  (Figure 3.14 (b)). The relative contraction amplitudes  $\Delta\ell_z^{max}/H = 0.40$  and  $\Delta\ell_y^{max}/W = 0.14$  are significantly different (Figures 3.14 (a) and (b)). In the absence of motors, buckling is undetectable in confocal images but contraction is similar in both passive and active fluids. The passive origin of contraction is further supported by the fact that its amplitude is strongly dependent on the concentration of the depletion agent (Figure 3.14 (c)).

### 3.3.2 Motor concentration tunes pattern properties

#### A hydrodynamic theory that predicts the wavenumber of the corrugations

The behavior of active fluids, including those composed of microtubules and kinesins [241, 140, 319, 174], has been successfully described with the hydrodynamic theory of liquid crystals supplemented with a stress term resulting from activity (derived from the simple model presented in Section 2.1.4). We now demonstrate that this framework, applied to a thin film that can buckle in the third dimension, can provide an explanation and theoretical estimates of the wavenumber  $q^* = 2\pi/\lambda$  and of the formation rate  $\omega^*$  of the corrugated pattern (see the Appendix C for the detailed theory developed by A. Maitra and R. Voituriez).

To do so, we consider the periodic undulation of the thin sheet made of microtubules and motors in the  $xz$  plane, supposing that passive forces have already collapsed the 3D fluid into a thin 2D sheet. The nematic active fluid sheet has bending modulus  $K$  and its director  $\hat{\mathbf{n}}$  is on average

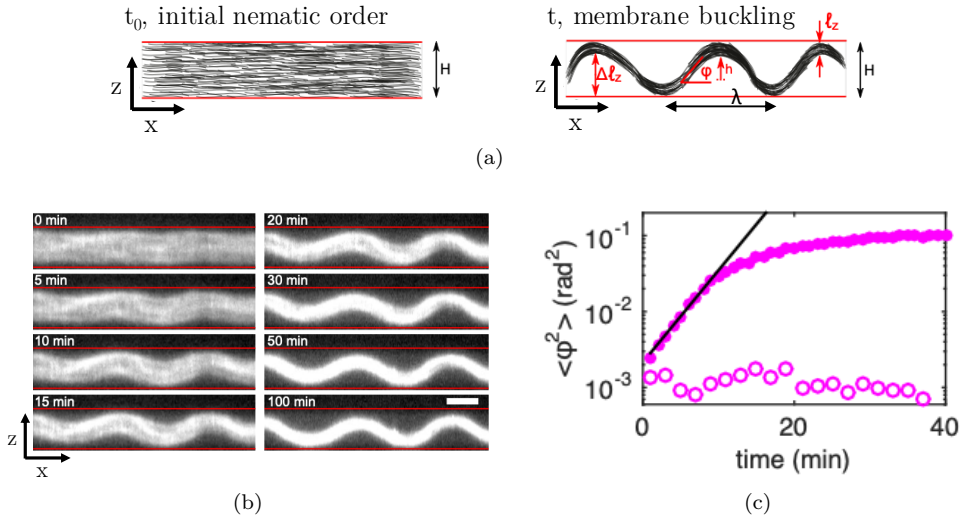


Figure 3.13 | **Dynamics and mechanism of the formation of the corrugated patterns.** (a) Sketch of the observations indicating the measured quantities  $\Delta \ell_z$ ,  $\phi$ ,  $h$ , and  $\ell_z$ . (b) Time-lapse confocal fluorescence images of the active fluid in the  $xz$  plane. Scale bar is  $100 \mu\text{m}$ . (c) Average of  $\phi^2$  along the  $x$  direction versus time in the presence (filled disks) and in the absence (empty circles) of motors. All data correspond to  $0.5 \text{ nM}$  K430-HSNAP motors except empty circles in (c). Movie A.4 [[↓](#), [▶](#)].

parallel to the  $x$  axis:  $\hat{\mathbf{n}}_0 = \hat{x}$ . The fluctuation of the membrane about a fiducial plane parallel to the  $xy$  plane (here, taken to be the mid-plane of the channel) is denoted by  $h(x, y)$  (Figure 3.15).

The deflection of the director in the  $xz$  plane,  $\delta \mathbf{n}_z$ , leads to a buckling of the membrane in the  $z$  direction:  $\delta \mathbf{n}_z \approx \partial_x h \hat{z}$ . The passive elasticity of the nematic fluid  $\propto (\nabla \mathbf{n})^2$  then yields a bending energy  $\propto (K/2)(\partial_x^2 h)^2$  for the buckling of the thin sheet in the  $z$  direction. The standard active force [287, 135, 226, 173, 222] is  $-\zeta(c)\nabla \cdot (\mathbf{nn})$ , where  $\zeta(c) > 0$  is the strength of the extensile activity that is a function of motor concentration  $c$ . This leads to a force  $\propto -\zeta(c)\partial_x^2 h \hat{z}$  that tends to destabilize the flat membrane and that is similar to an effective *negative* surface tension [170]. The interplay between the negative surface tension, arising from activity, and the stabilizing bending modulus, due to nematic elasticity, leads to the selection of a pattern with wavenumber

$$q^* \sim \sqrt{\zeta(c)/K}. \quad (3.5)$$

The pattern arises with a rate  $\omega$  whose exact expression is provided in the Appendix E. Note that in the absence of confinement, we expect the pattern to be unstable.

The theory thus shows that an out-of-plane buckling instability compatible with our observations results from the interplay of active forcing  $\zeta(c)$  and passive elastic restoring forces,  $K$ ; the same ingredients that in previous microtubule-kinesin active fluid provided dramatically different patterns [241, 140, 46, 207, 174] and that we will discuss in the next section. The instability described here does not result in coherent or incoherent flow, of either the active or the embedding fluid, in contrast with theories describing 2D or 3D active fluids that do not form sheets [153, 305, 58].

This qualitative interpretation has two advantages. Firstly, it is parsimonious because a single

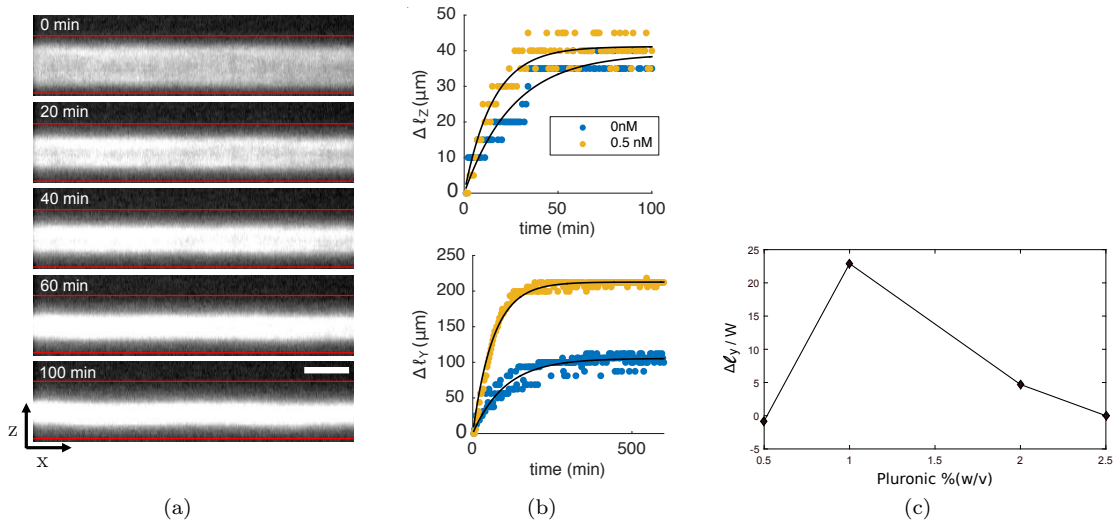


Figure 3.14 | **Passive formation of the gel sheet in the absence of motors.** (a) Time-lapse confocal fluorescence images of the passive gel in the  $xz$  plane. (b) Comparison of contractions along  $z$  (top) and  $y$  (bottom) between gels with and without motors.  $\Delta l_z^{max}$  was undistinguishable while  $\Delta l_y^{max}$  and the rates  $\omega_z$  and  $\omega_y$  were two-fold smaller in the absence of motors. (c) Gel contraction along the  $y$  axis as a function of pluronic concentration. Contraction depends non-monotonically on the concentration in depletion agent, with a maximum at 1 % (w/v) pluronic concentration.

feature, activity, explains the 3D out-of-plane buckling observed here and the 2D in-plane buckling [241, 174] and 3D chaotic flows [319] observed previously in a similar system. Secondly, it predicts that decreasing depletion forces precludes the formation of the thin sheet and thus the emergence of out-of-plane buckling in favor of 3D chaotic flows. In the following we analyze these two questions in more detail. However, although hydrodynamic theories, such as the one just described, provide an informative qualitative description of the physics of active fluids, they feature phenomenological parameters, such as  $\zeta(c)$  and  $K$ , that are difficult to measure experimentally. To our knowledge, the only quantitative test of such theories in the kinesin-microtubule system has been recently performed by Martinez-Prat and colleagues [174], where they have obtained  $\zeta(c) \sim c^2$ . Using their scaling, our semi-empirical prediction reads

$$q^* \sim c/\sqrt{K}. \quad (3.6)$$

### Evolution of the nematic sheet according to motor concentration

To test the prediction  $q^* \sim c$ , we investigate the behavior of the fluid over a range of motor concentrations  $c$  spanning more than two orders of magnitude (Figure 3.16 and Movie A.5 [↓, ⏪]). Below 0.5 nM motors the fluid behaves as described in Figure 3.12: buckling in the  $xz$  plane and contractions in the  $z$  and  $y$  directions. As  $c$  increases from 1 to 2.5 nM, buckling in the  $xz$  plane is initially observed and followed by buckling in the  $xy$  plane that distorts the corrugated pattern without breaking it. Finally, between 5 and 50 nM motors, buckling in the  $xz$  plane is still observed at early times but the pattern breaks into a 3D active chaotic (Movies A.6 [↓, ⏪] and A.7 [↓, ⏪])

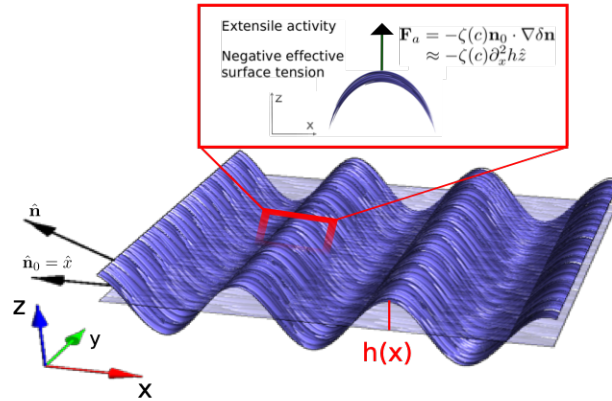


Figure 3.15 | **Sketch of the mechanism for the active buckling of a thin membrane.** The negative tension  $F_a$  is proportional to the active stress  $\zeta(c)$  and the Laplacian of the height  $h(x)$  of the sheet above its fiducial plane.

state similar to the one already reported in this active fluid [241] and developed in more details in the next section (Section 3.4). However, the velocity of this flow state is significantly lower in our case, possibly because the solution is more viscous.

The transition to the chaotic state happens qualitatively through two processes: the accumulated tension on the hills and valleys of the corrugations breaks the microtubule bundles and the frozen fluid locally flows or the dislocations in the corrugations become motile leading to a shearing of the pattern and its consequent destruction. In our experiments the chaotic state is never observed before the buckled state. However if the characteristic time of active transport is much shorter than the time of passive contraction one would observe only the spontaneous flow instability and would not observe the buckling instability (which happens in ref. [241]). Nevertheless, first observing spontaneous flow instability and then the buckling instability is unlikely because the first one would destroy the nematic order that allows passive buckling.

### Quantitative characterization

The measured wavenumber of the corrugations is in agreement with the predicted linear scaling (Figure 3.17 (a)), in particular in the range 0.5 – 10 nM. A linear fit  $q^* = a_1 + a_2 c$  of the data yields  $a_1 = 5 \times 10^{-3} \mu\text{m}^{-1}$  and  $a_2 = 1.4 \times 10^{-3} \mu\text{m}^{-1} \text{nM}^{-1}$ , where the constant term  $a_1$  results from the weak contribution of Euler buckling in the absence of motors. Indeed, activity controls the wavenumber only if the active wavenumber is larger than the one selected by passive Euler buckling, a crossover that happens at  $c = 0.5$  nM in our experiments.

The growth rate of the patterns,  $\omega^*$ , increases slightly with  $c$  in the range 0.1 – 0.5 nM, then drastically between 0.5 and 1 nM, and saturates at higher  $c$  (Figure 3.17 (b)), resulting in  $\omega^*$  also increasing and then saturating with  $q^*$ . For the hydrodynamics-dominated approximation, the theory predicts  $\omega^* \sim q^3$  for  $q^* H \gg 1$  and  $\omega^* \sim q^6$  for  $q^* H \ll 1$ , while our experiments correspond to  $q^* H = 1.3 - 4$ . In the range  $c = 0.1 - 0.5$  nM, the data are compatible with the scaling  $\omega^* \sim q^3$ , but their precision does not allow us to conclude.

Comparing the results of our out-of-plane instability with the instability introduced qualita-

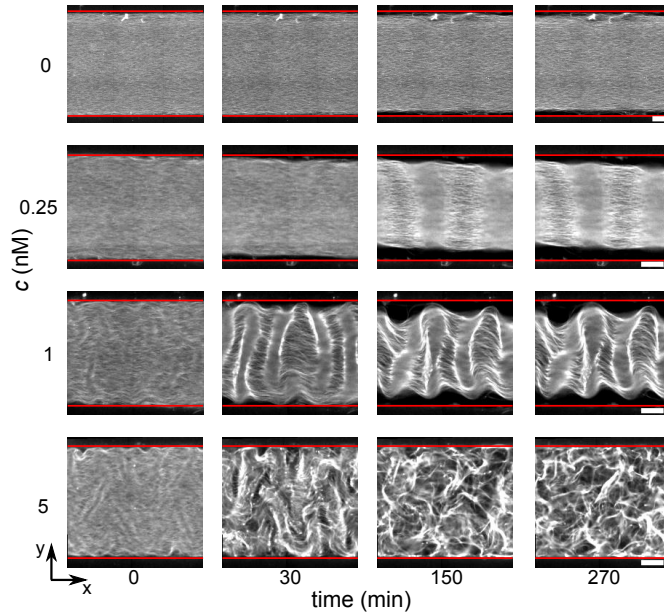


Figure 3.16 | **Dynamics, shape, and stability of the patterns as function of K430-HSNAP motor concentration.** Time-lapse epifluorescence images of active fluids with different motor concentrations  $c$ . Red lines indicate channel walls. Scale bars are  $200 \mu\text{m}$ . Movies [A.5](#) [[↓](#), [🕒](#)], [A.6](#) [[↓](#), [🕒](#)] and [A.7](#) [[↓](#), [🕒](#)].

tively in Section 3.4 and quantitatively in [174], we find similar wavenumbers ( $1$  to  $7 \times 10^{-2} \mu\text{m}$  in our case versus  $0.5$  to  $3 \times 10^{-2} \mu\text{m}$ ) but significantly slower dynamics ( $1$  to  $4 \times 10^{-2} \text{min}^{-1}$  versus  $6$  to  $240 \text{min}^{-1}$ , respectively). In addition, topological defects seem to play no role in the emergence of our patterns, in contrast with what happens in 2D active nematic systems [46, 155]. We do observe dislocations in the corrugations that rarely move along the  $y$  axis, although they do so too slowly to play a significant role.

### 3.3.3 Dependence on the geometry and on the microtubule concentration

To test the prediction  $q^* \sim 1/\sqrt{K}$  we vary the thickness and the aspect ratio of the confinement of the active fluid at low motor concentration, with the hypotheses  $K \sim \ell_z$  and  $\ell_z \sim H$ . We measure  $\ell_z$  and  $q^*$  for  $H$  in the range  $70 - 540 \mu\text{m}$  and confirm that the data are in agreement with  $\ell_z \sim H$  (Figure 3.18 (a)) and with  $q^* \sim 1/\sqrt{\ell_z}$ , with the exception for the thinnest fluid (Figure 3.18 (b)).

Reducing the aspect ratio of the channel section results in some portions of the fluid buckling in the  $xz$  plane and others in the  $xy$  plane at  $W/H = 4.6$  and no preferential direction of buckling at  $W/H = 1$  (Figure 3.19). In addition, in all the cases where both  $xy$  and  $xz$  buckling are observed, the wavenumbers in the two planes are in qualitative agreement with the aforementioned argument that essentially yields  $q^* \sim 1/\sqrt{H} > q_{xy}^* \sim 1/\sqrt{W}$  when  $H < W$  and  $q^* = q_{xy}^*$  when  $H = W$ .

Another way to influence  $K$  is to change the microtubule concentration  $\mu$  (Figure 3.20). Increasing  $\mu$  in the range  $0.5 - 2 \text{mg/mL}$  decreases  $q^*$  in agreement with the expectation that  $K$  should increase with  $\mu$ . In contrast at  $\mu = 0.25 \text{mg/mL}$  global contraction, instead of corrugations,

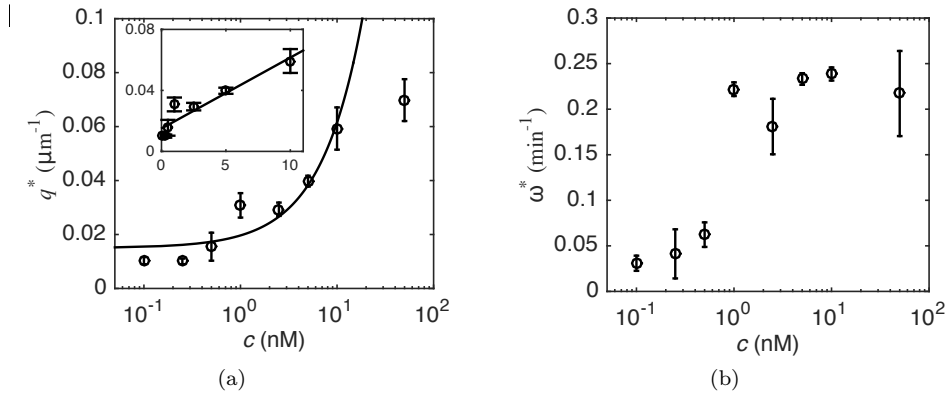


Figure 3.17 | **Wavenumber and growth rate of the patterns as a function of K430-HSNAP motor concentration.** (a) Wavenumber  $q^*$  of the corrugations versus motor concentration. The inset is the linear-linear representation of the main plot and the line corresponds to a linear fit to the data in the range  $c = 0.1 - 10$  nM with regression coefficient  $r^2 = 0.9$ . (b) Growth rate versus motor concentration. Error bars indicate the standard deviation of a triplicate experiment where a single motor-filament mix is distributed into three different channels.

is observed as described in the previous section.

### 3.3.4 Partial conclusion

In this section, we have demonstrated that *in vitro* active fluids can be designed to form static or transient suspended sheets with periodic corrugated patterns of tunable wavelength. The mechanism of pattern formation that we have proposed combines passive and active processes that can be controlled physico-chemically. Passive depletion forces — which depend on depletion agent concentration, filament length and ionic strength — induce the spontaneous condensation of a 3D nematic fluid into a thin 2D nematic sheet. Active stresses buckle the fluid sheet out of plane to form corrugations with well-defined wavelength that can be controlled by activity. In addition, we have used an active gel theory to demonstrate that the observed patterns result from an out-of-plane buckling instability induced by active extensile stresses along the nematic axis of the fluid sheet.

However, the buckling instability that we have reported does not involve filament flows and therefore fundamentally differs from both contractile instabilities in anisotropic active fluids and spontaneous flow transitions in nematic active fluids that have been described theoretically [153, 305, 173], and shown to be characterized by hydrodynamic flows and in-plane buckling of the director field in the case of 2D systems. Such spontaneous flows have been observed in various active matter systems [241, 310, 336, 155, 46, 54, 207, 174]. In practice they yield either chaotic or large scale coherent flows, but so far no static spatial patterns. We explore this regime of active flows in the next section.

Importantly, the observation of corrugated patterns expands the state diagram depicted in Section 3.2 (Figure 3.11). The patterns are obtained for a concentration in microtubules  $> 250 \mu\text{g}/\text{mL}$  — beyond the regimes of a prestressed network, a global contraction and a local contraction — regardless the concentration in kinesin clusters. However the patterns are only stable at low kinesin

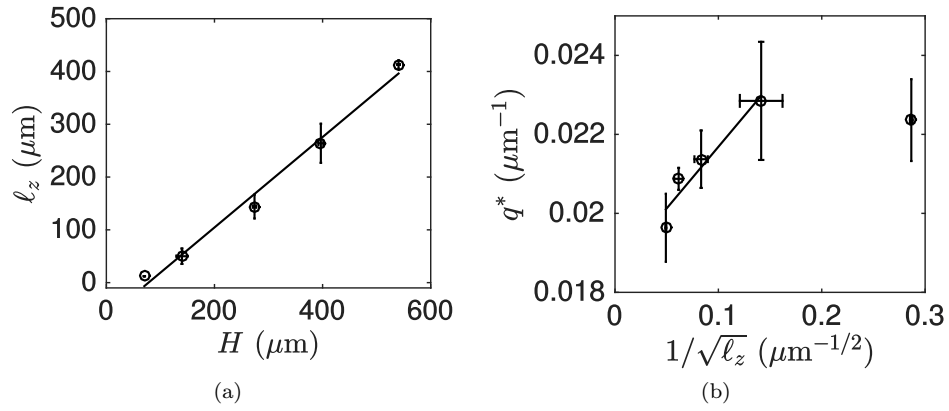


Figure 3.18 | **Effect of the geometrical confinement on corrugated patterns.** (a) Final thickness  $l_z$  versus channel height  $H$ . (b) Wavenumber  $q^*$  versus  $1/\sqrt{l_z}$ . Increasing the thickness of the fluid reduces the wavenumber. Error bars indicate the SD of a triplicate experiment where a single motor-filament mix is distributed into three different channels. Solid lines correspond to linear fits. Experiments shown are done at 1 nM motors.

concentrations ( $< 5$  nM of K430-HSNAP) and are transient at higher concentrations.

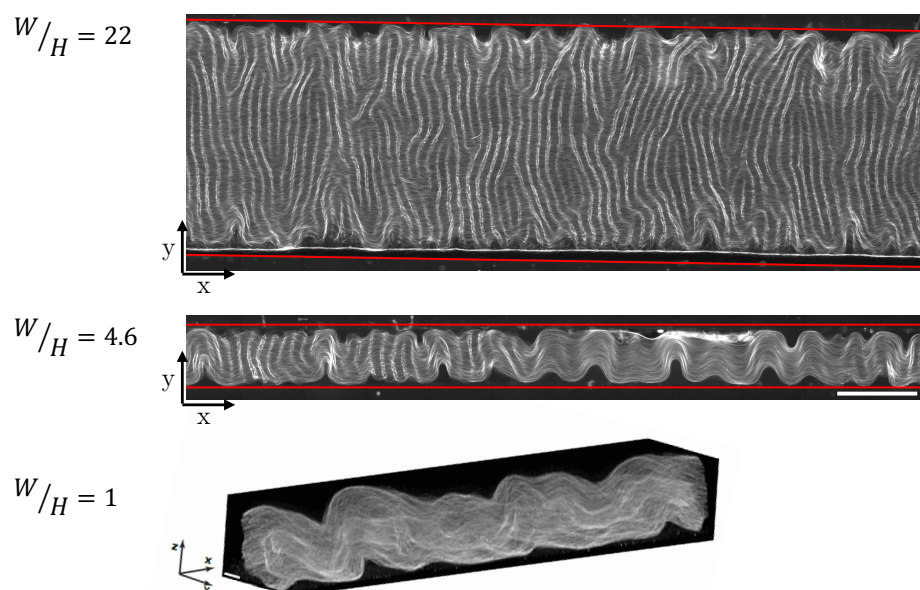


Figure 3.19 | **Effect of the channel ratio width/height on corrugated patterns.** Reducing the aspect ratio of the channel section results in some portions of the fluid buckling in the  $xz$  plane and others in the  $xy$  plane at  $W/H = 4.6$  ( $W = 0.6$  mm,  $H = 0.13$  mm) and no preferential direction of buckling at  $W/H = 1.0$  ( $W = H = 0.5$  mm). Scale bar is 1 mm for the two first channels and  $100 \mu\text{m}$  for the last one.

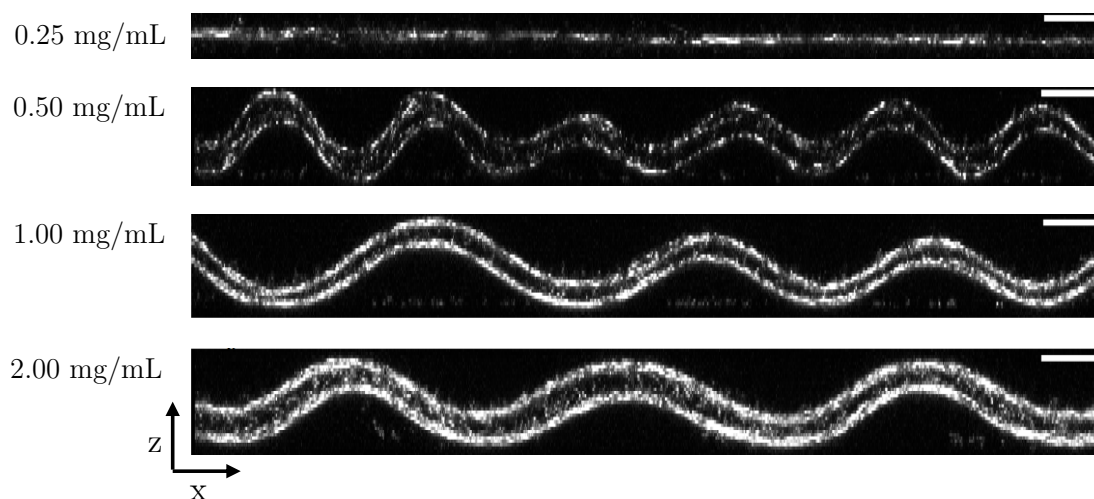


Figure 3.20 | **Effect of the microtubule concentration on corrugated pattern.** Confocal images of corrugated patterns for different microtubule concentrations at 1 nM of K430-HSNAP motors. No corrugation is observed at 0.25 mg/mL but there is a strong contraction of the whole system. At higher concentrations the wavelength of the corrugations increases with increasing microtubule concentration. Scale bars are  $100 \mu\text{m}$ .



### 3.4 From aligned nematics to active flows

The length of the microtubules has a strong impact on the observed structures. When instead of 8- $\mu\text{m}$ -long taxol-stabilized microtubules, 1.5- $\mu\text{m}$ -long GMPCPP-stabilized ones are used at a high concentration ( $> 500 \mu\text{g/mL}$ ), no contraction of the fluid is observed along  $z$  or  $y$  anymore, precluding the formation of a thin sheet that could buckle out-of-plane. In this case chaotic flow is observed at high activity. These observations are consistent with the expected linear dependence of the depletion free energy on filament length, which, in our geometry makes long microtubules condense into a thin sheet. Interestingly, lowering either the concentration of the depletion agent or the ionic strength of the buffer leads to the same observation with 8- $\mu\text{m}$ -long microtubules.

The chaotic state is characterized by microtubule bundles that are constantly interacting with each other: they merge, extend, buckle, and recombine. As demonstrated by Sanchez, Dogic and collaborators [241], these bundles are locally polarity-sorted. The merge of bundles is equally likely to happen in the same or opposite polarity, the latter results in a relative sliding. The extension induces bundles to buckle, to thin and eventually break producing new bundle ends, which are free to merge. Thus, the active gel globally exhibits extensile behavior. The system is in a dynamic steady-state for hours thanks to the ATP regeneration system. The active network is internally driven by the kinesin clusters leading to chaotic flows, hydrodynamical instabilities and enhanced fluid mixing. Many efforts have been undertaken to characterize such fluids both in 3D [319] and when constrained in 2D where they organize into active nematics [46, 174, 207, 108].

In this section, we focus in the dynamics of the transition from an initial nematic aligned state to a turbulent flow state, when the depletion forces are not high enough to induce the formation of a corrugated nematic sheet. To achieve this we essentially consider in this section short GMPCPP-microtubules. Using the same set-up as previously — a channel of typical sizes of 1 cm, 1 mm and 100  $\mu\text{m}$  respectively in the  $x$ ,  $y$  and  $z$  directions — we are able to observe the early times of 3D turbulent flows powered by the active fluid. We first describe qualitatively this transition by looking in particular at the successive orthogonal bending instabilities that drive the system to chaotic flows. As in the 2D case [174] the bending instabilities are the main generators of the transition, but here topological defect pairs are not created since the gel is not constrained in 2D and so can form thick bundles that can buckle in the third dimension. We then quantify the transition by looking at the orientation of the bundles over time. We successively compute the orientation map, the angle distribution and the local and the global order parameters of the active fluid.

We would like to point out to the reader that we often use the terms ‘chaotic’ or ‘turbulent’ to characterize the fluid. These terms are equally used in the field to describe this regime. Besides, recent works have investigated these questions by looking theoretically at the scaling properties of active turbulence [3] and experimentally at the chaotic mixing of the topological defects [277].

#### 3.4.1 Successive instabilities generate chaotic flows from an initial nematic ordered state

Initially, microtubule bundles are aligned along the  $x$  axis, like the taxol-stabilized microtubules described in the methods of the present chapter. Then, the bundles undulate as they extend and

they buckle in the  $xy$  plane at a well-defined wavelength (Figure 3.21 and Movie A.8 [[↓](#), [▶](#)]), contrary to what happens to the previously described corrugated sheet where the buckling happens in the  $xz$  plane (Section 3.3).

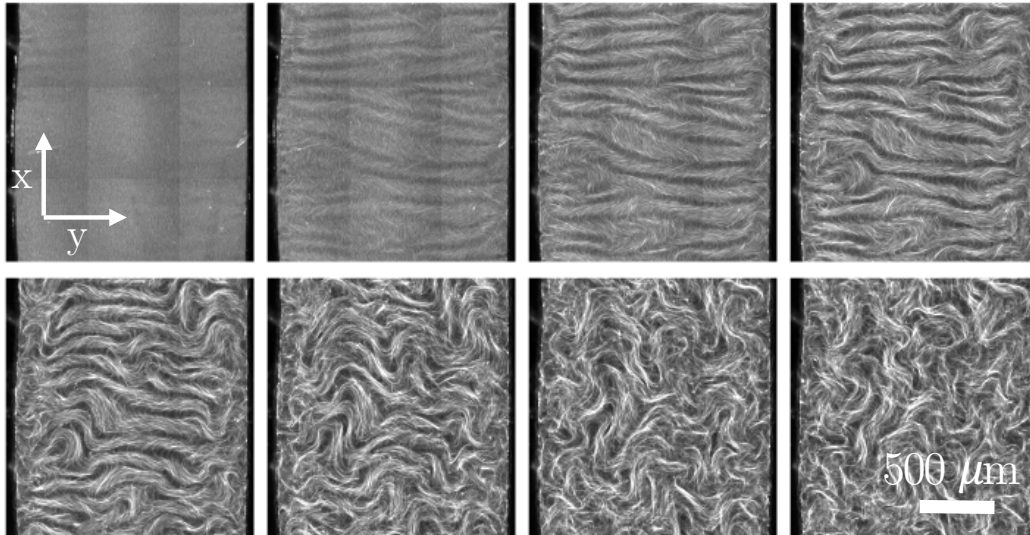


Figure 3.21 | **Bending instabilities and wavelength selection in a 3D active gel.** Time-lapse of the initial pattern formation. In this experiment  $K430\text{-HSNAP} = 25\text{ nM}$ ,  $\text{GMPCPP-microtubules} = 0.75\text{ mg/mL}$  and  $\text{pluronic} = 2\%(w/v)$ . Images are taken every minute. Movie A.8 [[↓](#), [▶](#)].

This first bend-type instability forms in the  $y$  direction and spans almost the whole width of the 1.5 mm channel. Immediately after — or concomitantly for higher motor concentrations — the system is submitted to a second instability in the orthogonal direction ( $x$  direction). These two first instabilities are represented in Figure 3.22. Then they repeat several times until the initial orientational order is completely destroyed. It is a similar process to what happens in purely 2D active nematics [174] but without the formation of  $\pm\frac{1}{2}$  defect pairs since the bundles are not confined in 2D and can buckle in the third direction. Usually two instabilities are sufficient to greatly destabilize the pattern. It is a mechanism of transition to the turbulent regime different from the one encountered in the corrugated pattern. Indeed, as mentioned in Section 3.3, the corrugated patterns are destroyed through two processes: the accumulated tension on the hills and valleys of the corrugations breaks the microtubule bundles and the dislocations become motile leading to a shearing of the pattern and its consequent destruction.

We look at the effect of K430-HSNAP motor concentration on the initial wavelength  $\lambda$  and the wavenumber  $q^* = 1/\lambda$  of the pattern formed by the first bending instability (Table 3.4). Higher the concentration is, lower the wavelength is and the faster the patterns are erased. We do not include the concentration 50 nM in the analysis since the pattern is already destroyed after only 2 min (the time needed to inject the active mix in the channels, close them and start imaging). Patterns at low kinesin clusters concentration (5 nM) do not break into turbulent flows and stay frozen probably because the motor forces are not sufficient to completely destroy the nematic order and overpass passive restoring forces (Figure 3.23).

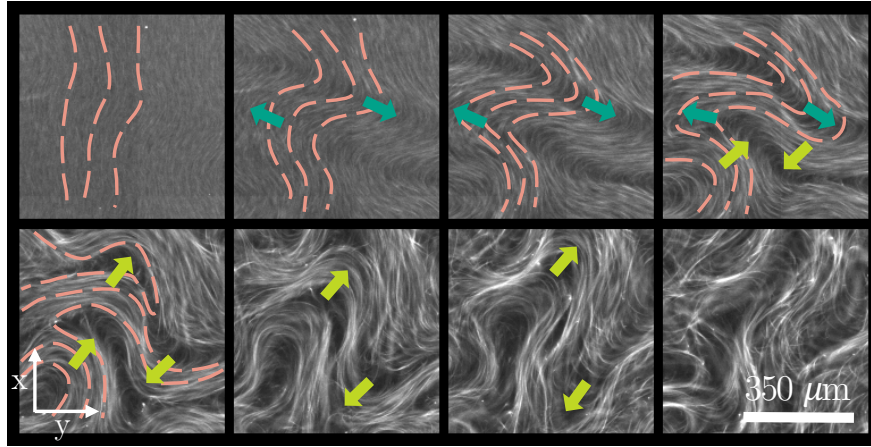


Figure 3.22 | **Successive orthogonal bending instabilities lead to chaotic flows.** The first instability happens in the  $y$  direction (dark green arrows) whereas the second one happens in the  $x$  direction (light green arrows). For the sake of comprehension, we represent the alignment of bundles thanks to three red dashed-lines that deform as the result of the successive instabilities. In this experiment  $\text{K430-HSNAP} = 25 \text{ nM}$ ,  $\text{GMPCPP-microtubules} = 0.75 \text{ mg/mL}$  and  $\text{pluronic} = 2 \text{ \%}(w/v)$ . Images are taken every 1 min.

K430-HSNAP (nM)	$\lambda$ ( $\mu\text{m}$ )	$q^*$ ( $\text{mm}^{-1}$ )
5	$430 \pm 20$	$2.3 \pm 0.1$
10	$370 \pm 20$	$2.7 \pm 0.2$
25	$150 \pm 20$	$6.7 \pm 0.9$

Table 3.4 | **Relation between K430-HSNAP concentration and the initial wavelength in the active gel composed of GMPCPP-microtubules.**

Previously (Section 3.3) we have found a linear relation between the wavenumber  $q^*$  of the corrugated pattern and the concentration in kinesin clusters. In 2D active nematics a linear scaling with the streptavidin concentration has also been found [174]. Although our data seem to suggest that a similar dependence is possible, we do not have enough data points to conclude. It would be of interest to investigate this dependence in the future.

### 3.4.2 Dynamics of the loss of nematic order

The dynamics of the loss of the initial nematic order can be quantified by using the evolution of the orientation of the microtubule bundles. To do so we compute the structure tensor of each image from the time-lapse experiments as described in the data processing paragraph of Section 3.1. We obtain a map of local bundle orientations (Figure 3.24). At initial time, most of the bundles are oriented according to the long axis  $x$  (the angle between the  $x$  axis and the bundles is near to zero) even though the active fluid has started to form very regular periodical regions of opposite orientation (the mean value of the initial angle between the  $x$  axis and the bundles is given at  $\pm 20^\circ$ ). These regions are bands along the  $y$  axis containing bundles that rotate: their angle go from  $0^\circ$  to almost  $\pm 90^\circ$ . At this point ( $t = 5 \text{ min}$  for  $\text{K430-HSNAP} = 25 \text{ nM}$ ), the perpendicular instability has begun to break the first pattern. The spatial distribution of this second instability

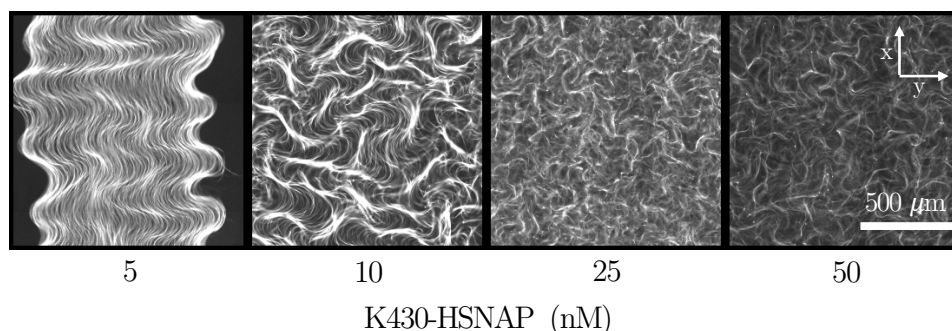


Figure 3.23 | **Final patterns obtained for different K430-HSNAP concentrations.** In this experiment GMPCPP-microtubules = 0.75 mg/mL and pluronic = 2 %(w/v).

is not as regular as the first one, they indeed mostly happen at the edges of the channels and in regions where the first pattern is not homogeneous.

This transition can be easily visualized by plotting the distribution of angles (Figure 3.26 (a)). At early times the distribution is centered around  $0^\circ$ . After one minute a majority of bundles has an orientation of  $\pm 50^\circ$ . Then, the bundles continue to rotate and once they reach an angle near  $90^\circ$ , the second instability arises and most of the other angles are now possible. Finally after a few minutes the chaotic regime is reached: the distribution of angles becomes flat.

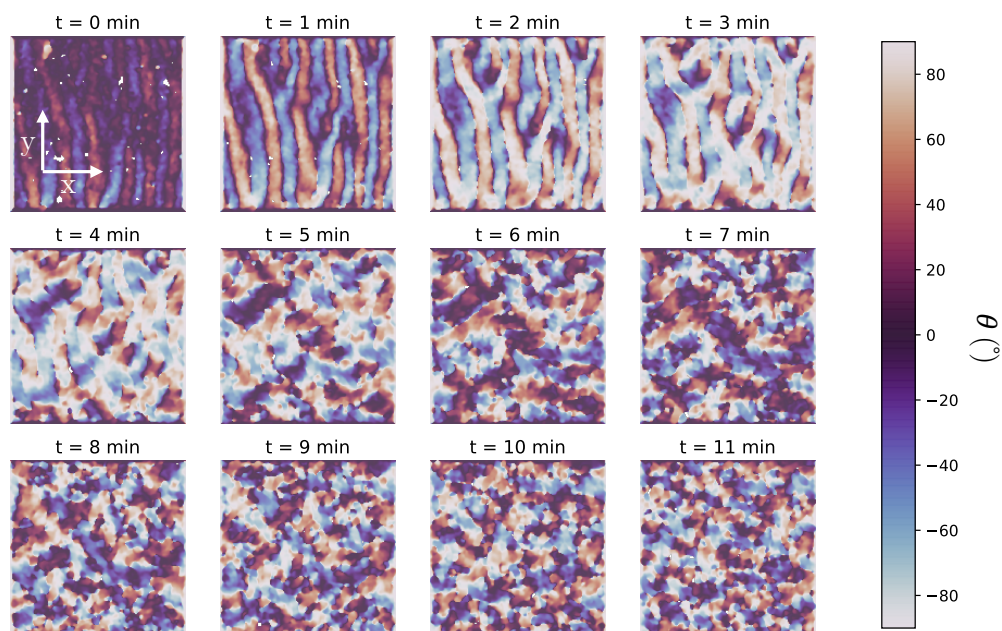


Figure 3.24 | **Evolution of the local orientation of bundles.** Note that compared to previous figures, axis have been rotated of  $90^\circ$  in order to have the horizontal axis as the origin axis. In this experiment K430-HSNAP = 25 nM, GMPCPP-microtubules = 0.75 mg/mL and pluronic = 2 %(w/v).

Bending instabilities disorient the bundles in a dramatic way: in neighboring regions, bundles

can display a difference in their orientation as big as  $180^\circ$  (oriented angles). In these regions the local order parameter — defined as  $Q = \sqrt{\langle \cos 2\theta \rangle^2 + \langle \sin 2\theta \rangle^2}$  where the mean  $\langle \cdot \rangle$  is taken locally in a window of 5 px (the entire image is  $600 \times 600$  px) — is close to 0 (Figure 3.25). We can follow the becoming of this regions as a function of time. At the beginning they are parallel lines orthogonal to the initial nematic alignment, they are then destabilized and gradually cut in smaller lines. They surround regions with the same orientation that become smaller as the turbulent regime settles down. The line formation can be understood as a competition between motor activity (active forces) and a counterbalanced elasticity which tries to prevent the deformation (passive forces). It is a similar process to the one described in Section 3.3 and modeled in Appendix C. Here again this competition selects a dominant length scale [281].

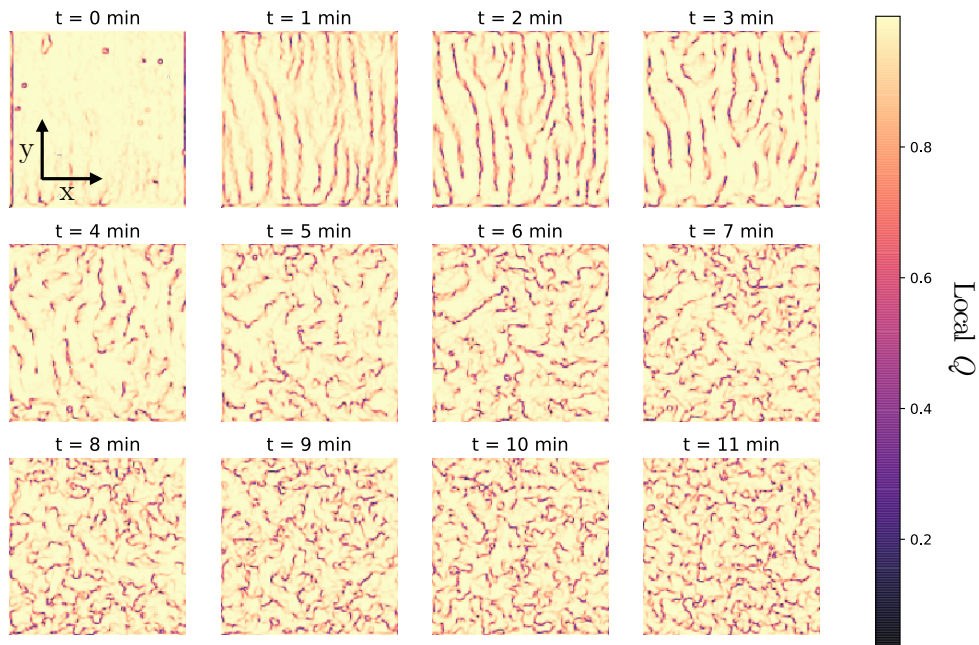


Figure 3.25 | **Evolution of the local order parameter.** In this experiment  $K430\text{-HSNAP} = 25$  nM,  $\text{GMPCPP-microtubules} = 0.75$  mg/mL and  $\text{pluronic} = 2$  %(w/v).

We compute the global order parameter (now  $\langle \cdot \rangle$  is taken on the whole field of view) (Figure 3.26 (b)). At initial time the network is very well aligned onto the same orientation, the one of the long axis ( $x$ ) of the channel. The global order parameter  $Q$  has a high value near 1. The first bending instability leads to a decrease of  $Q$ . However, at intermediary concentrations (10 and 25 nM) the second instability appears relatively late, meaning that the bundles have the time to almost reorient at  $90^\circ$ :  $Q$  is increasing again. From here the successive instabilities start to disorder the active fluid resulting in a decrease of the global order parameter. At the highest concentration in kinesin clusters (50 nM), the pattern is mostly destroyed after only 2 min, it is then difficult to analyze the behavior. At the lowest concentration (5 nM) the system stays frozen (Figure 3.23): the orientation is preserved and the global order parameter remains high.

Due to time constraints, we have not looked precisely at the dynamics, but it would be interest-

ing to perform experiments at a higher temporal resolution and to precisely control the initiation time — especially for high concentrations — by using for instance caged-ATP, a protected version of ATP which remains inactive until its illumination by UV light.

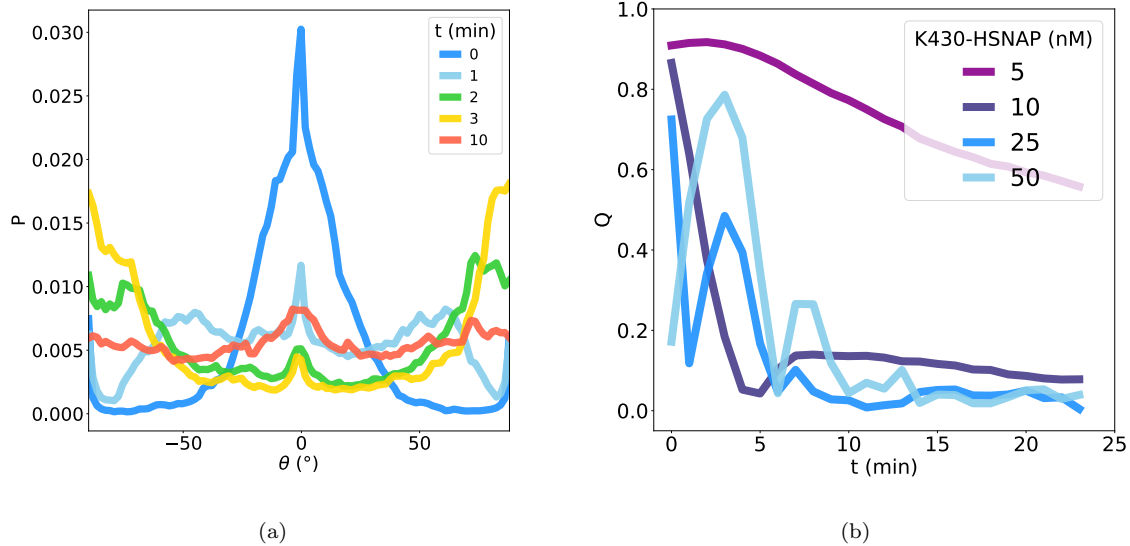


Figure 3.26 | **Distribution of local bundle orientations and evolution of the global order parameter.** (a) Normalized probability distribution of angles for different times. In this experiment K430-HSNAP = 25 nM, GMPCPP-microtubules = 0.75 mg/mL and pluronic = 2 %(w/v). (b) Time evolution of the order parameter  $Q$  for the different K430-HSNAP concentrations.

Similar investigations using the order parameter to quantify the dynamics of active nematic or polar systems have been conducted. Many of them include the study of bacterial communities or tissues [336, 245, 55]. Compared to reconstituted active gels these systems grow and divide. It leads to the opposite orientational dynamics: at early time the cells do not touch each other and are oriented in all directions. But because of growth and steric interactions, the empty spaces are gradually filled and long-range orientational order starts to appear.

## 3.5 Compartmentalization of active nematics

When geometrically constrained into droplets, active gels exhibit new behaviors which have some similarities with the ones already described in this chapter. Such confinement is important to study both the active structures and for the design of artificial cells by mimicking a cell-like environment,. In this short section we first review some of the works done to compartmentalize active gels. We then present two simple experimental methods that generate water-in-oil droplets. Lastly we list a number of open questions that, we think, would be interesting to solve using this system.

### 3.5.1 Brief state of the art

Encapsulation of cytoskeletal active gels inside water-in-water vesicles or water-in-oil droplets is used as a biomimetic system to understand the organization of the cytoskeleton in cell-like conditions and to design systems capable of deformation. For a recent extensive review on the topic the reader can refer to ref. [14]. The deformation of vesicles containing growing microtubules or polymerizing actin in the absence of motors was demonstrated in the early 1990s by Hotani and co-workers [118, 181]. Polymerizing microtubules deform vesicles into a rugby-ball shape with thin tubes later emerging from each pole [118, 218] in the absence of motors. Polymerizing actin filaments form dumbbell-shaped vesicles in liposomes [181]. In the presence of kinesin clusters, cortical bundles and asters emerge [17, 136] (Figure 3.27 (a)). Crosslinked actin and actomyosin gels display a wide variety of structures: actin rings, webs and cortices [219], 3D gels and contracting cortices [32]. When connected to the membrane, actomyosin gels can shape and deform vesicles [165, 263] (Figures 3.27 (b) and (c)). Recently, membraneless actomyosin droplets in an aqueous solution supplemented with the crosslink protein filamin have been reported to form and divide [308].

The encapsulation of short microtubules under depletion forces and kinesin clusters inside droplets generates 2D flows at the membrane interface. The activity allows the formation of several structures such as the distortion of the spherical shape of the liposome with, for instance, the generation of filopodia-like protrusions [140]. When adsorbed into the surface, short microtubules present pairs of topological defects (with a charge of  $\pm\frac{1}{2}$ ) that are created and annihilated [241, 140], and lead — in the case of small droplets — to oscillations of these defects. When immersed in a passive liquid crystal oil, these active nematic droplets produce a strong coupling between the active and the passive liquid crystals through the defects [103] (Figure 3.27 (d)). Because of the activity, these droplets are also able to self-propel [241].

### 3.5.2 Experimental systems and preliminary results

Using our active gel in the configuration of short microtubules, we produce active droplets using two different methods. The first one simply consists in vortexing the active mix with an oil to water ratio of 1:5 and a fluorosurfactant at 2%(v/v<sub>oil</sub>). We typically use the volumes displayed in Table 3.5.

The mix is briefly vortexed ten times during one second each time. Because the oil phase is denser than the aqueous phase, the droplets rise to the top of the tube. They are then gently

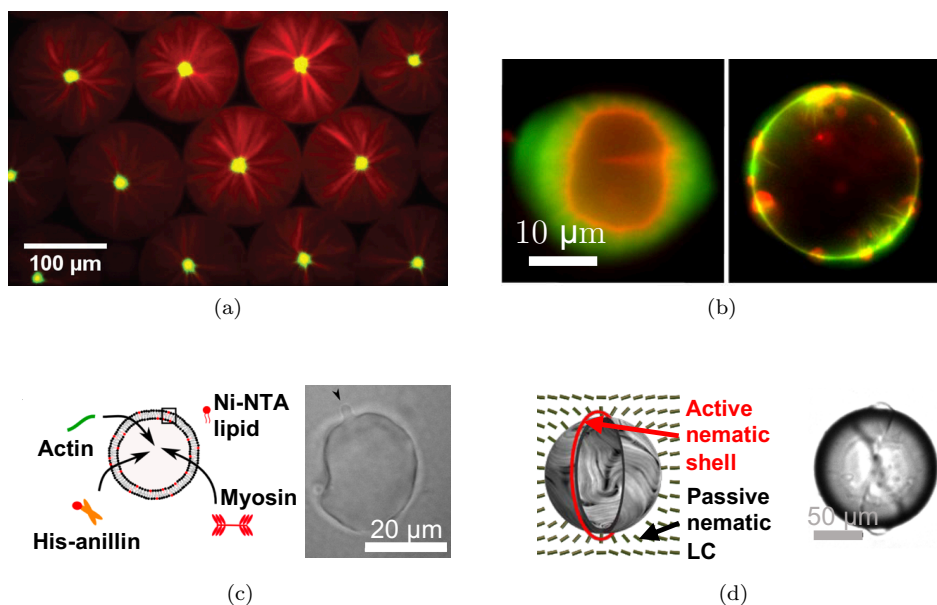


Figure 3.27 | **Recent experiments on the compartmentalization of cytoskeletal active gels.** (a) Spherical network contractions organized in asters in surfactant-stabilized droplets. Adapted from [136]. (b) A dynamic, branched actin network initiates both inward and outward membrane deformations. Adapted from [263]. (c) An actomyosin network encapsulated into vesicles deforms the membrane in the presence of a crosslinker (anillin) bound to the inner membrane. Adapted from [165]. (d) An active droplet composed of microtubule bundles and kinesin clusters immersed in a passive nematic solution shows an oscillating Saturn ring. Adapted from [103].

Name	Volume	Stock
HFE 7500 oil (3M)	35 $\mu\text{L}$	100 % (v/v)
008-FluoroSurfactant (RAN biotechnologies)	7 $\mu\text{L}$	10 % (v/v <sub>oil</sub> ) in
Active Mix	7 $\mu\text{L}$	1 X

Table 3.5 | **Volumes of oil and water phases for droplets production.**

pipetted and put in a channel built from glass slides and parafilm as previously described. This method leads to a very broad dispersion of sizes (Figure 3.28 (a) and Movie A.9 [[↓](#), [🔍](#)]), with radii spanning from as small as 10  $\mu\text{m}$  to nearly 300  $\mu\text{m}$ .

In order to obtain mono-dispersed droplets, we use a recently developed technique [297]. The method is based on the periodic extraction of a pending droplet across the oil-air interface. The interface forms a capillary trap inside which a droplet can be captured and detached. Because its production rate is of the order of a second, it has been used to engineer connected lipid bilayer networks [298], where low production rates are required to allow surfactants to stabilize droplets. By lack of time this technique has not been optimized for our experiments: fusion of droplets is often observed due to a lower concentration in surfactants.

We produce functional droplets with an active system inside and we observe the transition from a 3D network embedded in the entire droplet to a 2D active nematics located at the water-oil interface. This transition is particularly visible in large droplets ( $> 150 \mu\text{m}$  in radius): microtubules powered by the kinesin clusters and the depletion forces form bundles that go to the inner surface



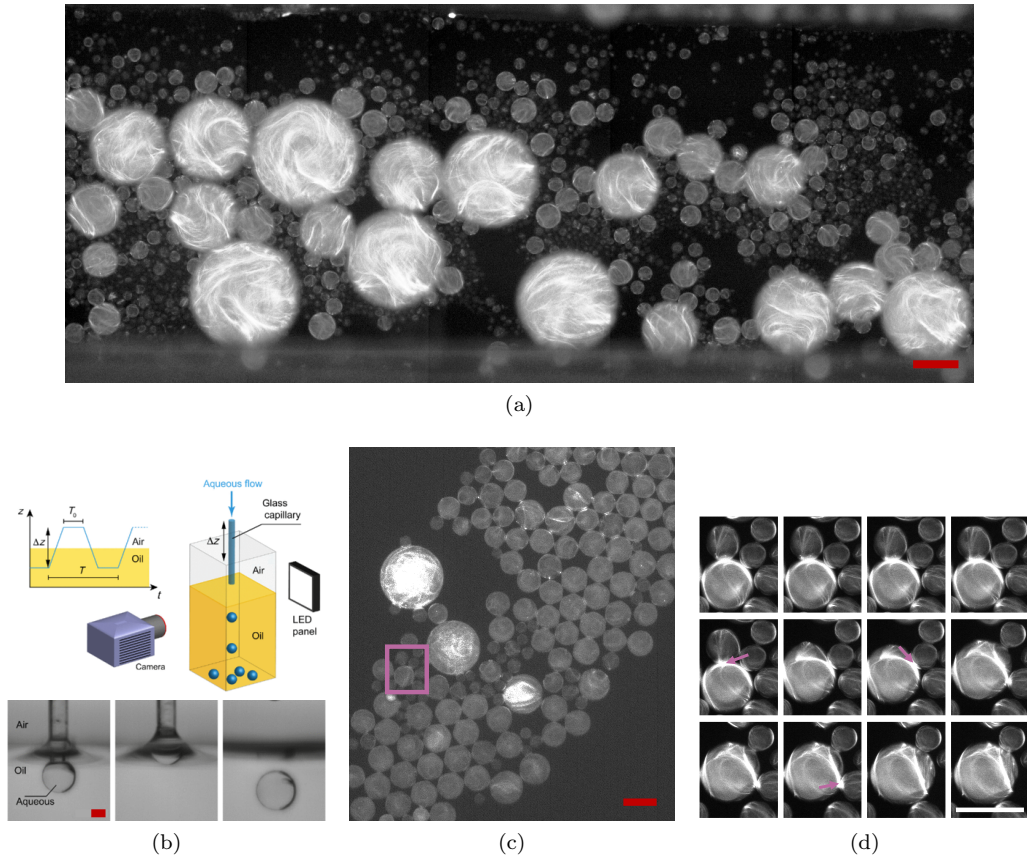


Figure 3.28 | **Methods of production of water-in-oil droplets.** (a) Droplets obtained by vortexing lead to a very broad dispersion of sizes. Movie A.9 [[↓](#), [▶](#)]. (b) Quasistatic microdroplet production in a capillary trap. A syringe pump imposes a flow of water through a glass capillary fixed to a translation stage. The capillary tip is moved vertically according to the graphical inset. Adapted from [297]. (c) Capillary trap method generates droplets of about the same size. (d) Formation of large droplets by fusion of smaller droplets. Arrows indicate the contact of two droplets just before fusion. The interval between each image is 3 min. All scale bars are 200  $\mu\text{m}$ .

(Figure 3.29 (a) and Movie A.10 [[↓](#), [▶](#)]). This transition is visible by the increase of the surface covered by the microtubules and by the emergence of 2D topological defects of  $\pm 1/2$  that continuously move. After this transient regime the system recovers the previously described active 2D nematic regime that has been observed in droplets [241], a flat geometry [241, 46, 207, 174, 108] or a torus-shaped shell [60]. In smaller droplets ( $< 150 \mu\text{m}$  in radius) only a few defects are present and move dynamically around the droplet as described in [140] (Figure 3.29 (b), Movie A.10 [[↓](#), [▶](#)]).

The formation and propagation of defects apply stresses on the surrounding oil and on the top chamber surface. This stress has been characterized for droplets immersed in passive liquid crystals [103]. Since the droplet and the surface are coupled, a force is induced on the droplets, opposing the direction of defect propagation. The interplay between internal active nematic flows and soft confinement is able to generate translation and rotation dynamics [75]. Unfortunately, because of the non-flatness of our set up we often have large hydrodynamical flows that prevent us to observe droplet motility (Movie A.9 [[↓](#), [▶](#)]).

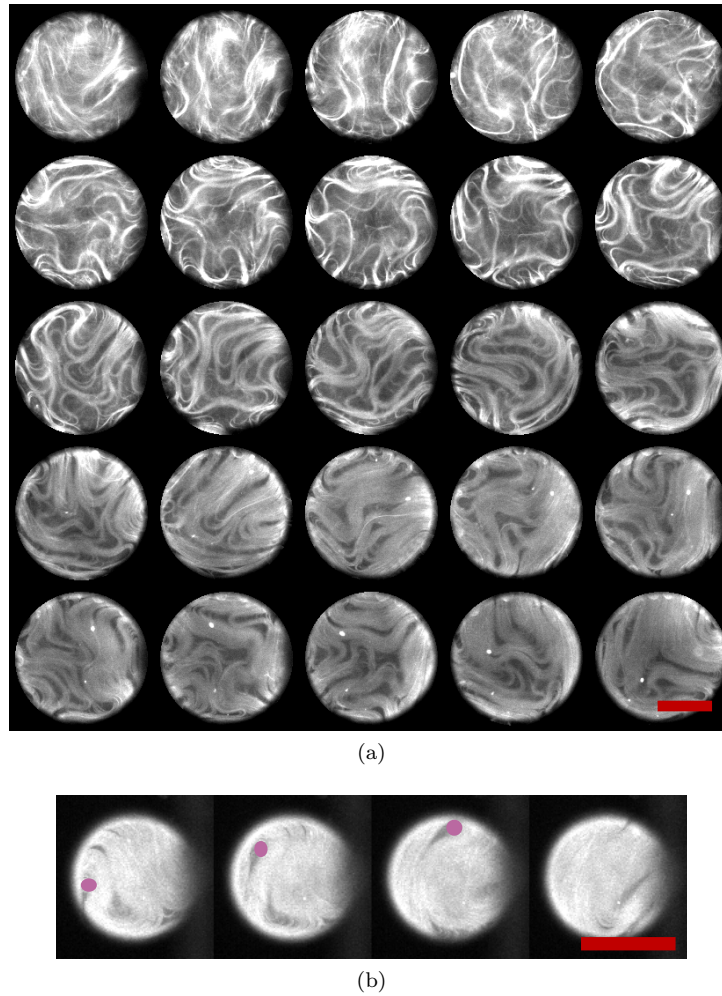


Figure 3.29 | **Formation of 2D active nematics on the inner surface of a droplet.** (a) Time-lapse images of confined microtubules for a droplet with a radius of  $240 \mu\text{m}$ . The interval between each image is 4 min. (b) Propagation of a  $+\frac{1}{2}$  defect (in magenta) over the spherical surface. The interval between each image is 2 min. Scale bars are  $100 \mu\text{m}$ . Movie A.10 [[↓](#), [▶](#)].

### 3.5.3 Open questions

We have presented preliminary results on the compartmentalization of the microtubules-kinesin system in the regime of active nematics. Not much is known about the experimental structure of active nematics flows in a droplet and the dynamic of self-propelled ATP-driven active particles. We think that our set up can help to address these features by answering the following questions (some of which are being addressed by Guillaume Sarfati's PhD work, in the lab):

- What is the dynamic of bundle formation? How do the concentration of the depleting polymer and the composition affect the absorption of bundles on the surface? What is the structure of the flow inside a large droplet: are there internal vortices [41]?
- What are the interactions between the droplet, the surface and the external fluid? Are droplets rotating when constrained between two flat surfaces? What are the required con-

ditions to observe the motility of a droplet in a 2D infinite environment as described in ref. [241]? Can we design channels where droplets move like real cells [164]? What is the nature of the motion, is it comparable to the motion of encapsulated passive nematics [114]?

- What types of collective effects would emerge in such an active system (see the examples of motorized colloids in Chapter 2). Is it possible to observe active jamming of soft particles [110], motility-induced phase separation patterns [83] or tissue-like spontaneous flows [54]?

## 3.6 Conclusion

In this chapter we have determined what are the fundamental elements necessary to achieve a dynamic or a static pattern in a reconstituted active gel. We have underlined the importance of both passive and active forces in shaping active matter and demonstrated that an active gel can behave as a contractile system, a static corrugated material or an active fluid.

### 3.6.1 Summary

More precisely, building on the initial work of Nédélec, Surrey and collaborators and the more recent work of Sanchez, Dogic and collaborators, we have engineered an active gel using two different strategies to construct clusters of kinesins: via a biotin-streptavidin link or via non-specific interactions. Using these guidelines we have produced and purified three kinesins. We have assembled an active mix composed of these motor clusters, taxol or GMPCPP-microtubules, a depleting polymer, ATP and all the necessary ingredients such as anti-oxidant elements and an energy regeneration system.

From this purified reconstituted system we have showed that it organizes over a broad range of patterns depending on the kinesin cluster concentration, the microtubule length and concentration and the depletion forces. In a weakly connected network of microtubules, bundles form thanks to the depletion forces. Concomitantly kinesins apply forces on these bundles leading to aster-like active structures. At higher microtubule concentrations, the system can either behave as a prestressed gel, or contract either globally or locally as motor concentration increases.

An initially aligned dense active network ( $> 500 \mu\text{g/mL}$ ) of taxol-stabilized microtubules spontaneously forms a 2D free-standing nematic active sheet that actively buckles out-of-plane into a centimeter-sized periodic corrugated sheet which is stable for several days at low activity. The corrugated state and the wavelength and stability of the corrugations are controlled by the motor and the microtubule concentration and by the depletion forces, in agreement with a hydrodynamic theory. When shorter microtubules are used or depletion forces lowered, chaotic active flows are observed for a high enough concentration of kinesins. These flows are created from an initially aligned nematic state by successive bending instabilities, after a first wavelength selection that depends on the motor concentration. Step by step the orientational order is lost as we have quantified by computing the local and the global order parameters.

Interestingly, in a recent study, Roostalu, Surrey and collaborators [236] have also recapitulated these different described regimes using a unique system: they use dynamic filaments that grow at the extremity. In this situation, chaotic flows are observed in the absence of a depletion agent. The authors have demonstrated that the same system can form asters, contract, or display chaotic flows, depending on the control parameters. High filament concentrations and growth rates promote chaotic flows, while low concentrations and growth rates favor aster formation. Increasing motor and filament concentrations promotes global contractions.

Finally, we have performed preliminary experiments where active flows are confined in water-in-oil droplets. They then condensate to the inner surface of the compartment and form 2D active liquid crystals that have moving topological defects of  $\pm\frac{1}{2}$ . In the last five years the study of these 2D systems has revealed very exciting physics on the flow structures [241, 46, 174, 108, 277, 207]

and asked questions on the motion of active droplets [241]. Furthermore, we would like to note that we have not examined the coherent flows that can emerge when active gels are enclosed in toroids, disks, or other complex geometries [319], even if it is an attractive manner to actively mix and transport matter over long distances without the presence of external forces.

Using this knowledge, we will design in Chapter 4 a unique experiment comprising two self-organizing systems: the present active gel and a reaction-diffusion front made of DNA strands and a few enzymes, which may open the way to the design of 3D biomimetic materials capable of self-organization.

### 3.6.2 Perspective: patterning with light

The unique properties of active gels and nematics can be further controlled externally using liquid crystals [101, 102], magnetic interactions [306] or light [20, 8] thanks in particular to the use of caged-ATP. The latter is a chemically protected version of ATP which upon UV illumination releases the protector group. As a non-reversible activation system, it can be used to precisely initiate the activity at a specific time, in a specific location. We have experimentally tested this system using a UV LED (NCSU276AT-0365 Nichia, 365 nm 780 mW, 2-Pin Surface Mount package), an illumination at 365 nm for 2 min and our active system in the regime of corrugated patterns (Figure 3.30). This system could be used to impose initial and boundary conditions like, for instance, study the path to turbulent flows described in Section 3.4.

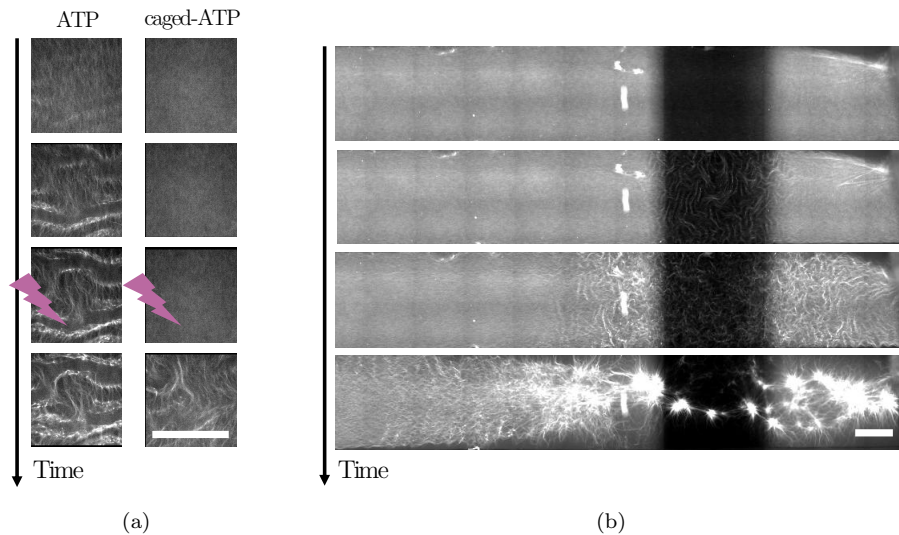


Figure 3.30 | **Caged-ATP as a tool to impose boundary conditions.** Time-lapse images of light-activated active gel. (a) Comparison of activity in presence of ATP or caged-ATP before and after UV illumination. 5 min between images. (b) UV illumination is initiated only in the dark region. The remaining part of the channel is protected from illumination by an aluminum foil. The three first images are separated by 10 min, the last one is taken 15 hours after. Scale bars are 1 mm in both figures.

Recently, reversible light-activated clusters of kinesin motors have been created thanks to the optically dimerizable iLID proteins [237]. This light-switchable active-matter system enables the

optical control of asters formation. A similar approach has been used in a 2D active nematics solution of actin and light-switchable myosin motors leading to spatially confined flows and topological defects [334].



## Chapter 4

# Coupling a DNA reaction-diffusion front and a cytoskeletal active gel

<b>4.1 Finding common conditions for the reaction-diffusion front and the active gel</b> . . . . .	<b>104</b>
4.1.1 Material and methods . . . . .	104
Detection of DNA concentration . . . . .	104
Reaction assembly . . . . .	104
Monitoring and data processing of the kinetic experiments . . . . .	105
4.1.2 Assessing experimental conditions . . . . .	106
Temperature condition . . . . .	106
Buffer condition . . . . .	108
4.1.3 The dynamics of the autocatalyst can be tuned by the PEN-DNA enzymes and dGTP concentrations . . . . .	110
<b>4.2 Propagation of a reaction-diffusion front in an active gel</b> . . . . .	<b>112</b>
4.2.1 Material and methods . . . . .	112
Reaction assembly . . . . .	112
Channel assembly . . . . .	112
Imaging . . . . .	113
Data processing . . . . .	113
4.2.2 RD front and active contractions happen independently . . . . .	114
4.2.3 A global contraction accelerates the front . . . . .	115
4.2.4 Coupling through dGTP resources . . . . .	117
<b>4.3 Hydrodynamical coupling: design of a three-letter autocatalyst</b> . . . . .	<b>123</b>
4.3.1 Design of an autocatalyst without dGTP . . . . .	123
4.3.2 Temporal dynamics . . . . .	123
4.3.3 Propagation of fronts . . . . .	124
<b>4.4 Chemical coupling: towards active matter controlled by DNA</b> . . . . .	<b>126</b>
4.4.1 Procedures to attach DNA on kinesin . . . . .	126
From amino-DNA to BG-DNA . . . . .	127
Formation of the DNA-kinesin . . . . .	128



4.4.2	Going 2D: gliding assays . . . . .	129
<b>4.5</b>	<b>Conclusion . . . . .</b>	<b>132</b>
4.5.1	Summary . . . . .	132
4.5.2	Perspectives: reacting beads immersed in an active bath . . . . .	133

The successful coupling of self-organization mechanisms is a key step in the conception of self-sustained, programmable, biocompatible materials. Reaction-diffusion patterns that meet these criteria have been successfully designed using DNA (Section 2.2.4). We have shown in the previous chapter (Chapter 3) that the behavior of an active gel composed of kinesin clusters and microtubules can be precisely tuned using a few parameters. This chapter is dedicated to the combination of these two self-organizing mechanisms into a unique system.

In the first section we describe the optimization of experimental conditions in order to find a favorable buffer and a working temperature compatible with both PEN-DNA reactions and gel activity. We quantify the temporal dynamics of the autocatalyst as a function of polymerase, nicking enzyme, dGTP and microtubule concentrations. In the second section, we look at the dynamics of a PEN-DNA reaction-diffusion front propagating in the active gel studied in Chapter 3. First, we describe the methods, in particular the assembly of the mix into channels and the data processing. We then examine the front propagation and show that a front can propagate in the active gel, either in the presence of taxol-microtubules or GMPCPP-microtubules. Interestingly when GMPCPP-microtubules are used the active chaotic flow regime is not observed. However, in a regime of low dGTP, the chaotic flows are restored but, at the same time the speed and the lifetime of the DNA front are reduced, leading to an inhomogeneous patterning of the channel, both chemically (concentration of DNA) and morphologically (active gel state). In the third section, we show some preliminary results concerning the design of an autocatalyst that consumes only three dNTP. In this system, the removal of dGTP allows the generation of a DNA front inside an active gel sustaining ATP-driven chaotic flows, which may lead to the first programmable and biocompatible reaction-diffusion-advection self-organizing system. To do so, a suitable nicking enzyme is identified and new sequences are designed. We demonstrate that, in our experimental conditions, this system behaves in a complex manner in tubes but can still give birth to fronts that propagate in the absence of the active gel. However, in its presence, small aggregates appear, disabling the activity of the gel. In the fourth section, we explain how to create a specific chemical coupling using DNA and the SNAP-tag of the kinesins designed in Chapter 3. We describe the two steps needed to connect DNA to the SNAP-tag in a covalent manner, in order to make a DNA-kinesin chimera. Finally, we propose an experimental system in which it would be possible to test this DNA-chimera: a DNA-controlled gliding assay.

## 4.1 Finding common conditions for the reaction-diffusion front and the active gel

The active gel used in Chapter 3 and the PEN-DNA toolbox presented in Chapter 2 work in different experimental conditions. In this section, we modify the active buffer of the previous chapter (Table 3.2) in order to find conditions in which the PEN-DNA toolbox can operate. We first describe the methods and the assembly of the reaction. We then explain the main differences — in terms of temperature and buffer — and display the process that leads us to find suitable common conditions. Lastly, we show that the autocatalyst temporal dynamics can be experimentally tuned by varying PEN-DNA enzyme or dGTP concentrations.

### 4.1.1 Material and methods

#### Detection of DNA concentration

The evolution of DNA concentrations during PEN-DNA reactions is usually monitored thanks to two methods based on fluorescence. The first method is widely used in quantitative PCR (qPCR): an intercalating dye with preferential binding to dsDNA, such as Evagreen (Biotium) denoted ‘EG’ or SYBRGreen I (Invitrogen) denoted ‘SGI’, allows the monitoring of the overall concentration of dsDNA (Figure 4.1 (a)). The second method is based on the labeling of a DNA strand with a fluorescent modification on one of its termini. The fluorescence signal is modulated by the non-radiative energy transfer from the fluorophore to the nucleobases on the complementary strand. This nucleobase quenching (‘N-quenching’ [211]) allows the detection of a specific DNA species as the quenching of the fluorescence increases with the input concentration (Figure 4.1 (b)). In our experiments we do not use this method. Indeed, in the presence of strong anti-oxidant systems (DTT, glucose-oxidase, catalase and glucose, see Table 4.2), N-quenching does not work and the fluorescence intensity remains constant. Thus, we only monitor the total concentration of dsDNA using intercalator dyes. We mostly use SGI, and sometimes EG, this last one having a smaller change in fluorescence in the presence of microtubules. The correspondence between the fluorescence intensity and the DNA concentration is done by titrating a DNA template with its complementary strand input. For example, in Figures 4.1 (c) and (d) the DNA template T1\_20 is titrated by its complementary strand input d-1 (these two DNAs are described in the next paragraph) in the presence of 1X EG. The relation is monotone and presents a saturation for high value of input.

#### Reaction assembly

The autocatalytic reaction is composed of a buffer, PEN-DNA enzymes, DNA strands and dNTPs. We use two different buffers: the canonical buffer of the PEN-DNA toolbox [12] — called here the ‘PEN buffer’ (Table 4.1) — and the active-PEN buffer (Table 4.2) — similar to the active buffer used in the previous chapter (Table 3.2) with some modifications regarding sodium and magnesium ions concentrations.

The final mix is assembled on ice and consists in the buffer supplemented with the PEN-DNA enzymes Nt.BstNBI (referred from now on as ‘NBI’) and the Bst Large Fragment polymerase

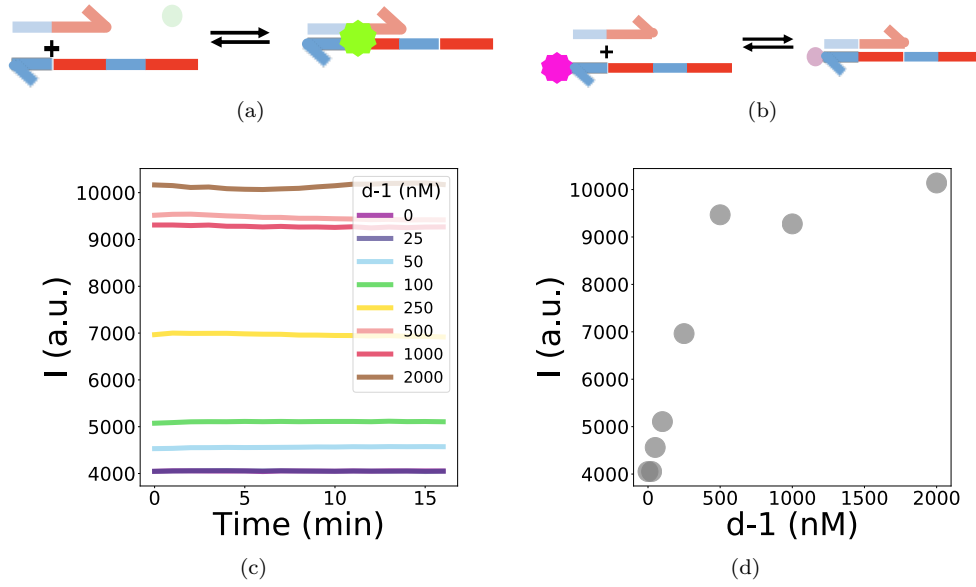


Figure 4.1 | **Monitoring of DNA.** (a) The fluorescence of an intercalator dye increases in the presence of dsDNA. (b) Principle of the N-quenching. Depending on the fluorophore and the number of unpaired bases, the fluorescence can increase or decrease in the presence of the second DNA strand. (c, d) Titration of the DNA template T1\_20 (200 nM) by its complementary input  $d-1$ . This experiment is performed in the active-PEN buffer (Table 4.2) with 0.15X PEM-KOH, 0.60X PEM-NaOH, 12.5 mM  $MgSO_4$  and 1X EG at 25°C.

(referred from now on as ‘BstLF’), the DNA strands of the autocatalytic system and the dNTP, in a final volume of 10  $\mu$ L. The concentrations of BstLF and NBI are given in this thesis in %(v/v) relative to the manufacturer stock (New England BioLabs), they correspond to 8000 units/mL and 10000 units/mL, respectively.

### Monitoring and data processing of the kinetic experiments

Kinetic experiments are performed in a real-time qPCR machine (Biorad CFX96) using the 10  $\mu$ L of solution and a temperature of 24°C.

The dynamics of the autocatalyst is quantified by the time  $\tau_{1/2}$  needed to reach the value 0.5 of the normalized intensity (Figure 4.2 (b)). In an autocatalytic system with a saturation, like for example a carrying capacity  $K$ , the dynamic of production of the input  $A$  is given by

$$\frac{dA}{dt} = kA \left( 1 - \frac{A}{K} \right). \quad (4.1)$$

where  $k$  denotes the kinetic constant. One can deduce analytically the time at half-saturation  $\tau_{1/2}$ , starting from the concentration  $A_0$  when  $K \gg A_0$

$$\tau_{1/2} = \frac{1}{k} \log \left( \frac{K}{A_0} - 1 \right) \approx \frac{1}{k} \log(K) - \frac{1}{k} \log(A_0). \quad (4.2)$$

So, if a system is autocatalytic, the time  $\tau_{1/2}$  should decrease linearly with the inverse of logarithm of the initial concentration. We note that the use of a simple exponential model and a criteria such

Name	Concentration
NaCl	50 mM
Tris-HCl	20 mM
(NH <sub>4</sub> ) <sub>2</sub> SO <sub>4</sub>	10 mM
KCl	10 mM
MgSO <sub>4</sub>	7 mM
Pluronic F-127	2%(w/v)
DTT	3 mM
BSA	0.5 mg/mL

Table 4.1 | **Composition of the PEN buffer.**

Name	Concentration
PEM-KOH <sup>1</sup>	0.6X
PEM-NaOH <sup>2</sup>	0.2X
MgSO <sub>4</sub>	8 mM
Pluronic F-127	1.5%(w/v)
DTT	3 mM
Trolox	1 mM
D-glucose	20 mM
Glucose oxidase	150 μg/mL
Catalase	25 μg/mL
BSA	1 mg/mL
Taxol* (paclitaxel)	20 μM
ATP	1 mM
CK	5 μg/mL
CP	20 mM

Table 4.2 | **Composition of the active-PEN buffer.** The concentrations of the elements highlighted in blue are the result of the buffer optimization presented in the following. <sup>1</sup>80 mM PIPES, 1 mM EGTA, 1 mM MgCl<sub>2</sub>, adjusted with 130 mM KOH to pH 6.9. <sup>2</sup>80 mM PIPES, 1 mM EGTA, 1 mM MgCl<sub>2</sub>, adjusted with 135 mM NaOH to pH 6.9. \*Taxol is used only if the microtubules are taxol-stabilized and not GMPCPP-stabilized.

as ‘the time needed to reach the intensity X’ leads to the same dependence (but with a different constant).

## 4.1.2 Assessing experimental conditions

### Temperature condition

The working temperature of the PEN DNA toolbox is usually set according to the melting temperature of the DNA strands as well as to the optimum temperature of the polymerase and the nicking enzyme, and possibly the exonuclease. This gives a range of temperatures usually comprised between 35°C and 50°C. However, the activity and the lifetime of the active gel is greatly reduced as the temperature increases (Table 4.3). Although not studied in detail, we can speculate on the origin of the drastic lifetime decrease with temperature. It would be because of the weak stability of kinesin motors with temperature (many in vitro experiments are done at room temperature) and because of the formation of pluronic micelles that may lead to a decrease of activity [16].

Temperature	Lifetime (min)
22°C	> 300
30°C	≈ 180
40°C	≈ 20

Table 4.3 | **The lifetime of the active system strongly depends on temperature.**

From this data, it would be difficult to adapt the active gel temperature to reach a temperature higher than 25°C. We thus build an autocatalytic system that works at 25°C. It is based on the nicking enzyme NBI. At this relatively low temperature, the DNAs must have a melting temperature as low as possible. To do so, we use the 10-nucleotide long input ‘d-1’ that is amplified from the 20-nucleotide long template ‘T1\_20’ (Table 4.4). It is an adaptation of the longer (in terms of number of nucleotides) system already used in the lab ‘T1\_22’ [186].

Name	Sequence (5’→3’)	5’ modif.	3’ modif.
d-1	CGAGTCTGTT	∅	∅
T1_20	A*A*CAGACTCGAACA <b>GACTC</b> G	∅	Phosphate

Table 4.4 | **Sequences of the low temperature autocatalyst.** The recognition site for the nicking enzyme NBI is shown in blue.

We test this system at a temperature of 25°C in the PEN buffer (Table 4.1) supplemented with 1X EG, 0.4 mM of each dNTP, 0.2%(v/v) BstLF and 1%(v/v) NBI. The concentration of the DNA template T1\_20 is set to 200 nM. The plots of EG fluorescence versus time for this autocatalyst display the sigmoid shape characteristic of PEN autocatalysis (Figures 4.2 (a) and (b)). We look at the dynamics of the autocatalysis by quantifying  $\tau_{1/2}$  (Figure 4.2 (c)). For d-1 concentrations ranging from 0.2 to 20 nM,  $\tau_{1/2}$  goes from 300 min to 40 min, in an exponentially decreasing manner. We note that at this relatively low temperature of 25°C and during the total duration of the experiment (10 h), neither self-start — when the autocatalytic amplification occurs even in the absence of the input — nor parasitic amplification — when new sequences or set of sequences are amplified with the help of enzymes [291] — is observed.

Figure 4.3 compares our autocatalytic system to the previously designed T1\_22 system by looking at the time  $\tau_{1/2}$  as a function of the working temperature. T1\_22 is a 22-nucleotide-long template that amplifies a 11-nucleotide-long input. As the temperature decreases from 45°C to 30°C, the time to reach half the saturation increases in both systems. As expected  $\tau_{1/2}$  is significantly lower at lower temperature for T1\_20 than for T1\_22. Interestingly, this evolution can provide valuable information on the activation energies of the reaction. Indeed, the use of the Arrhenius’ law  $k = \alpha e^{-E_a/RT}$  in eq. (4.2) leads to the following relation between  $\tau_{1/2}$  and the activation energy  $E_a$  of the reaction

$$\log \tau_{1/2} = \log \gamma + \frac{E_a}{R} \frac{1}{T}, \quad (4.3)$$

where  $\log \gamma$  is a constant and  $R$  the gas constant. We plot  $\log \tau_{1/2}$  against  $1/T$  (Figure 4.3 (b)) and obtain a linear relation with  $E_a(\text{T1}_22) = 205 \pm 10$  kJ/mol and  $E_a(\text{T1}_20) = 130 \pm 15$  kJ/mol.

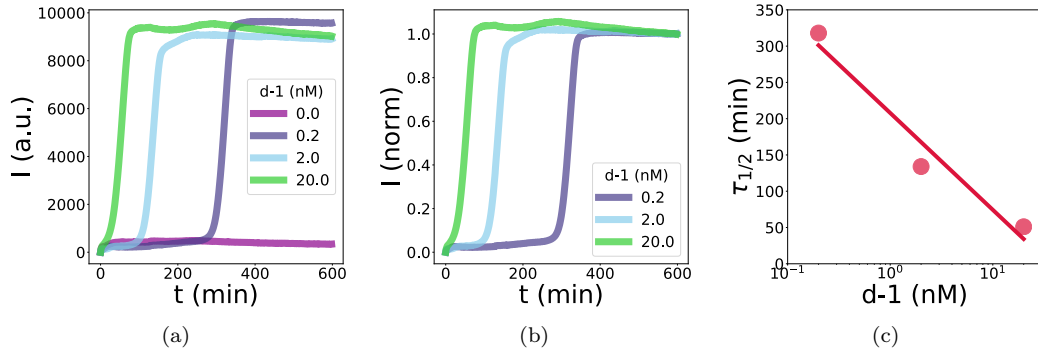


Figure 4.2 | **Dynamics of the T1\_20 autocatalyst system at 25°C.** (a) Raw and (b) normalized amplification curves. (c) Evolution of  $\tau_{1/2}$  according to d-1 initial concentration. This experiment is performed in the PEN buffer (Table 4.1) supplemented with 1X EG, 0.4 mM of each dNTP, 0.2%(v/v) BstLF, 1%(v/v) NBI and 200 nM T1\_20 at 25°C.

As expected,  $E_a(\text{T1}_22) > E_a(\text{T1}_20)$ . These values are of the same order as those obtained for the polymerization of the ssDNA M13mp18 primed with a 24-nucleotide oligomer by the Tli DNA polymerase (92 kJ/mol) [148] or the polymerization of the alternating ssDNA poly[d(A-T)] by the DNA polymerase I (71 kJ/mol) [176].

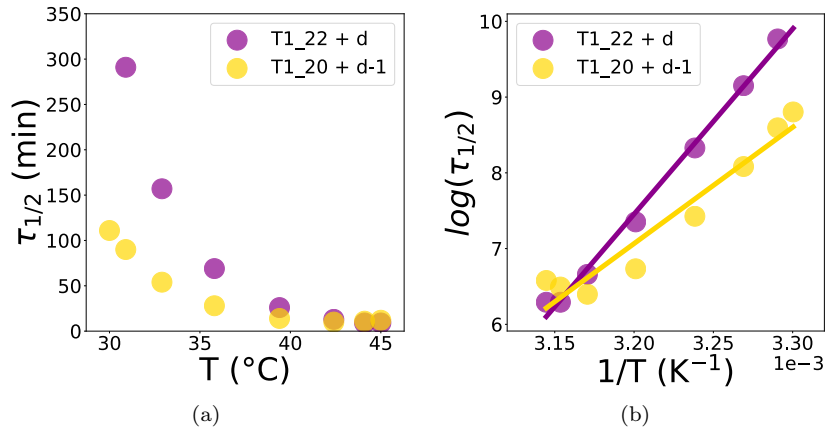


Figure 4.3 | **Effect of the temperature on the autocatalyst dynamics.** (a) The dynamics of the autocatalyst T1\_20 is slowing down as the temperature decreases. However it is still faster than the control T1\_22. (b) The relation between  $\log \tau_{1/2}$  and  $1/T$  is affine as predicted by the Arrhenius' law, with a slope given by the activation energy. This experiment is performed in the PEN buffer (Table 4.1) supplemented with 1X EG, 0.4 mM of each dNTP, 0.2%(v/v) BstLF, 1%(v/v) NBI, 200 nM T1\_20 or T1\_22 and 2 nM of input d-1 or d (the input of the T1\_22).

### Buffer condition

Besides the temperature, we also need to optimize the buffer of the active matter system in order to make the PEN-DNA toolbox functional. Starting from the active buffer used in Chapter 3 (Table 3.2), we create the active-PEN buffer (Table 4.2) by incorporating sodium cations (via

PEM-NaOH) and by adding more magnesium cations.

First, we set the maximum concentration of the PEM to 0.75X and we switch the associated base used to adjust the pH, to a mix between KOH and NaOH. We plot in Figure 4.4 (a)  $\tau_{1/2}$  as a function of the ratio between the concentrations of the two different PEM  $r_{\text{PEM}} = \frac{[\text{PEM-NaOH}]}{[\text{PEM-KOH}]}$ . Thus, we show that sodium ions accelerate the autocatalytic amplification compared to potassium ions. However, in order not to differ too far from the standard buffers of active gels (usually, they do not contain sodium ions), we choose to use the active-PEN buffer with PEM-NaOH = 0.2X and PEM-KOH = 0.6X as depicted in Table 4.2. Such a change represents a gain in time of about 30% compared to an active-PEN buffer in which only PEM-KOH is present.

Secondly, we add magnesium cations to the buffer (Figure 4.4 (b)). The presence of a large amount of  $\text{Mg}^{2+}$  is needed for activity — in the form of  $\text{MgSO}_4$  or  $\text{MgCl}_2$  — compared to previous experiments involving the PEN-DNA toolbox [325, 326]. It is mainly due to the presence of the creatine phosphate which seems to capture magnesium ions. We choose to add 8 mM of  $\text{MgSO}_4$  (in addition to the 1.6 mM  $\text{MgCl}_2$  already existing in the PEM buffers).

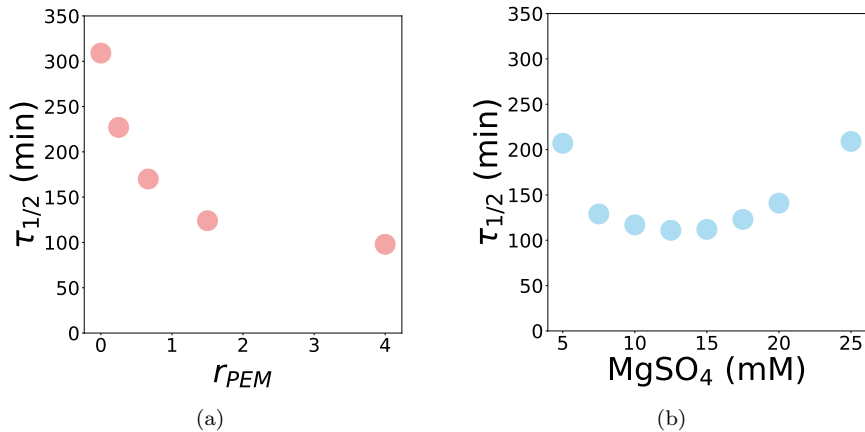


Figure 4.4 | **Effect of the buffer composition on the autocatalyst dynamics.** (a) Evolution of the time  $\tau_{1/2}$  as a function of the ratio  $r_{\text{PEM}}$  between PEM-NaOH and PEM-KOH. The total concentration of PEM is set to 0.75X. This experiment is performed in the active-PEN buffer (Table 4.2) with 6 mM  $\text{MgSO}_4$  and supplemented with 1X EG, 0.5 mM of each dNTP, 0.2%(v/v) BstLF, 2.5%(v/v) NBI, 200 nM T1\_20, 10 nM d-1. (b) Evolution of the time  $\tau_{1/2}$  as a function of  $\text{MgSO}_4$  concentration. This experiment is performed in the active-PEN buffer (Table 4.2) with 0.15X PEM-KOH, 0.60X PEM-NaOH and supplemented with 1X EG, 0.5 mM of each dNTP, 0.2%(v/v) BstLF, 2.5%(v/v) NBI, 200 nM T1\_20, 10 nM d-1. Both experiments are performed at 25°C.

Finally we reach the composition depicted in Table 4.2 and perform the experiments at 24°C. In this chapter we are interested to tune both the dynamics of the autocatalyst and the active gel. To do so, we will supplement the active-PEN buffer with the important parameters shown in Table 4.5. The microtubule and the K401-BCCP cluster concentrations (in a ratio K401-BCCP/streptavidin of 1:1) are related to the gel activity, whereas BstLF and NBI concentrations are related to the autocatalytic amplification. As we will see in the following, dGTP is involved in both systems.



Name	Concentration
Microtubules	0 - 1 mg/mL
K401-BCCP clusters	0 - 100 nM
dGTP	0 - 0,5 mM
BstLF	0 - 1 %(v/v)
NBI	0 - 5 %(v/v)

Table 4.5 | **Parameters used to tune the dynamics of the autocatalyst and the active gel.**

### 4.1.3 The dynamics of the autocatalyst can be tuned by the PEN-DNA enzymes and dGTP concentrations

The dynamics of the autocatalytic amplification depends on several parameters. We test the influence of a few of them: the concentration in polymerase BstLF, nicking enzyme NBI, one dNTP (dGTP) and microtubules. As previously, we quantify the dynamics using the measure of  $\tau_{1/2}$ .

The increase of concentration in the two enzymes BstLF and NBI, leads to a faster dynamics. Thus  $\tau_{1/2}$  ranges from 60 min at the highest concentration we have experimented, to 200 min. In the absence of one of the two enzymes, the fluorescence intensity of the intercalator does not increase: there is no autocatalytic amplification (Figure 4.5 (a)). We will see in the next section that dGTP has an impact in the activity of the gel. For this reason, we evaluate here its influence on the PEN-DNA dynamics. For a concentration of dGTP  $< 50 \mu\text{M}$  (the other dNTP are kept at  $500 \mu\text{M}$ ), the autocatalytic amplification is slowed by a factor 2 to 3 compared to a concentration of  $500 \mu\text{M}$ . Moreover, the presence of taxol-stabilized microtubules does not influence autocatalytic dynamics, in contrast with the presence of GMPCPP-microtubules that slows down the dynamics at low concentration of dGTP (Figure 4.5 (b)).

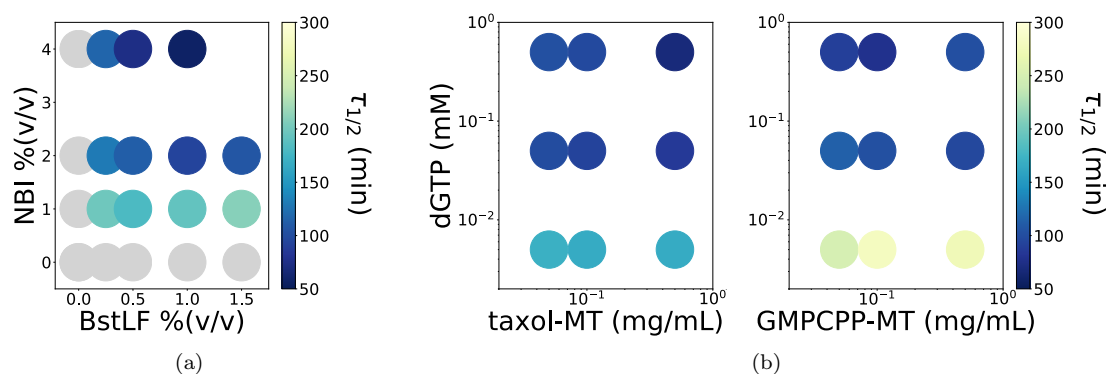


Figure 4.5 |  $\tau_{1/2}$  as a function of BstLF, NBI, dGTP and microtubule concentrations.

(a)  $\tau_{1/2}$  as a function of NBI and BstLF concentrations. Grey circles denote that the autocatalytic amplification is not observed. This experiment is performed in the active-PEN buffer (Table 4.2) supplemented with 0.4X SGI, 0.5 mM of each dNTP, 10 nM K401-BCCP clusters, 100 nM T1\_20, 20 nM d-1. (b)  $\tau_{1/2}$  for taxol-microtubules (left) and GMPCPP-microtubules (right). This experiment is performed in the active-PEN buffer (Table 4.2) supplemented with 0.4X SGI, 0.5 mM of each dNTP except dGTP, 10 nM K401-BCCP clusters, 0.5%(v/v) BstLF, 2.0%(v/v) NBI, 100 nM T1\_20, 20 nM d-1. Both experiments are performed at 24°C.

## 4.2 Propagation of a reaction-diffusion front in an active gel

In a homogeneous environment — such as an aqueous solution [327, 325] or a hydrogel [290] — a reaction-diffusion front emerging from an autocatalytic reaction propagates at constant velocity [63]. However, the propagation of a chemical wave in a complex environment can display a different behavior. For example, frozen fronts with sawtooth shapes arise from the propagation of a chemical front in the disordered flow field of a porous medium [10].

Here we describe for the first time the propagation of a reaction-diffusion front in an active gel. Both the front and the environment are out-of-equilibrium systems with unique patterning properties as we have seen in the previous chapters. We demonstrate that a reaction-diffusion front made of DNA can propagate in an active environment. We then present how to engineer an indirect coupling between the two systems through hydrodynamical interactions — when the active gel contracts globally — or chemical ones — when dGTP resources are low.

Note that these results have been obtained at the end of my PhD work and thus are preliminary. The repetition of some of the experiments presented here is needed in order to formulate a quantitative description.

### 4.2.1 Material and methods

#### Reaction assembly

The reaction is assembled on ice and consists in the active-PEN buffer (Table 4.2) supplemented with the important parameters shown in Table 4.5: K401-BCCP clusters (in a ratio between K401-BCCP and streptavidin of 1:1), BstLF, NBI, dNTP, T1\_20 and d-1. Microtubules are added at the end at room temperature.

#### Channel assembly

We perform the experiments into micro-drilled PMMA channels because the NBI nicking enzyme needed for the autocatalytic amplification tends to attach to the surface of non-coated glass. They are prepared from two PMMA sheets of 5 mm and 150  $\mu\text{m}$  in thickness. On the thick plate we micro-drill a channel of 150  $\mu\text{m}$  in depth and 1 mm in width with a micro-milling machine Minitech CNC, USA. The two plates are then cleaned using deionized water, isopropanol and again water before being air-dried. The two plates are assembled one over the other with a melted strip of parafilm in-between to assure the sealing of the system (Figure 4.6 (a)). For some experiments we also use commercial channels in PMMA with similar dimension (from the manufacturer ChipShop). We do not see any difference between the two devices.

PMMA channels are filled with the solution containing all the elements (active-PEN buffer and tunable parameters) except the DNA input (the total volume is typically between 5 to 10  $\mu\text{L}$ ). The initial condition containing the same solution with 1  $\mu\text{M}$  of DNA input is injected on one side of the channel (in a volume of about 0.5  $\mu\text{L}$ ). The surplus of liquid is carefully absorbed using a clean tissue. Finally both ends of the channel are closed using grease (Figure 4.6 (b)), starting from the side without input to avoid contamination and the appearance of a second front that would propagate in opposite direction to the main front.

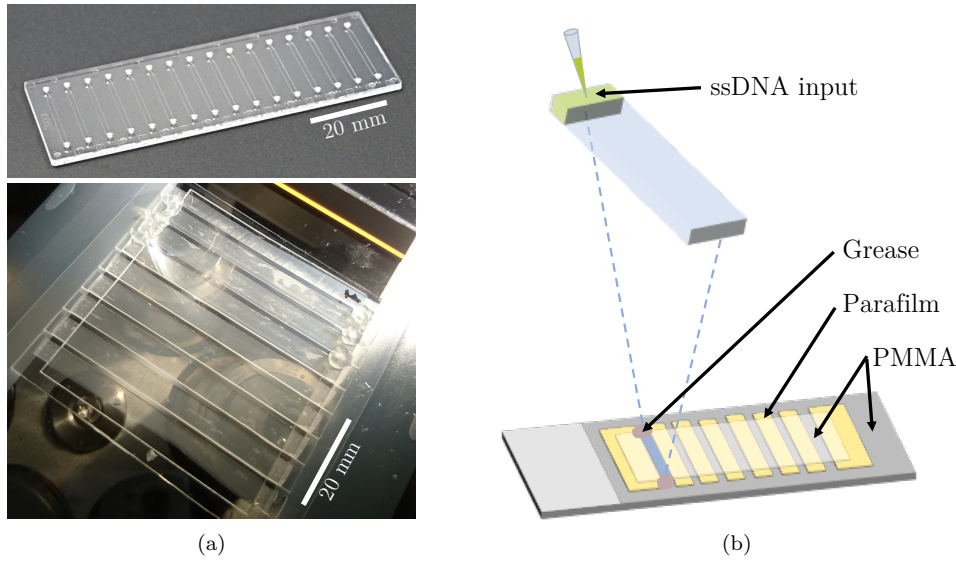


Figure 4.6 | **Pictures and sketch of PMMA channels.** (a) Pictures of commercial (top) and homemade (bottom) PMMA channels. (b) Sketch of a homemade PMMA channel.

### Imaging

Spatial-temporal experiments epifluorescence images are obtained with a Zeiss Observer 7 automated microscope equipped with a Hamamatsu C9100-02 camera, a 10 X objective, a motorized stage and controlled with MicroManager 1.4. Images are recorded automatically every 3 to 6 min using an excitation at 470 nm and at 550 nm with a CoolLED pE2. The temperature is controlled thanks to a transparent TokaiHit ThermoPlate. For optimal thermal conduction, mineral oil is added between the PMMA channels and the thermoplate on the microscope. The set-up is put in place at least 30 min before the filling of the channels in order to be sure that the temperature equilibrium (24°C) is reached.

### Data processing

Time-lapse images from microscopy experiments are treated by ImageJ/Fiji (NIH) and Python. Images of the channels are first cropped manually to remove the edges. We process the images differently for the DNA front (Figure 4.7 (a)) and the microtubules (Figure 4.7 (b)).

- The DNA front images are recorded using a 470 nm excitation. The first image (initial time) is subtracted to the time-lapse in order to remove background fluorescence. Using a Python routine, images are then filtered using a gaussian filter. The intensity is normalized between 0 and 1. Finally, the contrast is adjusted by putting 10% of the highest (respectively lowest) intensity values to 1 (respectively 0). At each time the intensity is averaged along the width of the channel ( $y$  axis). We fit this 1D array of averaged intensity by the expression  $\frac{e^{(x_0-x)/l_0}}{1+e^{(x_0-x)/l_0}}$  where  $x_0$  is the position of the front (the intensity is equal to 0.5) and  $l_0$  its width. Thus we obtain the position of the front as a function of time and we can derive the velocity of the front at each time.

- Fluorescent microtubules are recorded using a 550 nm excitation. In order to quantify the dynamics of active structures we first apply a gaussian filter, normalize the intensity and then we compute the standard deviation of the normalized intensity along the  $y$  axis (width)  $\sigma_{I_y}$  for each position  $x$  of the channel length. For example, if the regime of the active gel is chaotic, the intensity along the width of the channel will be quite homogeneous, thus  $\sigma_{I_y}$  will be low. Now, if the network is contracting locally the intensity will be more localized, leading to a higher standard deviation.

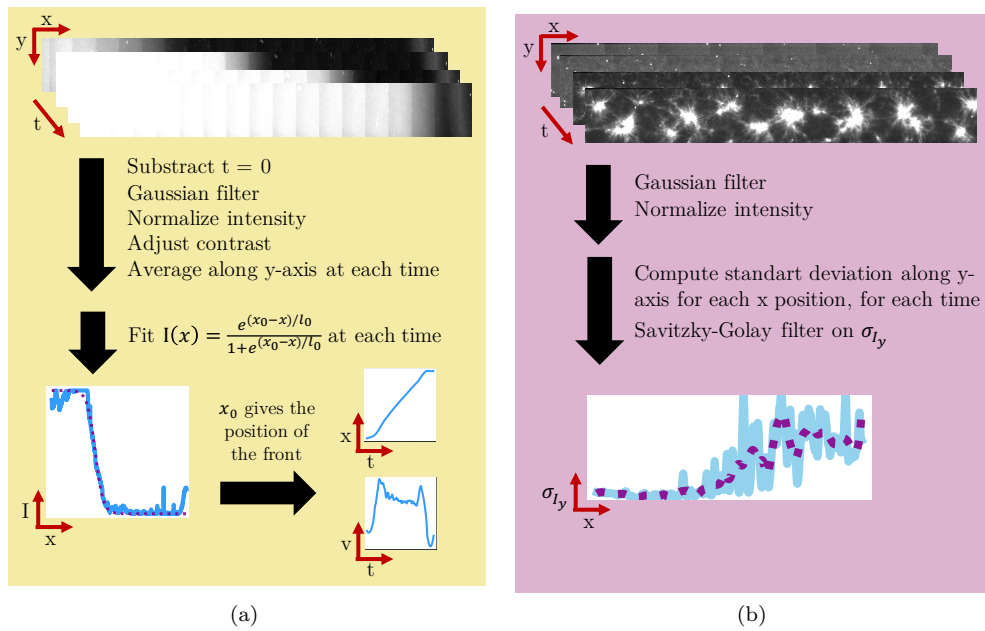


Figure 4.7 | **Data processing.** Analysis of (a) the DNA front and (b) the active gel.

### 4.2.2 RD front and active contractions happen independently

In the previous section, we have considered the temporal evolution of the autocatalytic amplification in a qPCR tube. Presently, we look at the spatio-temporal propagation of the DNA front and the evolution of the active gel. The front is initiated by the addition of 1  $\mu\text{M}$  of the ssDNA input d-1 at one side of the channel. In order to perturb as little as possible the initiation solution — which is exactly the same than in the rest of the channel but supplemented with the ssDNA input — has a small volume of 0.5  $\mu\text{L}$ , compared to the 10  $\mu\text{L}$  total volume. The formation of dsDNA by the input and the template T1\_20 is visible at initial time thanks to the intercalating dye SGI. The parabolic Poiseuille profile of the initial condition rapidly homogenizes laterally and the front begins to propagate. At the same time, taxol-microtubule bundles form bright spots, preceding the local contractions of the active network (Figure 4.8 and Movie A.11 [[↓](#), [🔍](#)]).

We fit the normalized profile of the front by the aforementioned sigmoidal function. From the value of  $x_0$ , we deduce the velocity of the front as a function of time (Figure 4.9 (b, green)). The

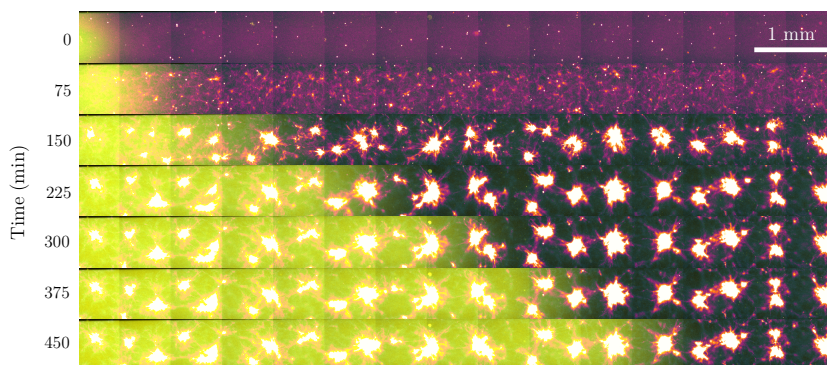


Figure 4.8 | **Reaction-diffusion front in the presence of the active gel.** Time-lapse composite images of the DNA front (yellow) and the active gel (magenta). This experiment is performed in the active-PEN buffer (Table 4.2) supplemented with 0.4X SGI, 0.5% BstLF, 2.0% NBI, 0.5 mM of each dNTP except dGTP, 100 nM T1\_20, 1  $\mu\text{M}$  d-1, 10 nM K401-BCCP and 0.50 mg/mL taxol-microtubules. The final concentration of taxol is here of 2  $\mu\text{M}$  instead of 20  $\mu\text{M}$ . Movie A.11 [[↓](#), [▶](#)].

velocity displays three phases. During the first 15 min, the velocity increases rapidly from 0 to about 15  $\mu\text{m}/\text{min}$ . These first 15 min also correspond to the homogenization time of the Poiseuille profile. Then, from 15 min to 90 min, the velocity of the front continues to increase until it reaches 22  $\mu\text{m}/\text{min}$ . From this time point, the front propagates at 20  $\mu\text{m}/\text{min}$ , value that very slowly decreases over time (it takes more than 6 hours to go from 22 to 18  $\mu\text{m}/\text{min}$ ), before reaching the end of the channel, which leads to an abrupt decrease of the velocity. The speed of this front is lower than the one of a similar front propagating in an aqueous solution at 38°C [325] (about 60  $\mu\text{m}/\text{min}$ ) but comparable to the one propagating without the active gel or in an agarose gel [290] at 44°C. A control experiment performed in the same conditions but without the active gel exhibits the same behavior (Figure 4.9 (b, dashed grey)).

The active contraction of the microtubule network is quantified thanks to the evolution of the distribution of fluorescence intensity. At early times the network is homogeneous: bundles of microtubules are oriented towards the main direction of the channel. After one hour brighter regions and a darker background appear: the distribution of intensities becomes larger. A pertinent measure is the variance of the distribution  $\sigma_{I_y}$  averaged on the  $y$  direction (Figure 4.9 (a)). Along the channel, peaks of  $\sigma_{I_y}$  emerge as proxy of the contractions which condensate the fluorescent microtubules into large bright areas. The global measure of  $\langle \sigma_{I_y} \rangle_x$  (averaged over all the images) shows that the contractions start after about one hour and last for 100 min (Figure 4.9 (b)).

Both reaction-diffusion and active matter systems seem to evolve independently as the control propagating front (without the active gel) proves it.

### 4.2.3 A global contraction accelerates the front

At a lower concentration in K401-BCCP (5 nM), it is possible to recover the corrugated patterns of the active gel described in Section 3.3. However instead of breaking into chaotic flows after the formation of the pattern, the active network once again contracts, but this time in a global manner (Figure 4.10 and Movie A.12 [[↓](#), [▶](#)]). As we will see in the following part, this contraction is due to

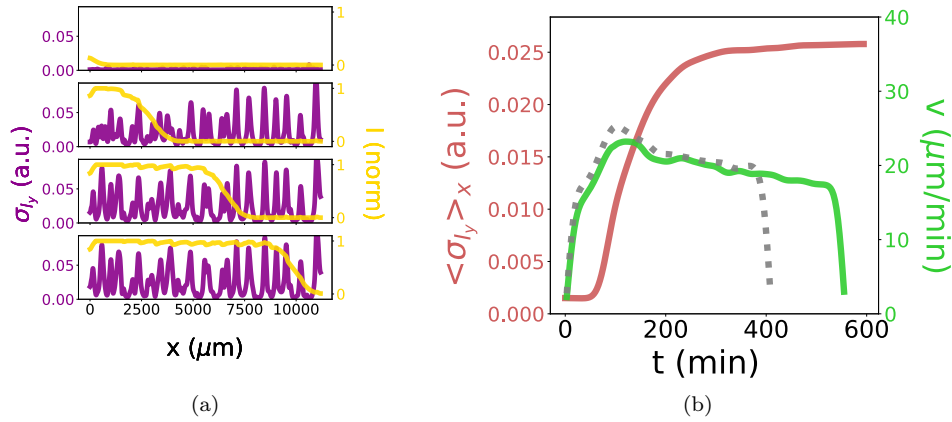


Figure 4.9 | **Quantification of the front and the active gel.** (a) Normalized profile of the reaction-diffusion front (yellow) and variance of the intensity distribution of the fluorescent microtubules  $\sigma_{I_y}$  (purple) at  $t = 0, 150, 300, 450$  min. (b) Evolution of  $v$  the velocity of the front (green) and  $\langle \sigma_{I_y} \rangle_x$  the average of the variance of the fluorescence intensity distribution over the entire field of view. The velocity of a propagating front in the absence of the active gel is plotted in dashed grey. The experimental conditions are the same as those of Figure 4.8.

the presence of dGTP which interacts with microtubules. To the best of our knowledge this behavior has not been described and we can only formulate hypothesis to explain it. Firstly, exchange of nucleotide may occur between GMPCPP and dGTP (the latter being a better promoter of microtubule polymerization [191]) as it occurs with GTP [217]. Moreover, the presence of dGTP leads to a microtubule growth rate similar to the one in the presence of GTP [191, 217]. Secondly, the dynamic instability — the stochastic switching between growth and shrinkage — of microtubules may also play a role. Indeed, GMPCPP is known to suppress dynamic instability [124] contrary to dGTP [217]. Lastly, it has been reported that microtubule binding proteins such as kinesins can discriminate between the nucleotide states of microtubules by having different affinities [193].

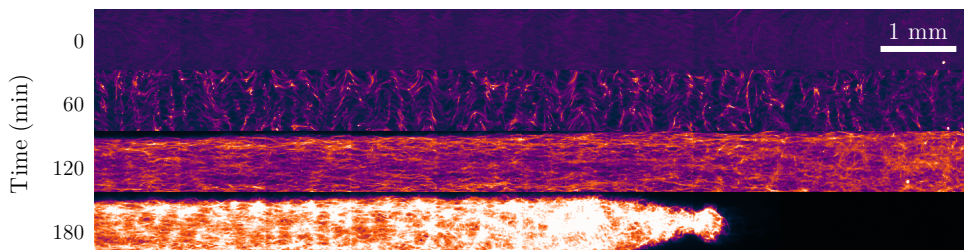


Figure 4.10 | **Corrugated patterns in the presence of a reaction-diffusion front.** This experiment is performed in the active-PEN buffer (Table 4.2) supplemented with 0.4X SGI, 0.5% BstLF, 2.0% NBI, 0.5 mM of each dNTP except dGTP, 100 nM T1.20, 1  $\mu\text{M}$  d-1, 5 nM K401-BCCP, 0.50 mg/mL taxol-microtubules and 20  $\mu\text{M}$  taxol. Movie A.12 [📄, 🎥].

We test the influence of K401-BCCP cluster concentration on the velocity of the reaction-diffusion front (Figure 4.11). As described earlier, the front is propagating in the channel with a velocity that increases during the first 60 min and then slowly stabilizes around 20  $\mu\text{m}/\text{min}$  until

the end of the experiment. Around 60 min — for all conditions — it seems that the velocity exhibits a noisier peak (Figure 4.11 (b)) than the one displayed in Figure 4.9 (b). However, it does not correspond to a characteristic feature of this experiment configuration, and it is mostly due to noisier data. At the highest concentration of K401-BCCP clusters (5 nM), the active gel forms corrugated patterns and after 100 min starts to contract (Figures 4.10 and 4.11 (a, dashed red)). Simultaneously, the reaction-diffusion front accelerates to almost  $50 \mu\text{m}/\text{min}$  probably because of the large motions of matter inside the channel that rapidly transport the DNA input. Finally, at time  $t = 250$  min the front regains its cruising speed of about  $20 \mu\text{m}/\text{min}$  until it reaches the end of the channel.

Thus, even if only about 0.1 to 1% of the volume is composed of active elements (essentially microtubules), it is sufficient to give rise to macroscopic flows that enhance the mixing of components over distances of several millimeters. Thanks to these hydrodynamical flows the active gel influences the reaction-diffusion front.

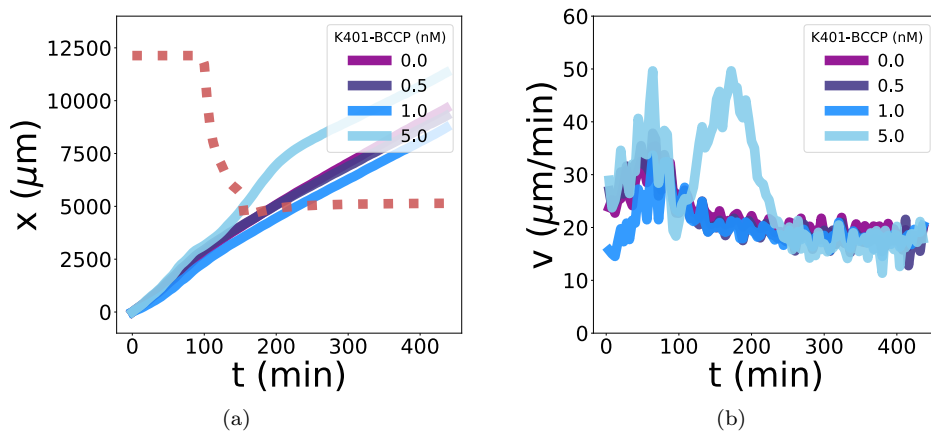


Figure 4.11 | **The velocity of the front does not depend on kinesin concentration.** (a) Evolution of the position of the DNA front as a function of time. The position of the extremity of the contracting active gel is displayed in dashed red. (b) Evolution of the velocity of the DNA front as a function of time. The contraction of the microtubule network (at 5 nM of K401-BCCP) leads to an acceleration of the front starting from 180 min. The experimental conditions are the same as those of Figure 4.10.

#### 4.2.4 Coupling through dGTP resources

In addition to large hydrodynamical flows, the active gel and the front are coupled through dGTP resources. Indeed, the presence of dGTP changes both the behavior of the active gel (Figure 4.10) and the autocatalytic amplification dynamics (Figure 4.5). In this situation, we investigate the influence of dGTP on active gels based on GMPCPP-microtubules, that are supposed to exhibit active flows (Chapter 3.4). To do so, we perform an active gel experiment (in the active buffer (Table 3.2) as in Chapter 3, without the components needed for the reaction-diffusion front) in the presence of each of the four nucleotides (at a concentration of 0.5 mM). Contractions of the active network appear only in the presence of dGTP (Figure 4.12 and Movie A.13 [[↓](#), [▶](#)]) and not in the presence of the three other nucleotides in which active flows are sustained as detailed in Section



3.4. This behavior supports our previously mentioned hypothesis about the effects of dGTP on microtubules. Knowing that, we explore the regime of low dGTP concentration in order to recover the chaotic flows in the presence of the reaction-diffusion front.

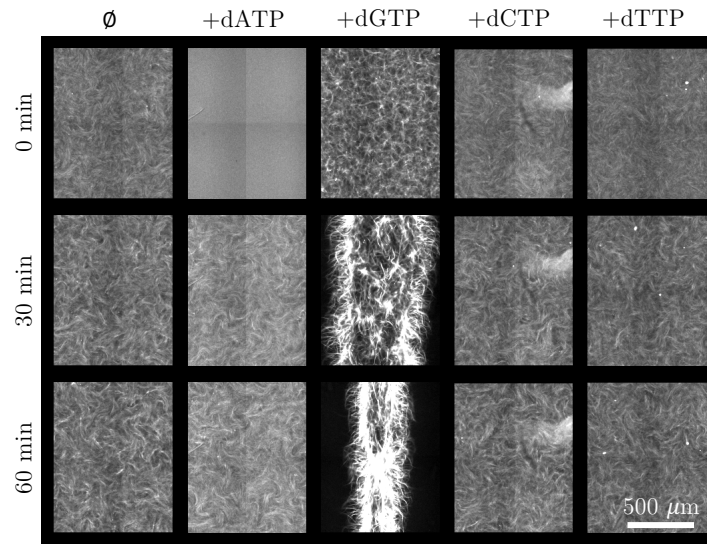


Figure 4.12 | **Influence of dNTP on internally driven chaotic flows.** The active fluid collapses in the presence of 0.5 mM of dGTP. This experiment is performed at 22°C in the active buffer (Table 3.2) supplemented with 25 nM K401-BCCP and 0.50 mg/mL GMPCPP-microtubules. Movie A.13 [[↓](#), [🎥](#)].

For dGTP concentrations below 25  $\mu\text{M}$ , the reaction-diffusion front is not sustained and stops (Figure 4.13 and Movie A.14 [[↓](#), [🎥](#)]). At 2.5  $\mu\text{M}$  of dGTP, the front slows down passing from 20 to 10  $\mu\text{m}/\text{min}$  at the end of the experiment. As expected, no front is observed in the absence of dGTP. At a higher concentration of dGTP, the front propagates in the chaotic environment but the velocity is not as constant as in the case of a contracting network. For example, in the presence of 25  $\mu\text{M}$  of dGTP, the velocity varies from 20  $\mu\text{m}/\text{min}$  after 30 min, to almost 40  $\mu\text{m}/\text{min}$  at the end of the experiment (8 h) (Figure 4.14 (b, green)). In control experiments — without the active gel — the front is propagating at a constant velocity of 25  $\mu\text{m}/\text{min}$  (Figure 4.14 (b, dashed grey)) for dGTP concentrations superior to 25  $\mu\text{M}$  (after its initial increase).

From the point of view of the active gel, a change in dGTP concentration in the presence of the reaction-diffusion front — that also used dGTP to polymerize new DNA strands — leads to spatially inhomogeneous channels (Figure 4.13 and Movie A.14 [[↓](#), [🎥](#)]). As before, the bundles are initially aligned in the direction of the channel. With no dGTP we recover the turbulent regime which is sustained for a relatively long time ( $> 4$  hours). Increasing dGTP concentration to 2.5  $\mu\text{M}$  leads to the same behavior. However, after some time, the right part of the channel begins to exhibit some contractions, although the regime is still turbulent. We then observe a spatial difference of gel activity, depending on the initial presence of the DNA front. At a higher concentration in dGTP (25  $\mu\text{M}$ ), no more flows are observed, only contractions. However, here again a spatial difference appears between the left and the right parts of the channel: at the point where the front

starts, the network is less contracted. At  $dGTP = 250 \mu M$ , the network organizes spaced asters but does not have enough force to form separated structures. They are uniformly distributed in the channel. We interpret the emergence of these patterns as a competition mechanism between the reaction-diffusion front and the active gel, since both systems use dGTP to self-organize.

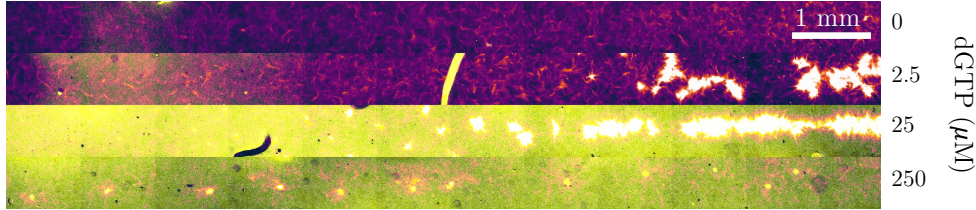


Figure 4.13 | **Different dGTP concentrations lead to inhomogeneous patterns.** Composite images of the DNA concentration (yellow) and the active gel (magenta) for different dGTP concentrations after 600 min. This experiment is performed in the active-PEN buffer (Table 4.2) supplemented with 0.4X SGI, 0.5% BstLF, 2.0% NBI, 0.5 mM of each dNTP except dGTP, 100 nM T1\_20, 1  $\mu M$  d-1, 25 nM K401-BCCP and 0.50 mg/mL GMPCPP-microtubules. Movie A.14 [[↓](#), [▶](#)].

As before, the measure of the local  $\sigma_{I_y}$  quantifies the active gel (Figure 4.14 (b)). In order to smooth its value,  $\sigma_{I_y}$  is locally averaged over 150  $\mu m$ . When the concentration in dGTP is null or is larger than 250  $\mu M$ , the active gel has a homogeneous activity along the channel: turbulent flows or uniformly distributed asters. In terms of  $\sigma_{I_y}$ , this translates into a low value of  $\sigma_{I_y}$  along the channel. In contrast, at intermediary concentrations in dGTP, the patterning of the channel becomes inhomogeneous:  $\sigma_{I_y}$  starts to increase from 60 min in the right part of the channel, meaning that the active gel forms dense areas where bundles of microtubules contract (Figure 4.14 (b)). Interestingly, at these intermediary dGTP conditions, local contracted structures move and are transported by the active turbulent ‘bath’.

We build a simple phenomenological model to account for the inhomogeneous patterning of the channel by the active gel, when dGTP resources are low. We consider the evolution of the three following variables: the concentration in DNA input denoted ‘A’, the concentration in dGTP denoted ‘G’ and the state of the active gel denoted ‘S’. This state can either correspond to chaotic flows or a contracting network, when  $S = 0$  or  $S = 1$ , respectively. The model is composed of reaction-diffusion equations that describe the two processes which consume dGTP. Indeed, dGTP is used by the autocatalytic amplification to make more DNA input, and it is used by the active gel as a means to go from chaotic flows to a contracting network. We take into consideration that the rate of dGTP consumption should saturate as well as the values of S (which saturates at 1) and A (because without it, the system would grow exponentially). Lastly, because the active gel rapidly goes from chaotic flows to a contracting network, we describe the increase of S as a

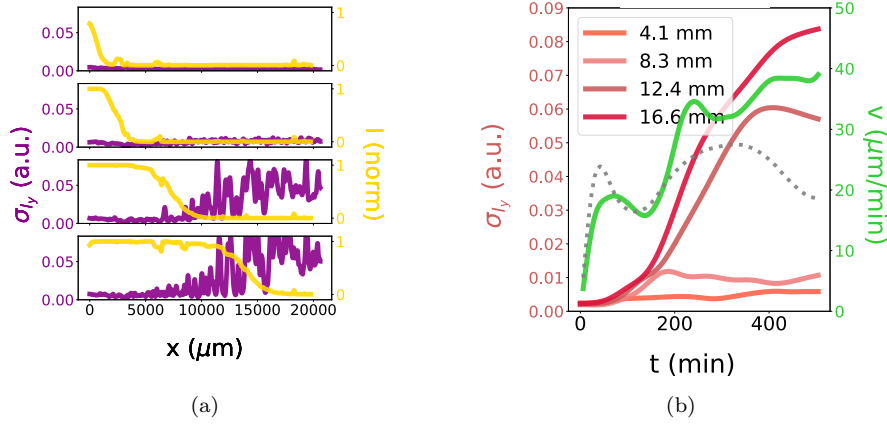


Figure 4.14 | **Evolution of the inhomogeneous patterning of the active gel in the presence of 25  $\mu\text{M}$  of dGTP.** (a) For dGTP = 25  $\mu\text{M}$  a reaction-diffusion front propagates in an inhomogeneous active gel environment created by the lack of dGTP resources. Profiles are taken at  $t = 0, 200, 400$  and  $600$  min. (b) Evolution of  $v$  the velocity of the front (green) and  $\sigma_{I_y}$  the average of the variance of the fluorescence intensity distribution for different positions along the channel. The velocity of a propagating front in the absence of the active gel is plotted in dashed grey. The experimental conditions are the same as those of Figure 4.13.

quadratic amplification. We finally reach the following set of differential equations:

$$\frac{\partial A}{\partial t} = k_0^A A \left(1 - \frac{A}{K_A}\right) \frac{G}{G + K_G} + D_A \frac{\partial^2 A}{\partial x^2}, \quad (4.4)$$

$$\frac{\partial G}{\partial t} = -k_0^A A \left(1 - \frac{A}{K_A}\right) \frac{G}{G + K_G} - k_0^S S^2 \left(1 - \frac{S^2}{K_S}\right) \frac{G}{G + K_G} + D_G \frac{\partial^2 G}{\partial x^2}, \quad (4.5)$$

$$\frac{\partial S}{\partial t} = k_0^S S^2 \left(1 - \frac{S^2}{K_S}\right) \frac{G}{G + K_G}. \quad (4.6)$$

We simulate these equations using the kinetic constants  $k_0^A = 1$  and  $k_0^S = 0.5$ , the equilibrium constants  $K_A = 50 \mu\text{M}$ ,  $K_G = 10 \mu\text{M}$  and  $K_S = 1$ , and the diffusion constants  $D_A = 1$  and  $D_G = 10$ . Note that these values are chosen manually but in order to have a complete picture of the system, these parameters should be derived from the systematic variations of experimental parameters. The simulation is performed on a 1D array of size 80 with fixed boundary conditions. The spatial step is  $dx = 1$  and the time step is set to  $dt = 0.01$ . Initially  $S = 0.1$  and  $G = 0.001, 2.5, 25$  or  $250 \mu\text{M}$  and they are both homogeneously distributed.  $A$  is initialized by an exponential profile on one side of the 1D array. The results of the simulation are represented as kymographs (Figure 4.15 (a)). A kymograph is an intensity versus time versus space 3D plot. At each time point the intensity profile along the  $x$  axis makes one horizontal line in the kymograph. Time goes vertically from top to bottom. A front of  $A$  is able to propagate for  $G$  values greater than  $25 \mu\text{M}$ . Additionally, the state  $S$  goes from 0 to 1 for the same range of  $G$ . At the intermediary value  $G = 25 \mu\text{M}$ , the state  $S$  is not homogeneous in space and exhibits a spatial transition between the left part and the right part of the axis. We can also note that the velocity of the front is not constant over time but has two different velocities, the second one being greater than the first one.

The time of change in velocity coincides with the time of the transition of  $S$  from 0 to 1, suggesting that  $G$  is not used anymore by  $S$  but only by the front of  $A$ .

The model is in qualitative agreement with the experiments displayed in Figure 4.13 and Movie A.14 [↓, ▶]. They are plotted as kymographs in Figure 4.15 (b). These are built from the evolution of the SGI fluorescence intensity (averaged along the width of the channel) and  $\sigma_{I_y}$  which describes the state of the active gel. Interestingly, we observe the same break in velocity at the transitional time when the gel goes from chaotic flows to a contracting network.

Further investigations are necessary to conclude on the accuracy of the model. For instance, the system could be studied by varying the gel activity — through the K401-BCCP concentration — and the front velocity — through the PEN-DNA enzymes concentrations.

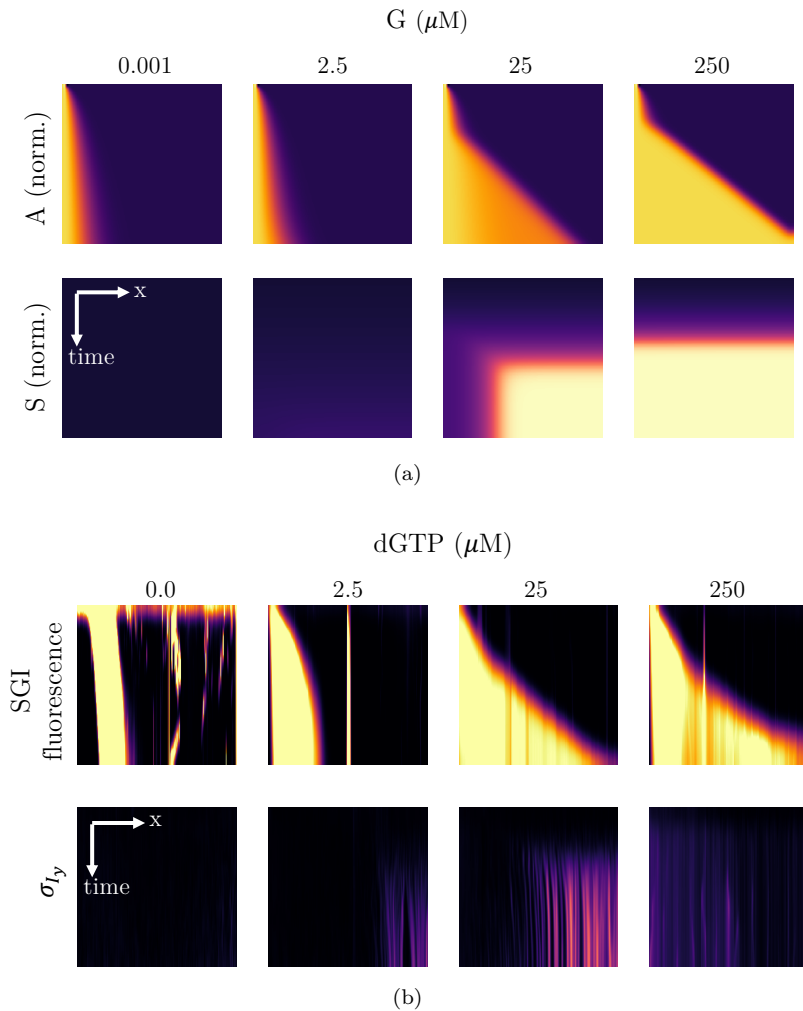


Figure 4.15 | **Qualitative comparison between experimental and simulated kymographs as a function of dGTP concentration.** (a) Normalized simulated kymographs of  $A$  and  $S$ . Bright colors represent values near 1. Total time corresponds to 5000 iterations. (b) Kymographs (space versus time) of the PEN-DNA front and the active gel experiments displayed in Figure 4.13, through the measures of SBI intensity averaged along the width  $y$  and  $\sigma_{I_y}$ , respectively. Bright colors represent high values of fluorescence or  $\sigma_{I_y}$ . Total time is 10 h, and the total length is 17 mm.

We have demonstrated that a DNA reaction-diffusion front can propagate in an active gel environment. Although the two out-of-equilibrium systems operate independently, they can interact when certain conditions are met: large internal flows or competition for dGTP resources. It will be interesting to explore the space of tunable parameters for both the front and the active gel in more details. For example, it could be interesting to study what is happening when the concentration in microtubules is greatly increased and the environment becomes denser. Direct chemical coupling could also be investigated: what are the effects of the attachment of DNA strands — involved in the autocatalytic reaction (mostly the templates) — on kinesins (the method is described in Section 4.4) or on microtubules? In the next section, we propose an experimental system in which the hydrodynamical coupling between the DNA front and the active gel can be further examined. More particularly, we look at the turbulent regime thanks to the design of an autocatalyst where dGTP is not needed anymore.

### 4.3 Hydrodynamical coupling: design of a three-letter autocatalyst

The presence of dGTP radically changes the behavior of the reaction-diffusion front and the active gel. In this configuration only contractions are observed at longer time and ATP-driven chaotic flows are not sustained. However, it would be interesting to create a tunable reaction-diffusion-advection system that would exhibit complex dynamics and patterning properties. Active gels can flow either locally [241] or in a coherent manner over large distances [319]. Furthermore, in idealized cases the coupling of hydrodynamics with reaction-diffusion chemical systems could lead to a richer dynamics even for simple chemical reactions [30]. In this section we expose the preliminary results of the design on an autocatalyst that works without dGTP.

#### 4.3.1 Design of an autocatalyst without dGTP

In order to get rid of the local and global contraction regime and restore the chaotic flows, we have to remove dGTP from the mix. To this end we have to design DNA strands that do not use dGTP during the reaction: it means that the only nucleobases allowed in the sequence of the DNA templates are A, T and G and not C. We have found a single commercial nicking enzyme which can recognize a target sequence without C on the template: Nt.CviPII (New England BioLabs). One has to be careful in the design of an autocatalyst with this enzyme since it can cut the ‘top’ strands sequences CCT, CCG and CCA. According to the manufacturer CCT is cut less efficiently than CCG and CCA. Knowing that, we design the autocatalyst ‘LT2LT\_20’ which catalytically amplifies the 10 nucleobase-long input ‘LT\_10’ (Table 4.6).

Name	Sequence (5'→3')	5' modif.	3' modif.
LT_10	CCAATCTATT	∅	∅
LT2LT_20	AATAGAT TGG AATAGATTGG	∅	Phosphate

Table 4.6 | **Sequences of the autocatalyst without dGTP (LT2LT\_20).** The recognition site for the nicking enzyme Nt.CviPII is shown in blue.

Using the same conditions than before (but without dGTP), we study the temporal dynamics of this new autocatalyst, and its ability to form reaction-diffusion fronts in the absence and in the presence of microtubules and kinesin clusters.

#### 4.3.2 Temporal dynamics

We first test the temporal dynamics of this new autocatalytic system by recording the fluorescence intensity in a qPCR machine. We tune the range of the nicking enzyme Nt.CviPII from 0 to 0.5%(v/v) (0 to 10 units/mL) (Figure 4.16 (a)). In this range, the rate of amplification largely varies. It saturates for a concentration greater than 0.5%(v/v). The addition of K401-BCCP clusters greatly modifies the dynamics of the autocatalyst (Figure 4.16 (b)) and has three main effects. Firstly, the kinetics is slowed down and appears more linear than before, especially for kinesin concentrations greater than 25 nM. Secondly the transition between the regime of amplification and the regime of saturation becomes sharper, suggesting that a heterogeneity appears in the mix.

Lastly the final level of fluorescence decreases with the increase in cluster concentration. For a K401-BCCP concentration of 50 nM, no more amplification is observed.

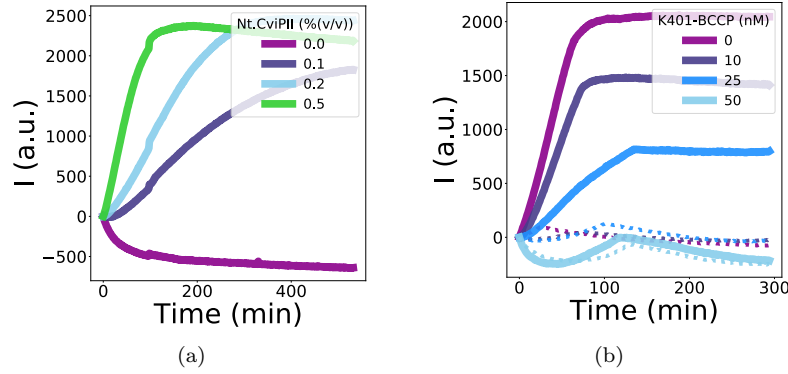


Figure 4.16 | **Bulk dynamics of the LT2LT system as a function of Nt.CviPII and K401-BCCP concentrations.** (a) Range of Nt.CviPII. This experiment is performed in the active-PEN buffer (Table 4.2) supplemented with 1X EG, 0.3% BstLF, 0.5 mM of each dNTP except dGTP, 200 nM LT2LT<sub>20</sub> and 25 nM LT<sub>10</sub>. (b) Range of K401-BCCP. Dashed lines correspond to the negative control without the ssDNA input LT<sub>10</sub>. This experiment is performed in the active-PEN buffer (Table 4.2) supplemented with 1X EG, 0.3% BstLF, 0.6% Nt.CviPII, 0.5 mM of each dNTP except dGTP, 200 nM LT2LT<sub>20</sub> and 25 nM LT<sub>10</sub>. Both experiments are performed at 24°C.

### 4.3.3 Propagation of fronts

We now look at the reaction-diffusion dynamics of the autocatalytic system using the set-up described in the previous section (Section 4.2). The channel is filled with the solution containing all the components except the ssDNA input LT<sub>10</sub>. This latter is added at one of the ends of the channel. The experiments are performed in PMMA channels (Section 4.2.1).

We observe the propagation of a front. It exhibits two phases (Figures 4.17 (a) and (b)). The first one consists in a rapid acceleration of the front (up to 100  $\mu\text{m}/\text{min}$ ) during the first 20 min of observation. It is followed by a decrease of velocity, until the system settles in its cruising speed of about 20  $\mu\text{m}/\text{min}$ . The velocity remains constant until the front reaches an edge of the channel. Using longer channels we notice that self-start appears after about 10 h. The system is kept out-of-equilibrium for a least 16 h (the maximum duration of the experiment we have performed). However, as the 0D case, we observe that K401-BCCP has a great influence on the front pattern. Indeed, the presence of kinesin clusters leads to the immediate formation of visible precipitates (of several  $\mu\text{m}$  in size) (Figure 4.17 (c) and Movie A.15 [[↓](#), [🎥](#)]) that can be quantified by the mean raw fluorescence intensity  $\langle I \rangle$  of the channel and its standard deviation  $\sigma_I$ , in the region where the input DNA is not present. A too high concentration in kinesins is able to stop the front after about 100 min, suggesting that precipitates are composed of essential elements needed for the observation of the reaction-diffusion fronts such as DNA and PEN-DNA enzymes. Furthermore, in the presence of microtubules, no motion is observed probably because these precipitates also contain kinesin clusters.

These preliminary results show the importance of identifying, in the future, the reasons of

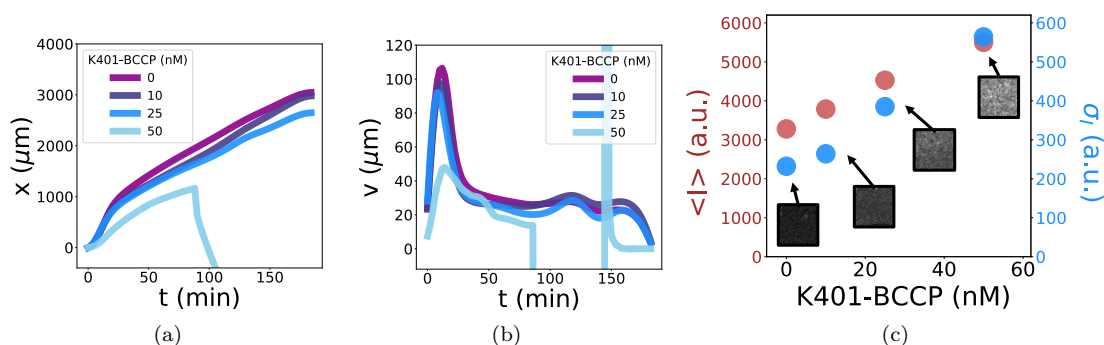


Figure 4.17 | **Propagation of a front (LT\_10) in the presence of K401-BCCP.** (a) Evolution of the position of the DNA front as a function of time. (b) Evolution of the velocity of the DNA front as a function of time. (c) The formation of precipitates is quantified by the mean raw fluorescence intensity  $\langle I \rangle$  of the channel and its standard deviation  $\sigma_I$ , in the region where the input DNA is not present. This experiment is performed at  $24^\circ\text{C}$  in the active-PEN buffer (Table 4.2) supplemented with 1X EG, 0.3% BstLF, 0.6% Nt.CviPII, 0.5 mM of each dNTP except dGTP, 200 nM LT2LT\_20 and  $1 \mu\text{M}$  LT\_10. Movie A.15 [[↓](#), [▶](#)].

the formation of these precipitates, hypothetically composed — among others — of kinesins and nicking enzymes. For instance, is it due to the presence of biotin or streptavidin? In all cases, controls with other kinesin clusters (K430-HSNAP and K430-FLAG-SNAP) should be performed as well as adjustments of the buffer. Resolving these issues may allow the creation of a unique reaction-diffusion-advection system with tunable properties.

Hydrodynamical interactions are one way to couple self-organized mechanisms. In the next section we are going to explore a second manner to achieve such a coupling using the chemical linking between DNA and motors.



## 4.4 Chemical coupling: towards active matter controlled by DNA

It is possible to go further in the interaction between reaction-diffusion patterns and active matter by considering a direct chemical coupling. A system could then chemically act on the other by autonomously creating or destroying a link between them, without the intervention of an external operator. For example a DNA program made with the PEN-DNA toolbox could produce a ssDNA ‘linker’ that would be able to hybridize with a DNA-modified protein and create a multimeric version of this protein. This approach has been applied to the controlled aggregation of passive colloidal particles [329, 326]. Using the same approach in an active gel, a propagating front with a linker production could potentially lead to contractions or active flows. In particular, the aggregating state of molecular motors could be internally controlled or DNA linkers could induce the formation of microtubule bundles instead of depletion forces due to the presence of a depleting polymer. Furthermore, the active gel would influence the DNA reaction-diffusion pattern by, for example, the presence of hydrodynamical interactions due to a global contraction or active flows.

In this section we present our progress regarding the coupling of DNA and kinesin motors thanks to the specific reaction between a benzylguanine-modified DNA and the SNAP-tag of the kinesins K430-FLAG-SNAP and K430-HSNAP. First, we detail the methods of the chemical coupling and we then mention the experiments that could be done using this direct coupling, in particular in gliding assay experiments.

### 4.4.1 Procedures to attach DNA on kinesin

DNA has been coupled to molecular motors using different strategies such as the reaction between a maleimide group and a cystein residue [182], zinc fingers that attach to dsDNA [314] or the use of the biotin-neutravidin interaction [244].

Here we use another method based on the specific reaction between a protein tag and a substrate: the SNAP-tag reaction on a benzylguanine (BG) substrate [141]. This method has been described in Section 3.1.1. As a reminder, it is based on a variant of the human O6-alkylguanine-DNA-alkyltransferase which specifically interacts with a substrate conjugated to a BG group. Thus, virtually any molecule which contains a BG group can be covalently attached. In order to attach DNA, we use a ‘linker’ molecule holding two reactive groups: one BG group (reaction with the SNAP-tag) and one N-hydroxysuccinimide (NHS) group (reaction with an amino-modified DNA), the BG-GLA-NHS molecule. DNA has been successfully attached to kinesins [48, 73], dyneins [48] and myosins [104] using this method.

In the next two parts we are going to detail the experimental protocols. We first modify DNA into a DNA-reactive substrate for SNAP protein (Figure 4.18, step i.). We then attach this modified DNA to the the SNAP-labeled kinesin K430-FLAG-SNAP that we have purified in Section 3.1.1 (Figure 4.18, step ii.).

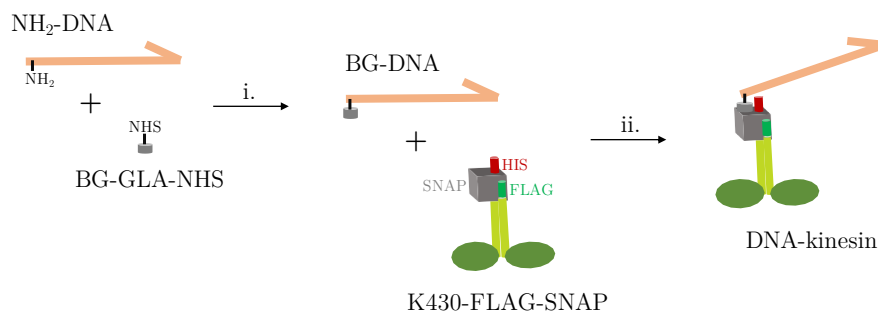


Figure 4.18 | **Strategy to attach DNA on SNAP-tag kinesin motors.** Amino-modified DNA is first modified using the linker molecule BG-GLA-NHS and the reaction between the amino group and the NHS ester group (step i.). After purification the newly formed BG-DNA is covalently attached to the kinesin via the SNAP-tag (step ii.).

### From amino-DNA to BG-DNA

The coupling is based on the reaction between the NHS-ester and the amino group of the modified bases. The reaction between BG-GLA-NHS and a DNA containing a modified base (the amino group is attached to the base thanks to a C6-aminolink, ‘six carbon atoms’) is depicted in Figure 4.19.

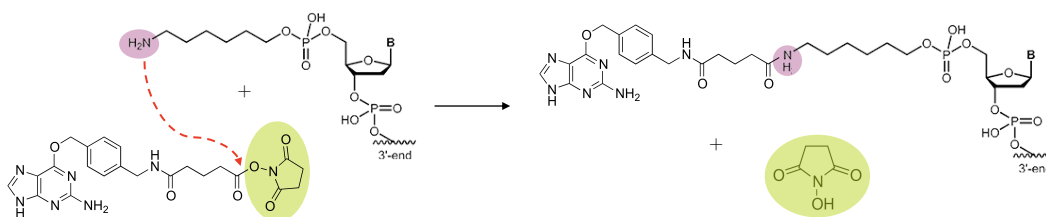


Figure 4.19 | **Chemical reaction between the amino-DNA and BG-GLA-NHS.** NHS-ester and amino groups are highlighted in green and purple respectively.

BG-GLA-NHS is ordered from New England BioLabs and arrives as a lyophilized powder that has to be kept at  $-20^{\circ}\text{C}$ . Before use, it is diluted in DMSO to a concentration of 20 mM and kept at  $-20^{\circ}\text{C}$ . It then has to be used within a month. Amino-DNAs are ordered from Biomers with 5' or 3' C6-aminolink modifications. We also design strands that contain the fluorescent dyes Cy3 and Cy5 (Table 4.7). They are kept at  $-20^{\circ}\text{C}$  in water.

Name	Sequence (5'→3')	5' modif.	3' modif.
NH <sub>2</sub> -Lk	GGATGAGTAGATGGT	Aminolink-C6	Phosphate
Li-NH <sub>2</sub>	G*T*G*GGAGAATGAAGT	∅	Aminolink-C6
NH <sub>2</sub> -Lk-Cy5	GGATGAGTAGATGGT	Aminolink-C6	Cy5
Cy3-Li-NH <sub>2</sub>	G*T*G*GGAGAATGAAGT	Cy3	Aminolink-C6

Table 4.7 | **Sequences of amino-modified DNA.** Asterisks stand for phosphorothioate backbone modifications.

The coupling reaction is performed by mixing 50  $\mu\text{M}$  of amino-DNA and BG-GLA-NHS (ranging

from 0 to 5000  $\mu\text{M}$ ) in 50 mM HEPES pH 8.5, at 30°C for 2 h. We analyze the reaction on a 20% denaturing polyacrylamide electrophoresis. An excess of 1:100 in BG-GLA-NHS is necessary to achieve a total reaction (Figure 4.20 (a)). We purify the newly formed BG-DNA from the excess of BG-GLA-NHS using filters with a molecular weight cut-off of 3 kDa (the DNA strands that we use are superior to 5 kDa in weight and BG-GLA-NHS is 0.5 kDa). In order to achieve a proper purification, we have to do multiple rounds of filtration (Figure 4.20 (b)) using 0.5 mL of  $\text{H}_2\text{O}$  each time. In order to know the number of filtrations needed, we follow the evolution of the UV-visible absorption of the concentrate containing the BG-DNA and the filtrate containing the excess of BG-GLA-NHS. The molecule BG-GLA-NHS has a strong absorption at 275 nm. The follow-up of the absorbance at 256 nm and 275 nm (Figure 4.20 (c)) shows that a least 5 rounds of filtration are needed to divide the initial absorption of the filtrate (quantified by  $r_A$  the ratio between the absorbance and the initial absorbance) by a factor 100. BG-DNA can be conserved at -20°C for several weeks. Once the amino-DNA has been converted into a BG-DNA it can be used to label the SNAP-tag kinesin.

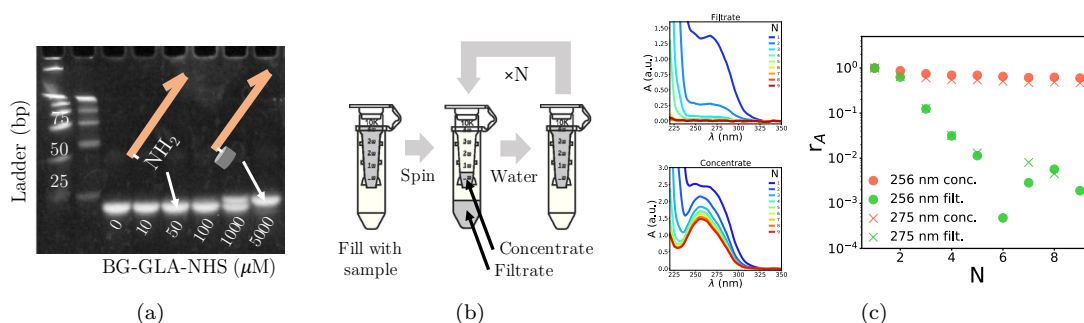


Figure 4.20 | **Analysis and purification of the reaction between an amino-DNA and BG-GLA-NHS.** (a) Polyacrylamide gel of the titration reaction between an amino-DNA and BG-GLA-NHS. A shift equivalent to one base pair (bp) is visible between the amino-DNA and the BG-DNA. (b) Removal of the excess of BG-GLA-NHS is performed using a filter with a molecular weight cut off of 3 kDa. (c) Evolution of UV-visible spectra and the absorbance ratio  $r_A$  of the concentrate and the filtrate after the  $N^{\text{th}}$  round of filtration. After  $N = 5$  rounds the absorption of the filtrate is divided by 100.

### Formation of the DNA-kinesin

The second step is the formation of the DNA-kinesin from the reaction between the BG group of the modified DNA and the SNAP-tag of kinesin (Figure 4.21).

The reaction is performed in a 1X PBS (phosphate-buffered saline) buffer supplemented with 1 mM DTT at 30°C for 2 h. BG substrate is in excess compared to the kinesin: usually 5-10  $\mu\text{M}$  of substrate is used for 100-500 nM of SNAP-tag kinesin.

We first test the functionality of the SNAP-tag present in the K430-FLAG-SNAP. To do so we use the commercial BG small fluorescent substrate SNAP-Vista Green (New England BioLabs). This substrate is derived from the fluorescein and is fluorescent upon UV illumination. We combine it with K430-FLAG-SNAP which has been only HIS-tag purified (so the mix is composed of K430-FLAG-SNAP and K430-HSNAP) (Figure 4.22 (a), lane 1) or which has been HIS-tag and then

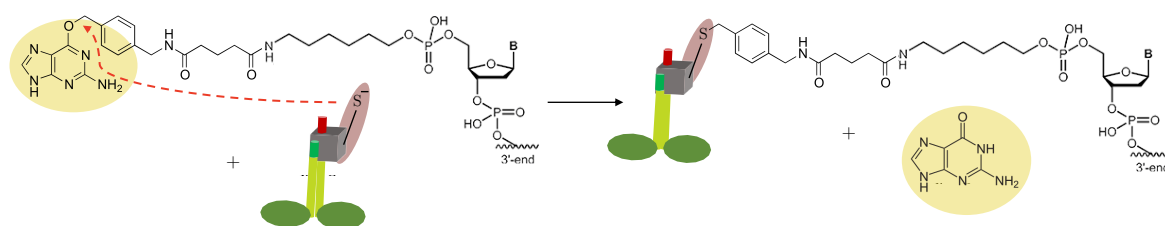


Figure 4.21 | **Chemical reaction between the BG-DNA and kinesin K430-FLAG-SNAP.** BG group and SNAP-tag end are highlighted in yellow and violet respectively.

FLAG-tag purified (the mix is composed of K430-FLAG-SNAP only) (Figure 4.22 (a), lane 2). Thanks to the fluorescence of the BG substrate, we are able to show that the SNAP-tag of K430-FLAG-SNAP is functional. Indeed only the SNAP-tag arm of the kinesin becomes fluorescent. We also notice that in the first case, the protein band at 20 kDa is due to the independent production of a SNAP-tag (BG reactive), as described in Section 3.1.

Then, the reaction between BG-modified DNA is performed. Here, we use the two DNAs  $\text{NH}_2\text{-Lk-Cy5}$  and  $\text{Cy3-Li-NH}_2$  which have been transformed into  $\text{BG-Lk-Cy5}$  and  $\text{Cy3-Li-BG}$ . The reaction takes place in the same conditions as before, and once again, we analyze the output on a SDS-PAGE (Figure 4.22 (b)). After the reaction the SNAP-tag arm of K430-FLAG-SNAP exhibits a new shifted protein band: it is due to the covalent attachment of DNA on the arm, since the protein is now heavier of about 5 kDa. The total yield is about 60%. Kinesins are then separated from the unreacted DNA by successive centrifugations using a filter with a MWCO of 30 kDa.

Unfortunately, DNA-modified kinesins exhibit an activity — in an active gel experiment — in the absence of a DNA linker that would attach to the DNA strands  $\text{Lk-Cy5}$  and  $\text{Cy3-Li}$ . As discussed in Chapter 3 this suggests that K430-FLAG-HSNAP kinesin forms non-specific aggregates. Nevertheless, they could still be used in gliding assays where it is not anymore the state of the clusters which is controlled by DNA but their attachment to the surface. In this situation, the dynamics of an autocatalytic reaction built from the PEN-DNA toolbox and in which a ssDNA template is attached to kinesin clusters could be investigated.

#### 4.4.2 Going 2D: gliding assays

DNA molecules have been used to engineer controllable 2D systems in which motors are attached to surfaces. More particularly it is the interaction between the microtubules or the interaction between the motors and the surface which are tuned. Two recent systems of great relevance have been developed. The first one controls the formation of vortices thanks to the selective formation of microtubule bundles [142]. The second one consists of vesicles containing microtubules and kinesins coupled to the vesicles' membrane through DNA hybridization. When the kinesins are linked to the membrane, the latter shows deformation [244]. Motivated by these works and in collaboration with Yuliia Vyborna in the lab, we have started to develop a gliding assay where the attachment state could be controlled by the PEN-DNA toolbox.

So far we have tested if gliding assays were compatible with PEN-DNA fronts. To do so, we attach K430-HSNAP motors non specifically to a glass surface. First, motors are infused — in the buffer used in Section 3.1 — into a glass channel until the entire volume is filled (about 10  $\mu\text{l}$ )

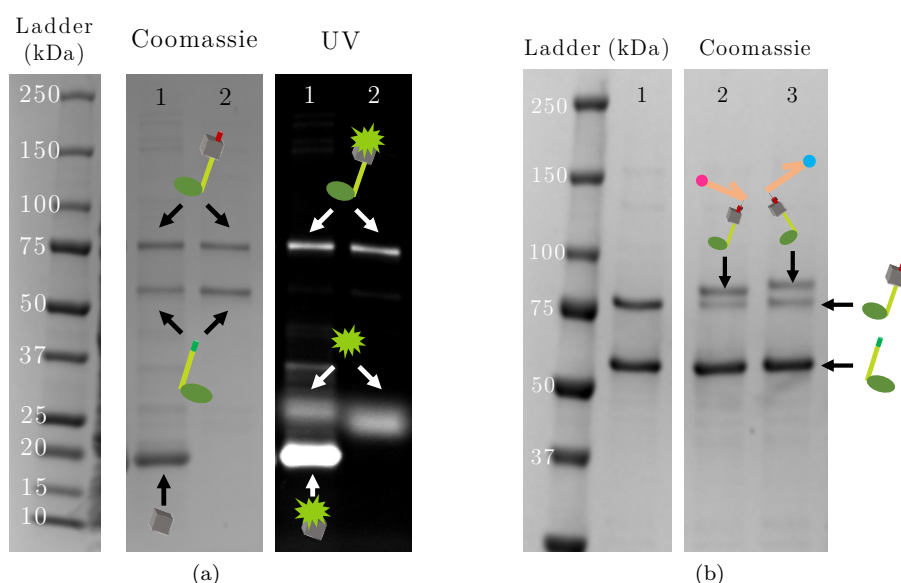


Figure 4.22 | **SDS-PAGE analysis of the reaction between K430-FLAG-SNAP and BG substrates** (a) Reaction between HIS-tag purified K430-FLAG-SNAP (lane 1) or HIS-tag and FLAG-tag purified K430-FLAG-SNAP (lane 2) and the fluorescent BG substrate SNAP-Vista Green. The gel is shown after coomassie staining with a white light and under UV illumination. (b) Reaction between K430-FLAG-SNAP (HIS-tag and FLAG-tag purified) (lane 1) with BG-modified BG-Li-NH<sub>2</sub> ssDNA (lane 2) or BG-Lk-Cy5 ssDNA (lane 3).

and then incubated for 5-10 min. The channel is then washed using the same buffer but without motors, typically with a volume of 30  $\mu\text{L}$ . To do so the buffer is injected on one side and adsorbed by capillarity using a tissue located on the other side. Then the surface is blocked by infusing 10  $\mu\text{L}$  of 2%(w/v) pluronic or 0.5%(w/v) casein for 5 min. Finally the channel is washed again and infused with polymerized microtubules at a concentration of about 5  $\mu\text{g}/\text{mL}$ . Since the concentration in microtubules is low, it is not necessary to wash the channel after this step.

The channel is imaged with a 20X objective and images are recorded every 3 s (Figure 4.23 (a) and Movie A.16 [📄, 🎥]). This experiment is done by Yuliia Vyborna. Microtubules move at a velocity of  $1.1 \pm 0.7 \mu\text{m}/\text{s}$ , computed with the *ToAST* tracking plugin in ImageJ using the 30 first images (Figure 4.23 (b)). This value is comparable to the one found with the kinesin K430-FLAG-SNAP [73]. Interestingly, the density of microtubules on the surface is increasing with time. Indeed microtubules from the bulk of the channel are moving and then are kept on the surface by the motors.

Very recent results (not displayed here) show that gliding experiments work in the presence of the autocatalytic amplification based on the T1\_20/d-1 system in PMMA channels. It would be interesting to implement the aforementioned ideas in order to control the motility.

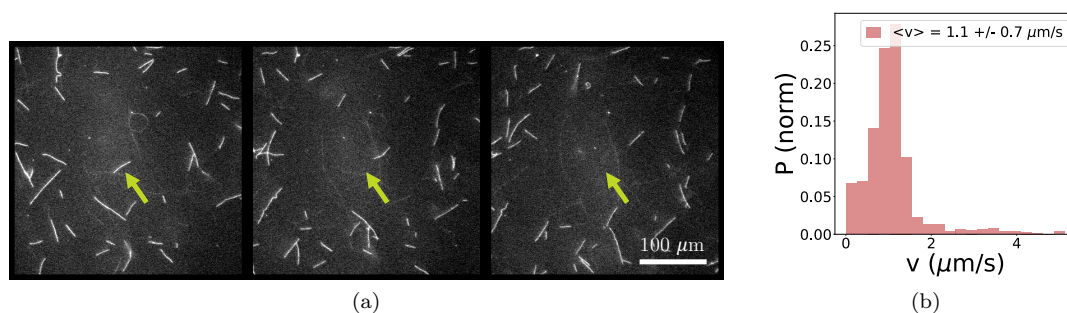


Figure 4.23 | **Gliding motility assay.** (a) Microtubules are propelled by K430-HSNAP kinesins attached to the surface of a glass channel. The green arrow indicates the initial position of one microtubule. The interval between images is 30 s. This experiment is done by Yuliia Vyborna. Movie [A.16](#) [[↓](#), [▶](#)]. (b) Normalized probability distribution of microtubule velocities.

## 4.5 Conclusion

### 4.5.1 Summary

In this chapter we have combined two molecular self-organization systems into a unique one. We have found compatible experimental conditions for both the active gel, composed of microtubules and clusters of kinesin, and the PEN-DNA toolbox. The main resolved problems have been with regards to the temperature and the buffer conditions. With this, we have shown that a reaction-diffusion front can propagate in an active gel. The two out-of-equilibrium systems behave independently but can indirectly interact physically or chemically. Physically, the global contraction of the active gel leads to large hydrodynamical flows in the channel that enhance the mixing of the DNA molecules involved in the front, thus accelerating the front. Chemically, both systems use nucleotides as a chemical source of energy. In particular dGTP is shared between the autocatalytic system — it is used to polymerize new ssDNA — and the active system — microtubules hypothetically use dGTP for their extension. Then, in a regime where dGTP is a scarce resource, the two systems compete. This led to an inhomogeneous patterning of the channel both in terms of gel activity and DNA concentrations. Because of the presence of dGTP and its impact on microtubules, the active gel does not exhibit sustained active flows. However, it would be interesting to recover the turbulent flows in the presence of the DNA front to form a programmable, self-sustained, biocompatible reaction-diffusion-advection system. In this perspective, we have designed an autocatalytic system where dGTP is not needed anymore. To do so we have identified a new nicking enzyme that is able to recognize sites that do not contain dCTP (complementary to dGTP). This new construct exhibits more complex bulk dynamics than a simple autocatalytic amplification, even though fronts can still propagate in PMMA channels. However, in the presence of the active gel, visible precipitates containing kinesin clusters form and greatly perturb the activity of the system. Lastly, we have demonstrated that, using the SNAP-tag, it is possible to covalently attach DNA on kinesins motors. Although non-specific kinesin clusters are still present, it may be possible to use this approach to control the organization of active matter in different configurations, like for instance in a gliding assay.

The coupling between DNA molecules involved in chemical reaction networks and reconstituted active gels could be further studied. For example, DNA could be attached to microtubules in order to dynamically control the assembly of bundles thanks to the production of a DNA linker (from the PEN-DNA toolbox). In addition, DNA templates could be attached on kinesins; the motors becoming the support of the reaction. Other DNA patterns could also be designed. Although oscillations are probably difficult to engineer because of the low temperature, stable DNA patterns built from a bistable chemical reaction network seem feasible. The stability of such a static pattern in the presence of the active gel would be interesting to look at.

From a material science perspective, the formation of patterns is an important process that needs to be connected to other processes in order to design functional materials. For example, it can control spatially and temporally the downstream production of a molecule of interest using the transcription-translation machinery.

### 4.5.2 Perspectives: reacting beads immersed in an active bath

Various living systems exhibit collective behaviors that arise from interactions between many physically separated elements. They chemically communicate through the exchange of molecular information. For example, bacteria use quorum sensing to regulate various physiological activities [180]. Inspired by the work of Gines, Rondelez and coworkers [87], we have started to explore the possibility of localizing DNA amplification reactions on sepharose beads immersed in an active bath of microtubules and kinesin clusters. We prepare the beads according to the protocol displayed in Appendix B using the biotinylated DNA template LT2LT\_20. In order to attach it on streptavidin-modified sepharose beads, the template contains a 5'-biotin modification and an adenosine nucleotide between the biotin and the coding sequence. In the absence of the active gel we have performed a front experiment where the beads have been dispersed in the channel and the front has been initiated by adding 1  $\mu\text{M}$  of input LT\_10 on one side of the channel. The front is very slow with a velocity of about 5  $\mu\text{m}/\text{min}$  (Figure 4.24 (b) and Movie A.17 [↓, ▶]), but the beads still act as autocatalytic templates (Figure 4.24 (c)). Importantly, control experiments show that in the absence of DNA input, no self-start was observed for more than 6 h.

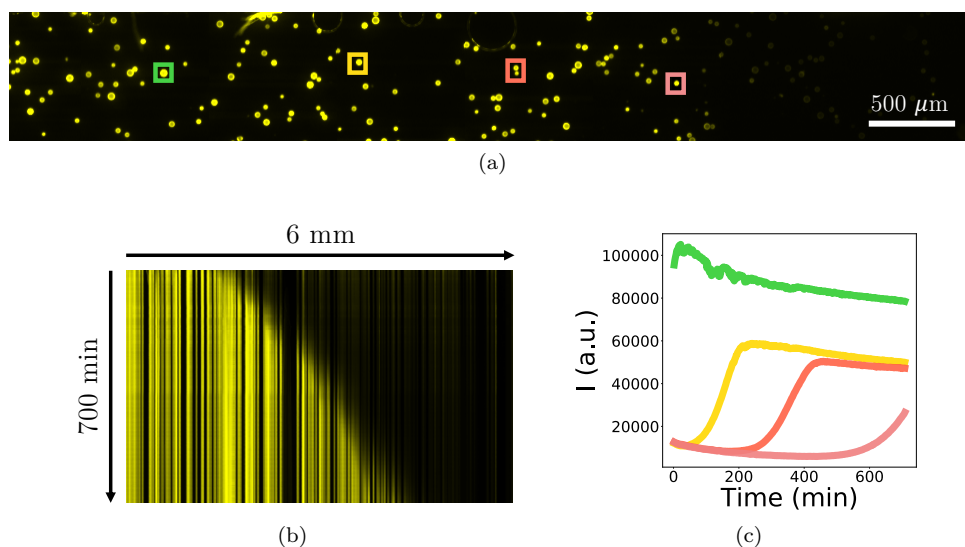


Figure 4.24 | **Propagation of a front in a population of DNA-functionalized beads.** (a) Final image of the DNA-beads using SGI intercalator. (b) Kymograph (using the maximum of intensity as projection) showing the propagation of the front across the population of beads. Movie A.17 [↓, ▶]. (c) Evolution of the fluorescence intensity of the four beads annotated in (a).

In the presence of 0.5 mg/mL GMPCPP-microtubules and 25 nM K401-BCCP in a ratio with streptavidin of 1:1 (Figure 4.25 (a) and Movie A.18 [↓, ▶]), the beads are moderately advected by the active flow. We can notice that the initial bending instability of the active gel described in Section 3.4 is observed here. From an initial homogeneously dispersed solution of beads, turbulent flows tend to form groups of 5-10 beads (Figure 4.25 (b)). These groups become then immobile. We identify two main reasons for this slow-down in motion. First, the beads are relatively big colloidal particles (34  $\mu\text{m}$  in diameter) and sediment to the bottom of the channel. Secondly,



unlike the case in which only the active gel is present or the one described in Section 4.2, here bundles do not coarsen with time. On the contrary, they become less dense — fluorescence intensity is blurred — and potentially exert less forces on the beads. Unfortunately, regarding DNA amplification, no front is observed. However the beads are still active as the increase of fluorescence attests (Figure 4.25 (c)): in the control experiment in which the polymerase BstLF is not put in the mix, the average fluorescence of the beads decreases. Furthermore, this experiment suggests that the localization of DNA templates on sepharose beads reduces the formation of the previously mentioned precipitates, as the gel activity shows.

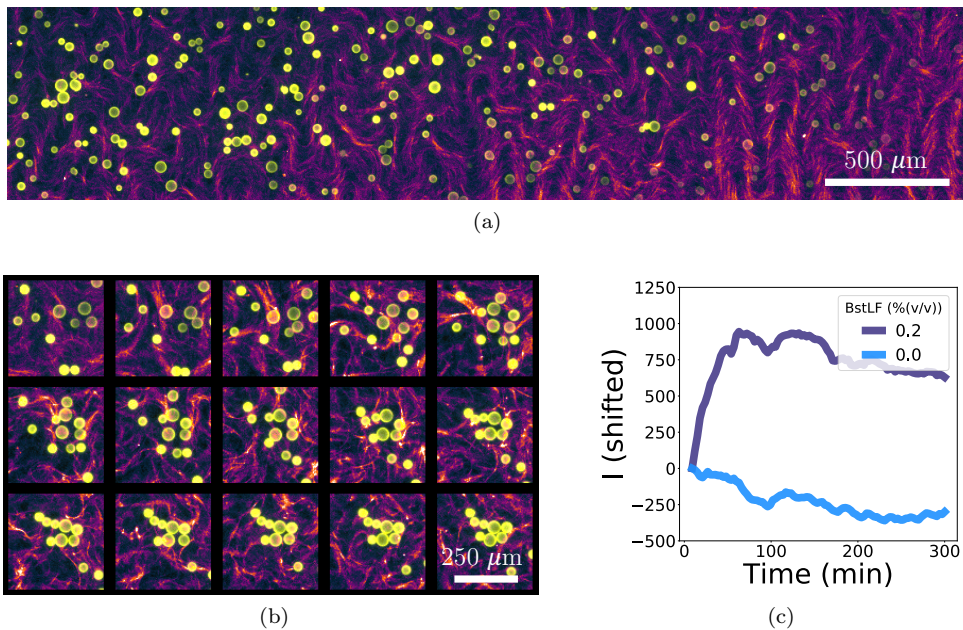


Figure 4.25 | **DNA-functionalized beads immersed in an active bath.** (a) Initial image of a channel containing DNA-functionalized beads in a turbulent active gel. The first bending instability of the active gel is visible. Movie A.18 [[↓](#), [🔍](#)]. (b) The turbulent flow tends to aggregate sepharose beads. Interval between images is 3 min. (c) Average intensity of the beads. No front is observed but the fluorescence increases in the presence of the polymerase BstLF.

Using this system, two populations of beads could be mixed together — for example one with and one without the input — in order to look at their communication [199]. For instance, their dependence in activity (the concentration in ATP) could be examined. Smaller beads — such as 1  $\mu\text{m}$ -diameter streptavidin-coated, paramagnetic beads [326] — would probably be transported more easily by the turbulent active gel, possibly leading to larger bead motions. Moreover the use of streptavidin beads may not be the best choice of coupling. Indeed, K401-BCCP kinesin may be exchanged from the clusters to the beads. Its substitution by K430-HSNAP or K430-FLAG-SNAP could be investigated. The dynamics of reacting beads advected by internally driven microtubule flows may also exhibit interesting collective behaviors.

## Chapter 5

# RNA control of genetic expression in a cell-free system

<b>5.1 RNA and genetic regulation</b> . . . . .	<b>138</b>
5.1.1 Principles of genetic regulation . . . . .	138
Central dogma of molecular biology . . . . .	138
Genetic regulation . . . . .	139
5.1.2 Using RNA to control genetic expression . . . . .	140
5.1.3 De novo design of RNA riboregulators . . . . .	141
<b>5.2 A cell-free TXTL system for the study of RNA riboregulators</b> . . . . .	<b>142</b>
5.2.1 TXTL system, reproducibility and control . . . . .	142
PURE cell-free TXTL systems . . . . .	143
Rapid prototyping of genetic parts and networks . . . . .	143
5.2.2 Description of the riboregulators used . . . . .	144
<b>5.3 Experimental protocol and assembly of the system</b> . . . . .	<b>147</b>
5.3.1 DNA and RNA preparation . . . . .	147
5.3.2 Preparation of the PURE TXTL system . . . . .	147
5.3.3 Fluorescence measurements . . . . .	147
5.3.4 Electrophoretic mobility shift assays . . . . .	148
5.3.5 Kinetic model . . . . .	148
<b>5.4 In vitro TXTL provides valuable information on RNA riboregulators</b> ★ . . . . .	<b>149</b>
5.4.1 Cell-free production of the GFP from a DNA or a RNA template in the absence of regulation . . . . .	149
Experimental results . . . . .	149
Kinetic model . . . . .	149
5.4.2 Dynamic range of a regulator . . . . .	152
Definition . . . . .	152
Measurement . . . . .	154
Comparison of the dynamic range of riboregulators in vivo and in vitro . . . . .	155
5.4.3 Translation from RNA characterizes the reaction between RNA strands . . . . .	156

Dissociation constant . . . . .	156
Measurement . . . . .	157
<b>5.5 Conclusion . . . . .</b>	<b>160</b>

The design of stimuli-responsive materials activated by biological signals is a major challenge in biotechnology. In the Chapters 3 and 4 we have looked at the self-organization of reconstituted molecular systems — active gels and reaction-diffusion fronts made of DNA — that can be used to engineer biocompatible, self-sustained, programmable materials. The chemo-mechanical material presented in Chapter 4 was designed as the combination of a regulatory chemical reaction network — the PEN-DNA autocatalytic reaction — and a chemo-mechanical transduction system — the active gel. We have seen in 2 that there are other ways to implement regulatory reaction networks in vitro. A particularly important one is gene regulation, that is the focus of this chapter. From a nucleic acid template it is possible to produce a protein in a controlled manner. Thanks to their programmable nature, nucleic acids can also be used to control this process. In this chapter we study the regulation of the protein production based on RNA molecules using a reconstituted transcription-translation (TXTL) system. More particularly, these RNA regulators are designed to modify the rate of expression, only by changing their structure according to base-pairing rules.

We first introduce important concepts of genetic regulation with a focus on RNA molecules. We explain why and how these molecules are used to control protein expression. In particular we look at RNA riboregulators. These are short RNA sequences that upon binding to a ligand, change their secondary structure and influence the expression rate of a downstream gene. They constitute an attractive alternative to transcription factors for building synthetic gene regulatory networks because they can be engineered de novo. In a second section we present the experimental system. We describe first the recombinant cell-free TXTL system used to study the translational regulation performed by designed RNA molecules. Then, the RNA regulators and their preparation are depicted. Finally we explicit the assembly of the reaction and the monitoring method. In the third section we present experimental results showing that this system can dynamically produce a protein in a controlled manner from a DNA or an RNA template. In particular, we show that it can provide valuable information about the performances of in silico designed riboregulators, such as the dynamic range and the dissociation constant between two RNA molecules.

## 5.1 RNA and genetic regulation

In addition to their role of coding protein sequences, RNA molecules contribute to a diverse set of gene-regulatory elements. More particularly, RNA riboregulators have been engineered — from natural sources or completely de novo — to perform regulatory functions and expand the number of tools available in synthetic biology.

### 5.1.1 Principles of genetic regulation

#### Central dogma of molecular biology

DNA, RNA and proteins are linear biological polymers. The sequence of monomers, nucleotides or amino acids, encodes genetic information. Can we build a polymer from the sequence of another and if so, how? This question has been formulated by Francis Crick in his ‘Central dogma of molecular biology’ [43]. It postulates all the possible transfers of information that exist and can exist from one biopolymer to another. There are nine possible transfers between the three molecules of life: some can be done, some have never been observed. DNA can be copied into DNA (replication), DNA can be copied into messenger RNA (mRNA) (transcription), proteins can be synthesized using information from mRNA (translation). Moreover, ‘special’ transfers exist, for example in some viruses: RNA can be replicated into RNA and RNA can be copied into DNA (reverse transcription). Some transfers do not exist: making nucleic acids from proteins has never been observed. These transfers are summarized in Figure 5.1.

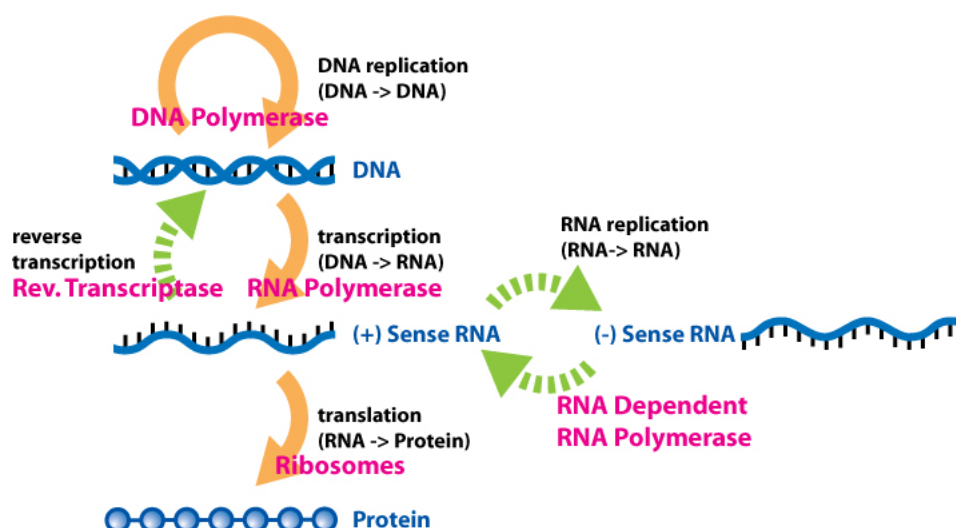


Figure 5.1 | **Sketch of the Central dogma of molecular biology.** Information transfers between the different biopolymers are indicated by orange arrows (so-called ‘usual’ transfers) and the green arrows (‘unusual’ transfers). The enzymes responsible for the transfers are indicated in pink. Adapted from Wikipedia.

## Genetic regulation

The mechanisms of information transfer, such as transcription and translation, are not always active. Indeed, cells only express a small part of their genes: they respond dynamically to their environment and regulate their expression by adjusting the level of certain genes. There are several levels of gene expression regulation:

- **Transcriptional: is the gene transcribed into mRNA?** Both in prokaryotic and eukaryotic cells, there are DNA sequences on which the RNA polymerase attaches to initiate transcription, which are called promoters. Thus, it is possible to regulate the transcription positively or negatively, with mechanisms that differ in eukaryotes and prokaryotes.

In prokaryotic organisms, regulation is organized around functional units called operons: a set of genes whose functions are linked and which are transcribed together into one long mRNA from a single promoter. It is only at the next step — translation — that ribosomes differentiate between each gene (with the presence of start and stop codons). The lactose operon is probably the best known example [131]. It is used for the transport and metabolism of lactose in *E. coli*. It is built around three structural genes: *lacZ*, *lacY* and *lacA* and is regulated by several external factors, such as the availability of glucose and lactose. With rare exceptions, eukaryotic genomes are not organized in operons.

A second major difference is the presence of histones on their DNA. These proteins form, together with DNA, a very dense structure called chromatin. Thus, RNA polymerase and the various activators and repressors of transcription cannot physically access DNA.

A third important difference is the existence of post-transcriptional chemical modifications of mRNAs. Indeed, they can be edited in different ways: addition of a 5'-cap (usually a modified methylated guanosine), deletions of introns (sequences deleted during RNA maturation), or addition of a 3'-tail rich in adenosine.

- **Translational: is RNA translated into protein?** Most of the mechanisms involved in the regulation of translation take place at the beginning of decoding by the ribosome. The presence or the absence of the ribosome on the start codon determines the rate of production of a downstream protein. The adjustment of this rate is tuned by the accessibility of the initiation codon to the small ribosome subunit. In prokaryotes the 30S subunit of the ribosome goes directly to the start codon, by binding to a specific upstream sequence, called ribosome binding site (RBS). In eukaryotes, the 40S subunit binds to the 5'-cap of mRNA via initiation factors, and then scans the mRNA in order to find the start codon.
- **Post-translational: is the protein in an active or inactive form? Is the protein stable or not? Are there chemical modifications?** Following their synthesis, proteins undergo many post-translational modifications to form a mature protein. Most of the time they occur on the amino acid side chains or at the C-terminal or N-terminal side. In addition to correct 3D folding, functional chemical groups can be attached to proteins via phosphorylation, glycosylation, acetylation, alkylation, ubiquitination, ... or can even be cleaved. These processes are essential in cells: for example the addition of an hydrophobic group allows the protein to localize on the membrane.

In this chapter we look at the translational regulation. We show how RNA is used to perform the regulation of this step and, in particular, how this regulation can be evaluated *in vitro*.

### 5.1.2 Using RNA to control genetic expression

RNA is not only the messenger of information. Indeed multiple cellular functions are regulated by non-coding RNAs. In addition to transfer RNAs (tRNA) and to RNAs that form ribosomes (rRNA), there is a very large number of RNA molecules fulfilling other functions. They appear to be particularly important when specific recognition of nucleic acids, such as modifications of other RNAs [57], is required. They also have important regulatory, enzymatic and structural roles. Some of them are even able to self-cleave. This diversity of functions arises from RNA's ability to form complex 3D structures that can interact with other nucleic acids, proteins and small molecules. The main classes of RNA regulators in prokaryotes are [127]:

- **Antisense RNA.** They repress (or 'silence') gene expression by targeting specific mRNA sequences.
- **Riboregulators.** They are relatively small RNAs which activate or repress bacterial gene expression by base pairing with one or more target RNA. Usually *in vivo* this interaction is mediated thanks to the chaperone protein Hfq (which also prevents the degradation by RNAses). These riboregulators are expressed in response to a change of conditions such as oxidative stress, the presence of toxins, changes in temperature or fluctuations in the concentrations of other RNA molecules or RNA-binding proteins. An example of a natural riboregulator is represented in Figure 5.2.
- **Ribozymes.** A portmanteau of RNA and enzyme. They catalyse biochemical reactions such as nucleotide splicing and phosphodiester bond cleavage and formation. They operate in a sequence-specific fashion and often use metal cofactors.
- **Riboswitches.** They contain aptamer domain sites with highly specific pockets that bind small molecules or ligands. The binding of a ligand triggers a conformational change in the RNA structure and leads to a change in gene expression.

In eukaryotes there are similar regulatory RNAs (antisense RNA and riboswitches). We can also find small interfering RNAs (siRNAs) and microRNAs (miRNAs) whose origin is different (probably coming from the cleavage of an hairpin structure) but also rely on pairing with a mRNA in order to disable gene translation.

Its strong presence in the regulatory stages and the diversity of its mechanisms, make RNA an essential element for synthetic biology and for the development of genetic regulatory modules. Furthermore, regulation using RNA has other advantages compared to processes that use proteins: the kinetics of regulation is faster [177], there is no toxicity due to over-expression of proteins and RNA systems are more energy efficient [35]. Since the early 2000s, natural RNAs have been used to create artificial genetic regulation modules, like for example the fine tuning of the RBS strength towards ribosome, the creation of aptazymes (aptamers fused with ribozymes) [156], the control of the transcription termination by small transcription activating RNA (STAR) [37] or the *in vitro*

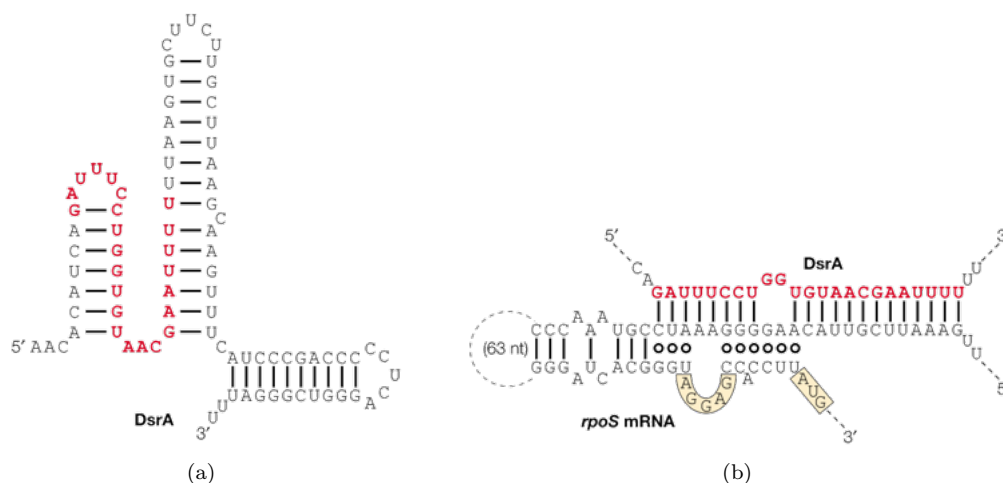


Figure 5.2 | **Example of a natural riboregulator found in *E. coli*.** (a) The DsrA RNA has a secondary structure composed of three hairpins. (b) In the presence of the mRNA *rpoS*, DsrA unzips to interact by base pairing, freeing the Shine-Dalgarno sequence and the start site AUG (yellow boxed-sequences). Thus, for *rpoS*, DsrA acts as a translational activator, which is proposed to happen by competition with an occluding secondary structure. Adapted from [158] and [57].

reconstitution of the CRISPR/Cas9 system [225]. These modules have started to be assembled to build complex genetic regulatory networks [156].

### 5.1.3 De novo design of RNA riboregulators

We focus on translational riboregulators. Unlike ribozymes and riboswitches, they are only made up of RNA. It is then easier to understand the interactions between components of a regulator (interactions between bases) for predictive purposes. From an experimental point of view, regulation between RNA strands does not require the use of external molecules. Indeed all the elements needed to build regulators are already present in cells. Since they were first used in synthetic biology more than a decade ago [128], several riboregulators have been designed and implemented in vivo both in prokaryotic [311, 37] and eukaryotic cells [233]. At first redesigned from natural riboregulators they are now designed using powerful structure-prediction models and tools available online [338, 320, 324, 168]. However, models do not yet precisely capture the complexity involved in the folding of RNA species several hundreds of nucleotides long. In silico design relies on a structural model of riboregulation, which needs to be transformed into predictable features in order to generate optimized sequences. After their design, riboregulators are tested in vivo where it is hard to control and tune the number of genes. Thus testing new parts in vivo often provides information that is difficult to correlate with thermodynamic parameters used in silico [234, 98]. Including a phase of in vitro testing in the workflow of engineering riboregulators could potentially solve these problems. In the following we describe such a method.



## 5.2 A cell-free TXTL system for the study of RNA riboregulators

In order to overcome the difficulties mentioned in the previous section and accelerate the improvement of in silico designs, cell-free TXTL systems are attractive tools for testing RNA riboregulators and more generally, genetic regulatory modules. Furthermore, because they are biocompatible by design, they are used in a growing number of applications in synthetic biology including the building of artificial cells [262].

### 5.2.1 TXTL system, reproducibility and control

Originally used to determine the genetic code [203], cell-free protein synthesis has gained a large interest because of its relatively simple composition, its reproducibility, the easy mathematical modeling and the increasing democratization of protocols. A TXTL system is composed of three components:

- **Cell extract or recombinant proteins.** It is the main source of the machinery required to perform the transcription and the translation. Two different plans can be considered:
  - *Cell extract.* A chosen source strain is grown in enriched media and lysed in order to obtain a functional extract. The extract already contains a large part of enzymes and molecules needed for transcription and translation such as ribosomes, RNAP, sigma factors, initiation factors, elongation factors, metabolic enzymes. Depending on the application, some additional post-lysis purification steps may be performed. Although any organism can potentially provide a source of crude lysate, most common cell-free TXTL systems consist of extracts from *E. coli*, rabbit reticulocytes, wheat germ or insect cells.
  - *Recombinant elements.* Here the approach is different and it relies on a minimal set of proteins necessary for in vivo protein production. These proteins are expressed, produced and purified independently and then reconstituted. A major contribution to this method has been done by Y. Shimizu [258] with a system called PURE (Protein synthesis using recombinant elements). This system has a lower yield and lasts for less time, but the composition is very well known and can be easily modified in order to study a particular dependency or to add an external component.
- **Reaction mixture.** It is composed of essential cofactors for protein synthesis: salts, buffers, amino acids, tRNAs, nucleotides, energy sources and their regeneration systems. Polyamines, molecular crowding agents and metabolic cofactors are also usually added. Other specific molecules can be added like for example, metabolic additives such as oxalate to inhibit gluconeogenesis or glutathione for disulfide bond formation. Its composition greatly depends on the origin of the previous mixture (cell extract or recombinant proteins).
- **Nucleic acid template.** The template containing the genetic information can be either a DNA plasmid, a linear DNA obtained from PCR or an RNA. Usually the concentration of

the template ranges between 0.1 to 10 nM for a DNA template and 10 to 100 nM for an RNA one.

Important advances have been achieved in the field in the past ten years. Now, cell-free protein production has started to become cost-effective for small volume production of complex proteins, where yields have reached several grams per liter of reaction mixture. Volumes of reaction have been increased up to 100 L. Continuous exchange of reaction by-products and a nutrients sustains the production for several days. Many different proteins have been produced with applications in functional genomics, structural biology or personalized medicine [33]. For a recent review of cell-free gene expression applications, the reader may be interested in ref. [262].

### PURE cell-free TXTL systems

In this chapter, we use the PURE TXTL system [258, 259] composed of individually-purified recombinant elements necessary for in vitro expression produced by Shimizu and collaborators. Its composition is well-controlled and it contains low levels of ribonucleases and proteases that degrade DNA, RNA templates and proteins. Protein products can be purified using affinity chromatography, as described in Chapter 3. A minimal set of components has been identified, purified and reconstituted — in a suitable buffer — in order to successfully produce protein (Figure 5.3):

- **Transcription.** Its composition includes T7 RNA polymerases and 4 nucleotides (ATP, GTP, CTP and UTP).
- **Aminoacylation of tRNAs.** Composed of 20 aminoacyl-tRNA synthetases (ARS), methionyl-tRNA trans-formylase (MTF), tRNA mix and 10-formyl-5,6,7,8-tetrahydrofolic acid (formyl donor).
- **Energy regeneration.** Containing pyrophosphatase, creatine kinase, myokinase, nucleoside diphosphate kinase and creatine phosphate.
- **Translation.** Including 20 amino acids, three initiation factors (IF1, IF2 and IF3), three elongation factors (EF-G, EF-Tu and EF-Ts), three release (or termination) factors (RF1, RF2 and RF3), a ribosome recycling factor (RRF) and ribosomes (purified from *E. coli*).

### Rapid prototyping of genetic parts and networks

Cell-free expression systems have been used to characterize transcription-translation dynamics [137, 269, 202]. The prototyping of simple regulatory elements has been investigated, for example the effect of a promoter sequence on the transcription or translation rate. The validation of such an approach is done by correlations with in vivo results [36, 272]. Larger genetic networks can be built in vitro by combining small elements with well-known behavior and optimized with a higher throughput than in vivo experiments. Thus, TXTL in vitro testing have be used to qualitatively evaluate the performances of new gene regulatory networks [272, 200, 76], to compute complex logic operations [276] or to build oscillators [201]. They can also provide quantitative data such as thermodynamic and kinetic rates [119] that are of great value for the improvement of in silico methods. Since cell-free TXTL systems are more rapid than experiments in cells — mainly because

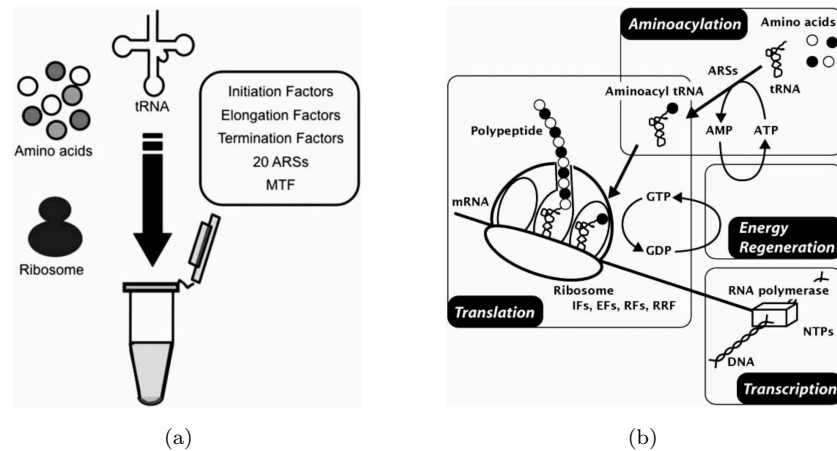


Figure 5.3 | **The PURE TXTL system: composition and main reactions.** (a) Illustration of the PURE system. (b) Main reactions in the PURE system (ARS: aminoacyl-tRNA synthetase, MTF: methionyl-tRNA trans-formylase). Adapted from [205].

genetic constructs do not need to be assembled into a plasmid or integrated in a genome — they are helpful for studying non-model host organisms.

### 5.2.2 Description of the riboregulators used

The general principle of RNA translational regulation is based on a change in the secondary structure of the coding strand in the presence of a second strand (Figure 5.4). The first RNA forms in the 5' untranslated region (5'-UTR), a hairpin secondary structure, which sequesters the RBS and/or the initiation codon of the translation (start codon, AUG). This RNA is said to be cis-repressed and it is abbreviated 'crRNA' and noted  $R_{cr}$ . Protein translation is allowed when the gene is activated by a second trans-activating RNA (taRNA,  $R_{ta}$ ) designed to hybridize specifically with parts of the crRNA. Thus, they form an RNA duplex in which the RBS is exposed to ribosomes, allowing the start of the translation. We consider in this study two types of de novo designed riboregulators, that work as follows:

- **RAJ system.** In these designs by Rodrigo et al. [234], the structures of the two RNA are imposed. The RBS sequence of the crRNA is buried inside a unique hairpin structure and taRNAs are picked among several naturally-occurring structures (SokC, FinP, and DsrA) and two artificial structures (also hairpins). Thus, the secondary structures of the two RNAs are specified as constraints, with some tolerance to perturbations (Figures 5.4 (a) and 5.5 (a)). Then, starting from random or specified sequences satisfying the constraints, the algorithm generates many sequences that evolve in parallel against a function that accounts for stability, structures and interactions of the RNA (by the computation of the free energies of the unfolded, individual folding, transition and intermolecular folding states).
- **G system.** Often, the design of RNA regulatory systems is constrained by different sequences, such as the hybridization of the RBS or the start codon inside the hairpin of the crRNA. These constraints dramatically reduce the space of available sequences. To solve this

problem, Green et al. [98] designed in 2014 hundreds of regulators called toehold switches, using the NUPACK online software [324], with a design that removes the constraints by leaving the RBS and the start codon regions completely unpaired. They repress translation through base pairs before and after the start codon. crRNA-taRNA hybridization is initiated via linear-linear interaction domains called toeholds (of about 12-nucleotides long) located in the upstream region of the regulator. The toehold domain binds to a complementary domain on the taRNA (Figure 5.4 (b) and Figure 5.5 (b)). Thanks to these rules, they were able to design about 100 different regulators with a high level of orthogonality.

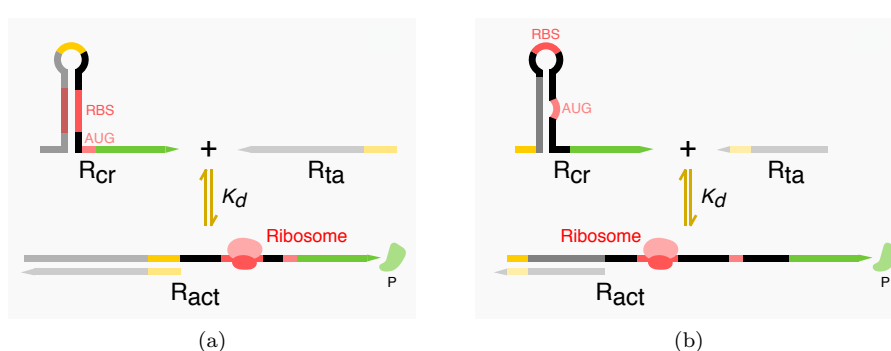


Figure 5.4 | **Sketches of conventional riboregulators and toehold switches.** The 5'-UTR of  $R_{cr}$  RNA forms a hairpin that hides either the ribosome binding site (RBS, (a)) or the start codon (AUG, (b)) away from the ribosome.  $R_{ta}$  hybridizes with  $R_{cr}$ , unwinding the hairpin and liberating the RBS and/or the AUG promoting translation. Variable sequences are shown in gray, whereas conserved or constrained sequences are represented by different colors.

In the following we study two riboregulators of the RAJ type and three of the G type whose sequences are listed in Table 5.1 and predicted structures are presented in Figure 5.5. In order to assess the regulation level of the translation, each crRNA is composed of a sequence coding for the green fluorescent protein (GFP) following the cis-repressed region. Thus, the measure of fluorescence of the TXTL solution due to GFP can be linked to the dynamics of protein production.

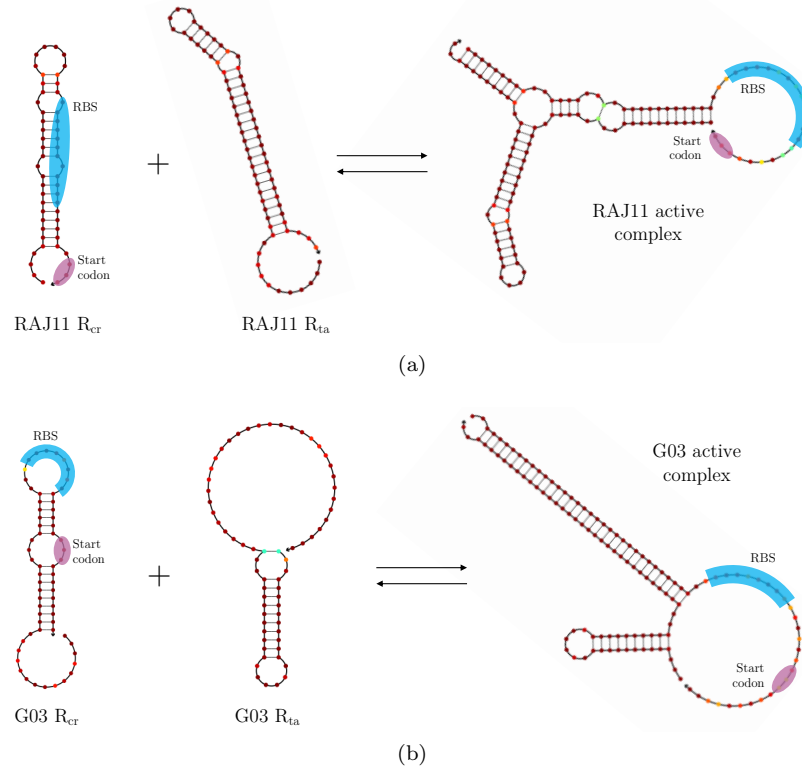


Figure 5.5 | **Secondary structures of the two types of riboregulator used.** The pairing between the  $R_{cr}$  and the  $R_{ta}$  frees the RBS (blue) and the start codon (pink). (a) RAJ11 and (b) G03. The structures have been made using the online server NUPACK [324].

Name	Sequences (5' → 3')
cr <sup>-</sup> RNA	AAAGAGGAGAAA UUAUGA AUG
RAJ11 $R_{cr}$	CUCGCAUAAUUUCACUUCUCAAUCCUCCGUU AAAGAGGAGAAA UUAUGA AUG
RAJ11 $R_{ta}$	GGGAGGGUUGAUUGUGUGAGUCUGUCACAGUUCAGCGGAAACGUUGAUGCUGUGACAGAUUUUUGCGAGGC
RAJ12 $R_{cr}$	ACCCAGUAUCAUUCUCUUCUUCUCCGCCACGCGG AAAGAGGAGAAA GGUGUA AUG
RAJ12 $R_{ta}$	GGGCAGGAAGAAGGGUUCUUUGAGCGAAUCUAGCGGCACCUCGCUAGGAUUUGCUCGAAGGGAUUCUGGG
G01 $R_{cr}$	GGGUGAAUGAAUUGUAGGCUUGUUUAUGUUAUGAAC AGAGGAGA CAUAAC AUG AACAAGCCU
G01 $R_{ta}$	GGGACCGUGGACCGCAUGAGGUCCACGGUAAACAUAACUAUAACAAGCCUACA AUUCAUCAAAC
G03 $R_{cr}$	GGGUGAUGGAAUAAGGCUGUGUAUAUGAUGUUAGAC AGAGGAGA UAACAU AUG AUACACAGC
G03 $R_{ta}$	GGGUCAGUUCUGAGGUACCAGGAACUGAAACUAACAUAUAACACAGCCUUAUUCACACAC
G80L18 $R_{cr}$	GGGUGAAUUUGAUUGACUAGAAUGAUGAUACGAAGACAAGAAC AGAGGAGA UCGUAU AUG CAUUCUAGU
G80 $R_{ta}$	GGGCCACGCGUUGUCCUAUCAACGCGUGGAAAUCGUUAUCAUAUUCUAGUCAAUCAAUUCAAAG

Table 5.1 | **RNA sequences of the regulators.**  $R_{cr}$  sequences are listed from the end of the T7 promoter to the end of the regulating part. The ribosome binding site is indicated in blue, the start codon in pink.  $R_{ta}$  sequences are listed from the end of the T7 promoter and before the beginning of the T7 terminator.

## 5.3 Experimental protocol and assembly of the system

The RNA regulators are prepared from DNA plasmids. These plasmids are cloned, purified and then used as template to prepare linear DNAs by PCR. The linear DNAs are finally in vitro transcribed into RNA. The cloning of the plasmids coding for the riboregulators is performed as described in Chapter 3, in *E. coli* DH5 $\alpha$  strain. A detailed version of the protocol is reproduced in Appendix B.2.

### 5.3.1 DNA and RNA preparation

DNA templates are prepared by PCR amplification of plasmids encoding the RNA translational regulators, followed by affinity column purification. RAJ devices do not contain T7 parts, thus primers used for PCR amplification have to contain a T7 promoter or a T7 terminator. RNA templates are prepared by in vitro transcription followed by purification. The DNA and RNA integrity are determined by a 1.5% agarose gel and the concentrations are determined by absorbance at 260 nm. The sequences of the riboregulator domains are shown in Table 5.1. The sequences of the PCR primers are shown in Table B.1 (Appendix B.2).

We also prepare positive control templates lacking the cis-repressing elements. To do so, we build by PCR a linear DNA fragment coding for a green fluorescent protein with no upstream regulatory region: it is called cr<sup>-</sup>DNA. It is composed of a T7 RNAP promoter, an RBS, the GFP-coding sequence and a T7 terminator. In addition, we prepare by in vitro transcription the corresponding RNA (cr<sup>-</sup>RNA) from the cr<sup>-</sup>DNA.

### 5.3.2 Preparation of the PURE TXTL system

We prepare the PURE system according to ref. [259]. Its composition is indicated in Table B.3 (Appendix B.2). We receive from the Yoshihiro Shumizu's lab a mix containing most of the enzymes (Solution B). In the lab, we prepare four different tubes containing: (a) buffers and 20 amino acids, (b) NTP and creatine phosphate, (c) formyl donor (d) tRNA. They are then flash frozen in liquid nitrogen and kept at -80°C. Just before use, the reaction mix is assembled on ice starting from water, then the homemade tubes and lastly Solution B. We include an RNAase inhibitor (New England BioLabs) to prevent RNA degradation. For the control experiments and in order to test the reproducibility we use the commercially available PURExpress (New England BioLabs). It is only composed of two solutions which have to be mixed together, in the presence of the RNAase inhibitor and the template.

### 5.3.3 Fluorescence measurements

Rotor-GeneQ real-time PCR (Qiagen) is used to record fluorescence from GFP expression (excitation  $470 \pm 10$  nm, emission  $510 \pm 5$  nm) over time in an 8 or 15  $\mu$ L volume. The temperature is set to 37°C, and fluorescence is recorded every minute for at least 3 h.

### 5.3.4 Electrophoretic mobility shift assays

Electrophoretic mobility shift assays are performed with a 2100 Bioanalyzer System (Agilent Technologies) and an RNA Nano chip Kit. Samples are prepared by mixing RNA strands in 50 mM Hepes-KOH pH 7.6, 13 mM magnesium acetate, 100 mM potassium glutamate, 2 mM spermidine, 1 mM DTT and nuclease free water. They are incubated at 37°C for 10 min before being loaded into the electrophoresis chip. Electropherograms are manually aligned along the time axis. Affine curves corresponding to the backgrounds of the regions of interest are subtracted. Areas under peaks are determined by numerical integration and are normalized using the RNA marker provided in Agilent's kit.

### 5.3.5 Kinetic model

We use normal differential equations to model the transcription and the translation. This approach has been used to model TXTL systems from *E. coli* cell extract [137] and for the PURE TXTL system [269]. Details of the calculations can be found in Appendix D.

## 5.4 In vitro TXTL provides valuable information on RNA riboregulators ★

This section is adapted from our article *Quantitative characterization of translational riboregulators using an in vitro transcription-translation system* that has been published in ACS Synthetic Biology [254]. It is reproduced in Appendix F.

### 5.4.1 Cell-free production of the GFP from a DNA or a RNA template in the absence of regulation

#### Experimental results

We first characterize the translation and expression reactions of the PURE system in the absence of riboregulation. We vary the concentration of the input and we measure the fluorescence emitted by the GFP produced over time (Figure 5.6).

Starting from cr<sup>-</sup>RNA, the translation module of the TXTL system actively produces GFP during 2 hours. The translation kinetics displays three different phases: during about 5 min no signal is discernible from the background level, then follows a phase of quasi-linear increase during 100 min, that slows down until a plateau is reached (Figure 5.6 (a)). In the range 0 – 80 nM of cr<sup>-</sup>RNA, both the final intensity and the maximum rate of fluorescence growth,  $v_{tx}^{max}$ , increase linearly with the initial quantity of coding RNA (Figure 5.6 (b)). For higher concentrations there is a saturation: putting more RNA template does not increase significantly the final yield or the maximal production rate. When using cr<sup>-</sup>DNA as the initial input, the dynamics of the fluorescence intensity show both common and contrasting features with the previous case (Figure 5.6 (c)). Three phases are still observed: delay, growth and a plateau. However, the delay observed before an increase of fluorescence is now 15 min. Finally, the quantity of DNA required to saturate the maximum rate of fluorescence growth,  $v_{tx}^{max}$ , is almost two orders of magnitude lower than the quantity of RNA that saturates translation (Figure 5.6 (d)).

#### Kinetic model

We propose a simple analytical kinetic model that fits our data. To take into account the saturation of the production rates we assign Michaelis-Menten kinetics to the transcription and the translation reactions. As a plausible source of the initial delay in the translation reaction, we include a first-order step of maturation of the non-fluorescent GFP protein, noted P, into the functional fluorescent protein P\*. We neglect DNA and RNA degradation and we do not take into consideration the depletion of resources because we analyse our data between 0 and 50 min. For these reasons, our model does not reach a plateau in P\* concentration (Figure 5.6 (a) and (c)). These approximations are valid as long as the RNA molecules do not deteriorate and the enzymatic resources, more



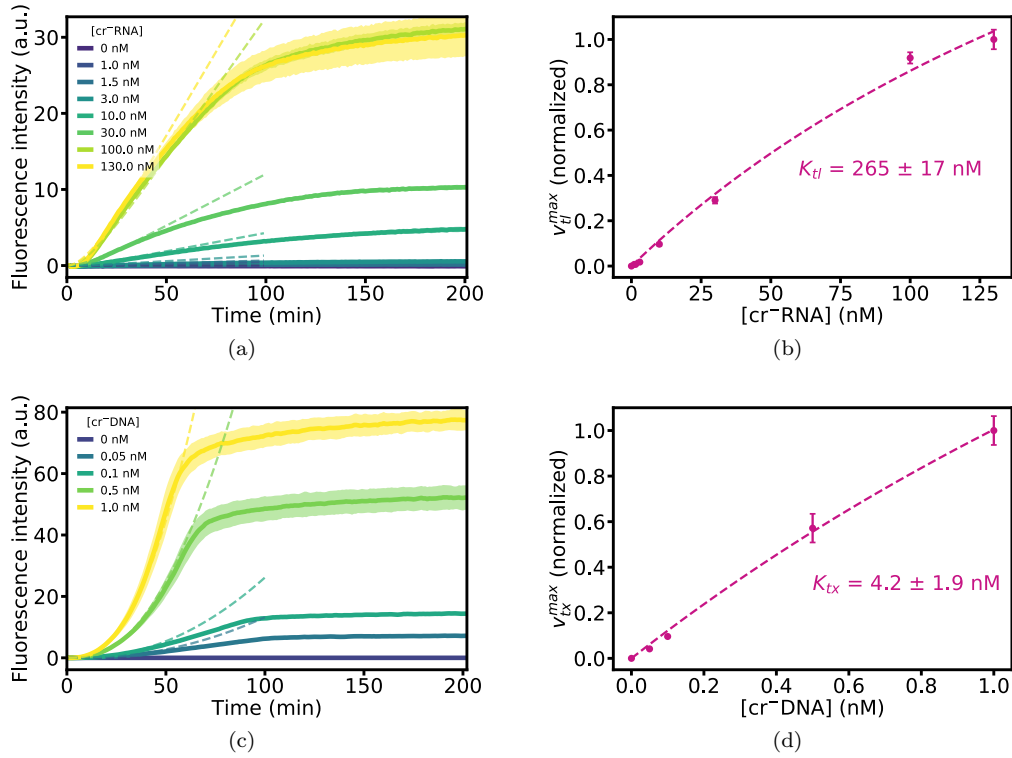


Figure 5.6 | **Production of GFP with the TXTL cell-free system from a DNA or a RNA template** Characterization of the TXTL system in the absence of riboregulation. Translation dynamics (a) and maximum fluorescence production rate (b) for increasing concentrations of an unregulated mRNA fragment coding for GFP. Expression (transcription and translation) dynamics (c) and maximum fluorescence production rate (d) for increasing concentrations of an unregulated linear DNA fragment coding for GFP. Solid lines (a, c) and disks (b, d) represent data, dotted lines are fits to the data. All experiments are performed in triplicate. Shading around the lines and error bars correspond to one standard deviation.

specifically the ribosomes [269], are not depleted. We thus write the following mechanism:



where  $D_{act}$  and  $R_{act}$  are, respectively,  $cr^-DNA$  and  $cr^-RNA$  and  $r_{tx}$ ,  $r_{tl}$  and  $r_m$  are, respectively, the transcription, translation and maturation rates. With the aforementioned hypotheses, this mechanism is associated with the rate equations

$$\frac{dD_{act}}{dt} = 0 \quad (5.4)$$

$$\frac{dR_{act}}{dt} = r_{tx} = \frac{k_{tx} \cdot D_{act}}{K_{tx} + D_{act}} \quad (5.5)$$

$$\frac{dP}{dt} = r_{tl} - r_m = \frac{k_{tl} \cdot R_{act}}{K_{tl} + R_{act}} - k_m \cdot P \quad (5.6)$$

$$\frac{dP^*}{dt} = r_m = k_m \cdot P \quad (5.7)$$

where  $k_\theta$  and  $K_\theta$  are, respectively, the rate and the Michaelis-Menten constants of reaction  $\theta$  and species concentrations are noted in italics. Equations (5.5-5.7) have exact solutions both for initial conditions corresponding to the translation ( $D_{act}(0) = 0, R_{act}(0) \neq 0$ ) and expression experiments ( $D_{act}(0) \neq 0, R_{act}(0) = 0$ ). For translation we obtain:

$$P^*(t) = \frac{R_{act}(0)}{K_{tl} + R_{act}(0)} \frac{k_{tl}}{k_m} (e^{-k_m t} + k_m t - 1). \quad (5.8)$$

The term  $(e^{-k_m t} - 1)$ , due to protein maturation, makes the kink of the curves in Figure 5.6 (a) at  $t = 10$  min, while the linear term in time dominates for  $t = 20 - 50$  min. Note that when the ribosome is not saturated,  $R_{act}(0) \ll K_{tl}$ , and for  $t \gg k_m^{-1}$  we can write

$$P^*(t) \approx \frac{k_{tl}}{K_{tl}} \cdot R_{act}(0) \quad (5.9)$$

explicitly showing that translation acts as a linear amplifier of the initial concentration of active RNA.

For expression, the exact solution is given in Appendix D.3. Here we provide an approximated solution when  $R_{act}(t) \ll K_{tl}$ ,

$$P^*(t) \approx \frac{D_{act}(0)}{K_{tx} + D_{act}(0)} \frac{k_{tx} k_{tl}}{2K_{tl}} \left( t^2 - \frac{2}{k_m} t + \frac{2}{k_m^2} (1 - e^{-k_m t}) \right). \quad (5.10)$$

Again, if  $D_{act}(0) \ll K_{tx}$  and  $t \gg k_m^{-1}$ , expression quadratically amplifies  $D_{act}(0)$  into a fluorescence signal.

Considering that the fluorescence intensity is proportional to  $P^*$  we fit eq. (5.8) and eq. (5.10) to the data in Figure 5.6. We obtain  $K_{tx} = 4.2 \pm 1.9$  nM,  $K_{tl} = 265 \pm 17$  nM and  $k_m = 0.10 \pm 0.01$  min<sup>-1</sup>, in fair agreement with previous measurements reporting  $K_{tx} = 4 - 9$  nM for T7 RNAP [269, 202],  $K_{tl} = 66$  nM [269] and  $k_m = 0.2$  min<sup>-1</sup> [137, 269]. Note that although cell-extract TXTL uses *E. coli* instead of T7 RNAP, the reported [137] value of  $K_{tx}$  is similar, 1-10 nM.

The saturation of transcription by DNA occurs at a concentration two-orders of magnitude lower than the saturation of translation by RNA. Below saturation, the TXTL system acts as a linear amplifier of the concentration of active RNA,  $R_{act}$ , and as a quadratic amplifier of  $D_{act}$  with a readout of intensity fluorescence. As a result we can use GFP fluorescence as a measure of the concentration of  $R_{act}$ .

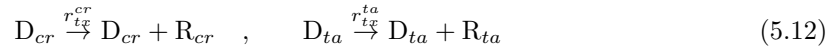
### 5.4.2 Dynamic range of a regulator

#### Definition

When riboregulators are used in vivo the DNA sequences  $D_{cr}$  and  $D_{ta}$ , respectively coding for the cis-repressed and trans-activator RNA  $R_{cr}$  and  $R_{ta}$ , can either be inserted in the chromosome, in the same plasmid or in two different plasmids. The performance of a riboregulator in vivo is assayed by fusing  $D_{cr}$  with a GFP and measuring the dynamic range, defined as

$$\rho_{ON/OFF} = \frac{\text{GFP fluorescence in the presence of } D_{ta}}{\text{GFP fluorescence in the absence of } D_{ta}}. \quad (5.11)$$

In vivo it is common to use a two-plasmid strategy [98], trying to improve  $\rho_{ON/OFF}$  by inserting  $D_{ta}$  in a high-copy plasmid. The simplicity of in vitro TXTL allows us to provide a quantitative definition of  $\rho_{ON/OFF}$  and to test the effect of  $D_{ta}$  concentration on  $\rho_{ON/OFF}$ . We start by writing the simplest model of riboregulation dynamics from DNA that is consistent with the results of the previous section. Within the TXTL system the two DNA molecules,  $D_{cr}$  and  $D_{ta}$ , are transcribed into the corresponding RNA strands, which associate into a coding RNA,  $R_{act}$ . The production of P mainly comes from the translation of  $R_{act}$  but also may come from  $R_{cr}$ , when cis-repression is not very effective. We thus write the following mechanism,



We model reactions (5.12-5.15) with the following set of ODEs, that takes into account the competition for transcriptional resources,

$$\frac{dR_{cr}}{dt} = r_{tx}^{cr} = \frac{k_{tx}^{cr} \cdot D_{cr}}{K_{tx} + D_{cr} + D_{ta}} \quad (5.16)$$

$$\frac{dR_{ta}}{dt} = r_{tx}^{ta} = \frac{k_{tx}^{ta} \cdot D_{ta}}{K_{tx} + D_{cr} + D_{ta}} \quad (5.17)$$

$$R_{act} = \frac{R_{cr}R_{ta}}{K_d} \quad (5.18)$$

$$\frac{dP}{dt} = r_{tl}^{act} + r_{tl}^{cr} \approx \frac{k_{tl}^{act}}{K_{tl}} R_{act} + \frac{k_{tl}^{cr}}{K_{tl}} R_{cr} \quad (5.19)$$

$$\frac{dP^*}{dt} = r_m = k_m \cdot P \quad (5.20)$$

where we have assumed that  $D_{cr}$  and  $D_{ta}$  may have different transcription rate constants  $k_{tx}^i$ . We have also assumed, as previously, that transcription follows Michaelis-Menten dynamics, that translation can be considered a non-saturated Michaelis-Menten ( $R_{cr}, R_{act} \ll k_{tl}^{act}$ ) and further that the hybridization reaction (5.13) is fast compared with the others and can thus be considered at equilibrium. We have seen in the previous section that the maturation reaction (5.15) introduces an additional term ( $e^{-k_m t} - 1$ ) that vanishes when  $t \gg k_m^{-1} = 10$  min. To facilitate subsequent

calculations we will suppose  $t \gg k_m^{-1}$  and thus  $P = P^*$ .

We define  $\alpha = \frac{D_{ta}}{D_{cr}}$  and integrate eq. (5.16-5.19) to obtain:

$$P^*(\alpha) = \frac{k_{tl}^{act} \alpha}{3K_d k_{tl}^{act}} \frac{k_{tx}^{ta} k_{tx}^{cr}}{\left(1 + \alpha + \frac{K_{tx}}{D_{cr}}\right)^2} t^3 + \frac{k_{tl}^{cr}}{2k_{tl}^{act}} \frac{k_{tx}^{cr}}{1 + \alpha + \frac{K_{tx}}{D_{cr}}} t^2 \quad (5.21)$$

where we have indicated explicitly that  $P^*$  is a function of  $\alpha$ . We can naturally define the dynamic range of the riboregulator as

$$\rho_{ON/OFF}^{th} = \frac{P^*(\alpha)}{P^*(\alpha=0)} = \frac{1 + \frac{K_{tx}}{D_{cr}}}{\left(1 + \alpha + \frac{K_{tx}}{D_{cr}}\right)} \left[ 1 + \frac{2}{3} \frac{k_{tx}^{ta} k_{tl}^{act}}{K_d k_{tl}^{cr}} \frac{\alpha}{\left(1 + \alpha + \frac{K_{tx}}{D_{cr}}\right)} t \right] \quad (5.22)$$

where the superscript *th* indicates that this is a theoretical quantity defined in the framework of model (eq. (5.16-5.20)). This equation reveals three important points. Firstly,  $\rho_{ON/OFF}^{th}$  depends linearly on time and it is thus difficult to compare  $\rho_{ON/OFF}$  between two experiments, in vivo or in vitro, if they have not been calculated at the same time. This linear dependence comes from the fact that protein production from the riboregulator is cubic in time, while the leak production from  $D_{cr}$  alone is quadratic as written in eq. (5.21). In vivo one may expect that  $\rho_{ON/OFF}^{th}$  reaches a plateau due to degradation. However a linear increase of  $\rho_{ON/OFF}$  is observed over 4 h for riboregulator 7 in ref. [98]. Secondly,  $\rho_{ON/OFF}^{th}$  is proportional to the aggregate factor  $\beta = \frac{k_{tx}^{ta} k_{tl}^{act}}{K_d k_{tl}^{cr}}$ .  $\rho_{ON/OFF}^{th}$  is proportional to the transcription rate constant  $k_{tx}^{ta}$ , and thus will differ between different RNAPs and promoters. It is also proportional to the ratio between the translation rate constant of the active and the inactive state, which is intuitive, and it is inversely proportional to the equilibrium constant of dissociation between  $R_{cr}$  and  $R_{ta}$ . Finally,  $\rho_{ON/OFF}^{th}$  is strongly and non-trivially dependent on the concentration of  $D_{cr}$  and  $D_{ta}$  (through  $\alpha = D_{ta}/D_{cr}$ ). A simulation of the dynamic range as a function of  $D_{cr}$  and  $\alpha$  is shown in Figure 5.7.

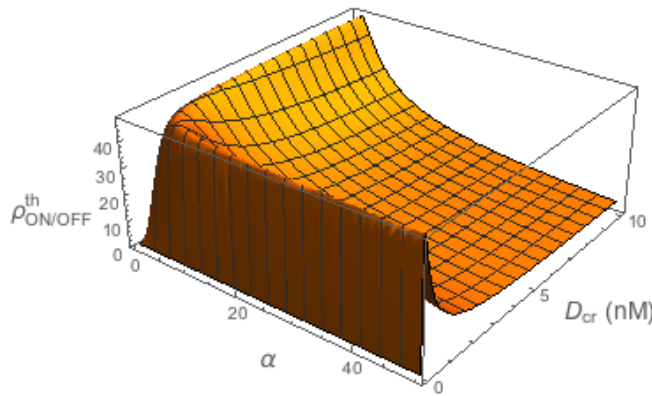


Figure 5.7 | **Simulation of the dynamic range.** For a fixed time,  $\rho_{ON/OFF}^{th}$  defined in eq. 5.22 is plotted as a function of  $D_{cr}$  and  $\alpha$  (using  $\beta = 286$  and  $K_{tx} = 4.2$  nM).

The maximum of  $\rho_{ON/OFF}^{th}$  is obtained for (Appendix D.5)

$$D_{ta} = D_{cr} + K_{tx}. \quad (5.23)$$

### Measurement

To test the model's prediction that  $\rho_{ON/OFF}$  strongly depends on  $\alpha$  and thus on  $D_{ta}$ , we titrate riboregulator G03 by keeping  $D_{cr} = 0.25$  nM constant, varying  $D_{ta}$  in the range 0 – 100 nM and recording GFP fluorescence over time (Figure 5.8). Increasing  $D_{ta}$  in the range 0 – 5 nM results in an increased fluorescence signal. However, for  $D_{ta} > 5$  nM the fluorescence signal dramatically decreases until reaching 10% of the maximum production rate at  $D_{ta} = 100$  nM. Equation (5.22) fits the data with a single free parameter  $\beta = 286$  (Figure 5.8 (b), pink line), indicating that the bell-like shape of  $\rho_{ON/OFF}$  arises from the competition of  $D_{ta}$  and  $D_{cr}$  for transcriptional resources. To further test this interpretation we titrate  $cr^-$  DNA, which lacks the cis-regulatory region, with the  $D_{ta}$  of riboregulator G03 (Figure 5.8 (b), yellow line). The data are quantitatively predicted by eq. (5.22) taking the limit  $K_d \rightarrow \infty$  (Appendix D eq. (D.30)) without fitting parameters. Importantly, the addition of nontranscribing DNA had little effect on the expression dynamics (Figure 5.9).

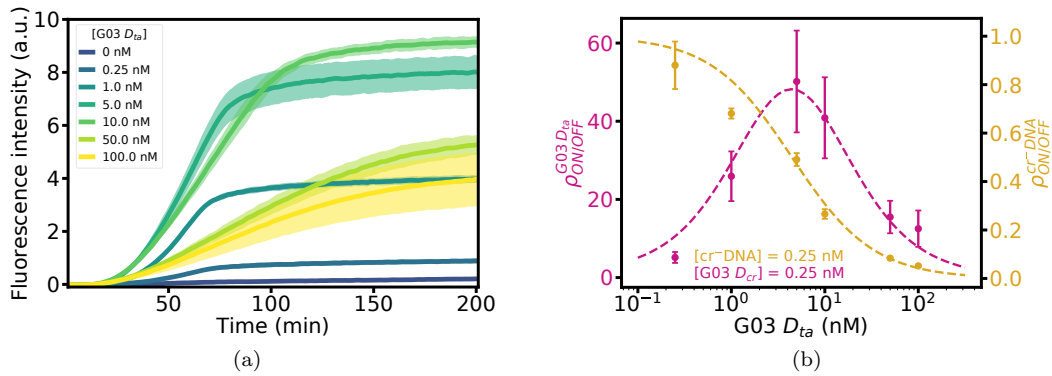


Figure 5.8 | **The dynamic range of a riboregulator strongly depends on the concentration of the trans-activating DNA.** (a) Fluorescence intensity versus time for the in vitro expression of 0.25 nM of  $D_{cr}$  DNA, coding for GFP, with increasing concentrations of  $D_{ta}$  DNA, for riboregulator G03. (b) Dynamic range  $\rho_{ON/OFF}$  at time 75 min for a  $D_{cr}$  with (G03) or without ( $cr^-$ ) a cis regulatory region, as a function of the concentration of  $D_{ta}$  from the riboregulator G03. The dashed lines correspond to a fit to eq. (5.22) with a single free parameter  $\beta = \frac{k_{ta}^{ta} k_{rl}^{act}}{K_d k_{rl}^{cr}}$  (pink) and to eq. (5.22) with  $\beta = 0$  without fit (yellow), both using  $K_{tx} = 4.2$  nM as measured in Figure 5.6 (d). All experiments are performed in triplicate. Shading around the lines and error bars correspond to one standard deviation.

The observation that an increase in non-coding (but transcribed) DNA concentration reduces protein expression in TXTL systems has already been reported [260, 276] and it has been modeled [261] in the absence of riboregulation, although a quantitative comparison between the model and the data has not been reported. Our model explicitly takes into account the competition between the two DNA substrates  $D_{ta}$  and  $D_{cr}$  and the predicted dependence of  $\rho_{ON/OFF}^{th}$  on  $D_{ta}$  is in agreement with the data. Hu et al. have proposed a kinetic model for transcriptional riboregulators [119] and compared their model with in vitro TXTL experiments. Our model is of the same type in the sense that they describe the kinetics with a set of ODEs at the level of concentrations. In contrast, the model of Hu et al. has significantly more parameters than ours,

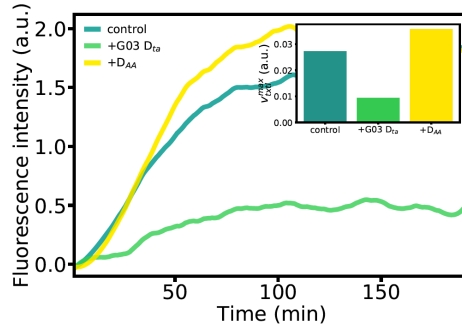


Figure 5.9 | **Effect of a non-coding DNA strand on the overall gene expression.** We compare the expression of 0.25 nM of  $cr^-$  DNA alone (dark green) or in the presence of 50 nM of G03  $D_{ta}$  (light green) or 100 nM of  $D_{AA}$  (CGAGAGGAATGCGAGAGGAATG) (yellow). We do not observe a decrease of expression when  $D_{AA}$  is added to the mix.  $v_{max}^{txtl}$  calculated between 0 min and 60 min is plotted in the insert.

13 instead of 5, and takes into account the degradation of both RNA and protein. As a result, the authors cannot provide analytical results that clearly pinpoint the important parameters to design functional riboregulators.

Saturation of transcriptional resources is particularly important in the context of riboregulators, where the non-coding DNA produces a regulatory RNA that has an important effect in the gene regulatory network. The similar value of  $K_{tx}$  for T7 and *E. coli* RNAP, together with previous observations of transcriptional saturation in *E. coli*-based TXTL systems, suggest that this behavior is not due to a particular property of the T7 RNAP. Our model and in vitro results thus predict that inserting  $D_{ta}$  in a high-copy plasmid will decrease the performance of the riboregulator activator and suggest a trade-off between resource competition and the over-expression of antisense RNAs. This prediction shall be tested in a future work.

### Comparison of the dynamic range of riboregulators in vivo and in vitro

To evaluate how dynamic ranges determined in vitro compare with in vivo measurements, we perform in vitro GFP expression experiments at 1 nM  $D_{cr}$  in the presence and in the absence of 5 nM of the corresponding  $D_{ta}$ . We choose  $D_{cr}$  and  $D_{ta}$  that verify eq. (5.23) to determine the maximum dynamic range. In vivo, the dynamic range is generally defined without subtracting the autofluorescence of the cells [234, 98]. In order to take this into account, we compute here  $\rho'_{ON/OFF}$ , where the prime indicates that autofluorescence is not subtracted (contrary to the previously defined  $\rho_{ON/OFF}$  in which the autofluorescence of the PURE system has been subtracted).

The agreement between the values obtained in vivo and in vitro is remarkable. Of course, the absolute values of  $\rho'_{ON/OFF}$  in vivo and in vitro are different, which is expected because  $\rho_{ON/OFF}^{th}$  is proportional to time and in vivo and in vitro data are obtained at different times (Table 5.2). In contrast, the relative order of  $\rho'_{ON/OFF}$  is similar in vivo and in vitro. Moreover the ratio between the two is constant for all riboregulators — except for G80L18 that is twice more active in vivo — indicating that TXTL experiments predict well  $\rho'_{ON/OFF}$  in vivo. The measured value of  $\rho'_{ON/OFF}$  for RAJ12 is close to unity. However, increasing the DNA concentrations to  $D_{cr} = D_{ta} = 50$  nM, which increases protein production according to eq. (5.21) while respecting eq. (5.23), demonstrates

that RAJ12 is indeed functional and we obtain  $\rho'_{ON/OFF} = 7$  at these concentrations. Comparing the values of  $I_{OFF}$  (OFF raw fluorescence) shows that RAJ type regulators leak significantly less than G type regulators while G80L18 leaks slightly more than G01 and G03. Finally, our experiments show that the remarkable  $\rho'_{ON/OFF}$  values of G type devices come from their high  $I_{ON}$  (ON raw fluorescence), and thus a very active ON state. We conclude that in vitro TXTL provides values of  $\rho'_{ON/OFF}$  that correlate well with in vivo measurements, in agreement with previous reports comparing protein expression in vivo and in vitro [276, 261, 36].

Device	in vivo $\rho'_{ON/OFF}$	TXTL $\rho'_{ON/OFF}$	TXTL $I_{ON}$ (a.u.)	TXTL $I_{OFF}$ (a.u.)	ratio $\rho'_{ON/OFF}$ in vivo/ TXTL
G01	$290 \pm 20$	$37 \pm 10$	$116 \pm 25$	$3.1 \pm 0.5$	$8 \pm 2$
G03	$260 \pm 30$	$26 \pm 6$	$81 \pm 10$	$3.1 \pm 0.6$	$10 \pm 3$
G80L18	$500 \pm 150$	$23 \pm 3$	$93 \pm 8$	$4.1 \pm 0.4$	$22 \pm 8$
RAJ11	$11 \pm 2$	$1.9 \pm 0.3$	$2.1 \pm 0.3$	$1.1 \pm 0.1$	$6 \pm 1$
RAJ12	$8 \pm 1$	$1.2 \pm 0.1$	$1.2 \pm 0.2$	$1.1 \pm 0.1$	$7 \pm 1$

Table 5.2 | **Comparison of the performance of five riboregulators in vivo and in vitro.** Dynamic range calculated without subtracting the autofluorescence  $\rho'_{ON/OFF}$  for the experiments performed in vivo and in TXTL, ON and OFF raw fluorescence signals ( $I_{ON}$  and  $I_{OFF}$ ) in TXTL, and the ratio of  $\rho'_{ON/OFF}$  in vivo relative to in vitro. In vivo data are extracted from ref. [98] for G type devices and from ref. [234] for RAJ type devices. TXTL data are measured at  $D_{cr} = 1$  and  $D_{ta} = 5$  nM at  $t = 75$  min. The typical value of autofluorescence is  $0.07 \pm 0.01$  a.u.. Error correspond to one standard deviation of a triplicate experiment.

### 5.4.3 Translation from RNA characterizes the reaction between RNA strands

#### Dissociation constant

The regulatory step of translational riboregulators takes place when the two RNA fragments,  $R_{cr}$  and  $R_{ta}$ , hybridize and thereby change the accessibility of the ribosome to a site needed for initiating translation (RBS or AUG). The core of the riboregulation process can thus be described with reactions (5.13) and (5.14), where the first one involves the hybridization of  $R_{cr}$  with  $R_{ta}$  to form an active RNA complex  $R_{act}$  that can be translated, and the second one is the translation of  $R_{act}$  into protein P. We have seen that the thermodynamics of the first reaction play an important role in  $\rho_{ON/OFF}^{th}$  through  $K_d$  (eq. (5.22)). However  $K_d$  is not straightforward to determine. One possibility is to use an electrophoretic mobility shift assay in a polyacrylamide gel. Another way uses the property of a reverse transcriptase to terminate on stable RNA duplexes [128]. In both cases these assays characterize the species  $R_{act}$  for being a duplex RNA but they are not sensitive to its translational activity. Here, instead, we probe the equilibrium concentration of  $R_{act}$  that is active for translation. Our method is thus more meaningful to evaluate the design performances of a riboregulator.

For the bimolecular reaction between  $R_{cr}$  and  $R_{ta}$  to give complex  $R_{act}$  with initial concentrations of, respectively,  $R_{cr}^0$ ,  $R_{ta}^0$  and  $R_{act}^0 = 0$  we have

$R_{cr}$	+	$R_{ta}$	=	$R_{act}$
$R_{cr}^0$		$R_{ta}^0$		0
$R_{cr}^0(1 - X)$		$R_{ta}^0(1 - \frac{R_{cr}^0}{R_{ta}^0}X)$		$R_{cr}^0X$

where  $X$  denotes the extent of the reaction. The dissociation constant  $K_d$  is defined by

$$K_d = \frac{\bar{R}_{cr}\bar{R}_{ta}}{\bar{R}_{act}} = \frac{R_{ta}^0(1 - \bar{X})(1 - \frac{R_{cr}^0}{R_{ta}^0}\bar{X})}{\bar{X}} \quad (5.24)$$

where bars denote equilibrium. Solving (5.24) we obtain:

$$\bar{X}^2 - \frac{K_d + R_{cr}^0 + R_{ta}^0}{R_{cr}^0}\bar{X} + \frac{R_{ta}^0}{R_{cr}^0} = 0. \quad (5.25)$$

The only non-negative solution of this second order equation is

$$\bar{X} = \frac{1}{2} \left( \frac{K_d + R_{cr}^0 + R_{ta}^0}{R_{cr}^0} - \sqrt{\left( \frac{K_d + R_{cr}^0 + R_{ta}^0}{R_{cr}^0} \right)^2 - 4 \frac{R_{ta}^0}{R_{cr}^0}} \right). \quad (5.26)$$

And thus we have

$$\bar{R}_{act} = R_{cr}^0 \bar{X}. \quad (5.27)$$

From the data, we obtain  $I_{norm}$  by normalizing the value of GFP fluorescence at 200 min for each concentration of  $R_{ta}$  using 0 for the fluorescence of the PURE TXTL system without any template and 1 for the GFP fluorescence obtained from the template  $cr^- RNA$  at 5 nM, that serves as a control of batch-to-batch variability. We fit  $I_{norm}$  using three parameters  $a$ ,  $b$  and  $K_d$  with  $I_{norm}(\bar{X}(R_{ta}^0)) = a\bar{X}(R_{ta}^0) + b$ , where  $\bar{X}(R_{ta}^0)$  is given by (5.26).

## Measurement

To characterize reaction (5.13) we in vitro transcribe the five riboregulators described previously (Figure B.2). We study their translation dynamics by titrating 5 nM  $R_{cr}$  with increasing concentrations of its corresponding  $R_{ta}$  in the range 0 – 1000 nM (Figure 5.10). Because translation linearly amplifies  $R_{act}$  (Figure 5.6 (b) and eq. (5.9)), measuring the GFP intensity at a given time is directly proportional to the concentration of  $R_{act}$  that is translationally active. We thus plot the normalized GFP fluorescence at 200 min as a function of the log of  $R_{ta}$  concentration. For a bimolecular equilibrium such as (5.13) one expects these plots to be described by

$$I_{norm} \sim \bar{R}_{act} = \frac{1}{2} R_{cr}^0 \left( \frac{K_d + R_{cr}^0 + R_{ta}^0}{R_{cr}^0} - \sqrt{\left( \frac{K_d + R_{cr}^0 + R_{ta}^0}{R_{cr}^0} \right)^2 - 4 \frac{R_{ta}^0}{R_{cr}^0}} \right) \quad (5.28)$$

where  $\bar{R}_{act}$  is the equilibrium concentration of  $R_{act}$  and superscript 0 indicates initial concentrations. Our experimental data follow this trend (Figure 5.10). We thus fit eq. (5.28) to the data and find dissociation equilibrium constants in the range 10 – 2000 nM (Table 5.3), in agreement with



$K_d$  values of the order of 100 nM that have already been reported for loop-mediated activators [128]. Values of  $K_d$  obtained from different batches of PURE are within 50 %.

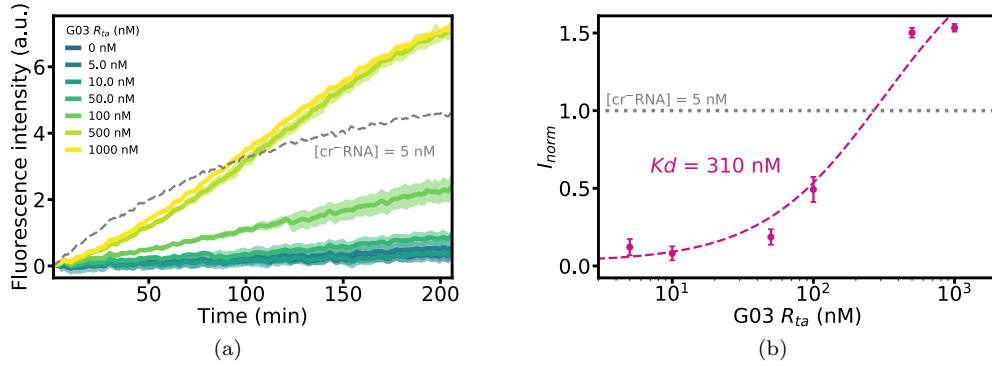


Figure 5.10 | **Titration of a riboregulator at the RNA level measures the dissociation constant of the riboregulator complex.** (a) GFP fluorescence produced over time for different trans-activator concentrations  $R_{ta}$  for riboregulator G03. As a control, the fluorescence intensity produced by the translation of 5 nM of an unregulated cr<sup>-</sup>RNA is shown in grey dashes. (b) Normalized maximum fluorescence titration of  $R_{ta}$  for riboregulator G03. Disks correspond to experimental data and the dashed line is a fit of eq. (5.28) to the data. All experiments are performed in triplicate. Shading around the lines and error bars correspond to one standard deviation.

To further assess the performance of our method for measuring  $K_d$ , we independently measure it with a standard mobility-shift assay performed with capillary gel electrophoresis. We use the same purified  $R_{cr}$  and  $R_{ta}$  that we mix together at 37°C in a buffer with identical salt composition than the TXTL system during the 10 min before performing the electrophoresis assay. The  $R_{cr}$  concentration is 8.3 nM and the  $R_{ta}$  concentration ranges from 0 to 200 nM. Figure 5.11 (a) shows the electropherograms for riboregulator G03, in which a peak in intensity at a given time point corresponds to an RNA structure. We detect three main peaks corresponding to  $R_{ta}$  at 28 s and  $R_{cr}$  and  $R_{act}$  complex between 37 and 40 s. Interestingly, species  $R_{cr}$  and  $R_{act}$  yield well-resolved peaks for toehold-mediated but not for loop-mediated riboregulators, which suggests a structural difference between the two. As a result this method only provides  $K_d$  for some but not all of the tested riboregulators, in contrast with the TXTL method (Figure 5.11 (b) and Table 5.3). The values obtained are of the same order of magnitude as those obtained by TXTL. However, mobility-shift assay yields  $K_d$  in a narrower range of 100-250 nM, while TXTL is able to better discriminate  $K_d$  for the same species and provides values in the range of 15-2200 nM (Table 5.3).

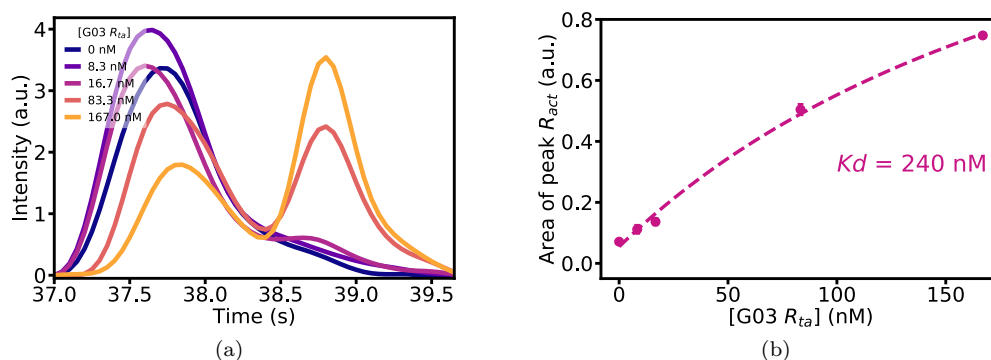


Figure 5.11 | **Titration of translational riboregulator G03 by mobility shift capillary electrophoresis.** (a) Corrected electropherograms versus elution time. (b) Peak area for different concentrations of  $R_{ta}$ . Experiments are performed in triplicate. Error bars correspond to one standard deviation. Dashed line is a fit of eq. (5.28) to the data.

Device	$K_d^{txtl}$ (nM)	$K_d^{ms}$ (nM)
G01	$46 \pm 56$	$180 \pm 20$
G03	$310 \pm 154$	$240 \pm 110$
G80L18	$31 \pm 19$	$110 \pm 90$
RAJ11	$15 \pm 14$	N.M.
RAJ12	$2220 \pm 950$	N.M.

Table 5.3 | **Dissociation constants  $K_d$  at 37°C for the studied riboregulator devices.**  $K_d$  is measured using the cell-free translation method (*txtl*) and the mobility-shift method (*ms*). N.M. indicates that the electropherogram shows ill-defined peaks from which  $K_d$  could not be extracted. Error correspond to one standard deviation of the fit. Values for G03 and RAJ11 are fitted to data in triplicate.

## 5.5 Conclusion

Gene regulation is an essential feature of living systems. The production of proteins has to be controlled in space and in time to ensure the homeostasis of the organism. This regulation can be done at all stages of the production: before and after the transcription, or after the translation. In particular, the regulation of this latter step can be realized by RNA molecules. Indeed a change in their secondary structures — encoded in their nucleotide sequences — can lead to a change in the protein expression thanks to the specific pairing between RNA strands. Here we have studied *de novo* designed RNA riboregulators that regulate the translation of a coding RNA into a protein. *In vitro* TXTL systems are an attractive platform to quantitatively characterize such translational riboregulators. We have taken advantage of the ribosome as a molecular machine that not only recognizes RNA complexes that are translationally active but also measures their concentration. The simplicity of the TXTL system allowed us to propose an analytical expression for the dynamic range of a riboregulator. In quantitative agreement with this model we have shown that increasing the DNA concentration of the trans-activating species first promotes and later inhibits expression. This result suggests that inserting trans-activating elements in high-copy plasmids *in vivo* could limit the efficiency of translational activators, a prediction that shall be tested in future work. Furthermore, relative dynamic ranges measured *in vitro* are in agreement with those reported *in vivo* for four out of five measured riboregulators. Finally, by titrating the *cis*-repressed gene with the trans-activating species at the RNA level we have determined dissociation constants,  $K_d$ , for the RNA hybridization reaction in a very simple manner. Our method has thus provided a simple and rapid way for the quantitative characterization of riboregulators.

*De novo* designed RNA regulators are used in increasingly complex tasks such as cellular logic computation [97] or ultra-specific detection of mutations [116]. Combined with other biomolecular techniques such as molecular beacons [202] or automated-based designs [64], cell-free transcription-translation systems are becoming essential for a wide brand of applications. They allow to verify theoretical predictions on both RNA structures and on the behavior of large scale regulatory networks. Their versatility is a real asset for conceiving new synthetic biological features [130] and creating innovative biomolecular tools such as paper-based synthetic gene networks [213] used to design low-cost detection systems of the Zika virus [214]. Cell-free TXTL systems have been expanded to non-model bacteria [187] and have recently entered the machine learning era [7, 296].

# Chapter 6

## Conclusion

In this thesis I have presented the work I have undertaken at the Laboratoire Jean Perrin at Sorbonne Université, under the supervision of André Estevez-Torres and Jean-Christophe Galas on the design of molecular systems to study pattern formation and gene regulation in reconstituted systems. This work was motivated by the construction of artificial systems that reproduce essential features of life. Using a cell-free approach, I have designed systems that self-organize and express proteins. I have obtained three main results. Firstly, I have reported the experimental observation of a new type of spatial instability in active gels: the corrugation of a 3D nematic fluid through the interplay of passive and active forces. Secondly, inspired from chemo-mechanical morphogenetic processes during embryo development, I have combined a reaction-diffusion patterning system with an active matter system capable of generating forces from the hydrolysis of nucleotides. Finally, I have proposed a method to characterize *in vitro* the performance of RNA regulators using a cell-free expression system.

More precisely, in Chapter 2 we have reviewed two main self-organization mechanisms in molecular systems: active matter and reaction-diffusion. These mechanisms are able to generate diverse spatio-temporal patterns. We have focused our description on two systems that were of special interest for our purposes. Firstly, we have discussed an *in vitro* active matter, and in particular, reconstituted active gels composed of cytoskeletal filaments, molecular motors and a source a chemical energy (often in the form of ATP). Secondly, we have described a programmable chemical system composed of ssDNA and a few enzymes: the PEN-DNA toolbox. By tuning the sequences of the DNA strands and the concentrations of the components, one can create various chemical systems that give rise to reaction-diffusion patterns. Active matter and reaction-diffusion are essential mechanisms to understand morphogenesis *in vivo*. They are intimately intertwined, especially during embryo development where many morphological changes take place. Finally, we have seen that *in vitro* efforts have been made to combine several self-organizing mechanisms and mimic the properties of living systems. However they either lack tunability, autonomy or biocompatibility. Parts of this chapter will be published in [89].

In Chapter 3, we have modified a previously-proposed molecular active gel composed of microtubules and clusters of kinesin [241], in particular by using long instead of short microtubules. Depending on the concentrations of motors, microtubules and depleting polymers, such a system

self-organizes into various structures: asters, contracted networks, corrugated nematic sheets and turbulent active flows. We have described each of the conditions and developed in more details the ones that led to a corrugated stable pattern. The wavelength of this pattern could be tuned by, among others, the motor concentration and the depletion forces, in qualitative agreement with a hydrodynamical theory. This work has been published in [253]. Moreover, using short microtubules we have characterized the path to turbulence — in terms of orientation — of an initially aligned bundle network in 3D, following work that characterized this instability in 2D [174]. Lastly, we have presented two methods for creating active droplets, and exposed some ideas that might be interesting to explore in the future.

In Chapter 4 we have combined this active gel with a programmable DNA reaction-diffusion front. We have shown that this front — made with the PEN-DNA toolbox — could propagate in an active gel. The two systems behave independently but could be coupled in some cases. Indeed, they could be linked through hydrodynamical interactions (when the active gels contract globally) and chemically via the competition for dGTP resources, leading to non-uniform patterning. We have also begun to develop an autocatalytic system that would work with a turbulent active fluid, which might form a reaction-diffusion-advection system. Lastly, we have detailed the protocol to covalently attach DNA on kinesin motors via the specific SNAP-tag. This method was originally devised to specifically couple through a DNA sequence the propagating front and the active gel. However, despite our efforts, this coupling could not be demonstrated due to the non-specific clustering of the SNAP-tag modified kinesin motors. This method could nevertheless be used in a gliding assay experiment in order to control the motor attachment to the surface thanks to DNA molecules.

Gene expression relies on regulatory reaction networks. In Chapter 5 we have reconstituted the machinery of transcription and translation in order to study the regulation of genetic expression thanks to RNA regulators. We have demonstrated that such a cell-free system is able to successfully produce protein in a controlled manner, depending on the concentration in regulators (starting from DNA or RNA). Moreover, the system could provide valuable information on the regulators such as the dynamic range and the dissociation constant of between RNA regulator strands. This work has been published in [254].

Several directions can be explored in future works. Firstly, reconstituted active gels could be associated to passive gels in order to tune their rheological properties. Secondly, the study of populations of active droplets also seems worthwhile: because of their activity, they show non-trivial behaviors — such as self-propelled motion — and potentially exhibit collective effects — such as ordering and synchronization — when embedded into an active emulsion [103]. Thirdly, the combination of active gels and the PEN-DNA toolbox can be enlarged to other reaction-diffusion structures such as stable stripes: what is the stability of a ‘French flag’ pattern [326] in the presence of an active gel? Moreover, the coupling with DNA reaction-diffusion patterns can be further examined using chemical interactions between DNA and molecular motors, microtubules or surfaces. Finally, DNA reactions can be localized on colloidal particles [87], leading to a system composed of numerous agents that communicate thanks to DNA signals and that are transported by local — or global, if constrained in particular geometry [319] — advection of the active gel. Furthermore, DNA can be attached to the surface of moving active droplets to form self-organized

emulsions.




RNA regulators can be coupled to molecular programs designed with the PEN-DNA toolbox to perform, for instance, the sensing of a viral RNA genome [86, 214]. The potential of cell-free transcription-translation systems can be further exploited to produce specific enzymes [33].





































Insights from self-organized mechanisms and gene expression is useful to design smart autonomous materials [62, 151]. In combination with synthetic biology techniques, bio-printing, microfluidics and machine learning methods, they may help in the construction of artificial cells which produce molecules [204, 309, 91] and are assembled into multicellular artificial tissues capable of communication [302, 1, 56].



# Appendix A

## Movies

Movies of the time-lapse experiments are individually available for download  or online watching  (password: *pattern*). They are also available combined into one file ( .zip, 110 Mo).

- A.1 Bundles bend and break under the forces of kinesin clusters [, .
- A.2 Formation of an aster made of microtubule bundles [, .
- A.3 A connected active network can exhibit several morphologies depending on the motor concentration [, .
- A.4 Confocal images and  $xz$  sectioning of a 3D extensible, nematic gel made of microtubules and kinesin motors forming a corrugated sheet [, .
- A.5 Dynamics, shape and stability of the patterns depending on the motor concentration [, .
- A.6 A 3D extensible, nematic gel made of microtubules and kinesin motors forms a corrugated sheet that breaks into active turbulence at high motor concentration [, .
- A.7 Confocal images of a 3D extensible, nematic gel made of microtubules and kinesin motors forming a corrugated sheet that breaks into active turbulence at high motor concentration [, .
- A.8 Initial wavelength selection in active flows [, .
- A.9 Emulsion of active droplets in the presence of an external flow [, .
- A.10 Formation of 2D active nematics on the inner surface a droplet [, .
- A.11 Reaction-diffusion front in the presence of the active gel [, .
- A.12 Corrugated patterns in the presence of a reaction-diffusion front [, .
- A.13 Influence of dNTP on internally driven chaotic flows [, .
- A.14 Different dGTP concentrations lead to inhomogeneous patterns [, .
- A.15 Propagation of a front (LT\_10) in the presence of K401-BCCP [, .
- A.16 Gliding motility assay of microtubules [, .
- A.17 Propagation of a front in a population of DNA-functionalized beads [, .
- A.18 DNA-functionalized beads immersed in an active bath [, .





# Appendix B

## Protocols

### B.1 Supplementary protocols of Chapter 3 and Chapter 4

#### K430-FLAG-SNAP purification

Heterodimer K430-FLAG-SNAP is expressed in competent cells, Rosetta2 (DE3) (Novagen). The cells are cultured in LB supplemented with 100  $\mu\text{g}/\text{mL}$  ampicilin and 34  $\mu\text{g}/\text{mL}$  chloramphenicol at 37°C until  $\text{OD}_{660} = 0.6$ . The protein expression is induced by 0.1 mM IPTG for 5 hours at 22°C. The cells are collected by centrifugation at 4°C and resuspended in the Lysis Buffer: Buffer A (20 mM Na-Pi buffer pH 7.5, 1 mM  $\text{MgSO}_4$ , 250 mM NaCl, 0.015 mM ATP, 10 mM  $\beta$ -mercaptoethanol, 0.1%(v/v) Tween-20) supplemented with 10 mM imidazole and 1X protease inhibitor cocktail (Sigma-Aldrich). The cell suspension is then sonicated with a VCX-130 sonicator (Sonics Materials) at 40% of its maximal power, alternating 10 s of sonication and 30 s of pause during about 5 min. It is important that the solution does not heat in order to prevent denaturation and degradation of proteins. Then the lysate is centrifuged to collect cells debris. The supernatant is collected and filtrated before mixing with Ni-IMAC resin (Biorad) in a volume ratio 20:1 (lysate:resin). The mix is gently agitated at 6°C on a rotary wheel for 20 min. The resin is washed first with the Buffer A and 10 mM imidazole, and then with the same buffer but with 50 mM of imidazole. The resin is eluted with the Buffer A supplemented with 250 mM imidazole for 30 min.

This eluate is then bound to an anti-FLAG agarose column (Sigma-Aldrich), washed with Buffer A and then eluted with Buffer A supplemented with 0.35 mg/ml of the 3X FLAG peptide (Sigma-Aldrich or produced at the IBPS molecular interaction platform). The excess of 3X FLAG peptide is removed using an Amicon filter (30 kDa) and the Buffer C (80 mM PIPES-KOH pH 6.9, 250 mM K-acetate, 10 mM  $\text{MgSO}_4$ , 250 mM NaCl, 1 mM ATP, 1 mM DTT, 10% sucrose). The filtered protein is then flash frozen and kept at -80°C.

#### K430-HSNAP purification

From the plasmid coding for the heterodimer K430-FLAG-SNAP designed by Furuta et al. [73], we have built a homodimer version containing a SNAP-tag on each arm. Furuta's plasmid, pET-

32ark430(C7S)-FlagC-rk430(C7S)-SnapC-His, which expresses both the kinesin with a SNAP and HIS-tags and kinesin with a FLAG is digested at two EcoRI sites to split into two fragments of Kinesin-FLAG sequence and kinesin-SNAP-HIS with backbone sequence coding ampicillin resistance gene. The digested linear sequences are purified by QIAquick PCR Purification Kit (Qiagen) and recircularized by T4 DNA ligase using Rapid DNA Ligation Kit (Thermo Scientific). The recircularized plasmids are transformed into DH5 $\alpha$  competent cells and selected on 100  $\mu$ g/mL ampicillin including agar plate. The plasmids in colonies on agar plate are amplified in LB ampicillin medium and purified with Monarch Plasmid Miniprep Kit protocol (New England Biolabs). The sequence is verified by restriction enzyme digestion. K430-HSNAP is then purified using the HIS-tag on a Ni-IMAC resin in the exact same way than K430-FLAG-SNAP. Here, the eluate is then filled in 14 kDa MWCO cellulose tube (Sigma-Aldrich) and then dialyzed with Buffer A three times (2 times 1 hour and overnight) at 4°C. The dialyzed protein is further purified with a Superdex 200 Increase column (GE Healthcare). The kinesin corresponding peak fractions are collected, flash frozen and kept at -80°C.

### **K401-BCCP purification**

For K401-BCCP purification, pT7-7 DmKinesin 1-401 BCCP-CHis6 (pWC2) plasmid designed by Gelles [270] is expressed in competent cells Rosetta2 (DE3) (Novagen). The cells are cultured in LB supplemented with 100  $\mu$ M biotin, 100  $\mu$ g/mL ampicillin and 34  $\mu$ g/mL chloramphenicol at 37°C until OD<sub>660</sub> = 0.7. The protein expression is induced by 1 mM IPTG for 2 hours at 22°C and then the biotinylation is induced by 0.2 mM rifampicin for 20 hours at 22°C. The cells are collected and resuspended in the Buffer B (50 mM PIPES pH 7.2, 4 mM MgCl<sub>2</sub>, 50  $\mu$ M ATP, 10 mM  $\beta$ -mercaptoethanol) supplemented with 20 mM imidazole and 1X protease inhibitor cocktail (Sigma-Aldrich). The cell suspension is then sonicated (VCX-130, Sonics Materials) and centrifuged. The supernatant is collected and filtrated before mixing with Ni-IMAC resin (Biorad). The resin is washed with the Buffer B and 20 mM imidazole. The resin is eluted with the Buffer B and 500 mM imidazole. The eluate is filled in Float-A-Lyzer G2 (5 mL 50 kDa MWCO, Spector/Por), dialyzed with Dialysis Buffer (250 mM PIPES pH 6.7, 20 mM MgCl<sub>2</sub>, 0.25 mM ATP, 50 mM  $\beta$ -mercaptoethanol) three times (1 hour, 2.5 hours and overnight) at 4°C. The dialyzed protein supplemented with 36% sucrose and 2 mM dithiothreitol (DTT) is flash frozen and kept at -80°C.

### **Microtubule polymerization using GTP or GMPCPP**

Tubulin and TRITC-labeled tubulin are purchased from Cytoskeleton, dissolved at 10 mg/mL in 1X PEM buffer (80 mM PIPES pH 6.8, 1 mM EGTA, 1 mM MgSO<sub>4</sub>) supplemented with 1 mM GTP, flash frozen and stored at -80°C. The polymerization mix consists of 1X PEM, 1 mM GTP, 10%(w/v) glycerol and microtubules at 5 mg/mL (including 2.5%(v/v) fluorescent tubulin). First the mix is centrifuged at 4°C for 15 min at 16000g to remove small aggregates of tubulin. The corresponding supernatant is transferred into a new tube and incubated at 37°C for 15 min. 20  $\mu$ M of paclitaxel is added to the mix and let at 37°C for five more minutes. After polymerization, newly formed microtubules are centrifuged at room temperature for 10 min at 12000g to remove free tubulin monomers. The microtubules are redissolved into 1X PEM, 1 mM GTP, 10%(v/v) glycerol, 20  $\mu$ M taxol and kept in the dark at room temperature for a few days.

GMPCPP (Jena Bioscience) microtubules are polymerized from the tubulin stock solution that does not contain GTP, in the presence of 0.6 mM GMPCPP and 0.2 mM DTT at 37°C for 30 min and left at room temperature for 5 hours. They are used within the same day or flash frozen and kept at -80°C.

## Glass slides passivation, channel assembly and imaging

Glass slides and coverslips are washed and sonicated in deionized water and Helmanex (a commercial cleaning solution), then in ethanol and finally in a 0.1 M KOH solution, with rinsing with deionized water between each step. They are immersed in the silane-coupling solution (0.5%(v/v) 3-(Trimethoxysilyl)propylmethacrylate, 98.5%(v/v) ethanol and 1%(v/v) acetic acid) for 15 to 30 min, rinsed and then put in a degassed solution of 2%(w/v) acrylamide, 0.07%(w/v) ammonium persulfate and 0.035%(v/v) TEMED. They can be used 2 h after this last step and can be kept for one month in a closed container, in the acrylamide mix. Just before use, a glass slide and a coverslip are rinsed with water and dried with clean air.

Channels are assembled using an acrylamide-coated microscope glass slide (26×75×1 mm) and a coverslip (22×50×0.17 mm) separated by strips of parafilm cut with a Graphtec Cutting Plotter CE6000-40 for better reproducible channels.

Epifluorescence images are obtained with a Zeiss Observer 7 automated microscope equipped with a Hamamatsu C9100-02 camera, a 2.5 X, 10 X or 20 X objective, a motorized stage and controlled with MicroManager 1.4. Images are recorded automatically every 1 to 3 min using an excitation at 550 nm with a CoolLED pE2. In order to resolve 3D structures we record confocal images when needed. They are obtained either with a Leica TCS SP5 II confocal microscope with a 25 X water-immersion objective or a X-Light V2 Spinning Disk Confocal system mounted at the IBPS (Institut de Biologie Paris-Seine) imaging facility, or on an upright Nikon Eclipse 80i microscope with a 10 X objective in the lab. Images are recorded automatically every 1 to 10 min with a z step of 3 to 5  $\mu\text{m}$ .

## Attaching biotin-DNA on streptavidin-sepharose beads

We attach ssDNA biotin-modified template to the streptavidin-modified sepharose beads by following the protocol described in ref. [87]. Commercial 34  $\mu\text{m}$ -diameter streptavidin beads (GE Healthcare) are first washed three times in Buffer C (0.6X PEM-KOH, 0.2X PEM-NaOH, 8 mM  $\text{MgSO}_4$ , 1.5%(w/v) pluronic). It consists in successive rounds of addition of buffer, centrifugation and removal of buffer. Then beads are diluted to a concentration of 5000 beads/ $\mu\text{L}$ . Finally they are mixed at a concentration of 2500 beads/ $\mu\text{L}$  with 2.5  $\mu\text{M}$  of biotin-modified DNA template to reach a stock of 0.1 nmol of template for  $10^5$  beads (meaning that 100 beads/ $\mu\text{L}$  is equivalent to 100 nM of DNA template). The mix is incubated for 15 min at room temperature and washed three times to remove non-reacting DNA. If not used in an experiment, functionalized beads are kept at 4°C for several weeks. Just before use, the solution is vortexed and sheared by pipeting.

At this concentration DNA templates do not attach uniformly to the sepharose beads. They tend to concentrate more on the surface than the interior (Figure B.1). They form shells that cover the surface of the beads.

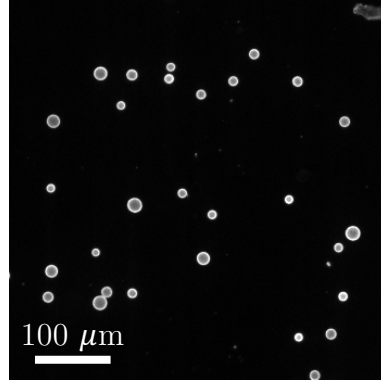


Figure B.1 | **DNA attached to sepharose beads.** Attached DNA form shells that cover the surface of beads and which are visible using SGI intercalator.

## B.2 Supplementary protocols of Chapter 5

### DNA preparation

DNA templates are prepared by PCR amplification of plasmids encoding for the RNA translational regulators, followed by affinity column purification using Monarch PCR Purification Kit (New England BioLabs) or PureLink PCR Purification Kit (Thermo Fisher Scientific). Primers used for PCR amplification contained a T7 promoter or a T7 terminator (Biomers) (Table B.1). DNA integrity is determined by a 1.5% agarose gel. Concentrations are determined by absorbance at 260 nm using a NanoDrop 2000 UV-vis spectrophotometer.

Primers	Sequences (5' → 3')
RAJ11 $D_{cr}$ FP	TAATACGACTCACTATAGGCCTCGCATAATTTCACTTCTTCAATCC
RAJ11 $D_{cr}$ RP	CAAAAAACCCCTCAAGACCCGTTTAGAGGCCCAAGGGGTTATGCTATTATTTGTATAGTTCATCCA TGCCATGTGTAATC
RAJ11 $D_{ta}$ FP	CAAAAAACCCCTCAAGACCCGTTTAGAGGCCCAAGGGGTTATGCTAGCCTCGCATAAATCTGTCA CAG
RAJ11 $D_{ta}$ RP	TAATACGACTCACTATAGGGGGAGGGTTGATTGTGTGAGTC
RAJ12 $D_{cr}$ FP	TAATACGACTCACTATAGGACCCAGTATCATTCTCTTCTTCTGCC
RAJ12 $D_{cr}$ RP	CAAAAAACCCCTCAAGACCCGTTTAGAGGCCCAAGGGGTTATGCTATCATCATTGTACAGTTCAT CCATACCATGC
RAJ12 $D_{ta}$ FP	ATCGTATTGGGGAACCCCGGAGATTGCCCAGAACTCCCCAAAAAGCCTCGCATAAATCTGTAC AGCATC
RAJ12 $D_{ta}$ RP	TAATACGACTCACTATAGGGGGCAGGAAGAAGGGTTCCTTT
G $D_{cr}$ and $D_{ta}$ FP	CGCGCTAATACGACTCACTATAGG
G $D_{cr}$ and $D_{ta}$ RP	CAAAAAACCCCTCAAGACCCGTT

Table B.1 | **List of PCR primers used to produce linear DNA templates.** The plasmids coding for the G regulators already contained T7 promoter and T7 terminator in their sequences. We use the two same primers to amplify the G regulators by PCR.

A typical protocol for the PCR is showed in Table B.2:

Step	Duration (min)	Temperature (°C)	Nb of cycles
Initial denaturation	2	95	1
Denaturation	0.5	95	30
Annealing	1	66	
Elongation	1	72	
Final denaturation	5	72	1

Table B.2 | **Typical PCR protocol to produce linear DNA templates.**

## RNA preparation

RNA templates are prepared by in vitro transcription (HiScribe T7 High Yield RNA Synthesis Kit, New England BioLabs) for 2 hours followed by purification using the MEGAclear Transcription Clean-Up Kit (Ambion). RNA integrity is determined by a 1.5%(w/v) agarose gel (Figure B.2). Concentrations are determined by absorbance at 260 nm using a NanoDrop 2000 UV-vis spectrophotometer.

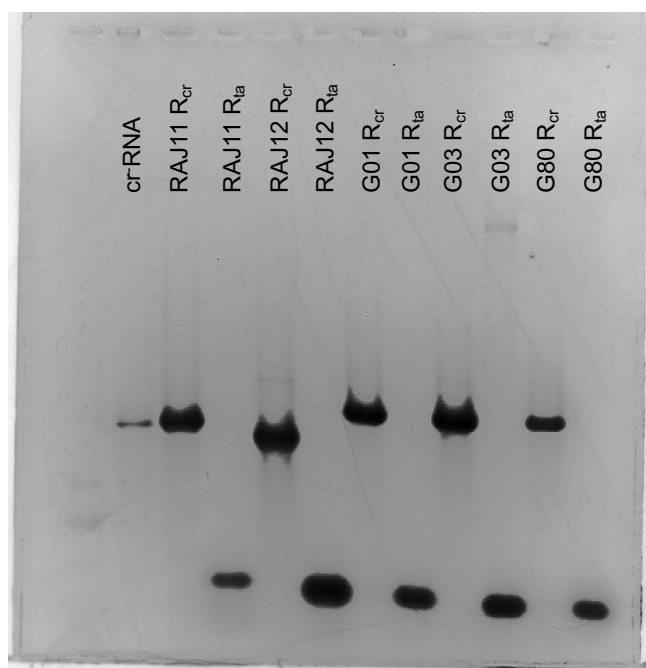


Figure B.2 | **Integrity of RNA regulators** Non-denaturing 1.5% agarose gel of the in vitro transcribed riboregulators.

## Composition of the PURE TXTL system

The PURE TXTL system is prepared according to ref. [259] to reach the composition depicted in Table B.3.

	Name	Concentration
Buffers	Hepes-KOH pH 7.6	50 mM
	Potassium glutamate	100 mM
	Magnesium acetate	13 mM
	Spermidine	2 mM
	DTT	1 mM
Translation factors	IF1	10 $\mu\text{g}/\text{mL}$
	IF2	40 $\mu\text{g}/\text{mL}$
	IF3	10 $\mu\text{g}/\text{mL}$
	EF-G	50 $\mu\text{g}/\text{mL}$
	EF-Tu	100 $\mu\text{g}/\text{mL}$
	EF-Ts	50 $\mu\text{g}/\text{mL}$
	RF1	10 $\mu\text{g}/\text{mL}$
	RF2	10 $\mu\text{g}/\text{mL}$
	RF3	10 $\mu\text{g}/\text{mL}$
	RRF	10 $\mu\text{g}/\text{mL}$
Energy sources	ATP, GTP	2 mM
	CTP, UTP	1 mM
	CP	20 mM
Other enzymes	Ribosomes	1.2 $\mu\text{M}$
	ARS	600-6000 U/mL [259]
	MTF	4500 U/mL
	Creatine kinase	4.0 $\mu\text{g}/\text{mL}$
	Myokinase	3.0 $\mu\text{g}/\text{mL}$
	Nucleoside-diphosphate kinase	1.1 $\mu\text{g}/\text{mL}$
	Pyrophosphatase	1.0 U/mL
T7 RNAP	10 $\mu\text{g}/\text{mL}$	
Other components	20 amino acids	0.3 mM
	10-formyl-5, 6, 7, 8-tetrahydrofolic acid	10 $\mu\text{g}/\text{mL}$
	tRNA mix	56 A260/ml
	RNase inhibitor Murine	1 units/ $\mu\text{L}$

Table B.3 | Composition of the PURE TXTL system

## Appendix C

# Hydrodynamic theory of an undulating active film

This theory has been developed by Ananyo Maitra and Raphael Voituriez.

In this section, we discuss an active fluid model [173, 226, 222, 135] to understand the buckling of the effectively two-dimensional sheet formed by the microtubules and obtain a theoretical estimate for the scaling of the wavelength of the undulatory pattern with motor concentration. The thickness of the nematic film, lying parallel to the  $xy$  plane, in the  $z$  direction is denoted by  $\ell_z$  and the channel thickness in the  $z$  direction by  $H$ . The width of the channel in the  $y$  direction is  $W$  and the length along  $x$  is  $L$ . The film is formed by injecting an isotropic microtubule fluid into the channel of dimensions  $L \times W \times H$ . The interaction mediated by depletion agents in the fluid then leads to the phase separation of the microtubule filaments and the fluid with a local concentration of filaments that exceeds the threshold for isotropic-nematic (I-N) transition. Due to the geometry of the channel, the nematic order develops along the long  $x$  axis, leading to the formation of a film which contracts along the  $y$  and  $z$  direction and extends along the  $x$  direction. This leads to a nematic film which is the thinnest along the  $z$  direction. The orientation of the nematic is described by the director field  $\hat{\mathbf{n}} = \cos \phi \hat{x} + \sin \phi \hat{z} = \hat{\mathbf{n}}_0 + \delta \mathbf{n}$ , with the unbuckled state having the director  $\hat{\mathbf{n}}_0 = \hat{x}$ .

This film buckles along the  $z$  direction due to the action of motors. We will now describe the physics of this buckling. We assume that the density of microtubules within the layer is fixed. We further assume that the nematic film buckles in the  $z$  direction as whole. The departure of the mid-plane of the film from a fiducial flat surface which we take to be the mid- $xy$  plane of the channel is described by the height field  $h(x, y, t)$  of the membrane point whose projection on that fiducial plane has the coordinates  $(x, y)$ . Such a buckling is possible due to tilting of the microtubule filaments in the  $xz$  plane  $\delta \mathbf{n} \approx \partial_x h \hat{z}$  to linear order.

In equilibrium, tilting of filaments is penalised by the Frank elasticity [45], considered here within a simplifying one Frank-constant approximation, which yields a bending modulus of the film:



$$F_{\text{Frank}} = \frac{\bar{K}}{2} \int d^3 \mathbf{r} (\nabla \hat{\mathbf{n}})^2 \approx \frac{K}{2} \int d^2 \mathbf{x} (\partial_x^2 h)^2. \quad (\text{C.1})$$

where  $K = \bar{K} \ell_z$  and  $\mathbf{x}$  describes the  $x - y$  plane. The membrane is confined in a channel of height  $H$ , which means that its mean-squared height fluctuations  $\langle h^2 \rangle \sim H^2$ . Following [66, 65, 68], we implement this constraint in an approximate manner by introducing a harmonic potential  $(\gamma/2)h^2$  in the effective free energy of the membrane i.e.,

$$F_h = \frac{1}{2} \int d^2 \mathbf{x} [K(\partial_x^2 h)^2 + \gamma h^2]. \quad (\text{C.2})$$

In equilibrium at a temperature  $T$ , equating the mean-squared fluctuation with  $H^2$  yields  $\gamma = (K_B T / 8H^2)^2 / K$ . The membrane does not have a passive surface tension since we assume that it is free to adjust its area to maintain the preferred areal density of microtubules due to the depletion forces constant [240]. However, in the experiments in which the channel is confined in the  $x$  direction as well, the microtubule sheet may have a pattern even in the absence of motors due to Euler buckling. Since this is only manifested for channels confined along the  $x$  axis and vanishes in other cases, we ignore this passive effect from here on and instead focus on the motor-driven periodic corrugation of the active membrane.

We model the dynamics of an active membrane with the passive restoring forces arising from the derivative of a free-energy given by eq. (C.2). Since the membrane is suspended in a fluid, it moves due to the motion of the fluid. Since  $h$  represent the height of a membrane point above a fiducial surface,  $\dot{h} \sim v_z|_m$  where  $v_z|_m$  is the  $z$  component of the fluid velocity at the membrane position. For the linear theory that we are interested in here,  $v_z|_m$  can be approximated by  $v_z(0)$  the  $z$  component of the velocity at the position of the fiducial plane. However, if fluid can pass (permeate) through the membrane, fluid flow need not correspond to the motion of the membrane. This relative velocity of the fluid and a passive membrane is  $\propto \mu \delta F_h / \delta h$ , where  $\mu$  is the permeation coefficient. In addition, active membranes may move relative to the background fluid due to an active speed  $\sim -\mu \bar{\zeta}(c) \hat{\mathbf{n}}_0 \cdot \nabla \delta \mathbf{n} \approx -\mu \bar{\zeta}(c) \partial_x^2 h \hat{z}$  [170]. For extensile filaments, the active coefficient, whose magnitude depends on the motor concentration,  $\bar{\zeta}(c) > 0$ . Thus, the hydrodynamic equation for  $h$  is

$$\dot{h} - v_z(0) = -\mu \frac{\delta F_h}{\delta h} - \mu \bar{\zeta}(c) \partial_x^2 h \quad (\text{C.3})$$

The Stokes equation for the velocity field containing the membrane composed of active units is

$$\eta \nabla^2 \mathbf{v} = \nabla \Pi + \zeta(c) \nabla \cdot (\mathbf{nn}) \delta(z) + \frac{\delta F_h}{\delta h} \hat{z} \delta(z) \approx \nabla \Pi + \left( \zeta(c) \partial_x^2 h + \frac{\delta F_h}{\delta h} \right) \hat{z} \delta(z) + \boldsymbol{\xi}_v \quad (\text{C.4})$$

where  $\Pi$  is the pressure that enforces the incompressibility constraint  $\nabla \cdot \mathbf{v} = 0$ ,  $\zeta$  is the coefficient of the standard active stress  $\zeta(c) > 0$  for extensile systems. Note that, in principle,  $\zeta(c)$  and  $\bar{\zeta}(c)$  can be different from each other, though their dependence on motor concentration is expected to be the same. To obtain the second approximate equality, we have ignored all fluctuations of the nematic director in the  $xy$  plane (we will discuss the consequence of this approximation later).

The fluid is in a channel of thickness  $H$ . We now use the Fourier transformed version of eq.

(C.4) to calculate  $v_z(0)$  by summing over all Fourier modes for which  $|q_z| > 2\pi/H$ , which takes the constraint due to the channel into account in an approximate manner. Eliminating the pressure by projecting the Fourier transformed velocity transverse to the wavevector direction, we obtain

$$v_z(0) = \frac{-1}{2\pi\eta} \left[ \int_{\frac{2\pi}{H}}^{\infty} dq_z \frac{q_x^2}{(q_x^2 + q_z^2)^2} G_z(q_x) + \int_{-\infty}^{-\frac{2\pi}{H}} dq_z \frac{q_x^2}{(q_x^2 + q_z^2)^2} G_z(q_x) \right] \quad (\text{C.5})$$

where  $G_z(q_x)$  is the Fourier transform of  $\zeta(c)\partial_x^2 h + \delta F_h/\delta h$ . This yields

$$v_z(0) = -\frac{1}{4\eta|q_x|} \left[ 1 - \frac{4H|q_x|}{4\pi^2 + H^2 q_x^2} - \frac{2}{\pi} \tan^{-1} \left( \frac{2\pi}{H|q_x|} \right) \right] G(q_x) \quad (\text{C.6})$$

The effective mobility goes to  $-1/4\eta|q_x|$  in the limit  $H \rightarrow \infty$  [29] and  $\sim q_x^2 H^3$  for  $q_x H \ll 1$  [96, 251]. The force

$$G(q_x) = (Kq_x^4 - \zeta(c)q_x^2 + \gamma)h_{\mathbf{q}}. \quad (\text{C.7})$$

Putting this back in the equation for height fluctuations, and Fourier transforming in space and time, we obtain

$$\omega = -\frac{i}{4\eta|q_x|} \left[ 1 - \frac{4H|q_x|}{4\pi^2 + H^2 q_x^2} - \frac{2}{\pi} \tan^{-1} \left( \frac{2\pi}{H|q_x|} \right) \right] (Kq_x^4 - \zeta(c)q_x^2 + \gamma) - i\mu(Kq_x^4 - \bar{\zeta}(c)q_x^2 + \gamma) \quad (\text{C.8})$$

Since both the hydrodynamic mobility and the permeation coefficient  $\mu$  are always positive, we clearly see that extensile activity leads to a positive growth rate for a band of wavenumbers. If permeation dominates over hydrodynamics, a band of wavevectors between

$$q_{x\pm}^2 = \frac{\bar{\zeta}(c) \pm \sqrt{\bar{\zeta}(c)^2 - 4K\gamma}}{2} \quad (\text{C.9})$$

is unstable. Note that, unlike usual active planar instabilities, the instability here is not long wavelength i.e., the membrane is stable for  $q_x \rightarrow 0$  due to the confinement. The fastest growing mode is

$$q_x^* = \sqrt{\frac{\bar{\zeta}(c)}{2K}}. \quad (\text{C.10})$$

We identify this with the wavevector of the pattern we observe. Further, it is known [174] that active forces scale as  $c^2$ . This implies that the wavelength of the buckled pattern should scale linearly with  $c$ , i.e.,  $\lambda = 2\pi/q^* \propto c$ . This linear scaling is observed in our experiments.

If hydrodynamics dominates over permeation (such that permeation can be ignored), the unstable band of wavevectors is given by (C.9), but with  $\bar{\zeta}(c)$  replaced by  $\zeta(c)$ . Furthermore, in the limits  $Hq_x \rightarrow \infty$  and  $Hq_x \rightarrow 0$ , the fastest growing mode is

$$q_x^* = \sqrt{\frac{\zeta(c)}{2K}}. \quad (\text{C.11})$$

While the observed selected wavelength in our system is in neither regime,  $Hq_x = 2\pi H/\lambda \sim \mathcal{O}(1)$ , we do not believe that this will significantly change the scaling with  $\zeta$ . Further, since  $\zeta(c)$  and  $\bar{\zeta}(c)$  should scale the same way with  $c$ , the scaling of the wavelength of the pattern with  $c$  remains the

same,  $\lambda \propto c$  for both permeation dominated and hydrodynamics dominated cases. However, the hydrodynamics dominated and the permeation dominated cases can be distinguished by looking at the dependence of the characteristic frequency on activity. For the permeation dominated case,

$$i\omega^* \sim \mu(Kq_x^{*4} - \bar{\zeta}(c)q_x^{*2} + \gamma). \quad (\text{C.12})$$

This implies that  $i\omega^* \sim \bar{\zeta}^2 \sim c^4$ . For the hydrodynamics dominated case, and for  $q_x H \gg 1$ ,  $i\omega^* \sim \zeta^{3/2} \sim c^3$  while for  $q_x H \ll 1$ ,  $\omega^* \sim \zeta^3 \sim c^6$ .

We have primarily discussed the fluctuation of the thin film along the  $z$  direction. The film also contracts along the  $y$  direction. A similar theory could be constructed for the undulations of the film in the  $y$  direction as well. Since the film is thicker in this direction, thus having a larger bending modulus,  $K_w \sim \bar{K}w$ , where  $w$  is the width of the film, these undulations have a longer wavelength since  $q_w^* \sim 1/\sqrt{K_w}$  and  $K_w > K \implies q_w^* < q^*$ . However, when the anisotropy of the channel is reduced such that  $W \sim H$  and therefore,  $w \sim \ell_z$ , buckling in both  $y$  and  $z$  direction should be observed simultaneously and should have roughly equal wavelengths. Ultimately, at high activities the coupling of undulations in  $y$  and  $z$  directions leads to the destruction of the periodically modulated state. Finally, We have not considered the fluctuation of the nematic order of the microtubules in the plane of the membrane. Taking into account such fluctuations is complicated (see [197, 198]) and, in any case, would not change the linear physics of the membrane modulation discussed here.

## Appendix D

# Kinetic model of the PURE TXTL system

### D.1 Translation

From eqs. (5.1-5.7) in the Chapter 5, translation corresponds to initial conditions ( $D_{act}(0) = 0$ ,  $R_{act}(0) = R_{act}^0$  and  $P(0) = P^*(0) = 0$ ). We should thus consider the system of equations

$$\frac{dP}{dt} = r_{tx} - r_m = \kappa_{tl} - k_m \cdot P \quad (\text{D.1})$$

$$\frac{dP^*}{dt} = r_m = k_m \cdot P \quad (\text{D.2})$$

where we have noted  $\kappa_{tl} = \frac{k_{tl} \cdot R_{act}^0}{K_{tl} + R_{act}^0}$ . Calling the total protein concentration  $P_{tot} = P + P^*$  and adding eq. (D.1) and eq. (D.2) we have

$$\frac{dP_{tot}}{dt} = \kappa_{tl} \quad (\text{D.3})$$

which solution is  $P_{tot}(t) = \kappa_{tl}t$ . Combining eq. (D.2) and eq. (D.3) we have

$$\frac{dP^*}{dt} = k_m(\kappa_{tl}t - P^*) \quad (\text{D.4})$$

that is a linear ODE that can be written in the form

$$g(t)y' = f_1(t)y + f_0(t), \quad (\text{D.5})$$

with  $g = 1$ ,  $f_1 = -k_m$  and  $f_0 = k_m\kappa_{tl}t$ . The solution of eq. (D.5) is

$$y = Ce^F + e^F \int e^{-F} \frac{f_0(t)}{g(t)} dt, \text{ where } F(t) = \int \frac{f_1(t)}{g(t)} dt \quad (\text{D.6})$$

We find  $F(t) = -k_m t$  and the solution of eq. (D.4) is thus

$$P^* = \frac{\kappa_{tl}}{k_m} (e^{-k_m t} + k_m t - 1) \quad (\text{D.7})$$

which corresponds to eq. (5.8) in Chapter 5.

## D.2 Expression with non-saturated translation

From eqs. (5.1-5.7) in Chapter ??, expression corresponds to initial conditions  $D_{act}(0) = D_{act}^0$ ,  $R_{act}(0) = P(0) = P^*(0) = 0$ . If we suppose that  $R_{act}(t) \ll K_{tl}$  and we note  $\kappa_{tx} = \frac{k_{tx} D_{act}^0}{K_{tx} + D_{act}^0}$  we should thus consider the system of equations

$$\frac{dR_{act}}{dt} = r_{tx} = \kappa_{tx} \quad (\text{D.8})$$

$$\frac{dP}{dt} = r_{tx} - r_m \approx \frac{k_{tl}}{K_{tl}} - k_m \cdot P \quad (\text{D.9})$$

$$\frac{dP^*}{dt} = r_m = k_m \cdot P \quad (\text{D.10})$$

we find  $R_{act} = \kappa_{tx} t$  and

$$P_{tot} \approx \frac{k_{tl}}{K_{tl}} \frac{\kappa_{tx}}{2} t^2 \quad (\text{D.11})$$

and the variation of  $P^*$  becomes

$$\frac{dP^*}{dt} \approx k_m \left( \frac{k_{tl}}{K_{tl}} \frac{\kappa_{tx}}{2} t^2 - P^* \right) \quad (\text{D.12})$$

which is again a linear ODE. Comparing eq. (D.12) with eq. (D.5) we have  $g = 1$ ,  $f_0 = k_m \frac{k_{tl}}{K_{tl}} \frac{\kappa_{tx}}{2} t^2$  and  $f_1 = -k_m$ . We find again  $F(t) = -k_m t$  and from eq. (D.6) the solution of eq. (D.12) is

$$P^*(t) \approx \frac{k_{tl}}{K_{tl}} \frac{\kappa_{tx}}{2} \left( t^2 - \frac{2}{k_m} t + \frac{2}{k_m^2} (1 - e^{-k_m t}) \right) \quad (\text{D.13})$$

## D.3 Expression with Michaelis-Menten translation

We now consider the full system of eqs. (5.4-5.7) presented in Chapter 5. The exact equation describing the variation of  $P_{tot}$  is

$$\frac{dP_{tot}}{dt} = \frac{k_{tl} \kappa_{tx} t}{K_{tx} + \kappa_{tx} t} \quad (\text{D.14})$$

which solution is

$$P_{tot} = k_{tl} \left( t - \frac{K_{tl}}{\kappa_{tx}} \ln \left( 1 + \frac{\kappa_{tx}}{K_{tl}} t \right) \right) \quad (\text{D.15})$$

and we may check that a second order Taylor expansion of eq. (D.15) is identical to eq. (D.11), as expected. Combining eq. (D.15) and eq. (D.10) with the conservation of protein we have

$$\frac{dP^*}{dt} = k_m(P_{tot} - P^*) \quad (D.16)$$

$$= k_m \left[ k_{tl} \left( t - \frac{K_{tl}}{\kappa_{tx}} \ln \left( 1 + \frac{\kappa_{tx}}{K_{tl}} t \right) \right) - P^* \right] \quad (D.17)$$

which is, once more, a linear ODE like (D.5) with  $g = 1$ ,  $f_1 = -k_m$  and  $f_0 = k_m P_{tot}$ . From (D.6) we obtain

$$P^* = C e^{-k_m t} + e^{-k_m t} \int e^{k_m t} k_m \left[ k_{tl} \left( t - \frac{K_{tl}}{\kappa_{tx}} \ln \left( 1 + \frac{\kappa_{tx}}{K_{tl}} t \right) \right) \right] dt \quad (D.18)$$

Using the integrals

$$\int t e^{\alpha t} dt = \frac{\alpha t - 1}{\alpha^2} e^{\alpha t} \quad (D.19)$$

$$\int e^{\alpha t} \ln(t) dt = \frac{1}{\alpha} \left( e^{\alpha t} \ln|t| - \int_{-t}^{\infty} \frac{e^{-\alpha t}}{\alpha t} dt \right) \quad (D.20)$$

we find

$$P^* = C e^{-k_m t} + \frac{k_{tl}}{k_m} (k_m t - 1) - \frac{k_{tl} K_{tl}}{k_m \kappa_{tx}} \ln \left| 1 + \frac{\kappa_{tx}}{K_{tl}} t \right| + e^{-k_m t} e^{-k_m K_{tl}/\kappa_{tx}} \int_{-1 - \frac{\kappa_{tx}}{K_{tl}} t}^{\infty} \frac{e^{-u}}{u} du \quad (D.21)$$

with  $C$  an integration constant.

## D.4 Integration of eqs. (5.16-5.20) presented in Chapter 5

We provide here the details of the integration of ODEs (5.16-5.20) presented in Chapter 5. We neglect the maturation reaction eq. 5.15 such that  $P = P^*$ . We integrate the trivial eqs. (5.16) and (5.17) to obtain

$$R_{cr} = \frac{k_{tx}^{cr}}{1 + \alpha + \frac{K_{tx}}{D_{cr}}} t \quad (D.22)$$

$$R_{ta} = \frac{k_{tx}^{ta} \alpha}{1 + \alpha + \frac{K_{tx}}{D_{cr}}} t \quad (D.23)$$

By combining eqs. (5.18-5.19) in Chapter 5 with eqs. (D.22-D.23) we get

$$\frac{dP^*}{dt} = \frac{k_{tl}^{act} \alpha}{K_d K_{tl}} \frac{k_{tx}^{cr} k_{tx}^{ta}}{\left( 1 + \alpha + \frac{K_{tx}}{D_{cr}} \right)^2} t^2 + \frac{k_{tl}^{cr}}{K_{tl}} \frac{k_{tx}^{cr}}{1 + \alpha + \frac{K_{tx}}{D_{cr}}} t \quad (D.24)$$

and after integration

$$P^*(\alpha) = \frac{k_{tl}^{act} \alpha}{3 K_d K_{tl}} \frac{k_{tx}^{cr} k_{tx}^{ta}}{\left( 1 + \alpha + \frac{K_{tx}}{D_{cr}} \right)^2} t^3 + \frac{k_{tl}^{cr}}{2 K_{tl}} \frac{k_{tx}^{cr}}{1 + \alpha + \frac{K_{tx}}{D_{cr}}} t^2 \quad (D.25)$$

where we have indicated explicitly that  $P^*$  is a function of  $\alpha$ . This last equation corresponds to eq. (5.21) in the Chapter 5.

## D.5 Maximum of $\rho_{ON/OFF}^{th}$

For convenience we remind

$$\rho_{ON/OFF}^{th} = \frac{P^*(\alpha)}{P^*(\alpha=0)} = \frac{1 + \frac{K_{tx}}{D_{cr}}}{\left(1 + \alpha + \frac{K_{tx}}{D_{cr}}\right)} \left[ 1 + \frac{2}{3}\beta \frac{\alpha}{\left(1 + \alpha + \frac{K_{tx}}{D_{cr}}\right)} t \right] \quad (D.26)$$

The maximum of  $\rho_{ON/OFF}^{th}$  is obtained for

$$\alpha^{max} = \frac{D_{cr} + K_{tx}}{D_{cr}} \frac{2\beta t - 3}{2\beta t + 3} \quad (D.27)$$

when  $\beta t \gg 3/2$  we have

$$\alpha^{max} \approx \frac{D_{cr} + K_{tx}}{D_{cr}} \quad (D.28)$$

and

$$\rho_{ON/OFF}^{max} \approx \frac{\beta}{6} t \quad (D.29)$$

## D.6 $\rho_{ON/OFF}^{th}$ for the case of $cr^-DNA + D_{ta}$

The exact expression for the dashed yellow line in Figure 5.8 (b) corresponds to the limit of eq. (D.26) when  $K_d \rightarrow \infty$

$$\rho_{ON/OFF}^{cr^-}(\alpha) = \frac{1 + \frac{K_{tx}}{D_{cr^-}}}{1 + \alpha + \frac{K_{tx}}{D_{cr^-}}} \quad (D.30)$$

## Appendix E

# Article: Tunable corrugated patterns in an active nematic sheet

Anis Senoussi, Shunnichi Kashida, Raphael Voituriez, Jean-Christophe Galas, Ananyo Maitra & André Estevez-Torres

Published in *Proceedings of the National Academy of Sciences*, 2019 [253] [[Online article](#)] [[pdf](#)]





## Appendix F

# Article: Quantitative characterization of translational ribo regulators using an *in vitro* transcription-translation system

Anis Senoussi, Jonathan Lee Tin Wah, Yoshihiro Shimizu, Jérôme Robert, Alfonso Jaramillo, Sven Findeiss, Ilka M. Axmann & André Estevez-Torres

Published in *ACS Synthetic Biology*, 2018 [254] [[Online article](#)] [[pdf](#)]



## Appendix G

### Résumé détaillé en français

Création de systèmes moléculaires  
artificiels pour la génération de motifs et  
la régulation génétique

## G.1 Introduction

Comment concevoir des matériaux se façonnant eux-mêmes ? Nous avançons dans cette thèse qu'il est possible de répondre en partie à cette question en s'inspirant des systèmes vivants. En effet, la nature a exploré et résolu de nombreux problèmes d'optimisation au cours des milliards d'années d'évolution : auto-assemblage, efficacité énergétique, autonomie et adaptation à l'environnement. Notamment, nous nous proposons de construire des systèmes moléculaires qui imitent deux caractéristiques essentielles de la vie : la formation de formes et motifs et la régulation génétique. De plus, ces systèmes doivent pouvoir s'auto-organiser, être autonomes, programmables (leurs propriétés sont changeable à souhait) et biocompatibles (c'est-à-dire fonctionner avec d'autres structures vivantes comme des cellules ou des enzymes).

Les travaux présentés dans cette thèse sont axés sur la formation de motifs et la régulation génétique, à la frontière entre la science des matériaux et la biologie de synthèse et avec pour objectif à long terme la conception de nouveaux matériaux possédant certaines des propriétés des systèmes vivants. Le chapitre 2 passe en revue deux mécanismes et systèmes impliqués dans l'auto-organisation des systèmes moléculaires : la matière active et les structures de réaction-diffusion. Le chapitre 3 décrit la production, le développement et la caractérisation d'un système de matière active reconstituée composé de microtubules et de multimères de kinésines. Ce système est également couplé dans le chapitre 4 avec la boîte à outils « PEN-ADN » (présentée au chapitre 2), un réseau de réactions chimiques programmables composé de brins d'ADN et de quelques enzymes. Le chapitre 5 présente les travaux concernant la régulation des gènes par l'ARN en utilisant un système de transcription-traduction reconstitué. Nous espérons que ces approches contribueront à la conception de matériaux hors-équilibre dotés de propriétés uniques.

## G.2 Matière active et réaction-diffusion, deux mécanismes d'auto-organisation dans les systèmes moléculaires

La construction de matériaux artificiels hors-équilibres ayant des propriétés similaires à celles des systèmes vivants commence par l'identification des mécanismes d'auto-organisation. Certains de ces mécanismes sont particulièrement manifestes lors du développement embryonnaire. Ce dernier peut être décrit comme un processus convertissant l'information chimique en un changement de composition et de forme. Schématiquement, il est composé des quatre processus suivants :

- **Formation d'un motif chimique** : des réseaux de réactions chimiques hors-équilibre génèrent des motifs de concentration structurant chimiquement ainsi l'embryon.
- **Morphogenèse** : l'embryon change de forme à partir de mouvements intra et extra-cellulaires ayant pour origine l'action des moteurs et filaments moléculaires.
- **Différenciation cellulaire** : les cellules deviennent structurellement et fonctionnellement différentes.
- **Croissance** : la masse de l'embryon augmente.

Ainsi, l'embryon est structuré par le jeu de forces chimiques et physiques. Notamment, des couplages chimico-mécaniques et mécano-chimiques relient les deux premiers processus qui, ensemble, contrôlent la différenciation et la croissance des cellules. Dans ce chapitre, nous passons en revue deux mécanismes permettant la formation de motifs et la morphogenèse à partir de systèmes moléculaires : la matière active et la formation de motifs par réaction-diffusion.

### G.2.1 Matière active

La matière active désigne des systèmes et des matériaux composés de nombreux composants capables de consommer de l'énergie à l'échelle individuelle et de la dissiper sous forme de travail mécanique. Cette définition couvre un bon nombre de systèmes de tailles très diverses (du micromètre à plusieurs dizaines de kilomètres). Elle s'applique notamment aux groupes d'animaux tels que les nués d'oiseaux ou les bancs de poissons ou encore aux communautés de cellules organisées. En plus de ces systèmes naturels, des efforts ont été faits pour concevoir des systèmes actifs artificiels, dans le but de simplifier et de comprendre les effets collectifs. En particulier, plusieurs stratégies ont été utilisées pour motoriser des colloïdes et créer des micronageurs synthétiques actifs.

De par leur capacité intrinsèque à fonctionner à partir d'énergie chimique (provenant notamment de l'hydrolyse de nucléotides), des molécules provenant de cellules vivantes ont été purifiées et utilisées *in vitro* dans la fabrication de systèmes actifs reconstitués. Une des classes les plus importantes de ces systèmes est appelée gels actifs. Ce sont des systèmes composés de filaments du cytosquelette associés à des moteurs moléculaires (Figure G.1 (a)). Ils possèdent des propriétés rhéologiques uniques en raison de leur capacité à convertir l'énergie chimique en contraintes macroscopiques. Le déplacement de ces filaments par les moteurs moléculaires induit le mouvement du gel et son auto-organisation en structures dynamiques : structures en étoiles, contractions ou écoulement (Figures G.1 (b) et (c)).

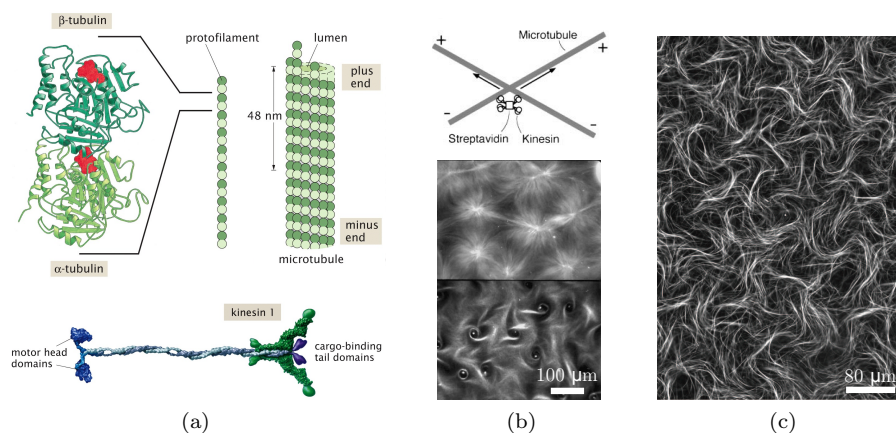


FIGURE G.1 | **Matière active - Gels actifs.** (a) Schéma d'un microtubule (haut) et d'une kinesine-1 (bas). (b) Structures en étoile et en vortex d'un mélange de microtubules et de multimères de kinésines. D'après [195]. (c) Régime turbulent d'un gel actif. D'après [241].

## G.2.2 Formation de structures et motifs par réaction-diffusion

Lorsque des molécules sont à la fois impliquées dans des réactions chimiques et sont transportées par diffusion, des motifs d'auto-organisation peuvent apparaître. Par exemple, la production autocatalytique d'une espèce chimique obéit à une équation de réaction-diffusion dont une solution consiste en un front chimique se déplaçant à vitesse constante.

Les structures de réaction-diffusion ont été principalement observées dans les réactions d'oxydoréduction, en particulier dans celle oscillante de Belousov-Zabotinski. Cependant, ces réactions restent difficiles à mettre au point de novo et sont en outre toxiques, anéantissant ainsi tout effort de conception de matériaux biocompatibles. Pour résoudre ce problème, des réseaux de réactions chimiques similaires à ceux présents in vivo ont été reconstitués, comme par exemple le système bactérien Min ou la machinerie de transcription-traduction capable de générer des fronts de réaction-diffusion. Ces systèmes sont nativement biocompatibles, mais reposent sur des interactions protéines-protéines qui sont difficiles à prédire. Les acides nucléiques, et en particulier l'ADN, peuvent aussi être utilisés pour créer des systèmes réacto-diffusifs biocompatibles et programmables. En effet la réactivité des acides nucléiques découle de leur structure en double-brin obéissant aux règles d'appariement de Watson-Crick (A/T, G/C). Nommément un système en particulier nous intéresse : la boîte à outils PEN-ADN composée de trois enzymes et de courts brins d'ADN. Suivant les règles d'hybridation, les séquences définissent la topologie du réseau de réaction, tandis que les enzymes produisent ou dégradent les ADN (Figure G.2 (a)). Des motifs de réaction-diffusion apparaissent alors lorsqu'on examine la dynamique spatio-temporelle de tels réseaux de réactions chimiques : ondes ou pics de concentration d'ADN (Figure G.2 (b)), structures stables à deux ou trois bandes.

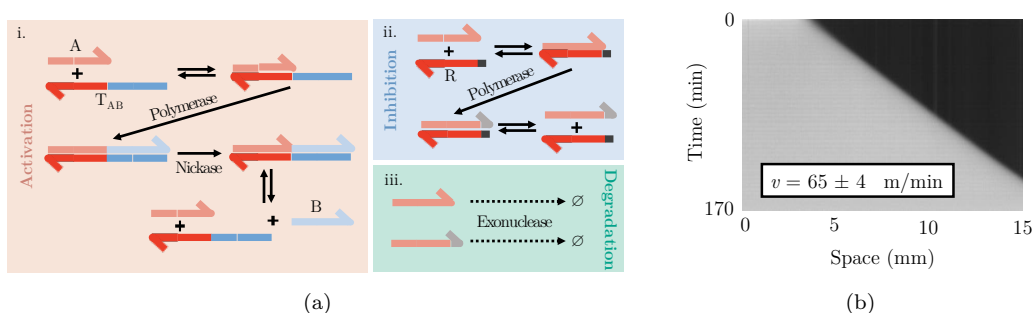


FIGURE G.2 | **Réaction-diffusion - La boîte à outil PEN-ADN.** (a) Réactions élémentaires possibles avec la boîte à outils PEN-ADN. (b) Propagation d'un front de réaction-diffusion d'ADN. D'après [325].

### G.2.3 Forces chimiques et mécaniques : deux exemples de l'embryogénèse

Les mécanismes décrits ci-dessus — matière active et réaction-diffusion — ne sont pas mutuellement exclusifs. Dans de nombreux cas, les deux se produisent de manière synchrone : c'est notamment le cas durant le développement embryonnaire, comme par exemple lors du développement du blastoderme de la drosophile ou l'établissement de la polarité cellulaire chez le ver *C. elegans*.

### G.2.4 Matière active et réaction-diffusion couplés in vitro

Ces deux mécanismes peuvent être utilisés pour créer des matériaux auto-organisés autonomes, programmables et biocompatibles. Bien que ne répondant pas à tous ces critères, certains systèmes ont déjà été réalisés avec succès, notamment des gels auto-oscillants ou des gels incorporant de l'ADN. Inspirés par ces travaux, nous proposons dans les deux prochains chapitres de créer un système dans lequel des structures réacto-diffusives et de la matière active sont couplées. Pour cela nous allons utiliser la boîte à outils PEN-ADN et un gel actif reconstitué composé de microtubules et de multimères de kinésine.



## G.3 Auto-organisation d'un gel actif composé de microtubules et de kinésines

Les gels actifs sont des systèmes maintenus hors-équilibre grâce à une réaction chimique, ce sont notamment ceux reconstitués à partir de protéines. En présence d'une source d'énergie (principalement sous forme d'ATP ou de GTP), ils s'auto-organisent en structures complexes. Inspirés par des travaux antérieurs, nous construisons expérimentalement dans ce chapitre un gel actif composé de microtubules polymérisés et de multimères de kinésines. Nous décrivons les différentes structures qui apparaissent et montrons qu'elles peuvent être comprises par un nombre relativement faible de paramètres : l'activité (en termes de concentration en moteurs), la longueur des microtubules, leur concentration et les forces de déplétion.

### G.3.1 Composition du gel actif

Les kinésines sont des éléments essentiels du gel actif. Elles sont capables d'exercer des forces sur plusieurs filaments de microtubules en même temps. Nous utilisons différentes stratégies pour créer des multimères de kinésines : via des interactions spécifiques (le lien biotine-streptavidine, pour créer la kinésine K401-BCCP) [195, 241] et via des interactions non-spécifiques (pour créer les kinésines K430-FLAG-SNAP et K430-HSNAP). Les autres éléments — tels que les microtubules fluorescents et le système de régénération d'énergie — sont ensuite préparés, mélangés ensemble et observés par microscopie dans des canaux en verre.

### G.3.2 Faisceaux en étoiles et contraction du réseau actif

Une solution diluée de microtubules fluorescents ( $< 50 \mu\text{g/mL}$ ) forme des faisceaux visibles à l'aide d'un simple microscope à fluorescence à faible grossissement (10X). Dans un même temps, les multimères de kinésines exercent des forces importantes sur ces faisceaux : ils les plient et parfois même les cassent. Initialement disposés en configurations aléatoires, les faisceaux de microtubules s'assemblent en structures en forme d'étoile sous l'action des moteurs (Figure G.3 (a)). Le même mélange — mais avec une concentration plus élevée de microtubules (entre 50 et 250  $\mu\text{g/mL}$ ) — forme un réseau connecté présentant diverses dynamiques spatio-temporelles. Une faible concentration de moteurs conduit à un réseau statique, alors qu'une concentration plus grande entraîne une contraction globale du réseau. À une concentration encore plus élevée en moteurs, le réseau est segmenté en sous-réseaux isolés qui se contractent. À partir de ces différents comportements, il est possible d'esquisser un diagramme d'état dépendant des deux paramètres que sont la concentration en microtubules et la concentration en multimères de kinésines (Figure G.3 (b)).

### G.3.3 Façonnage d'une feuille nématique active 3D régulièrement ondulée

Lorsque de longs microtubules stabilisés par le taxol forment un réseau dense ( $> 250 \mu\text{g/mL}$ ) initialement aligné, une nouvelle structure apparaît : cette solution active 3D forme spontanément une feuille nématique 2D qui se déforme activement hors du plan en une feuille ondulée périodique

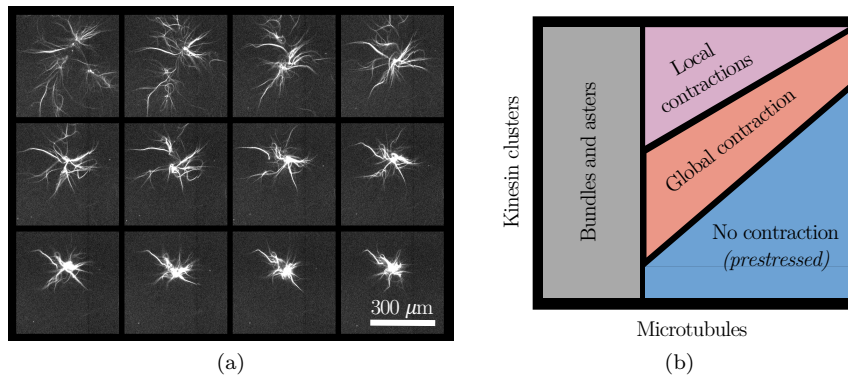


FIGURE G.3 | **Formation de faisceaux de microtubules en étoiles et contraction d'un réseau actif.** (a) Les faisceaux de microtubules s'organisent en étoiles polarisées. (b) Diagramme d'états expérimental d'un gel actif contractile.

stable pendant plusieurs jours à faible activité [253] (Figure G.4). Le fluide se contracte de manière anisotrope le long de ses deux plus courtes dimensions pour former une fine feuille flottante, principalement en raison des forces de déplétion passives. Simultanément, la contrainte active générée par les moteurs déforme la feuille dans la direction perpendiculaire à son plan, à une longueur d'onde définie (de l'ordre de 100 μm) sur une surface couvrant 10 mm<sup>2</sup>.

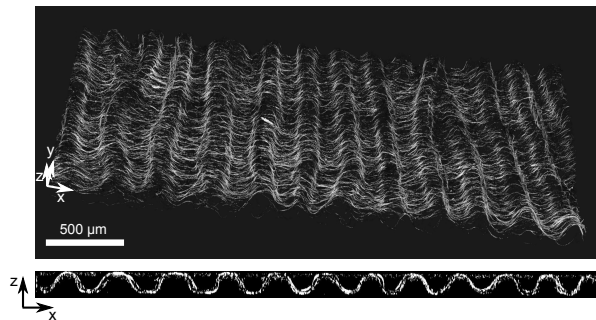


FIGURE G.4 | **Formation d'une feuille nématique active 3D.**

Lorsque l'activité est suffisamment élevée, le motif n'est que transitoire et finit par se briser en flux chaotiques (qui seront décrits dans la partie suivante). La transition entre des ondulations statiques et un écoulement chaotique est contrôlée expérimentalement par deux paramètres : la concentration en moteurs et l'attraction entre faisceaux de microtubules (par les forces de déplétion) (Figure G.5). Ces résultats soulignent l'importance des forces passives et actives dans l'organisation de la matière active. Ils démontrent de plus qu'un fluide actif s'écoulant spontanément peut être sculpté en un matériau statique par un mécanisme actif.

### G.3.4 Passage d'un fluide nématique actif à un fluide turbulent actif

Lorsque les forces de déplétion ne sont pas suffisamment élevées pour induire la formation d'une feuille nématique ondulée, le système transite différemment de l'état initial nématique à l'état d'écoulements turbulents. Nous utilisons de courts microtubules (polymérisés à l'aide de GMPCPP

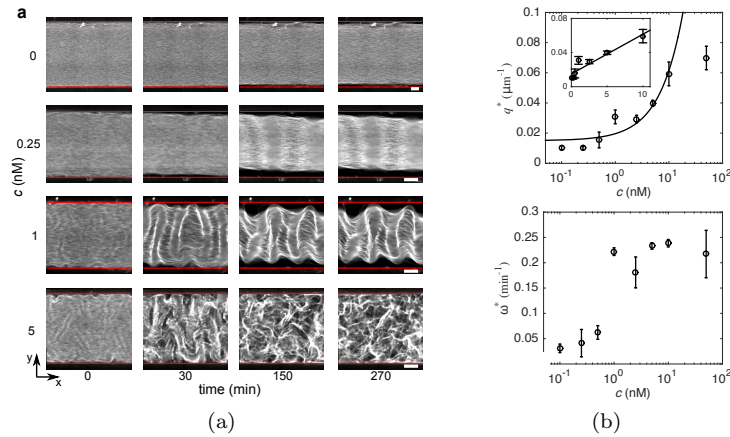


FIGURE G.5 | **Dynamique, structure et stabilité de la feuille nématique en fonction de la concentration en kinésines.** (a) L'évolution de la formation de la feuille nématique dépend de la concentration en kinésines. (b) Caractérisation quantitative de la longueur d'onde et de la dynamique de la feuille ondulée.

et non plus de GTP) pour réaliser cette condition. Grâce au même dispositif expérimental, nous sommes en mesure d'observer les premiers moments d'un écoulement turbulent 3D créé par le fluide actif. Cette transition est le fruit d'instabilités de flexion orthogonales, successives, conduisant ainsi un système ordonné à s'écouler chaotiquement (Figure G.6). Comme c'est le cas en deux dimensions [174], les instabilités de flexion sont les principaux générateurs de la transition. Cependant, ici les paires de défauts topologiques ne sont pas créées puisque le gel peut se déformer dans la troisième dimension. La taille de ces instabilités et leur dynamique dépendent de la concentration en kinésines. Cette transition peut être quantifiée par le suivi de l'orientation des faisceaux via le calcul du champ d'orientation, de la distribution des angles et des paramètres d'ordre local et global.

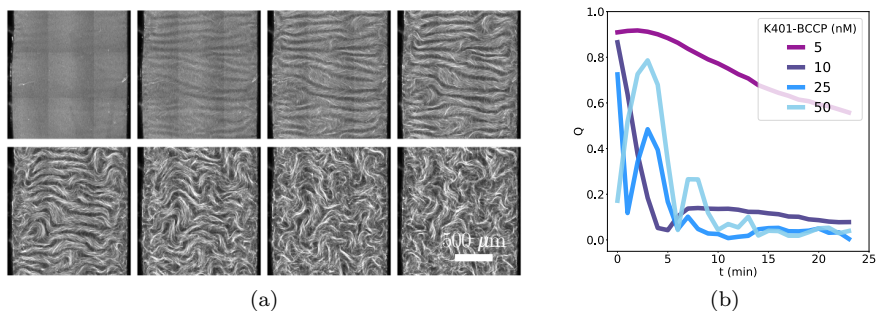


FIGURE G.6 | **Instabilités de flexion et perte de l'ordre orientational.** (a) Des instabilités de flexion successives détruisent l'ordre nématique initial. (b) Evolution du paramètre d'ordre global en fonction du temps.

### G.3.5 Compartimentation de nématiques actifs

La compartimentation du gel actif dans des gouttelettes est à la fois utile pour étudier les structures actives, mais aussi pour imiter un environnement semblable à celui des cellules. Ainsi de nombreux systèmes actine/myosine et microtubules/kinésines ont été encapsulés [14]. Nous montrons ici qu'il est possible de produire des gouttelettes fonctionnelles contenant le système actif à l'intérieur. Nous observons ainsi la transition temporelle entre un réseau 3D intégré à l'intérieur d'une gouttelette et la formation de nématiques actifs 2D localisés à l'interface eau-huile (Figure G.7). Un tel système peut être utilisé pour déterminer la structure interne des flux hydrodynamiques nématiques actifs et la dynamique de particules actives autopropulsées utilisant l'ATP comme source d'énergie.

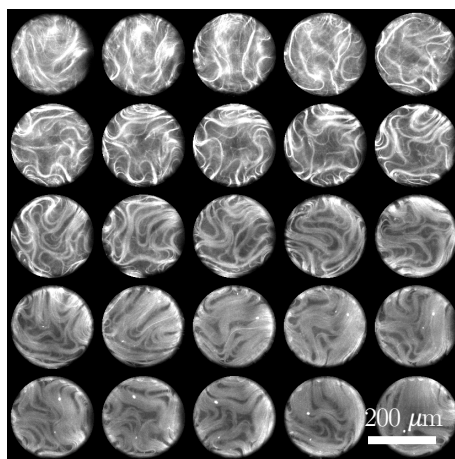


FIGURE G.7 | **Formation de nématiques actifs 2D à la surface d'une gouttelette.**

Dans ce chapitre, nous avons déterminé quels sont les éléments nécessaires pour obtenir des structures spatiales dynamiques ou statiques à partir d'un gel actif reconstitué. Nous avons souligné l'importance des forces passives et actives et avons démontré qu'un gel actif peut se comporter comme un système contractile, un matériau ondulé statique ou un fluide actif.

## G.4 Couplage entre un front réacto-diffusif d'ADN et un gel actif

Le couplage entre mécanismes d'auto-organisation est une étape clé dans la conception de matériaux autonomes, programmables et biocompatibles. Dans le chapitre précédent, nous avons montré que le comportement d'un de ces mécanismes — un gel actif composé de multimères de kinésines et de microtubules — peut être contrôlé avec précision. Ce chapitre est consacré au couplage entre ce gel actif et la boîte à outils PEN-ADN capable de générer des structures de réaction-diffusion, en particulier des fronts de concentration.

### G.4.1 À la recherche de conditions expérimentales communes aux deux systèmes

Le gel actif reconstitué et la boîte à outils PEN-ADN fonctionnent dans des conditions expérimentales différentes. Nous décrivons l'optimisation des conditions expérimentales afin de trouver un tampon favorable et une température de travail compatible avec les deux systèmes. Nous quantifions la dynamique temporelle de l'amplification autocatalytique en fonction des concentrations d'ADN initiateur (Figure G.8 (a)), de polymérase, de nickase, de dGTP et de microtubules.

### G.4.2 Propagation d'un front réacto-diffusif dans un gel actif

Nous examinons la dynamique d'un front de réaction-diffusion construit à partir de la boîte à outils PEN-ADN se propageant dans le gel actif décrit et étudié au précédent chapitre. Nous montrons qu'un front peut se propager dans ce gel actif (Figure G.8 (b)).

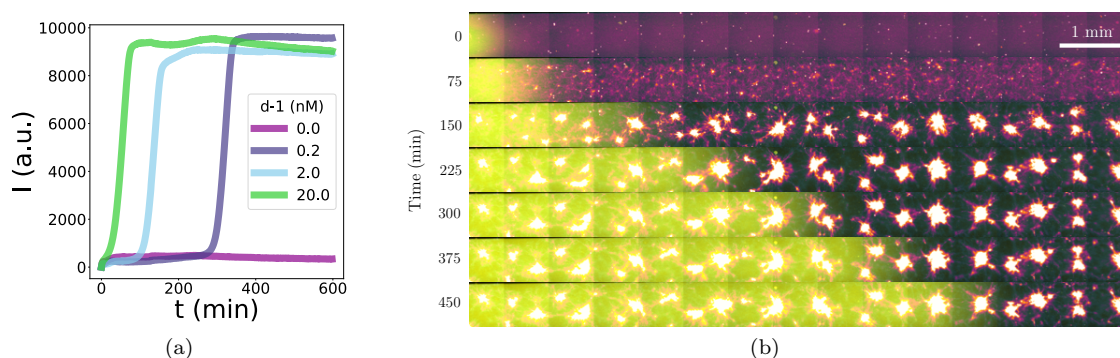


FIGURE G.8 | **Réaction autocatalytique de production d'ADN et propagation du front associé au sein du gel actif.** (a) Dynamique de l'autocatalyse en fonction de la concentration d'initiateur ajoutée. (b) Propagation d'un front de réaction-diffusion au sein du gel actif.

Il est intéressant de noter qu'en utilisant des microtubules polymérisés à partir de GMPCPP, le régime de flux chaotiques actifs n'est pas observé. Cependant lorsque la concentration initiale en dGTP est faible, les flux chaotiques sont rétablis entraînant une structuration inhomogène du canal, tant sur le plan chimique (concentration d'ADN) que morphologique (état du gel actif) (Figure G.9).

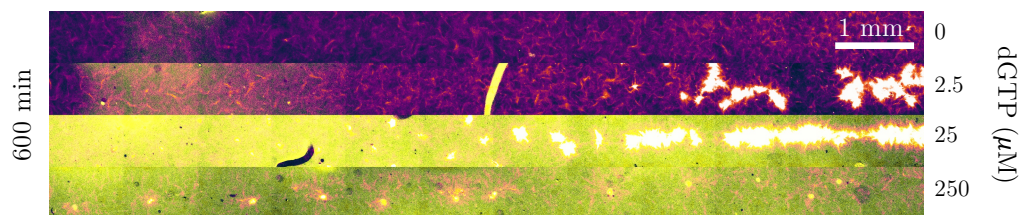


FIGURE G.9 | **En présence d'une faible concentration de dGTP le gel actif se structure de façon inhomogène.**

### G.4.3 Couplage hydrodynamique : création d'un système autocatalytique sans dGTP

La présence de dGTP dans nos expériences entraîne la contraction du gel actif. Dans le but de générer un front d'ADN à l'intérieur de flux chaotiques induits par l'ATP, nous construisons un deuxième système autocatalytique dans lequel dGTP n'est pas présent. Pour ce faire, nous identifions la nickase appropriée et concevons de nouvelles séquences. Nous démontrons que, dans nos conditions expérimentales, ce système peut donner naissance à des fronts se propageant en l'absence de gel actif. Cependant, l'ajout de ce dernier provoque la formation de petits agrégats qui inhibent l'activité du gel.

### G.4.4 Couplage chimique : vers une matière active contrôlée par de l'ADN

Nous utilisons une méthode basée sur la réaction spécifique entre la séquence protéique SNAP et un substrat contenant un groupe benzylguanine (BG) afin de fixer de l'ADN sur une kinésine. La réaction se déroule en deux temps (Figure G.10 (a)). Tout d'abord l'ADN (contenant une base modifiée avec un groupe amine) réagit sur la molécule de liaison BG-GLA-NHS dans le but de créer un substrat réactif pour la séquence protéique SNAP de la kinésine. Dans un deuxième temps, après purification, cet ADN réagit avec la kinésine K430-FLAG-SNAP. Le résultat de la réaction est analysé par un gel acrylamide dénaturant (Figure G.10 (b)). Le rendement total de la réaction est d'environ 50%. Malheureusement, ces kinésines modifiées présentent toujours une activité — dans une expérience de gel actif — suggérant la formation d'agrégats non-spécifiques. Néanmoins, ces constructions pourraient être utilisées dans des expériences de propulsion de microtubules par des moteurs attachés à la surface par de l'ADN.

### G.4.5 Conclusion et perspectives

Dans ce chapitre, nous avons combiné deux systèmes moléculaires capables d'auto-organisation. Nous avons trouvé des conditions expérimentales compatibles à la fois pour le gel actif et pour la boîte à outils PEN-ADN. Nous avons montré qu'un front de réaction-diffusion peut ainsi se propager dans ce gel actif. Nous avons également conçu un système autocatalytique fonctionnant sans dGTP, afin d'obtenir des flux de matière active. Finalement, nous avons démontré qu'en utilisant la séquence protéique SNAP d'une kinésine, il est possible d'y attacher de manière covalente de l'ADN.

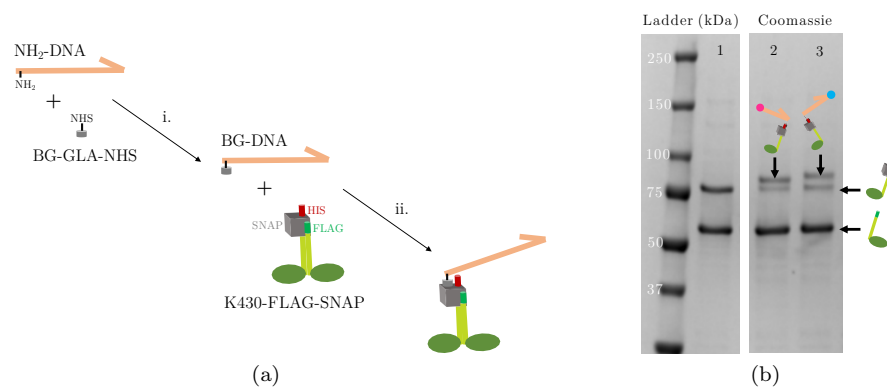


FIGURE G.10 | **Attacher de l'ADN sur une kinésine.** (a) Un amino-ADN réagit de façon spécifique sur la séquence SNAP par l'intermédiaire de la molécule BG-GLA-NHS. (b) Analyse de la réaction par un gel polyacrylamide dénaturant.

## G.5 Contrôle ARN de l'expression génétique dans un système reconstitué

La régulation des gènes est une caractéristique essentielle des systèmes vivants. La production de protéines doit pouvoir être contrôlée dans l'espace et dans le temps afin d'assurer l'homéostasie de l'organisme. Cette régulation peut se faire à tous les stades de la production de protéines, notamment entre la transcription et la traduction.

### G.5.1 Régulation ARN et système de transcription-traduction *in vitro*

La régulation de la traduction peut être réalisée par les molécules d'ARN. En effet, une modification de leurs structures secondaires — codées dans leur séquence nucléotidique — peut entraîner une modification de l'expression des protéines grâce à l'appariement spécifique entre brins d'ARN. Nous étudions ici la régulation ARN de la production de protéines à l'aide d'un système de transcription-traduction reconstitué. Ces régulateurs ARN sont conçus de telle façon qu'ils peuvent modifier le taux d'expression d'une protéine uniquement en changeant leur structure. Un premier ARN présente dans sa région non traduite 5' une structure secondaire en épingle à cheveux, qui séquestre le site de fixation du ribosome et/ou le codon d'initiation de la traduction (codon de départ). Cet ARN est ainsi dit *cis-réprimé* ( $R_{cr}$ ). La traduction des protéines est possible lorsque le gène est activé par un second ARN transactivateur ( $R_{ta}$ ) conçu pour s'apparier spécifiquement avec une partie du  $R_{cr}$ . Ils forment un duplex d'ARN dans lequel le site de fixation du ribosome est à nouveau exposé : la traduction peut commencer (Figure G.11 (a)). Nous étudions cinq riborégulateurs conçus *de novo* : deux sont issus des travaux de Rodrigo et al. [234] (système RAJ) et trois des travaux de Green et al. [98] (système G). Cette étude est faite à l'aide d'un système de transcription-traduction reconstitué, composé d'éléments recombinants purifiés individuellement (le système PURE [258]). Un ensemble minimal de composants a été identifié, purifié et reconstitué — dans un tampon approprié — afin de produire des protéines (Figure G.11 (b)). A chaque étape, nous utilisons des équations différentielles normales pour modéliser la transcription et la traduction en l'absence ou en présence de régulation.

### G.5.2 Résultats

Nous caractérisons les réactions de transcription et de traduction du système PURE en l'absence de régulation (Figure G.12). Le système agit comme un amplificateur linéaire de la concentration d'ARN actif,  $R_{act}$ , et comme un amplificateur quadratique de  $D_{act}$ , avec comme lecture l'intensité de fluorescence de la protéine GFP produite à partir de ces acides nucléiques. Cette fluorescence peut donc être utilisée comme mesure de la concentration de  $R_{act}$ .

La performance d'un riborégulateur est testée en fusionnant  $D_{cr}$  — ADN codant pour  $R_{cr}$  — avec une GFP et en mesurant la gamme dynamique, définie comme  $\rho_{ON/OFF} = \frac{\text{fluo. GFP avec } D_{ta}}{\text{fluo. GFP sans } D_{ta}}$ ,  $D_{ta}$  étant l'ADN codant pour  $R_{ta}$ . La simplicité du système de transcription-traduction *in vitro* nous permet de fournir une définition quantitative de  $\rho_{ON/OFF}$  et de tester l'effet de la concentration de  $D_{ta}$  sur  $\rho_{ON/OFF}$  (Figure G.13 (a)). L'augmentation de  $D_{ta}$  dans la fourchette 0 – 5 nM



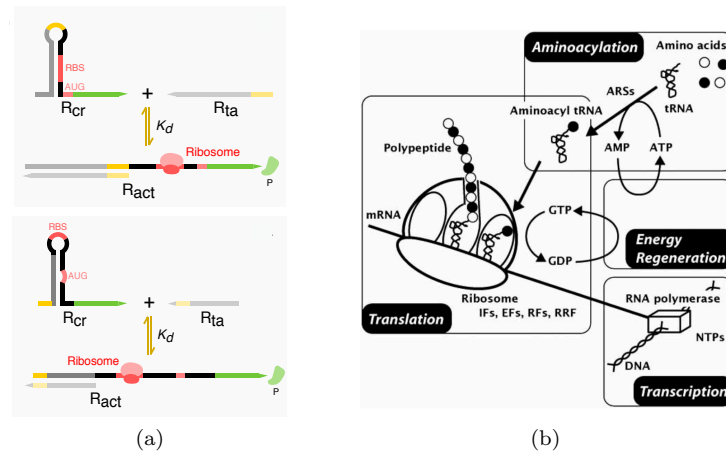


FIGURE G.11 | **Riborégulateurs ARN et système de transcription-traduction in vitro.** (a) Principe des deux types de régulateurs ARN utilisés. (b) Réactions reconstituées dans un système de transcription-traduction in vitro.

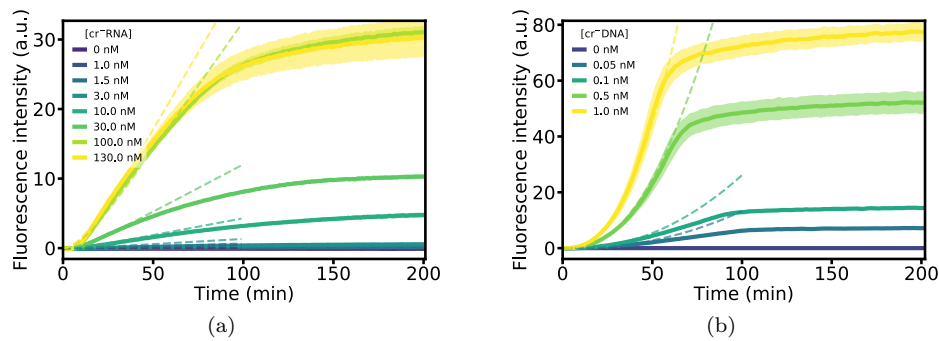


FIGURE G.12 | **Expression de la protéine GFP à partir d'un ARN ou d'un ADN codant.** (a) Production linéaire de GFP à partir d'un ARN codant non régulé. (b) Production quadratique de GFP à partir d'un ADN codant non régulé.

entraîne une augmentation du signal de fluorescence. Cependant, pour  $D_{ta} > 5$  nM, le signal de fluorescence diminue considérablement. Notre modèle prédit cette dépendance et la forme en cloche de  $\rho_{ON/OFF}$  : cela résulte de la concurrence de  $D_{ta}$  et de  $D_{cr}$  pour les ressources de transcription. La saturation des ressources transcriptionnelles est particulièrement importante dans le contexte des riborégulateurs, où l'ADN non codant produit un ARN régulateur qui a un effet important sur le réseau de régulation des gènes. Notre modèle et les résultats in vitro prédisent que l'insertion de  $D_{ta}$  dans un plasmide à forte copie diminuera la performance de l'activateur du riborégulateur et suggèrent un compromis entre la compétition des ressources et la surexpression des ARN antisens.

Pour caractériser la réaction entre ARN, nous transcrivons in vitro les cinq riborégulateurs. Nous étudions leur dynamique de traduction en titrant 5 nM  $R_{cr}$  par une concentration croissante (entre 0 et 1000 nM) de son  $R_{ta}$  (Figure G.13 (b)). Nous trouvons des constantes de dissociation de l'ordre de 10-2000 nM, en accord avec les valeurs précédemment déterminées pour des riborégulateurs possédant des structures en épingle à cheveux [128].

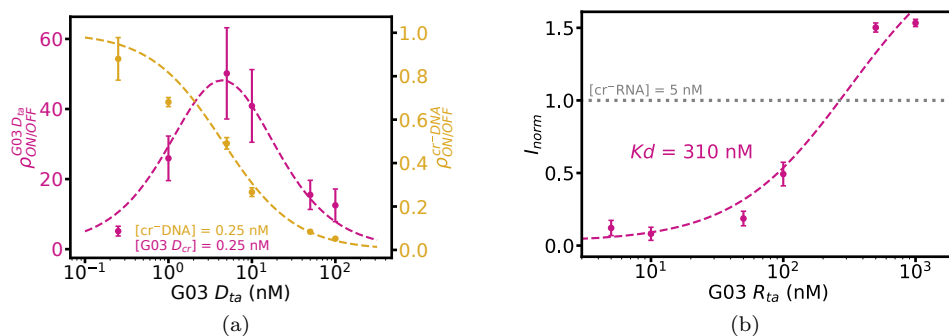


FIGURE G.13 | **Mesures de la gamme dynamique et de la constante de dissociation d'un régulateur ARN.** (a) Mesure de la gamme dynamique du régulateur ARN G03 par titration de  $D_{cr}$  par  $D_{ta}$ . (b) Mesure de la constante de dissociation entre deux brins ARN d'un régulateur par titration de  $R_{cr}$  par  $R_{ta}$ .

Nous avons étudié ici des riborégulateurs d'ARN conçus de novo qui régulent la traduction d'un ARN codant en une protéine. Les systèmes de transcription-traduction in vitro constituent une plate-forme intéressante pour caractériser quantitativement ces riborégulateurs de la traduction. De plus, leur simplicité nous a permis de proposer une expression analytique pour la gamme dynamique d'un riborégulateur. En accord quantitatif avec ce modèle, nous avons montré que l'augmentation de la concentration de l'ADN de l'espèce transactive favorise d'abord et inhibe ensuite l'expression. En outre, les gammes dynamiques relatives mesurées in vitro ont été en accord avec celles rapportées in vivo pour quatre des cinq riborégulateurs mesurés. En titrant le gène cis-réprimé avec l'espèce transactivante au niveau de l'ARN, nous avons pu déterminer de manière très simple des constantes de dissociation,  $K_d$ , pour la réaction d'hybridation de l'ARN. Notre méthode fournit ainsi un moyen simple et rapide pour la caractérisation quantitative des riborégulateurs.

## G.6 Conclusion

Dans cette thèse, j'ai présenté les travaux effectués au laboratoire Jean Perrin à Sorbonne Université, sous la direction d'André Estevez-Torres et de Jean-Christophe Galas, portant sur la conception de systèmes moléculaires reconstitués capables de former des motifs et de réguler des gènes. Ce travail a été motivé par la construction de systèmes artificiels reproduisant des caractéristiques de systèmes vivants : en utilisant une approche *in vitro*, j'ai conçu des systèmes qui s'auto-organisent et expriment des protéines. En particulier, j'ai combiné un système de formation de motifs par réaction-diffusion avec de la matière active capable de générer des forces. En outre, j'ai exploré la régulation de l'expression des protéines en milieu acellulaire à l'aide de régulateurs ARN.

Plusieurs directions peuvent être explorées dans de futurs travaux. Par exemple, des gels actifs reconstitués pourraient être associés à des gels passifs afin de changer leurs propriétés rhéologiques. L'étude de populations de gouttelettes actives semble également intéressante : du fait de leur activité, elles présentent des comportements non triviaux individuels — tels que l'autopropulsion — et potentiellement collectifs — tels que la synchronisation — lorsqu'elles sont assemblées en une émulsion active [103]. L'utilisation d'un gel actif avec la boîte à outils PEN-ADN peut être élargie à d'autres structures de réaction-diffusion telles que des bandes stables. De plus, le couplage entre motifs réacto-diffusifs et ADN peut être poussé plus loin via les interactions chimiques entre ADN et moteurs moléculaires, microtubules ou surfaces. De leur côté, les régulateurs d'ARN peuvent être couplés à des programmes moléculaires conçus avec la boîte à outils PEN-ADN pour effectuer, par exemple, des tâches de détection d'ARN viral [86, 214]. De plus, le potentiel des systèmes de transcription-traduction *in vitro* peut être exploité afin de produire des enzymes spécifiques [33].

L'étude des mécanismes d'auto-organisation et d'expression génétique peut s'avérer utile pour la conception de matériaux autonomes intelligents [62, 151]. Utilisés de pair avec les techniques de biologie de synthèse, de bio-impression 2D ou 3D, de microfluidique et d'apprentissage automatique, ces mécanismes peuvent aider à la construction de cellules artificielles capables de produire des molécules [204, 309, 91] et pouvant s'assembler en tissus artificiels [302, 1, 56].

# Bibliography

- [1] K. P. Adamala, D. A. Martin-Alarcon, K. R. Guthrie-Honea, and E. S. Boyden. Engineering genetic circuit interactions within and between synthetic minimal cells. *Nature chemistry*, 9(5):431, 2017. [Cited on pages [9](#), [163](#), and [200](#).]
- [2] L. M. Adleman. Molecular computation of solutions to combinatorial problems. *Science*, 266(5187):1021–1024, 1994. [Cited on pages [9](#) and [44](#).]
- [3] R. Alert, J.-F. Joanny, and J. Casademunt. Universal scaling of active nematic turbulence. *Nature physics*, pages 1–7, 2020. [Cited on page [86](#).]
- [4] J. Alvarado, M. Sheinman, A. Sharma, F. C. MacKintosh, and G. H. Koenderink. Molecular motors robustly drive active gels to a critically connected state. *Nature physics*, 9(9):591, 2013. [Cited on pages [29](#), [74](#), and [75](#).]
- [5] J. Alvarado, M. Sheinman, A. Sharma, F. C. MacKintosh, and G. H. Koenderink. Force percolation of contractile active gels. *Soft matter*, 13(34):5624–5644, 2017. [Cited on pages [75](#) and [76](#).]
- [6] E. S. Andersen, M. Dong, M. M. Nielsen, K. Jahn, R. Subramani, W. Mamdouh, M. M. Golas, B. Sander, H. Stark, C. L. Oliveira, et al. Self-assembly of a nanoscale dna box with a controllable lid. *Nature*, 459(7243):73–76, 2009. [Cited on page [44](#).]
- [7] N. M. Angenent-Mari, A. S. Garruss, L. R. Soenksen, G. Church, and J. J. Collins. Deep learning for rna synthetic biology. *bioRxiv*, page 872077, 2019. [Cited on page [160](#).]
- [8] S. Aoyama, M. Shimoike, and Y. Hiratsuka. Self-organized optical device driven by motor proteins. *Proceedings of the National Academy of Sciences*, 110(41):16408–16413, 2013. [Cited on page [98](#).]
- [9] S. Asakura and F. Oosawa. On interaction between two bodies immersed in a solution of macromolecules. *The Journal of chemical physics*, 22(7):1255–1256, 1954. [Cited on page [72](#).]
- [10] S. Atis, S. Saha, H. Auradou, D. Salin, and L. Talon. Autocatalytic reaction fronts inside a porous medium of glass spheres. *Physical review letters*, 110(14):148301, 2013. [Cited on page [112](#).]
- [11] A. Attanasi, A. Cavagna, L. Del Castello, I. Giardina, S. Melillo, L. Parisi, O. Pohl, B. Rossaro, E. Shen, E. Silvestri, et al. Collective behaviour without collective order in wild swarms of midges. *PLoS computational biology*, 10(7), 2014. [Cited on page [19](#).]

- [12] A. Baccouche, K. Montagne, A. Padirac, T. Fujii, and Y. Rondelez. Dynamic dna-toolbox reaction circuits: A walkthrough. *Methods*, 67(2):234–249, 2014. [Cited on pages 44 and 104.]
- [13] M. Ballerini, N. Cabibbo, R. Candelier, A. Cavagna, E. Cisbani, I. Giardina, V. Lecomte, A. Orlandi, G. Parisi, A. Procaccini, et al. Interaction ruling animal collective behavior depends on topological rather than metric distance: Evidence from a field study. *Proceedings of the national academy of sciences*, 105(4):1232–1237, 2008. [Cited on page 19.]
- [14] Y. Bashirzadeh and A. P. Liu. Encapsulation of the cytoskeleton: towards mimicking the mechanics of a cell. *Soft matter*, 15(42):8425–8436, 2019. [Cited on pages 92 and 193.]
- [15] S. Basu, Y. Gerchman, C. H. Collins, F. H. Arnold, and R. Weiss. A synthetic multicellular system for programmed pattern formation. *Nature*, 434(7037):1130, 2005. [Cited on page 8.]
- [16] T. E. Bate, E. J. Jarvis, M. E. Varney, and K.-T. Wu. Collective dynamics of microtubule-based 3d active fluids from single microtubules. *Soft matter*, 15(25):5006–5016, 2019. [Cited on page 106.]
- [17] H. Baumann and T. Surrey. Motor-mediated cortical versus astral microtubule organization in lipid-monolayered droplets. *Journal of Biological Chemistry*, 289(32):22524–22535, 2014. [Cited on page 92.]
- [18] J. M. Belmonte, M. Leptin, and F. Nédélec. A theory that predicts behaviors of disordered cytoskeletal networks. *Molecular Systems Biology*, 13(9), 2017. [Cited on page 32.]
- [19] W. M. Bement, M. Leda, A. M. Moe, A. M. Kita, M. E. Larson, A. E. Golding, C. Pfeuti, K.-C. Su, A. L. Miller, A. B. Goryachev, et al. Activator–inhibitor coupling between rho signalling and actin assembly makes the cell cortex an excitable medium. *Nature cell biology*, 17(11):1471, 2015. [Cited on page 53.]
- [20] P. M. Bendix, G. H. Koenderink, D. Cuvelier, Z. Dogic, B. N. Koeleman, W. M. Briehner, C. M. Field, L. Mahadevan, and D. A. Weitz. A quantitative analysis of contractility in active cytoskeletal protein networks. *Biophysical journal*, 94(8):3126–3136, 2008. [Cited on pages 29, 31, 74, and 98.]
- [21] E. Berliner, H. K. Mahtani, S. Karki, L. F. Chu, J. E. Cronan, and J. Gelles. Microtubule movement by a biotinylated kinesin bound to streptavidin-coated surface. *Journal of Biological Chemistry*, 269(11):8610–8615, 1994. [Cited on page 62.]
- [22] C. Bernard. *Leçons sur les phénomènes de la vie commune aux animaux et aux végétaux*, volume 1. Baillière, 1878. [Cited on page 4.]
- [23] A. Bernheim-Groswasser, S. Wiesner, R. M. Golsteyn, M.-F. Carlier, and C. Sykes. The dynamics of actin-based motility depend on surface parameters. *Nature*, 417(6886):308–311, 2002. [Cited on pages 24 and 26.]
- [24] O. J. Bertrand, D. K. Fygenson, and O. A. Saleh. Active, motor-driven mechanics in a dna gel. *Proceedings of the National Academy of Sciences*, 109(43):17342–17347, 2012. [Cited on page 55.]

- [25] J. S. Bois, F. Jülicher, and S. W. Grill. Pattern formation in active fluids. *Physical review letters*, 106(2):028103, 2011. [Cited on page 53.]
- [26] M. Braun, Z. Lansky, F. Hilitski, Z. Dogic, and S. Diez. Entropic forces drive contraction of cytoskeletal networks. *BioEssays*, 38(5):474–481, 2016. [Cited on page 30.]
- [27] A. Bricard, J.-B. Caussin, N. Desreumaux, O. Dauchot, and D. Bartolo. Emergence of macroscopic directed motion in populations of motile colloids. *Nature*, 503(7474):95, 2013. [Cited on page 21.]
- [28] J. Briscoe and S. Small. Morphogen rules: design principles of gradient-mediated embryo patterning. *Development*, 142(23):3996–4009, 2015. [Cited on page 53.]
- [29] F. Brochard and J. Lennon. Frequency spectrum of the flicker phenomenon in erythrocytes. *Journal de Physique*, 36(11):1035–1047, 1975. [Cited on page 175.]
- [30] M. Budroni, V. Upadhyay, and L. Rongy. Making a simple  $a + b \rightarrow c$  reaction oscillate by coupling to hydrodynamic effect. *Physical review letters*, 122(24):244502, 2019. [Cited on page 123.]
- [31] A. Cangialosi, C. Yoon, J. Liu, Q. Huang, J. Guo, T. D. Nguyen, D. H. Gracias, and R. Schulman. Dna sequence-directed shape change of photopatterned hydrogels via high-degree swelling. *Science*, 357(6356):1126–1130, 2017. [Cited on pages 9, 54, and 56.]
- [32] K. Carvalho, F.-C. Tsai, E. Lees, R. Voituriez, G. H. Koenderink, and C. Sykes. Cell-sized liposomes reveal how actomyosin cortical tension drives shape change. *Proceedings of the National Academy of Sciences*, 110(41):16456–16461, 2013. [Cited on page 92.]
- [33] A. Casini, F.-Y. Chang, R. Eluere, A. M. King, E. M. Young, Q. M. Dudley, A. Karim, K. Pratt, C. Bristol, A. Forget, et al. A pressure test to make 10 molecules in 90 days: external evaluation of methods to engineer biology. *Journal of the American Chemical Society*, 140(12):4302–4316, 2018. [Cited on pages 143, 163, and 200.]
- [34] V. Castets, E. Dulos, J. Boissonade, and P. De Kepper. Experimental evidence of a sustained standing turing-type nonequilibrium chemical pattern. *Physical review letters*, 64(24):2953, 1990. [Cited on page 39.]
- [35] F. Ceroni, R. Algar, G.-B. Stan, and T. Ellis. Quantifying cellular capacity identifies gene expression designs with reduced burden. *Nature methods*, 12(5):415, 2015. [Cited on page 140.]
- [36] J. Chappell, K. Jensen, and P. S. Freemont. Validation of an entirely in vitro approach for rapid prototyping of dna regulatory elements for synthetic biology. *Nucleic acids research*, 41(5):3471–3481, 2013. [Cited on pages 143 and 156.]
- [37] J. Chappell, M. K. Takahashi, and J. B. Lucks. Creating small transcription activating rnas. *Nature chemical biology*, 11(3):214, 2015. [Cited on pages 140 and 141.]
- [38] J. Chen and N. C. Seeman. Synthesis from dna of a molecule with the connectivity of a cube. *Nature*, 350(6319):631–633, 1991. [Cited on page 44.]

- [39] S. M. Chirieleison, P. B. Allen, Z. B. Simpson, A. D. Ellington, and X. Chen. Pattern transformation with dna circuits. *Nature chemistry*, 5(12):1000, 2013. [Cited on page 47.]
- [40] G. M. Cooper. *The cell: Molecular approach*. Sinauer Associates, 2000. [Cited on page 23.]
- [41] S. Čopar, J. Aplinc, Ž. Kos, S. Žumer, and M. Ravnik. Topology of three-dimensional active nematic turbulence confined to droplets. *Physical review X*, 9(3):031051, 2019. [Cited on page 95.]
- [42] D. L. Coy, M. Wagenbach, and J. Howard. Kinesin takes one 8-nm step for each atp that it hydrolyzes. *Journal of Biological Chemistry*, 274(6):3667–3671, 1999. [Cited on page 27.]
- [43] F. Crick. Central dogma of molecular biology. *Nature*, 227(5258):561–563, 1970. [Cited on page 138.]
- [44] R. E. Dawes-Hoang, K. M. Parmar, A. E. Christiansen, C. B. Phelps, A. H. Brand, and E. F. Wieschaus. Folded gastrulation, cell shape change and the control of myosin localization. *Development*, 132(18):4165–4178, 2005. [Cited on page 52.]
- [45] P.-G. De Gennes and J. Prost. *The physics of liquid crystals*, volume 83. Oxford university press, 1993. [Cited on pages 70 and 173.]
- [46] S. J. DeCamp, G. S. Redner, A. Baskaran, M. F. Hagan, and Z. Dogic. Orientational order of motile defects in active nematics. *Nature materials*, 14(11):1110, 2015. [Cited on pages 30, 79, 82, 83, 86, 94, and 97.]
- [47] M. Deforet, C. Carmona-Fontaine, K. S. Korolev, and J. B. Xavier. Evolution at the edge of expanding populations. *The American Naturalist*, 194(3):291–305, 2019. [Cited on page 19.]
- [48] N. D. Derr, B. S. Goodman, R. Jungmann, A. E. Leschziner, W. M. Shih, and S. L. Reck-Peterson. Tug-of-war in motor protein ensembles revealed with a programmable dna origami scaffold. *Science*, 338(6107):662–665, 2012. [Cited on pages 55 and 126.]
- [49] J. Deseigne, O. Dauchot, and H. Chaté. Collective motion of vibrated polar disks. *Physical review letters*, 105(9):098001, 2010. [Cited on page 20.]
- [50] J. Deseigne, S. Léonard, O. Dauchot, and H. Chaté. Vibrated polar disks: spontaneous motion, binary collisions, and collective dynamics. *Soft matter*, 8(20):5629–5639, 2012. [Cited on pages 20 and 21.]
- [51] M. Dogterom, M. Janson, C. Faivre-Moskalenko, A. Van der Horst, J. Kerssemakers, C. Tanase, and B. Mulder. Force generation by polymerizing microtubules. *Applied Physics A*, 75(2):331–336, 2002. [Cited on page 26.]
- [52] W. Driever and C. Nüsslein-Volhard. A gradient of bicoid protein in drosophila embryos. *Cell*, 54(1):83–93, 1988. [Cited on page 51.]
- [53] G. Duclos, R. Adkins, D. Banerjee, M. S. Peterson, M. Varghese, I. Kolvin, A. Baskaran, R. A. Pelcovits, T. R. Powers, A. Baskaran, et al. Topological structure and dynamics of three-dimensional active nematics. *Science*, 367(6482):1120–1124, 2020. [Cited on page 30.]

- [54] G. Duclos, C. Blanch-Mercader, V. Yashunsky, G. Salbreux, J.-F. Joanny, J. Prost, and P. Silberzan. Spontaneous shear flow in confined cellular nematics. *Nature physics*, 14(7):728–732, 2018. [Cited on pages [83](#) and [96](#).]
- [55] G. Duclos, C. Erlenkämper, J.-F. Joanny, and P. Silberzan. Topological defects in confined populations of spindle-shaped cells. *Nature physics*, 13(1):58, 2017. [Cited on pages [19](#) and [91](#).]
- [56] A. Dupin and F. C. Simmel. Signalling and differentiation in emulsion-based multi-compartmentalized in vitro gene circuits. *Nature chemistry*, 11(1):32, 2019. [Cited on pages [9](#), [163](#), and [200](#).]
- [57] S. R. Eddy. Non-coding rna genes and the modern rna world. *Nature reviews genetics*, 2(12):919–929, 2001. [Cited on pages [140](#) and [141](#).]
- [58] S. Edwards and J. Yeomans. Spontaneous flow states in active nematics: a unified picture. *Europhysics Letters*, 85(1):18008, 2009. [Cited on page [79](#).]
- [59] M. El Karoui, M. Hoyos-Flight, and L. Fletcher. Future trends in synthetic biology—a report. *Frontiers in bioengineering and biotechnology*, 7:175, 2019. [Cited on pages [8](#) and [10](#).]
- [60] P. W. Ellis, D. J. Pearce, Y.-W. Chang, G. Goldsztein, L. Giomi, and A. Fernandez-Nieves. Curvature-induced defect unbinding and dynamics in active nematic toroids. *Nature physics*, 14(1):85–90, 2018. [Cited on page [94](#).]
- [61] M. B. Elowitz and S. Leibler. A synthetic oscillatory network of transcriptional regulators. *Nature*, 403(6767):335–338, 2000. [Cited on page [8](#).]
- [62] M. A. English, L. R. Soenksen, R. V. Gayet, H. de Puig, N. M. Angenent-Mari, A. S. Mao, P. Q. Nguyen, and J. J. Collins. Programmable crispr-responsive smart materials. *Science*, 365(6455):780–785, 2019. [Cited on pages [9](#), [163](#), and [200](#).]
- [63] I. R. Epstein and J. A. Pojman. *An introduction to nonlinear chemical dynamics: oscillations, waves, patterns, and chaos*. Oxford University Press, 1998. [Cited on pages [38](#) and [112](#).]
- [64] A. Espah Borujeni, D. M. Mishler, J. Wang, W. Huso, and H. M. Salis. Automated physics-based design of synthetic riboswitches from diverse rna aptamers. *Nucleic acids research*, 44(1):1–13, 2015. [Cited on page [160](#).]
- [65] O. Farago. Membrane fluctuations near a plane rigid surface. *Physical review E*, 78(5):051919, 2008. [Cited on page [174](#).]
- [66] O. Farago and P. Pincus. Statistical mechanics of bilayer membrane with a fixed projected area. *The Journal of chemical physics*, 120(6):2934–2950, 2004. [Cited on page [174](#).]
- [67] P. J. Foster, S. Fürthauer, M. J. Shelley, and D. J. Needleman. Active contraction of microtubule networks. *Elife*, 4:e10837, 2015. [Cited on pages [30](#) and [73](#).]



- [68] J.-B. Fournier and C. Barbetta. Direct calculation from the stress tensor of the lateral surface tension of fluctuating fluid membranes. *Physical review letters*, 100(7):078103, 2008. [Cited on page 174.]
- [69] J. Fredens, K. Wang, D. de la Torre, L. F. Funke, W. E. Robertson, Y. Christova, T. Chia, W. H. Schmied, D. L. Dunkelmann, V. Beránek, et al. Total synthesis of escherichia coli with a recoded genome. *Nature*, 569(7757):514–518, 2019. [Cited on page 8.]
- [70] R. Freeman, M. Han, Z. Álvarez, J. A. Lewis, J. R. Wester, N. Stephanopoulos, M. T. McClendon, C. Lynsky, J. M. Godbe, H. Sangji, et al. Reversible self-assembly of superstructured networks. *Science*, 362(6416):808–813, 2018. [Cited on page 9.]
- [71] K. French. Harnessing synthetic biology for sustainable development. *Nature sustainability*, 2(4):250–252, 2019. [Cited on page 10.]
- [72] T. Fujii and Y. Rondelez. Predator–prey molecular ecosystems. *ACS nano*, 7(1):27–34, 2012. [Cited on pages 46 and 47.]
- [73] K. Furuta, A. Furuta, Y. Y. Toyoshima, M. Amino, K. Oiwa, and H. Kojima. Measuring collective transport by defined numbers of processive and nonprocessive kinesin motors. *Proceedings of the National Academy of Sciences*, 110(2):501–506, 2013. [Cited on pages 55, 63, 126, 130, and 167.]
- [74] J. Gačanin, C. V. Synatschke, and T. Weil. Biomedical applications of dna-based hydrogels. *Advanced Functional Materials*, page 1906253, 2019. [Cited on page 55.]
- [75] T. Gao and Z. Li. Self-driven droplet powered by active nematics. *Physical review letters*, 119(10):108002, 2017. [Cited on page 94.]
- [76] J. Garamella, R. Marshall, M. Rustad, and V. Noireaux. The all e. coli tx-tl toolbox 2.0: a platform for cell-free synthetic biology. *ACS synthetic biology*, 5(4):344–355, 2016. [Cited on page 143.]
- [77] A. Garcimartín, J. Pastor, L. Ferrer, J. Ramos, C. Martín-Gómez, and I. Zuriguel. Flow and clogging of a sheep herd passing through a bottleneck. *Physical review E*, 91(2):022808, 2015. [Cited on page 19.]
- [78] M. Gardel, J. H. Shin, F. MacKintosh, L. Mahadevan, P. Matsudaira, and D. Weitz. Elastic behavior of cross-linked and bundled actin networks. *Science*, 304(5675):1301–1305, 2004. [Cited on page 29.]
- [79] T. S. Gardner, C. R. Cantor, and J. J. Collins. Construction of a genetic toggle switch in escherichia coli. *Nature*, 403(6767):339–342, 2000. [Cited on page 8.]
- [80] C. Geary, P. W. Rothmund, and E. S. Andersen. A single-stranded architecture for co-transcriptional folding of rna nanostructures. *Science*, 345(6198):799–804, 2014. [Cited on page 44.]

- [81] E. W. Gehrels, W. B. Rogers, and V. N. Manoharan. Using dna strand displacement to control interactions in dna-grafted colloids. *Soft matter*, 14(6):969–984, 2018. [Cited on page 44.]
- [82] A. Genot, A. Baccouche, R. Sieskind, N. Aubert-Kato, N. Bredeche, J. Bartolo, V. Taly, T. Fujii, and Y. Rondelez. High-resolution mapping of bifurcations in nonlinear biochemical circuits. *Nature chemistry*, 8(8):760, 2016. [Cited on pages 46 and 47.]
- [83] D. Geyer, D. Martin, J. Tailleur, and D. Bartolo. Freezing a flock: Motility-induced phase separation in polar active liquids. *Physical review X*, 9(3):031043, 2019. [Cited on page 96.]
- [84] A. Gierer and H. Meinhardt. A theory of biological pattern formation. *Kybernetik*, 12(1):30–39, 1972. [Cited on page 38.]
- [85] C. Gilbert, G. Robertson, Y. Le Maho, Y. Naito, and A. Ancel. Huddling behavior in emperor penguins: dynamics of huddling. *Physiology & behavior*, 88(4-5):479–488, 2006. [Cited on page 20.]
- [86] G. Gines, R. Menezes, K. Nara, A.-S. Kirstetter, V. Taly, and Y. Rondelez. Isothermal digital detection of micrnas using background-free molecular circuit. *Science advances*, 6(4):eaay5952, 2020. [Cited on pages 163 and 200.]
- [87] G. Gines, A. Zadorin, J.-C. Galas, T. Fujii, A. Estevez-Torres, and Y. Rondelez. Microscopic agents programmed by dna circuits. *Nature nanotechnology*, 12(4):351, 2017. [Cited on pages 47, 133, 162, and 169.]
- [88] F. Ginot, I. Theurkauff, D. Levis, C. Ybert, L. Bocquet, L. Berthier, and C. Cottin-Bizonne. Nonequilibrium equation of state in suspensions of active colloids. *Physical review X*, 5(1):011004, 2015. [Cited on page 21.]
- [89] N. Giuseppone and A. Walther. *Out-of-Equilibrium Supramolecular Systems and Materials*. Wiley-VCH Verlag GmbH, 2020. [Cited on pages 12, 18, 32, and 161.]
- [90] P. Glock, F. Brauns, J. Halatek, E. Frey, and P. Schwill. Design of biochemical pattern forming systems from minimal motifs. *Elife*, 8:e48646, 2019. [Cited on pages 40 and 42.]
- [91] E. Godino, J. N. López, D. Foschepoth, C. Cleij, A. Doerr, C. F. Castellà, and C. Danelon. De novo synthesized min proteins drive oscillatory liposome deformation and regulate ftsafts cytoskeletal patterns. *Nature communications*, 10(1):1–12, 2019. [Cited on pages 163 and 200.]
- [92] N. W. Goehring and S. W. Grill. Cell polarity: mechanochemical patterning. *Trends in cell biology*, 23(2):72–80, 2013. [Cited on page 50.]
- [93] N. W. Goehring, P. K. Trong, J. S. Bois, D. Chowdhury, E. M. Nicola, A. A. Hyman, and S. W. Grill. Polarization of par proteins by advective triggering of a pattern-forming system. *Science*, 334(6059):1137–1141, 2011. [Cited on pages 35 and 50.]

- [94] L. M. González, N. Mukhitov, and C. A. Voigt. Resilient living materials built by printing bacterial spores. *Nature chemical biology*, 16(2):126–133, 2020. [Cited on page 9.]
- [95] D. M. Gordon, R. E. Paul, and K. Thorpe. What is the function of encounter patterns in ant colonies? *Animal Behaviour*, 45(6):1083–1100, 1993. [Cited on page 19.]
- [96] N. Gov, A. Zilman, and S. Safran. Hydrodynamics of confined membranes. *Physical review E*, 70(1):011104, 2004. [Cited on page 175.]
- [97] A. A. Green, J. Kim, D. Ma, P. A. Silver, J. J. Collins, and P. Yin. Complex cellular logic computation using ribocomputing devices. *Nature*, 548(7665):117, 2017. [Cited on page 160.]
- [98] A. A. Green, P. A. Silver, J. J. Collins, and P. Yin. Toehold switches: de-novo-designed regulators of gene expression. *Cell*, 159(4):925–939, 2014. [Cited on pages 141, 145, 152, 153, 155, 156, and 197.]
- [99] J. B. Green and J. Sharpe. Positional information and reaction-diffusion: two big ideas in developmental biology combine. *Development*, 142(7):1203–1211, 2015. [Cited on page 52.]
- [100] B. Groves, Y.-J. Chen, C. Zurla, S. Pochekailov, J. L. Kirschman, P. J. Santangelo, and G. Seelig. Computing in mammalian cells with nucleic acid strand exchange. *Nature nanotechnology*, 11(3):287, 2016. [Cited on page 43.]
- [101] P. Guillamat, J. Ignés-Mullol, and F. Sagués. Control of active liquid crystals with a magnetic field. *Proceedings of the National Academy of Sciences*, 113(20):5498–5502, 2016. [Cited on pages 30 and 98.]
- [102] P. Guillamat, J. Ignés-Mullol, and F. Sagués. Taming active turbulence with patterned soft interfaces. *Nature communications*, 8(1):564, 2017. [Cited on page 98.]
- [103] P. Guillamat, Ž. Kos, J. Hardoitiin, J. Ignés-Mullol, M. Ravnik, and F. Sagués. Active nematic emulsions. *Science advances*, 4(4):eaa01470, 2018. [Cited on pages 30, 92, 93, 94, 162, and 200.]
- [104] L. K. Gunther, K. Furuta, J. Bao, M. K. Urbanowski, H. Kojima, H. D. White, and T. Sakamoto. Coupling of two non-processive myosin 5c dimers enables processive stepping along actin filaments. *Scientific reports*, 4:4907, 2014. [Cited on pages 55 and 126.]
- [105] A. D. Haimovich, P. Muir, and F. J. Isaacs. Genomes by design. *Nature reviews genetics*, 16(9):501–516, 2015. [Cited on page 8.]
- [106] S. Hamada, K. G. Yancey, Y. Pardo, M. Gan, M. Vanatta, D. An, Y. Hu, T. L. Derrien, R. Ruiz, P. Liu, et al. Dynamic dna material with emergent locomotion behavior powered by artificial metabolism. *Science robotics*, 4(29):eaaw3512, 2019. [Cited on page 9.]
- [107] A. Hanna, A. Saul, and K. Showalter. Detailed studies of propagating fronts in the iodate oxidation of arsenous acid. *Journal of the American Chemical Society*, 104(14):3838–3844, 1982. [Cited on page 38.]

- [108] J. Hardoüin, R. Hughes, A. Doostmohammadi, J. Laurent, T. Lopez-Leon, J. M. Yeomans, J. Ignés-Mullol, and F. Sagués. Reconfigurable flows and defect landscape of confined active nematics. *Communications Physics*, 2(1):1–9, 2019. [Cited on pages 30, 86, 94, and 97.]
- [109] X. He, M. Aizenberg, O. Kuksenok, L. D. Zarzar, A. Shastri, A. C. Balazs, and J. Aizenberg. Synthetic homeostatic materials with chemo-mechano-chemical self-regulation. *Nature*, 487(7406):214–218, 2012. [Cited on page 57.]
- [110] S. Henkes, Y. Fily, and M. C. Marchetti. Active jamming: Self-propelled soft particles at high density. *Physical review E*, 84(4):040301, 2011. [Cited on page 96.]
- [111] C. Hentrich and T. Surrey. Microtubule organization by the antagonistic mitotic motors kinesin-5 and kinesin-14. *Journal of Cell Biology*, 189(3):465–480, 2010. [Cited on page 73.]
- [112] C. M. Heveran, S. L. Williams, J. Qiu, J. Artier, M. H. Hubler, S. M. Cook, J. C. Cameron, and W. V. Srubar III. Biomineralization and successive regeneration of engineered living building materials. *Matter*, 2020. [Cited on page 9.]
- [113] F. Hilitski, A. R. Ward, L. Cajamarca, M. F. Hagan, G. M. Grason, and Z. Dogic. Measuring cohesion between macromolecular filaments one pair at a time: depletion-induced microtubule bundling. *Physical review letters*, 114(13):138102, 2015. [Cited on pages 30 and 72.]
- [114] B. V. Hokmabad, K. A. Baldwin, C. Krüger, C. Bahr, and C. C. Maass. Topological stabilization and dynamics of self-propelling nematic shells. *Physical review letters*, 123(17):178003, 2019. [Cited on page 96.]
- [115] T. E. Holy, M. Dogterom, B. Yurke, and S. Leibler. Assembly and positioning of microtubule asters in microfabricated chambers. *Proceedings of the National Academy of Sciences*, 94(12):6228–6231, 1997. [Cited on pages 25 and 26.]
- [116] F. Hong, D. Ma, K. Wu, L. A. Mina, R. C. Luiten, Y. Liu, H. Yan, and A. A. Green. Precise and programmable detection of mutations using ultraspecific riboregulators. *Cell*, 2020. [Cited on page 160.]
- [117] S. Hoshika, N. A. Leal, M.-J. Kim, M.-S. Kim, N. B. Karalkar, H.-J. Kim, A. M. Bates, N. E. Watkins, H. A. SantaLucia, A. J. Meyer, et al. Hachimoji dna and rna: A genetic system with eight building blocks. *Science*, 363(6429):884–887, 2019. [Cited on page 8.]
- [118] H. Hotani and H. Miyamoto. Dynamic features of microtubules as visualized by dark-field microscopy. *Advances in biophysics*, 26:135–156, 1990. [Cited on page 92.]
- [119] C. Y. Hu, J. D. Varner, and J. B. Lucks. Generating effective models and parameters for rna genetic circuits. *ACS synthetic biology*, 4(8):914–926, 2015. [Cited on pages 143 and 154.]
- [120] J. Huang, S. Liu, C. Zhang, X. Wang, J. Pu, F. Ba, S. Xue, H. Ye, T. Zhao, K. Li, et al. Programmable and printable bacillus subtilis biofilms as engineered living materials. *Nature chemical biology*, 15(1):34–41, 2019. [Cited on page 9.]

- [121] F. Huber, A. Boire, M. P. López, and G. H. Koenderink. Cytoskeletal crosstalk: when three different personalities team up. *Current opinion in cell biology*, 32:39–47, 2015. [Cited on page 29.]
- [122] L. Huber, R. Suzuki, T. Krüger, E. Frey, and A. Bausch. Emergence of coexisting ordered states in active matter systems. *Science*, 361(6399):255–258, 2018. [Cited on page 29.]
- [123] C. A. Hutchison, R.-Y. Chuang, V. N. Noskov, N. Assad-Garcia, T. J. Deerinck, M. H. Ellisman, J. Gill, K. Kannan, B. J. Karas, L. Ma, et al. Design and synthesis of a minimal bacterial genome. *Science*, 351(6280):aad6253, 2016. [Cited on page 8.]
- [124] A. A. Hyman, S. Salser, D. Drechsel, N. Unwin, and T. J. Mitchison. Role of gtp hydrolysis in microtubule dynamics: information from a slowly hydrolyzable analogue, gmppcp. *Molecular biology of the cell*, 3(10):1155–1167, 1992. [Cited on page 116.]
- [125] Y. Ideses, V. Erukhimovitch, R. Brand, D. Jourdain, J. S. Hernandez, U. Gabinet, S. Safran, K. Kruse, and A. Bernheim-Groswasser. Spontaneous buckling of contractile poroelastic actomyosin sheets. *Nature communications*, 9(1):2461, 2018. [Cited on page 77.]
- [126] D. Inoue, B. Mahmot, A. M. R. Kabir, T. I. Farhana, K. Tokuraku, K. Sada, A. Konagaya, and A. Kakugo. Depletion force induced collective motion of microtubules driven by kinesin. *Nanoscale*, 7(43):18054–18061, 2015. [Cited on page 29.]
- [127] F. J. Isaacs, D. J. Dwyer, and J. J. Collins. Rna synthetic biology. *Nature biotechnology*, 24(5):545–554, 2006. [Cited on page 140.]
- [128] F. J. Isaacs, D. J. Dwyer, C. Ding, D. D. Pervouchine, C. R. Cantor, and J. J. Collins. Engineered riboregulators enable post-transcriptional control of gene expression. *Nature biotechnology*, 22(7):841–847, 2004. [Cited on pages 141, 156, 158, and 198.]
- [129] M. Isalan, C. Lemerle, and L. Serrano. Engineering gene networks to emulate drosophila embryonic pattern formation. *PLoS biology*, 3(3), 2005. [Cited on page 41.]
- [130] Y. Iwane, A. Hitomi, H. Murakami, T. Katoh, Y. Goto, and H. Suga. Expanding the amino acid repertoire of ribosomal polypeptide synthesis via the artificial division of codon boxes. *Nature chemistry*, 8(4):317, 2016. [Cited on pages 8 and 160.]
- [131] F. Jacob and J. Monod. Genetic regulatory mechanisms in the synthesis of proteins. *Journal of molecular biology*, 3(3):318–356, 1961. [Cited on page 139.]
- [132] J.-F. Joanny, F. Jülicher, K. Kruse, and J. Prost. Hydrodynamic theory for multi-component active polar gels. *New Journal of Physics*, 9(11):422, 2007. [Cited on page 35.]
- [133] M. R. Jones, N. C. Seeman, and C. A. Mirkin. Programmable materials and the nature of the dna bond. *Science*, 347(6224):1260901, 2015. [Cited on pages 9 and 44.]
- [134] D. Joshi, D. Bargteil, A. Caciagli, J. Burelbach, Z. Xing, A. S. Nunes, D. E. Pinto, N. A. Araújo, J. Brujic, and E. Eiser. Kinetic control of the coverage of oil droplets by dna-functionalized colloids. *Science advances*, 2(8):e1600881, 2016. [Cited on page 44.]

- [135] F. Jülicher, K. Kruse, J. Prost, and J.-F. Joanny. Active behavior of the cytoskeleton. *Physics reports*, 449(1-3):3–28, 2007. [Cited on pages 79 and 173.]
- [136] M. P. Juniper, M. Weiss, I. Platzman, J. P. Spatz, and T. Surrey. Spherical network contraction forms microtubule asters in confinement. *Soft matter*, 14(6):901–909, 2018. [Cited on pages 92 and 93.]
- [137] E. Karzbrun, J. Shin, R. H. Bar-Ziv, and V. Noireaux. Coarse-grained dynamics of protein synthesis in a cell-free system. *Physical review letters*, 106(4):048104, 2011. [Cited on pages 143, 148, and 151.]
- [138] E. Karzbrun, A. M. Tayar, V. Noireaux, and R. H. Bar-Ziv. Programmable on-chip dna compartments as artificial cells. *Science*, 345(6198):829–832, 2014. [Cited on page 41.]
- [139] S. Kassem, T. van Leeuwen, A. S. Lubbe, M. R. Wilson, B. L. Feringa, and D. A. Leigh. Artificial molecular motors. *Chemical Society Reviews*, 46(9):2592–2621, 2017. [Cited on page 57.]
- [140] F. C. Keber, E. Loiseau, T. Sanchez, S. J. DeCamp, L. Giomi, M. J. Bowick, M. C. Marchetti, Z. Dogic, and A. R. Bausch. Topology and dynamics of active nematic vesicles. *Science*, 345(6201):1135–1139, 2014. [Cited on pages 30, 78, 79, 92, and 94.]
- [141] A. Keppler, S. Gendreizig, T. Gronemeyer, H. Pick, H. Vogel, and K. Johnsson. A general method for the covalent labeling of fusion proteins with small molecules in vivo. *Nature biotechnology*, 21(1):86–89, 2003. [Cited on page 126.]
- [142] J. J. Keya, R. Suzuki, A. M. R. Kabir, D. Inoue, H. Asanuma, K. Sada, H. Hess, A. Kuzuya, and A. Kakugo. Dna-assisted swarm control in a biomolecular motor system. *Nature communications*, 9(1):453, 2018. [Cited on pages 55 and 129.]
- [143] J. Kim, K. S. White, and E. Winfree. Construction of an in vitro bistable circuit from synthetic transcriptional switches. *Molecular systems biology*, 2(1), 2006. [Cited on page 44.]
- [144] J. Kim and E. Winfree. Synthetic in vitro transcriptional oscillators. *Molecular systems biology*, 7(1), 2011. [Cited on page 44.]
- [145] G. H. Koenderink, Z. Dogic, F. Nakamura, P. M. Bendix, F. C. MacKintosh, J. H. Hartwig, T. P. Stossel, and D. A. Weitz. An active biopolymer network controlled by molecular motors. *Proceedings of the National Academy of Sciences*, 106(36):15192–15197, 2009. [Cited on pages 29 and 74.]
- [146] A. Kolmogorov, I. Petrovsky, and N. Piskunov. Étude de l'équation de la diffusion avec croissance de la quantité de matière et son application à un problème biologique. [investigation of the equation of diffusion combined with increasing of the substance and its application to a biology problem]. *Bull. Moscow State Univ. Ser. A: Math. Mech*, 1(6):1–25, 1937. [Cited on page 38.]
- [147] S. Kondo and R. Asai. A reaction–diffusion wave on the skin of the marine angelfish pomacanthus. *Nature*, 376(6543):765–768, 1995. [Cited on pages 47 and 49.]

- [148] H. Kong, R. Kucera, and W. Jack. Characterization of a dna polymerase from the hyperthermophile archaea *thermococcus litoralis*. vent dna polymerase, steady state kinetics, thermal stability, processivity, strand displacement, and exonuclease activities. *Journal of Biological Chemistry*, 268(3):1965–1975, 1993. [Cited on page 108.]
- [149] E. Kopperger, J. List, S. Madhira, F. Rothfischer, D. C. Lamb, and F. C. Simmel. A self-assembled nanoscale robotic arm controlled by electric fields. *Science*, 359(6373):296–301, 2018. [Cited on page 44.]
- [150] C. J. Krebs, R. Boonstra, S. Boutin, and A. R. Sinclair. What drives the 10-year cycle of snowshoe hares? the ten-year cycle of snowshoe hares—one of the most striking features of the boreal forest—is a product of the interaction between predation and food supplies, as large-scale experiments in the yukon have demonstrated. *BioScience*, 51(1):25–35, 2001. [Cited on page 37.]
- [151] S. Kriegman, D. Blackiston, M. Levin, and J. Bongard. A scalable pipeline for designing reconfigurable organisms. *Proceedings of the National Academy of Sciences*, 2020. [Cited on pages 8, 163, and 200.]
- [152] S. J. Kron and J. A. Spudich. Fluorescent actin filaments move on myosin fixed to a glass surface. *Proceedings of the National Academy of Sciences*, 83(17):6272–6276, 1986. [Cited on page 29.]
- [153] K. Kruse, J.-F. Joanny, F. Jülicher, J. Prost, and K. Sekimoto. Generic theory of active polar gels: a paradigm for cytoskeletal dynamics. *The European Physical Journal E*, 16(1):5–16, 2005. [Cited on pages 32, 35, 79, and 83.]
- [154] K. V. Kumar, J. S. Bois, F. Jülicher, and S. W. Grill. Pulsatory patterns in active fluids. *Physical review letters*, 112(20):208101, 2014. [Cited on page 53.]
- [155] N. Kumar, R. Zhang, J. J. de Pablo, and M. L. Gardel. Tunable structure and dynamics of active liquid crystals. *Science advances*, 4(10):eaat7779, 2018. [Cited on pages 30, 82, and 83.]
- [156] M. Kushwaha, W. Rostain, S. Prakash, J. N. Duncan, and A. Jaramillo. Using rna as molecular code for programming cellular function. *ACS synthetic biology*, 5(8):795–809, 2016. [Cited on pages 140 and 141.]
- [157] A. Lau, A. Prasad, and Z. Dogic. Condensation of isolated semi-flexible filaments driven by depletion interactions. *Europhysics Letters*, 87(4):48006, 2009. [Cited on page 68.]
- [158] R. A. Lease, M. E. Cusick, and M. Belfort. Riboregulation in *escherichia coli*: Dsra rna acts by rna: Rna interactions at multiple loci. *Proceedings of the National Academy of Sciences*, 95(21):12456–12461, 1998. [Cited on page 141.]
- [159] J. B. Lee, S. Peng, D. Yang, Y. H. Roh, H. Funabashi, N. Park, E. J. Rice, L. Chen, R. Long, M. Wu, et al. A mechanical metamaterial made from a dna hydrogel. *Nature nanotechnology*, 7(12):816, 2012. [Cited on page 54.]

- [160] J. Leira-Iglesias, A. Tassoni, T. Adachi, M. Stich, and T. M. Hermans. Oscillations, travelling fronts and patterns in a supramolecular system. *Nature nanotechnology*, 13(11):1021, 2018. [Cited on page 57.]
- [161] M. Leptin. Morphogenesis: Control of epithelial cell shape changes. *Current Biology*, 4(8):709–712, 1994. [Cited on page 52.]
- [162] Q. Li, G. Fuks, E. Moulin, M. Maaloum, M. Rawiso, I. Kulic, J. T. Foy, and N. Giuseppone. Macroscopic contraction of a gel induced by the integrated motion of light-driven molecular motors. *Nature nanotechnology*, 10(2):161, 2015. [Cited on page 57.]
- [163] T. Litschel, B. Ramm, R. Maas, M. Heymann, and P. Schwille. Beating vesicles: encapsulated protein oscillations cause dynamic membrane deformations. *Angewandte Chemie International Edition*, 57(50):16286–16290, 2018. [Cited on page 40.]
- [164] Y.-J. Liu, M. Le Berre, F. Lautenschlaeger, P. Maiuri, A. Callan-Jones, M. Heuzé, T. Takaki, R. Voituriez, and M. Piel. Confinement and low adhesion induce fast amoeboid migration of slow mesenchymal cells. *Cell*, 160(4):659–672, 2015. [Cited on page 96.]
- [165] E. Loiseau, J. A. Schneider, F. C. Keber, C. Pelzl, G. Massiera, G. Salbreux, and A. R. Bausch. Shape remodeling and blebbing of active cytoskeletal vesicles. *Science advances*, 2(4):e1500465, 2016. [Cited on pages 92 and 93.]
- [166] M. Loose, E. Fischer-Friedrich, J. Ries, K. Kruse, and P. Schwille. Spatial regulators for bacterial cell division self-organize into surface waves in vitro. *Science*, 320(5877):789–792, 2008. [Cited on pages 40 and 41.]
- [167] F. J. Lopes, F. M. Vieira, D. M. Holloway, P. M. Bisch, and A. V. Spirov. Spatial bistability generates hunchback expression sharpness in the drosophila embryo. *PLoS computational biology*, 4(9), 2008. [Cited on page 52.]
- [168] R. Lorenz, S. H. Bernhart, C. H. Zu Siederdissen, H. Tafer, C. Flamm, P. F. Stadler, and I. L. Hofacker. Viennarna package 2.0. *Algorithms for molecular biology*, 6(1):26, 2011. [Cited on page 141.]
- [169] R. Luther. Rauemliche fortpflanzung chemischer reaktionen. *Z. für Elektrochemie und angew. physikalische Chemie*, 12(32):506–600, 1906. [Cited on page 38.]
- [170] A. Maitra, P. Srivastava, M. Rao, and S. Ramaswamy. Activating membranes. *Physical review letters*, 112(25):258101, 2014. [Cited on pages 79 and 174.]
- [171] L. Manukyan, S. A. Montandon, A. Fofonjka, S. Smirnov, and M. C. Milinkovitch. A living mesoscopic cellular automaton made of skin scales. *Nature*, 544(7649):173, 2017. [Cited on page 47.]
- [172] C. Mao, T. H. LaBean, J. H. Reif, and N. C. Seeman. Logical computation using algorithmic self-assembly of dna triple-crossover molecules. *Nature*, 407(6803):493–496, 2000. [Cited on page 44.]



- [173] M. C. Marchetti, J.-F. Joanny, S. Ramaswamy, T. B. Liverpool, J. Prost, M. Rao, and R. A. Simha. Hydrodynamics of soft active matter. *Reviews of Modern Physics*, 85(3):1143, 2013. [Cited on pages [19](#), [30](#), [79](#), [83](#), and [173](#).]
- [174] B. Martínez-Prat, J. Ignés-Mullol, J. Casademunt, and F. Sagués. Selection mechanism at the onset of active turbulence. *Nature physics*, 15(4):362, 2019. [Cited on pages [30](#), [78](#), [79](#), [80](#), [82](#), [83](#), [86](#), [87](#), [88](#), [94](#), [97](#), [162](#), [175](#), and [192](#).]
- [175] M. Matsuda, M. Koga, K. Woltjen, E. Nishida, and M. Ebisuya. Synthetic lateral inhibition governs cell-type bifurcation with robust ratios. *Nature communications*, 6(1):1–12, 2015. [Cited on page [48](#).]
- [176] W. McClure and T. Jovin. The steady state kinetic parameters and non-processivity of escherichia coli deoxyribonucleic acid polymerase i. *Journal of Biological Chemistry*, 250(11):4073–4080, 1975. [Cited on page [108](#).]
- [177] A. D. Mehta, R. S. Rock, M. Rief, J. A. Spudich, M. S. Mooseker, and R. E. Cheney. Myosin-v is a processive actin-based motor. *Nature*, 400(6744):590–593, 1999. [Cited on pages [28](#) and [140](#).]
- [178] L. H. Meijer, A. Joesaar, E. Steur, W. Engelen, R. A. Van Santen, M. Merkx, and T. F. De Greef. Hierarchical control of enzymatic actuators using dna-based switchable memories. *Nature communications*, 8(1):1117, 2017. [Cited on page [46](#).]
- [179] J. B. Michaux, F. B. Robin, W. M. McFadden, and E. M. Munro. Excitable rhoa dynamics drive pulsed contractions in the early c. elegans embryo. *Journal of Cell Biology*, 217(12):4230–4252, 2018. [Cited on page [30](#).]
- [180] M. B. Miller and B. L. Bassler. Quorum sensing in bacteria. *Annual Reviews in Microbiology*, 55(1):165–199, 2001. [Cited on page [133](#).]
- [181] H. Miyata and H. Hotani. Morphological changes in liposomes caused by polymerization of encapsulated actin and spontaneous formation of actin bundles. *Proceedings of the National Academy of Sciences*, 89(23):11547–11551, 1992. [Cited on page [92](#).]
- [182] Y. Miyazono, M. Hayashi, P. Karagiannis, Y. Harada, and H. Tadakuma. Strain through the neck linker ensures processive runs: a dna-kinesin hybrid nanomachine study. *The EMBO journal*, 29(1):93–106, 2010. [Cited on page [126](#).]
- [183] M. R. Mofrad. Rheology of the cytoskeleton. *Annual Review of Fluid Mechanics*, 41:433–453, 2009. [Cited on page [29](#).]
- [184] A. Mogilner and G. Oster. The polymerization ratchet model explains the force-velocity relation for growing microtubules. *European Biophysics Journal*, 28(3):235–242, 1999. [Cited on page [25](#).]
- [185] K. Montagne, G. Gines, T. Fujii, and Y. Rondelez. Boosting functionality of synthetic dna circuits with tailored deactivation. *Nature communications*, 7:13474, 2016. [Cited on page [46](#).]

- [186] K. Montagne, R. Plasson, Y. Sakai, T. Fujii, and Y. Rondelez. Programming an in vitro dna oscillator using a molecular networking strategy. *Molecular systems biology*, 7(1), 2011. [Cited on pages 44, 46, 47, and 107.]
- [187] S. J. Moore, J. T. MacDonald, S. Wienecke, A. Ishwarbhai, A. Tsipa, R. Aw, N. Kylilis, D. J. Bell, D. W. McClymont, K. Jensen, et al. Rapid acquisition and model-based analysis of cell-free transcription–translation reactions from nonmodel bacteria. *Proceedings of the National Academy of Sciences*, 115(19):E4340–E4349, 2018. [Cited on page 160.]
- [188] C. Mora, D. P. Tittensor, S. Adl, A. G. Simpson, and B. Worm. How many species are there on earth and in the ocean? *PLoS biology*, 9(8), 2011. [Cited on page 5.]
- [189] S. Mostowy and P. Cossart. Septins: the fourth component of the cytoskeleton. *Nature reviews molecular cell biology*, 13(3):183–194, 2012. [Cited on page 23.]
- [190] S. Münster, A. Jain, A. Mietke, A. Pavlopoulos, S. W. Grill, and P. Tomancak. Attachment of the blastoderm to the vitelline envelope affects gastrulation of insects. *Nature*, 568(7752):395–399, 2019. [Cited on page 35.]
- [191] M. Muraoka and H. Sakai. Effects of purinenucleotide analogues on microtubule assembly. *Cell structure and function*, 24(5):305–312, 1999. [Cited on page 116.]
- [192] S. Nagahara and T. Matsuda. Hydrogel formation via hybridization of oligonucleotides derivatized in water-soluble vinyl polymers. *Polymer Gels and Networks*, 4(2):111–127, 1996. [Cited on page 54.]
- [193] T. Nakata, S. Niwa, Y. Okada, F. Perez, and N. Hirokawa. Preferential binding of a kinesin-1 motor to gtp-tubulin-rich microtubules underlies polarized vesicle transport. *Journal of Cell Biology*, 194(2):245–255, 2011. [Cited on page 116.]
- [194] V. Narayan, S. Ramaswamy, and N. Menon. Long-lived giant number fluctuations in a swarming granular nematic. *Science*, 317(5834):105–108, 2007. [Cited on page 20.]
- [195] F. Nedelec, T. Surrey, A. C. Maggs, and S. Leibler. Self-organization of microtubules and motors. *Nature*, 389(6648):305, 1997. [Cited on pages 29, 31, 62, 188, and 190.]
- [196] D. Needleman and Z. Dogic. Active matter at the interface between materials science and cell biology. *Nature reviews materials*, 2(9):17048, 2017. [Cited on page 29.]
- [197] D. Nelson and L. Peliti. Fluctuations in membranes with crystalline and hexatic order. *Journal de physique*, 48(7):1085–1092, 1987. [Cited on page 176.]
- [198] P. Nelson and T. Powers. Renormalization of chiral couplings in titled bilayer membranes. *Journal de Physique II*, 3(10):1535–1569, 1993. [Cited on page 176.]
- [199] H. Niederholtmeyer, C. Chaggan, and N. K. Devaraj. Communication and quorum sensing in non-living mimics of eukaryotic cells. *Nature communications*, 9(1):1–8, 2018. [Cited on page 134.]

- [200] H. Niederholtmeyer, V. Stepanova, and S. J. Maerkl. Implementation of cell-free biological networks at steady state. *Proceedings of the National Academy of Sciences*, 110(40):15985–15990, 2013. [Cited on page 143.]
- [201] H. Niederholtmeyer, Z. Z. Sun, Y. Hori, E. Yeung, A. Verpoorte, R. M. Murray, and S. J. Maerkl. Rapid cell-free forward engineering of novel genetic ring oscillators. *Elife*, 4:e09771, 2015. [Cited on page 143.]
- [202] H. Niederholtmeyer, L. Xu, and S. J. Maerkl. Real-time mrna measurement during an in vitro transcription and translation reaction using binary probes. *ACS synthetic biology*, 2(8):411–417, 2013. [Cited on pages 143, 151, and 160.]
- [203] M. W. Nirenberg and J. H. Matthaei. The dependence of cell-free protein synthesis in e. coli upon naturally occurring or synthetic polyribonucleotides. *Proceedings of the National Academy of Sciences*, 47(10):1588–1602, 1961. [Cited on pages 41 and 142.]
- [204] V. Noireaux and A. Libchaber. A vesicle bioreactor as a step toward an artificial cell assembly. *Proceedings of the National Academy of Sciences*, 101(51):17669–17674, 2004. [Cited on pages 163 and 200.]
- [205] H. Ohashi, T. Kanamori, Y. Shimizu, and T. Ueda. A highly controllable reconstituted cell-free system—a breakthrough in protein synthesis research. *Current pharmaceutical biotechnology*, 11(3):267–271, 2010. [Cited on page 144.]
- [206] L. Onsager. Reciprocal relations in irreversible processes. i. *Physical review*, 37(4):405, 1931. [Cited on pages 32 and 33.]
- [207] A. Opathalage, M. M. Norton, M. P. Juniper, B. Langeslay, S. A. Aghvami, S. Fraden, and Z. Dogic. Self-organized dynamics and the transition to turbulence of confined active nematics. *Proceedings of the National Academy of Sciences*, 116(11):4788–4797, 2019. [Cited on pages 30, 79, 83, 86, 94, and 97.]
- [208] E. Oron, M. Mannervik, S. Rencus, O. Harari-Steinberg, S. Neuman-Silberberg, D. Segal, and D. A. Chamovitz. Cop9 signalosome subunits 4 and 5 regulate multiple pleiotropic pathways in drosophila melanogaster. *Development*, 129(19):4399–4409, 2002. [Cited on page 52.]
- [209] A. Padirac, T. Fujii, A. Estévez-Torres, and Y. Rondelez. Spatial waves in synthetic biochemical networks. *Journal of the American Chemical Society*, 135(39):14586–14592, 2013. [Cited on pages 46 and 48.]
- [210] A. Padirac, T. Fujii, and Y. Rondelez. Bottom-up construction of in vitro switchable memories. *Proceedings of the National Academy of Sciences*, 109(47):E3212–E3220, 2012. [Cited on pages 46 and 47.]
- [211] A. Padirac, T. Fujii, and Y. Rondelez. Quencher-free multiplexed monitoring of dna reaction circuits. *Nucleic acids research*, 40(15):e118–e118, 2012. [Cited on page 104.]
- [212] J. Palacci, S. Sacanna, A. P. Steinberg, D. J. Pine, and P. M. Chaikin. Living crystals of light-activated colloidal surfers. *Science*, 339(6122):936–940, 2013. [Cited on page 21.]

- [213] K. Pardee, A. A. Green, T. Ferrante, D. E. Cameron, A. DaleyKeyser, P. Yin, and J. J. Collins. Paper-based synthetic gene networks. *Cell*, 159(4):940–954, 2014. [Cited on page 160.]
- [214] K. Pardee, A. A. Green, M. K. Takahashi, D. Braff, G. Lambert, J. W. Lee, T. Ferrante, D. Ma, N. Donghia, M. Fan, et al. Rapid, low-cost detection of zika virus using programmable biomolecular components. *Cell*, 165(5):1255–1266, 2016. [Cited on pages 160, 163, and 200.]
- [215] B. L. Partridge, J. Johansson, and J. Kalish. The structure of schools of giant bluefin tuna in cape cod bay. *Environmental Biology of Fishes*, 9(3-4):253–262, 1983. [Cited on page 19.]
- [216] R. Phillips, J. Theriot, J. Kondev, and H. Garcia. *Physical biology of the cell*. Garland Science, 2012. [Cited on pages 24, 28, 41, and 72.]
- [217] F.-A. Piedra, T. Kim, E. S. Garza, E. A. Geyer, A. Burns, X. Ye, and L. M. Rice. Gdp-to-gtp exchange on the microtubule end can contribute to the frequency of catastrophe. *Molecular biology of the cell*, 27(22):3515–3525, 2016. [Cited on page 116.]
- [218] M. Pinot, F. Chesnel, J. Kubiak, I. Arnal, F. Nedelec, and Z. Gueroui. Effects of confinement on the self-organization of microtubules and motors. *Current Biology*, 19(11):954–960, 2009. [Cited on page 92.]
- [219] L.-L. Pontani, J. Van der Gucht, G. Salbreux, J. Heuvingh, J.-F. Joanny, and C. Sykes. Reconstitution of an actin cortex inside a liposome. *Biophysical journal*, 96(1):192–198, 2009. [Cited on page 92.]
- [220] F. Praetorius and H. Dietz. Self-assembly of genetically encoded dna-protein hybrid nanoscale shapes. *Science*, 355(6331):eaam5488, 2017. [Cited on page 9.]
- [221] P. Praveschotinunt, A. M. Duraj-Thatte, I. Gelfat, F. Bahl, D. B. Chou, and N. S. Joshi. Engineered e. coli nissle 1917 for the delivery of matrix-tethered therapeutic domains to the gut. *Nature communications*, 10(1):1–14, 2019. [Cited on page 9.]
- [222] J. Prost, F. Jülicher, and J.-F. Joanny. Active gel physics. *Nature physics*, 11(2):111–117, 2015. [Cited on pages 79 and 173.]
- [223] P. A. Pullarkat, P. A. Fernández, and A. Ott. Rheological properties of the eukaryotic cell cytoskeleton. *Physics Reports*, 449(1-3):29–53, 2007. [Cited on page 29.]
- [224] H. Qi, M. Ghodousi, Y. Du, C. Grun, H. Bae, P. Yin, and A. Khademhosseini. Dna-directed self-assembly of shape-controlled hydrogels. *Nature communications*, 4:2275, 2013. [Cited on page 9.]
- [225] L. S. Qi, M. H. Larson, L. A. Gilbert, J. A. Doudna, J. S. Weissman, A. P. Arkin, and W. A. Lim. Repurposing crispr as an rna-guided platform for sequence-specific control of gene expression. *Cell*, 152(5):1173–1183, 2013. [Cited on page 141.]
- [226] S. Ramaswamy. The mechanics and statistics of active matter. *Annu. Rev. Condens. Matter Phys.*, 1(1):323–345, 2010. [Cited on pages 19, 79, and 173.]

- [227] D. M. Raskin and P. A. de Boer. Rapid pole-to-pole oscillation of a protein required for directing division to the middle of *Escherichia coli*. *Proceedings of the National Academy of Sciences*, 96(9):4971–4976, 1999. [Cited on page 40.]
- [228] P. Recho, A. Hallou, and E. Hannezo. Theory of mechanochemical patterning in biphasic biological tissues. *Proceedings of the National Academy of Sciences*, 116(12):5344–5349, 2019. [Cited on page 53.]
- [229] A.-C. Reymann, R. Boujemaa-Paterski, J.-L. Martiel, C. Guérin, W. Cao, H. F. Chin, M. Enrique, M. Théry, and L. Blanchoin. Actin network architecture can determine myosin motor activity. *Science*, 336(6086):1310–1314, 2012. [Cited on pages 29 and 74.]
- [230] A.-C. Reymann, F. Staniscia, A. Erzberger, G. Salbreux, and S. W. Grill. Cortical flow aligns actin filaments to form a furrow. *Elife*, 5:e17807, 2016. [Cited on page 19.]
- [231] R. Rezakhaniha, A. Agianniotis, J. T. C. Schrauwen, A. Griffa, D. Sage, C. v. Bouten, F. Van De Vosse, M. Unser, and N. Stergiopoulos. Experimental investigation of collagen waviness and orientation in the arterial adventitia using confocal laser scanning microscopy. *Biomechanics and modeling in mechanobiology*, 11(3-4):461–473, 2012. [Cited on page 70.]
- [232] B. Rieß, R. K. Grötsch, and J. Boekhoven. The design of dissipative molecular assemblies driven by chemical reaction cycles. *Chem*, 2019. [Cited on page 25.]
- [233] K. Rinaudo, L. Bleris, R. Maddamsetti, S. Subramanian, R. Weiss, and Y. Benenson. A universal rnai-based logic evaluator that operates in mammalian cells. *Nature biotechnology*, 25(7):795–801, 2007. [Cited on page 141.]
- [234] G. Rodrigo, T. E. Landrain, and A. Jaramillo. De novo automated design of small rna circuits for engineering synthetic riboregulation in living cells. *Proceedings of the National Academy of Sciences*, 109(38):15271–15276, 2012. [Cited on pages 141, 144, 155, 156, and 197.]
- [235] W. B. Rogers and V. N. Manoharan. Programming colloidal phase transitions with dna strand displacement. *Science*, 347(6222):639–642, 2015. [Cited on page 44.]
- [236] J. Roostalu, J. Rickman, C. Thomas, F. Nédélec, and T. Surrey. Determinants of polar versus nematic organization in networks of dynamic microtubules and mitotic motors. *Cell*, 175(3):796–808, 2018. [Cited on pages 73 and 97.]
- [237] T. D. Ross, H. J. Lee, Z. Qu, R. A. Banks, R. Phillips, and M. Thomson. Controlling organization and forces in active matter through optically defined boundaries. *Nature*, 572(7768):224–229, 2019. [Cited on page 98.]
- [238] P. W. Rothmund. Folding dna to create nanoscale shapes and patterns. *Nature*, 440(7082):297–302, 2006. [Cited on pages 9 and 44.]
- [239] M. Rubenstein, A. Cornejo, and R. Nagpal. Programmable self-assembly in a thousand-robot swarm. *Science*, 345(6198):795–799, 2014. [Cited on page 20.]

- [240] S. Safran. *Statistical thermodynamics of surfaces, interfaces, and membranes*. CRC Press, 2018. [Cited on page 174.]
- [241] T. Sanchez, D. T. Chen, S. J. DeCamp, M. Heymann, and Z. Dogic. Spontaneous motion in hierarchically assembled active matter. *Nature*, 491(7424):431, 2012. [Cited on pages 30, 31, 62, 63, 77, 78, 79, 80, 81, 83, 86, 92, 94, 96, 97, 98, 123, 161, 188, and 190.]
- [242] T. Sanchez and Z. Dogic. Engineering oscillating microtubule bundles. In *Methods in enzymology*, volume 524, pages 205–224. Elsevier, 2013. [Cited on page 68.]
- [243] T. Sanchez, D. Welch, D. Nicastro, and Z. Dogic. Cilia-like beating of active microtubule bundles. *Science*, 333(6041):456–459, 2011. [Cited on pages 62, 63, and 73.]
- [244] Y. Sato, Y. Hiratsuka, I. Kawamata, S. Murata, and S.-i. M. Nomura. Micrometer-sized molecular robot changes its shape in response to signal molecules. *Sci. Robot*, 2(4), 2017. [Cited on pages 55, 126, and 129.]
- [245] T. B. Saw, A. Doostmohammadi, V. Nier, L. Kocgozlu, S. Thampi, Y. Toyama, P. Marcq, C. T. Lim, J. M. Yeomans, and B. Ladoux. Topological defects in epithelia govern cell death and extrusion. *Nature*, 544(7649):212–216, 2017. [Cited on page 91.]
- [246] V. Schaller, C. Weber, C. Semmrich, E. Frey, and A. R. Bausch. Polar patterns of driven filaments. *Nature*, 467(7311):73, 2010. [Cited on pages 29 and 31.]
- [247] J. W. Schopf. Fossil evidence of archaean life. *Philosophical Transactions of the Royal Society B: Biological Sciences*, 361(1470):869–885, 2006. [Cited on page 5.]
- [248] E. Schrödinger. *What Is Life? The Physical Aspect of the Living Cell*. Cambridge University Press, 1944. [Cited on page 11.]
- [249] N. C. Seeman. Nucleic acid junctions and lattices. *Journal of theoretical biology*, 99(2):237–247, 1982. [Cited on page 44.]
- [250] N. C. Seeman and H. F. Sleiman. Dna nanotechnology. *Nature reviews materials*, 3(1):1–23, 2017. [Cited on page 44.]
- [251] U. Seifert. Dynamics of a bound membrane. *Physical review E*, 49(4):3124, 1994. [Cited on page 175.]
- [252] R. Sender, S. Fuchs, and R. Milo. Revised estimates for the number of human and bacteria cells in the body. *PLoS biology*, 14(8):e1002533, 2016. [Cited on page 5.]
- [253] A. Senoussi, S. Kashida, R. Voituriez, J.-C. Galas, A. Maitra, and A. Estévez-Torres. Tunable corrugated patterns in an active nematic sheet. *Proceedings of the National Academy of Sciences*, 116(45):22464–22470, 2019. [Cited on pages 11, 12, 77, 162, 181, and 191.]
- [254] A. Senoussi, J. Lee Tin Wah, Y. Shimizu, J. Robert, A. Jaramillo, S. Findeiss, I. M. Axmann, and A. Estevez-Torres. Quantitative characterization of translational riboregulators using an in vitro transcription–translation system. *ACS synthetic biology*, 7(5):1269–1278, 2018. [Cited on pages 12, 149, 162, and 183.]

- [255] S. H. Shabbir, M. M. Cleland, R. D. Goldman, and M. Mrksich. Geometric control of vimentin intermediate filaments. *Biomaterials*, 35(5):1359–1366, 2014. [Cited on page 24.]
- [256] R. Sheth, L. Marcon, M. F. Bastida, M. Junco, L. Quintana, R. Dahn, M. Kmita, J. Sharpe, and M. A. Ros. Hox genes regulate digit patterning by controlling the wavelength of a turing-type mechanism. *Science*, 338(6113):1476–1480, 2012. [Cited on page 47.]
- [257] T. S. Shim, Z. G. Estephan, Z. Qian, J. H. Prosser, S. Y. Lee, D. M. Chenoweth, D. Lee, S.-J. Park, and J. C. Crocker. Shape changing thin films powered by dna hybridization. *Nature nanotechnology*, 12(1):41, 2017. [Cited on page 9.]
- [258] Y. Shimizu, A. Inoue, Y. Tomari, T. Suzuki, T. Yokogawa, K. Nishikawa, and T. Ueda. Cell-free translation reconstituted with purified components. *Nature biotechnology*, 19(8):751–755, 2001. [Cited on pages 142, 143, and 197.]
- [259] Y. Shimizu, T. Kanamori, and T. Ueda. Protein synthesis by pure translation systems. *Methods*, 36(3):299–304, 2005. [Cited on pages 143, 147, 171, and 172.]
- [260] J. Shin and V. Noireaux. Efficient cell-free expression with the endogenous e. coli rna polymerase and sigma factor 70. *Journal of biological engineering*, 4(1):8, 2010. [Cited on page 154.]
- [261] D. Siegal-Gaskins, Z. A. Tuza, J. Kim, V. Noireaux, and R. M. Murray. Gene circuit performance characterization and resource usage in a cell-free “breadboard”. *ACS synthetic biology*, 3(6):416–425, 2014. [Cited on pages 154 and 156.]
- [262] A. D. Silverman, A. S. Karim, and M. C. Jewett. Cell-free gene expression: an expanded repertoire of applications. *Nature reviews genetics*, pages 1–20, 2019. [Cited on pages 41, 142, and 143.]
- [263] C. Simon, R. Kusters, V. Caorsi, A. Allard, M. Abou-Ghali, J. Manzi, A. Di Cicco, D. Lévy, M. Lenz, J.-F. Joanny, et al. Actin dynamics drive cell-like membrane deformation. *Nature physics*, page 1, 2019. [Cited on pages 92 and 93.]
- [264] I. Slavkov, D. Carrillo-Zapata, N. Carranza, X. Diego, F. Jansson, J. Kaandorp, S. Hauert, and J. Sharpe. Morphogenesis in robot swarms. *Science robotics*, 3(25):eaau9178, 2018. [Cited on page 20.]
- [265] R. S. H. Smith, C. Bader, S. Sharma, D. Kolb, T.-C. Tang, A. Hosny, F. Moser, J. C. Weaver, C. A. Voigt, and N. Oxman. Hybrid living materials: Digital design and fabrication of 3d multimaterial structures with programmable biohybrid surfaces. *Advanced Functional Materials*, page 1907401, 2019. [Cited on page 8.]
- [266] T. Song, A. Eshra, S. Shah, H. Bui, D. Fu, M. Yang, R. Mokhtar, and J. Reif. Fast and compact dna logic circuits based on single-stranded gates using strand-displacing polymerase. *Nature nanotechnology*, 14(11):1075–1081, 2019. [Cited on page 44.]

- [267] V. Soni, E. S. Bililign, S. Magkiriadou, S. Sacanna, D. Bartolo, M. J. Shelley, and W. T. Irvine. The odd free surface flows of a colloidal chiral fluid. *Nature physics*, 15(11):1188–1194, 2019. [Cited on page 21.]
- [268] N. Srinivas, J. Parkin, G. Seelig, E. Winfree, and D. Soloveichik. Enzyme-free nucleic acid dynamical systems. *Science*, 358(6369):eaal2052, 2017. [Cited on page 43.]
- [269] T. Stögbauer, L. Windhager, R. Zimmer, and J. O. Rädler. Experiment and mathematical modeling of gene expression dynamics in a cell-free system. *Integrative Biology*, 4(5):494–501, 2012. [Cited on pages 143, 148, 150, and 151.]
- [270] R. Subramanian and J. Gelles. Two distinct modes of processive kinesin movement in mixtures of atp and amp-pnp. *The Journal of general physiology*, 130(5):445–455, 2007. [Cited on pages 63 and 168.]
- [271] Y. Sumino, K. H. Nagai, Y. Shitaka, D. Tanaka, K. Yoshikawa, H. Chaté, and K. Oiwa. Large-scale vortex lattice emerging from collectively moving microtubules. *Nature*, 483(7390):448, 2012. [Cited on page 29.]
- [272] Z. Z. Sun, E. Yeung, C. A. Hayes, V. Noireaux, and R. M. Murray. Linear dna for rapid prototyping of synthetic biological circuits in an escherichia coli based tx-tl cell-free system. *ACS synthetic biology*, 3(6):387–397, 2013. [Cited on page 143.]
- [273] S. Sunagawa, L. P. Coelho, S. Chaffron, J. R. Kultima, K. Labadie, G. Salazar, B. Djahan-schiri, G. Zeller, D. R. Mende, A. Alberti, et al. Structure and function of the global ocean microbiome. *Science*, 348(6237):1261359, 2015. [Cited on page 5.]
- [274] T. Surrey, F. Nédélec, S. Leibler, and E. Karsenti. Physical properties determining self-organization of motors and microtubules. *Science*, 292(5519):1167–1171, 2001. [Cited on pages 29 and 62.]
- [275] B. Swalla. Building divergent body plans with similar genetic pathways. *Heredity*, 97(3):235–243, 2006. [Cited on page 6.]
- [276] M. K. Takahashi, J. Chappell, C. A. Hayes, Z. Z. Sun, J. Kim, V. Singhal, K. J. Spring, S. Al-Khabouri, C. P. Fall, V. Noireaux, et al. Rapidly characterizing the fast dynamics of rna genetic circuitry with cell-free transcription–translation (tx-tl) systems. *ACS synthetic biology*, 4(5):503–515, 2014. [Cited on pages 143, 154, and 156.]
- [277] A. J. Tan, E. Roberts, S. A. Smith, U. A. Olvera, J. Arteaga, S. Fortini, K. A. Mitchell, and L. S. Hirst. Topological chaos in active nematics. *Nature physics*, 15(10):1033–1039, 2019. [Cited on pages 86 and 97.]
- [278] A. M. Tayar, E. Karzbrun, V. Noireaux, and R. H. Bar-Ziv. Propagating gene expression fronts in a one-dimensional coupled system of artificial cells. *Nature physics*, 11(12):1037, 2015. [Cited on page 42.]



- [279] A. M. Tayar, E. Karzbrun, V. Noireaux, and R. H. Bar-Ziv. Synchrony and pattern formation of coupled genetic oscillators on a chip of artificial cells. *Proceedings of the National Academy of Sciences*, 114(44):11609–11614, 2017. [Cited on page 42.]
- [280] E. Te Brinke, J. Groen, A. Herrmann, H. A. Heus, G. Rivas, E. Spruijt, and W. T. Huck. Dissipative adaptation in driven self-assembly leading to self-dividing fibrils. *Nature nanotechnology*, 13(9):849, 2018. [Cited on page 25.]
- [281] S. P. Thampi, R. Golestanian, and J. M. Yeomans. Instabilities and topological defects in active nematics. *Europhysics Letters*, 105(1):18001, 2014. [Cited on page 90.]
- [282] I. Theurkauff, C. Cottin-Bizonne, J. Palacci, C. Ybert, and L. Bocquet. Dynamic clustering in active colloidal suspensions with chemical signaling. *Physical review letters*, 108(26):268303, 2012. [Cited on page 21.]
- [283] D. W. Thompson. *On Growth and Form*. Cambridge University Press, 1917. [Cited on pages 5 and 6.]
- [284] A. J. Thubagere, W. Li, R. F. Johnson, Z. Chen, S. Doroudi, Y. L. Lee, G. Izatt, S. Wittman, N. Srinivas, D. Woods, et al. A cargo-sorting dna robot. *Science*, 357(6356):eaan6558, 2017. [Cited on page 44.]
- [285] L. G. Tilney and D. A. Portnoy. Actin filaments and the growth, movement, and spread of the intracellular bacterial parasite, listeria monocytogenes. *The Journal of cell biology*, 109(4):1597–1608, 1989. [Cited on page 24.]
- [286] J. Toner and Y. Tu. Long-range order in a two-dimensional dynamical xy model: how birds fly together. *Physical review letters*, 75(23):4326, 1995. [Cited on page 32.]
- [287] J. Toner, Y. Tu, and S. Ramaswamy. Hydrodynamics and phases of flocks. *Annals of Physics*, 318(1):170–244, 2005. [Cited on page 79.]
- [288] T. Torisawa, D. Taniguchi, S. Ishihara, and K. Oiwa. Spontaneous formation of a globally connected contractile network in a microtubule-motor system. *Biophysical journal*, 111(2):373–385, 2016. [Cited on pages 30 and 73.]
- [289] A. M. Turing. The chemical basis of morphogenesis. *Philosophical Transactions of the Royal Society B: Biological Sciences*, 237(641):37–72, 1952. [Cited on page 38.]
- [290] G. Urtel, A. Estevez-Torres, and J.-C. Galas. Dna-based long-lived reaction–diffusion patterning in a host hydrogel. *Soft matter*, 15(45):9343–9351, 2019. [Cited on pages 46, 112, and 115.]
- [291] G. Urtel, M. Van Der Hofstadt, J.-C. Galas, and A. Estévez-Torres. rexpax: an isothermal amplification scheme that is robust to autocatalytic parasites. *Biochemistry*, 58(23):2675–2681, 2019. [Cited on page 107.]
- [292] R. D. Vale. The molecular motor toolbox for intracellular transport. *Cell*, 112(4):467–480, 2003. [Cited on page 28.]

- [293] R. D. Vale and R. A. Milligan. The way things move: looking under the hood of molecular motor proteins. *Science*, 288(5463):88–95, 2000. [Cited on page 27.]
- [294] R. D. Vale, T. S. Reese, and M. P. Sheetz. Identification of a novel force-generating protein, kinesin, involved in microtubule-based motility. *Cell*, 42(1):39–50, 1985. [Cited on page 26.]
- [295] R. D. Vale, B. J. Schnapp, T. S. Reese, and M. P. Sheetz. Organelle, bead, and microtubule translocations promoted by soluble factors from the squid giant axon. *Cell*, 40(3):559–569, 1985. [Cited on page 29.]
- [296] J. A. Valeri, K. M. Collins, B. A. Lepe, T. K. Lu, and D. M. Camacho. Sequence-to-function deep learning frameworks for synthetic biology. *bioRxiv*, page 870055, 2019. [Cited on page 160.]
- [297] M. Valet, L. L. Pontani, A. M. Prevost, and E. Wandersman. Quasistatic microdroplet production in a capillary trap. *Physical review applied*, 9(1):014002, 2018. [Cited on pages 93 and 94.]
- [298] M. Valet, L.-L. Pontani, R. Voituriez, E. Wandersman, and A. M. Prevost. Diffusion through nanopores in connected lipid bilayer networks. *Physical review letters*, 123(8):088101, 2019. [Cited on page 93.]
- [299] V. K. Vanag and I. R. Epstein. Pattern formation in a tunable medium: The belousov-zhabotinsky reaction in an aerosol of microemulsion. *Physical review letters*, 87(22):228301, 2001. [Cited on page 39.]
- [300] G. Vásárhelyi, C. Virágh, G. Somorjai, T. Nepusz, A. E. Eiben, and T. Vicsek. Optimized flocking of autonomous drones in confined environments. *Science robotics*, 3(20):eaat3536, 2018. [Cited on page 20.]
- [301] T. Vicsek, A. Czirók, E. Ben-Jacob, I. Cohen, and O. Shochet. Novel type of phase transition in a system of self-driven particles. *Physical review letters*, 75(6):1226, 1995. [Cited on page 32.]
- [302] G. Villar, A. D. Graham, and H. Bayley. A tissue-like printed material. *Science*, 340(6128):48–52, 2013. [Cited on pages 8, 57, 163, and 200.]
- [303] A. Vincent, J. T. Blankenship, and E. Wieschaus. Integration of the head and trunk segmentation systems controls cephalic furrow formation in drosophila. *Development*, 124(19):3747–3754, 1997. [Cited on page 52.]
- [304] R. Voituriez, J. Joanny, and J. Prost. Generic phase diagram of active polar films. *Physical review letters*, 96(2):028102, 2006. [Cited on page 35.]
- [305] R. Voituriez, J.-F. Joanny, and J. Prost. Spontaneous flow transition in active polar gels. *Europhysics Letters*, 70(3):404, 2005. [Cited on pages 30, 79, and 83.]
- [306] W.-A. Wang, M. G.-J. Navarro, and Z. Gueroui. Self-assembly of magnetically-functionalized molecular motors and microtubules into active gels. *Soft matter*, 2019. [Cited on page 98.]

- [307] J. D. Watson, F. H. Crick, et al. Molecular structure of nucleic acids. *Nature*, 171(4356):737–738, 1953. [Cited on page 7.]
- [308] K. L. Weirich, K. Dasbiswas, T. A. Witten, S. Vaikuntanathan, and M. L. Gardel. Self-organizing motors divide active liquid droplets. *Proceedings of the National Academy of Sciences*, 116(23):11125–11130, 2019. [Cited on page 92.]
- [309] M. Weiss, J. P. Frohnmayer, L. T. Benk, B. Haller, J.-W. Janiesch, T. Heitkamp, M. Börsch, R. B. Lira, R. Dimova, R. Lipowsky, et al. Sequential bottom-up assembly of mechanically stabilized synthetic cells by microfluidics. *Nature materials*, 17(1):89–96, 2018. [Cited on pages 163 and 200.]
- [310] H. H. Wensink, J. Dunkel, S. Heidenreich, K. Drescher, R. E. Goldstein, H. Löwen, and J. M. Yeomans. Meso-scale turbulence in living fluids. *Proceedings of the National Academy of Sciences*, 109(36):14308–14313, 2012. [Cited on page 83.]
- [311] M. N. Win and C. D. Smolke. A modular and extensible rna-based gene-regulatory platform for engineering cellular function. *Proceedings of the National Academy of Sciences*, 104(36):14283–14288, 2007. [Cited on page 141.]
- [312] A. T. Winfree. Spiral waves of chemical activity. *Science*, 175(4022):634–636, 1972. [Cited on page 39.]
- [313] B. C. Wintle, C. R. Boehm, C. Rhodes, J. C. Molloy, P. Millett, L. Adam, R. Breitling, R. Carlson, R. Casagrande, M. Dando, et al. Point of view: A transatlantic perspective on 20 emerging issues in biological engineering. *Elife*, 6:e30247, 2017. [Cited on page 10.]
- [314] A. J. Wollman, C. Sanchez-Cano, H. M. Carstairs, R. A. Cross, and A. J. Turberfield. Transport and self-organization across different length scales powered by motor proteins and programmed by dna. *Nature nanotechnology*, 9(1):44, 2014. [Cited on pages 55, 56, 63, and 126.]
- [315] V. Wollrab, J. M. Belmonte, L. Baldauf, M. Leptin, F. Nédélec, and G. H. Koenderink. Polarity sorting drives remodeling of actin-myosin networks. *J Cell Sci*, 132(4):jcs219717, 2019. [Cited on page 29.]
- [316] L. Wolpert. Positional information and the spatial pattern of cellular differentiation. *Journal of theoretical biology*, 25(1):1–47, 1969. [Cited on page 51.]
- [317] L. Wolpert and C. Tickle. *Principles of Development*. Oxford University Press, 2011. [Cited on page 51.]
- [318] J. Wong, A. Chilkoti, and V. T. Moy. Direct force measurements of the streptavidin–biotin interaction. *Biomolecular engineering*, 16(1-4):45–55, 1999. [Cited on page 62.]
- [319] K.-T. Wu, J. B. Hishamunda, D. T. Chen, S. J. DeCamp, Y.-W. Chang, A. Fernández-Nieves, S. Fraden, and Z. Dogic. Transition from turbulent to coherent flows in confined three-dimensional active fluids. *Science*, 355(6331):eaal1979, 2017. [Cited on pages 30, 63, 77, 78, 80, 86, 98, 123, and 162.]

- [320] A. Xayaphoummine, V. Viasnoff, S. Harlepp, and H. Isambert. Encoding folding paths of rna switches. *Nucleic acids research*, 35(2):614–622, 2006. [Cited on page 141.]
- [321] R. Yoshida, T. Takahashi, T. Yamaguchi, and H. Ichijo. Self-oscillating gel. *Journal of the American Chemical Society*, 118(21):5134–5135, 1996. [Cited on page 54.]
- [322] R. Yoshida and T. Ueki. Evolution of self-oscillating polymer gels as autonomous polymer systems. *NPG Asia Materials*, 6(6):e107–e107, 2014. [Cited on pages 54 and 55.]
- [323] B. Yurke, A. J. Turberfield, A. P. Mills, F. C. Simmel, and J. L. Neumann. A dna-fuelled molecular machine made of dna. *Nature*, 406(6796):605–608, 2000. [Cited on pages 43 and 44.]
- [324] J. N. Zadeh, C. D. Steenberg, J. S. Bois, B. R. Wolfe, M. B. Pierce, A. R. Khan, R. M. Dirks, and N. A. Pierce. Nupack: analysis and design of nucleic acid systems. *Journal of computational chemistry*, 32(1):170–173, 2011. [Cited on pages 141, 145, and 146.]
- [325] A. S. Zadorin, Y. Rondelez, J.-C. Galas, and A. Estevez-Torres. Synthesis of programmable reaction-diffusion fronts using dna catalyzers. *Physical review letters*, 114(6):068301, 2015. [Cited on pages 38, 46, 48, 109, 112, 115, and 189.]
- [326] A. S. Zadorin, Y. Rondelez, G. Gines, V. Dilhas, G. Urtel, A. Zambrano, J.-C. Galas, and A. Estévez-Torres. Synthesis and materialization of a reaction-diffusion french flag pattern. *Nature chemistry*, 9(10):990, 2017. [Cited on pages 46, 47, 48, 109, 126, 134, and 162.]
- [327] A. Zaikin and A. Zhabotinsky. Concentration wave propagation in two-dimensional liquid-phase self-oscillating system. *Nature*, 225(5232):535–537, 1970. [Cited on pages 39 and 112.]
- [328] A. Zambrano, A. Zadorin, Y. Rondelez, A. Estévez-Torres, and J.-C. Galas. Pursuit-and-evasion reaction-diffusion waves in microreactors with tailored geometry. *The Journal of Physical Chemistry B*, 119(17):5349–5355, 2015. [Cited on page 46.]
- [329] A. Zambrano Ramirez. *Synthesis of reaction-diffusion patterns with DNA: towards Turing patterns*. PhD thesis, Paris Saclay, 2016. [Cited on page 126.]
- [330] J. Zenk, D. Scalise, K. Wang, P. Dorsey, J. Fern, A. Cruz, and R. Schulman. Stable dna-based reaction–diffusion patterns. *RSC Advances*, 7(29):18032–18040, 2017. [Cited on page 47.]
- [331] D. Y. Zhang and G. Seelig. Dynamic dna nanotechnology using strand-displacement reactions. *Nature chemistry*, 3(2):103, 2011. [Cited on page 43.]
- [332] D. Y. Zhang and E. Winfree. Control of dna strand displacement kinetics using toehold exchange. *Journal of the American Chemical Society*, 131(47):17303–17314, 2009. [Cited on page 43.]
- [333] H.-P. Zhang, A. Be’er, E.-L. Florin, and H. L. Swinney. Collective motion and density fluctuations in bacterial colonies. *Proceedings of the National Academy of Sciences*, 107(31):13626–13630, 2010. [Cited on pages 19 and 20.]

- [334] R. Zhang, S. A. Redford, P. V. Ruijgrok, N. Kumar, A. Mozaffari, S. Zemsky, A. R. Dinner, V. Vitelli, Z. Bryant, M. L. Gardel, et al. Structuring stress for active materials control. *arXiv preprint arXiv:1912.01630*, 2019. [Cited on page 99.]
- [335] Y. Zhang, J. L. Ptacin, E. C. Fischer, H. R. Aerni, C. E. Caffaro, K. San Jose, A. W. Feldman, C. R. Turner, and F. E. Romesberg. A semi-synthetic organism that stores and retrieves increased genetic information. *Nature*, 551(7682):644, 2017. [Cited on page 8.]
- [336] S. Zhou, A. Sokolov, O. D. Lavrentovich, and I. S. Aranson. Living liquid crystals. *Proceedings of the National Academy of Sciences*, 111(4):1265–1270, 2014. [Cited on pages 83 and 91.]
- [337] K. Zieske and P. Schwille. Reconstitution of self-organizing protein gradients as spatial cues in cell-free systems. *Elife*, 3:e03949, 2014. [Cited on page 40.]
- [338] M. Zuker. Mfold web server for nucleic acid folding and hybridization prediction. *Nucleic acids research*, 31(13):3406–3415, 2003. [Cited on page 141.]

